Studies of Large Volcanoes on the Terrestrial Planets: Implications for Stress State, Tectonics, Structural Evolution, and Moat Filling

by

Patrick Joseph McGovern Jr.

S.B., Aeronautics and Astronautics
Massachusetts Institute of Technology
(1986)

Submitted to the Department of Earth, Atmospheric, and Planetary Sciences
in partial fulfillment of the requirements for the degree of

DOCTOR OF PHILOSOPHY

at the

MASSACHUSETTS INSTITUTE OF TECHNOLOGY

June 1996

Author .....
Department of Earth, Atmospheric, and Planetary Sciences
April 22, 1996

Certified by .....
Sean C. Solomon
Thesis Supervisor

Accepted by .....
Thomas H. Jordan
Department Head

Studies of Large Volcanoes on the Terrestrial Planets: Implications for Stress State, Tectonics, Structural Evolution, and Moat Filling

by

Patrick Joseph McGovern Jr.

Submitted to the Department of Earth, Atmospheric, and Planetary Sciences on April 22, 1996 in Partial Fulfillment of the Requirements for the Degree of Doctor of Philosophy in Geophysics

Abstract

Stresses and displacements associated with loading of the lithosphere by volcanic edifices are modeled using a finite element approach. A suite of models is considered to test the effects of elastic lithosphere thickness, edifice size, and basal boundary condition on the evolution of stresses in growing volcanoes. Calculated stresses are used to predict locations and types of faulting and magma movement paths in the lithosphere and the edifices. These predictions are compared to observed distributions of tectonic features and intrusion and eruption sites on large volcanoes on Earth, Mars, and Venus, in order to infer the conditions that determine the unique styles of large edifice construction on each planet.

The basal boundary condition plays a key role in the development of large volcanoes on Earth. Volcanoes emplaced on a > 100 m thick layer of abyssal clay sediments (the Hawaiian Islands and probably Reunion Island) are characterized by large size and well-defined linear loci of intrusive and eruptive activity, known as rift zones. The clay layer beneath these volcanoes acts as a basal decollement, facilitating lateral flank movement. The stress state in basally detached volcanoes is consistent with formation of rift zones radial to the central magma chamber and easy magma ascent to these structures. Volcanoes lacking such a basal clay layer (such as those in the Galapagos, Marquesas, and Canary chains) are characterized by smaller size and the lack of well-defined Hawaiian-style rift zones. These volcanoes are likely solidly attached (welded) to the underlying lithosphere. Horizontal compressive stresses (inversely proportional to elastic lithosphere thickness) in basally welded volcanoes inhibit magma ascent and thus inhibit volcano growth. A tradeoff between the strength of the mantle magma source and horizontal compressive stress determines the ultimate size of basally welded volcanoes.

Large volcanoes in the Tharsis region of Mars exhibit characteristics of basally detached volcanoes: large size, linear zones of eruption, and evidence for catastrophic flank failure. The Tharsis Montes (Arsia Mons, Pavonis Mons, and Ascraeus Mons), located high on

the Tharsis Rise, exhibit deep linear southwest-northeast oriented embayments that are the sources of voluminous flows. All three volcanoes also exhibit evidence of catastrophic flank failure to the northwest. These patterns are consistent with the interaction of a basal detachment with the regional slope of the Tharsis rise (down to the northwest). Olympus Mons, the largest known volcano in the solar system, lacks linear eruptive zones but exhibits a vast aureole of disrupted terrain, with greatest extent to the northwest. At the edge of the edifice above the aureole is a steep basal scarp ranging up to 10 km in height. The scarp is interpreted as the coalesced headwalls of large landslides which constitute the aureole deposits. These structures are indicative of a detached basal boundary condition, and are analogous to smaller structures on Hawaiian volcanoes.

Large volcanoes on Venus are characterized by a topographically prominent edifice and a surrounding relatively flat apron of radial flows. Only 3 out of 145 large volcanoes show evidence of a topographic moat. Venus volcanoes lack evidence for catastrophic flank failure and Hawaiian-style rift zones, characteristics of basally detached volcanoes. This evidence and current atmospheric conditions on Venus favor a welded basal boundary condition for these volcanoes. Basally welded volcanoes of these sizes will induce large growth-inhibiting compressive stresses. Edifice growth on Venus was likely limited to a time when the lithosphere was thick enough to support the loads at low levels of stress. Presuming that the volcanoes deflect the lithosphere, the resulting flexural moats are filled with the flows that constitute the radial flow aprons. Accounting for material filling the flexural depression and surrounding moat results in total volcano volumes up to an order of magnitude greater than those of the topographically prominent edifice alone.

Thesis Supervisor: Sean C. Solomon
Title: Professor of Geophysics

Acknowledgements

At last I sit down to type in my final contribution, which is to recognize the contributions of others to the completion of this thesis. Given the duration of my tenure at M.I.T., it is inevitable that there are many people worthy of acknowledgment. I apologize in advance to anyone I have inadvertenly left out: I hope you will forgive a frazzled veteran grad student in the very last stages of his trial.

The most obvious come first. So obvious, in fact, that I forgot to acknowledge them in my high school valedictorian speech. I guess I was too busy trying to impress my friends by sniping at the school administration to acknowledge those whose support I had taken for granted. But my parents, Patrick J. (Sr.) and Louise McGovern, deserve all the credit for my academic success. They did it all, from simply passing on the genes, to providing encouragment to and high expectations for scholarly pursuits, to dealing with the financial aspects of my decision to attend a notoriously "high rent" university (um, I mean Institute). This time I won't forget: I am grateful for their love and support over the years, and I hereby dedicate this thesis to them.

Some say that the expression "IHTFP" stands for "Institute has the finest professors". In many cases, that interpretation is correct. Although in one case, "has" would be changed to "had". Sean Solomon, now of the Department of Terrestrial Magnetism at the Carnegie Institution of Washington (although still a Visiting Professor at M.I.T.), has provided a consistent standard of scientific excellence, and I am grateful that he has held me to that high standard, even when it hurt! I am glad that we will continue to work together in the future, at Carnegie and wherever I subsequently end up. I am indebted also to my thesis committee, Fred Frey, Chris Marone, George McGill, and Maria Zuber, for their helpful and constructive criticisms of the thesis. Professors Brad Hager and Marcia McNutt also provided helpful advice (thanks also to Brad for shouldering some of the administrative burden). I also must thank Professor Gerry Schubert of U.C.L.A. for his support during my 1-year stint at that school (and for his good-natured acceptance of my defection back to

M.I.T.).

My other set of teachers, of course, consists of my fellow students. In particular, my colleagues in the planetary business, Susan Evans, Nori Namiki, and Mark Simons, have been reliable resources for science matters, computer minutiae, and just plain goofing around. Also in the planetary lab, U.R.O.P. students Chris Siren and Seth McGinnis cheerfully helped to digest the sheer volume of Magellan data. The rest of the students on the 5th through 8th floors (you know who you are) were also great folks to be around. Credit for keeping me sane (and keeping me from ballooning) goes to the EAPS sports teams. Softball, volleyball, soccer, and even basketball were loads of fun. Hockey of course gets its own singular mention. I can honestly say that the most useful courses I have ever taken at M.I.T. were the P.E. skating and hockey classes my freshman year (and they say M.I.T. doesn't teach "life skills"!) I will sorely miss EAPS hockey games and the folks who played on the teams. I hope you folks get good draft picks next year!

And no, I haven't forgotten the people who really make things work around here. The administrative staff on the 5th floor (formerly Katherine Ware, Libby Kurten, Marie Senat, Deb Sykes, and currently Darla Smutka) kept things running smoothly, making my task much easier. The computer system administrators Dave Krowitz, Linda Meinke, and Michael Batchelder, have also been indispensible to this effort. I would particularly like to thank Linda for going out of her way to make sure everything was o.k. down here even though it strictly speaking wasn't her responsibility.

My status as an M.I.T. "lifer" is about to come to an end. In the misty distant past (the mid-80s), the wild capers and madcap antics of my fellow undergraduate inmates prepared me to deal with the academic behemoth. I hereby salute my pals from those days, many of whom were, like me, unable to escape the pull of the 'tute and the Boston area. I perhaps should be less specific here; I also salute more than a decade's worth of 41st Westers (sometimes known as "larries") who I came to know both before and after getting my Aero/Astro degree. And thanks to anybody I ever played music with (especially the madmen of Dr. Lüst): I hope

to return to such activity soon. I must thank the denizens of Decomoronoanthropolis (the Dumb Guys) for taking me in during the last year and a half of my travail. Spoon!

And now for a word about our sponsors. This work was brought to you by the National Aeronautics and Space Administration under grants NAGW-1937, NAGW-3276, and NAGW-3425. I guess my thesis and TANG™ have something in common.

Table of Contents

Chapter 1

Introduction

Volcanism is a primary surface manifestation of the interior evolution of a planet. Volcanic deposits can take many forms; perhaps the most striking of these is the large shield volcano. On Earth, such structures are commonly found in linear chains within ocean basins. The formation of such volcanoes is attributed to melt production in an anomalously hot region of shallow mantle, termed a hotspot. Hotspots in turn are generally believed to be caused by hot plumes ascending from deep in the mantle. Spacecraft sent to the planets in the last several decades have returned a wealth of evidence indicating the presence of large shield volcanoes on other planets. In 1971, the Mariner 9 probe detected 4 prominent dark spots protruding from a global dust storm on Mars [*Snyder and Moroz*, 1992]. As the storm cleared, these features were revealed as massive shield volcanoes: Olympus Mons and the linearly-arrayed Tharsis Montes (Arsia Mons, Pavonis Mons, and Ascraeus Mons, from southwest to northeast). Image data from Mariner 9 and the subsequent Viking missions to Mars revealed several other large volcanoes in the Tharsis region, as well as a group of three large shields in the Elysium region [*Mouginis-Mark et al.*, 1992]. Evidence for the existence of large volcanoes on Venus was first obtained by United States and Soviet missions (radar mapping by the Pioneer Venus and Venera missions, respectively) in the early 1980's (with significant contributions from Earth-based radar imaging as well). The near-global high-resolution radar

imaging coverage provided by the Magellan mission has allowed identification of nearly 150 large shield volcanoes [*Head et al.*, 1992]. By analogy to comparable structures on Earth, large volcanoes on Mars and Venus are frequently interpreted as surface manifestations of mantle plumes (e.g., [*Schubert et al.*, 1992] and [*Head et al.*, 1992], respectively).

Studies of large terrestrial volcanoes benefit from the opportunity to perform a wide range of studies, both in-situ and by remote sensing. Geophysical data, collected from seismic and gravity experiments, illuminate the deep structure of the volcano and its interaction with the lithosphere. Geodetic studies constrain the mechanisms of magma movement and flank growth and instability. Petrological studies constrain the composition of the magmatic source region and the history of magmatic ascent, storage and emplacement. Geological studies, including the generation of topographic and bathymetric maps and descriptions of subareal and subaqueous deposits, document the characteristic structures of volcanoes. Sample collection from drill holes bored into volcano flanks [*Rançon et al.*, 1989; *Hawaii Scientific Drilling Project*, 1995] and the surrounding seafloor [e.g., *Shipboard Scientific Party*, 1992b] allow reconstruction of the history of the volcano. Note that the extent and quality of the studies described above vary greatly among volcanoes. For example, extensive land development and a large population base facilitates studies of the volcanoes in the Hawaiian chain. More isolated and remote volcanoes, such as those of the Galápagos chain, are more sparsely and infrequently studied. Indeed, studies of these volcanoes may rely heavily on the same remote sensing techniques used in planetary missions [e.g., *Rowland and Munro*, 1992]. Models of large volcano structure and evolution are better constrained for the more well-studied volcanoes (such as those of Hawaii); consequently, observations from these volcanoes have had the greatest influence on the development of models for volcanic processes.

By contrast, studies of large volcanoes on the other terrestrial planets are currently limited to remotely sensed data from infrequent missions. No local seismic or geodetic data constrain the deep structure of these volcanoes. No rock samples from large volcanoes are available to constrain magmatic composition and emplacement mechanisms. Detailed field

mapping of individual flow units and small structures is generally precluded. At present, all conclusions about the structure and evolution of large volcanoes on Venus and Mars must be drawn or inferred from imaging, topography, gravity and multispectral mapping data obtained by orbiting spacecraft. Such data are nonetheless adequate to address basic questions about these volcanoes. Observed tectonic features provide strong constraints on the stress state in the volcanoes. The dimensions of edifices and flow units are readily measurable. Indeed, the quality and resolution of these data sometimes surpass those of data available for volcanoes on Earth, due to the obscuring effects of the ocean and subaqueously emplaced material derived from erosion and mass wasting of volcano flanks [e.g., *Holcomb and Searle*, 1991].

In this thesis, I attempt to determine the mechanical conditions that control the structural evolution of large volcanoes on Mars, Earth, and Venus. I use the image and topography data returned from missions to Mars and Venus to constrain the structure and stress state of the large volcanoes on these planets. I use both remote sensing data and data collected in-situ as constraints on the structure and stress state of terrestrial volcanoes. Conceptual structural models developed for the most well-studied volcanoes on Earth provide a basis for generating structural models of volcanoes on all three planets. These firmly-established models take into account the importance of flexure of the lithosphere in response to loading by the volcano. Previous treatments of plate flexure beneath volcanic loads have primarily relied on analytic elastic plate flexure solutions that fail to account for the state of stress in the volcano itself. I present quantitative models of the stress states in large volcanic edifices using a finite element approach which allows calculation of the stress state inside the edifice as well as in the lithosphere. The calculated stress state can be used to predict the style and orientation of faulting, by application of a Mohr-Coulomb failure criterion. These model predictions can then be compared to observed distributions of tectonic structures, to constrain the set of conditions (including basal boundary condition, elastic lithosphere thickness, and loading history) that governs the development of large volcanoes on a given planet.

Chapter 2 deals with the four largest volcanoes on Mars: Olympus Mons and the Tharsis Montes (Arsia Mons, Pavonis Mons and Ascraeus Mons). All four show evidence for landsliding or mass movement along their periphery. By analogy with the structure of the flanks of Hawaiian volcanoes, I propose the existence of a decollement at the base of these volcanoes. I use finite element models to calculate stresses and displacements in a volcanic edifice. These models can incorporate a basal detachment and simulate incremental edifice growth. I use the stress orientations and magnitudes (applying a Mohr-Coulomb failure criterion) to predict the types and orientations of faults in the edifice and lithosphere. I compare the predictions of the models to the observed distribution of tectonic features on and around the volcanoes. I conclude that the observed features are inconsistent with a completely welded basal boundary condition, but are consistent with a partial (Olympus Mons) to complete (Tharsis Montes) basal detachment. I also conclude that the long-wavelength topography of the Tharsis rise controls the distribution of graben and the orientation of rift and mass wasting structures on the flanks of the Tharsis Montes and Olympus Mons.

In Chapter 3, I investigate the structure of large volcanoes in five hotspot volcano chains on Earth. I explore in detail the nature of the interface between volcano and lithosphere. Conditions favorable to the formation of a basal detachment (a sufficiently thick clay sediment layer and low-amplitude basement topography) exist only at two of the five chains (Hawaii and Reunion). Volcanoes in these chains are significantly larger than those in other chains and are the only ones that exhibit well-defined volcanic rift zones. Volcanoes in the other chains (Galapagos, Marquesas, and Canaries) are much smaller and lack well-defined rift zones. I calculate finite element models for volcanoes both with and without basal detachments. The state of stress in basally detached volcanoes favors both sustained magma ascent and formation of linear rift zones. The orientations of such rift zones can be influenced by the topography of older shields in the chain (as originally demonstrated by *Fiske and Jackson* [1972] for Hawaii), but perhaps also by the orientations of abyssal hills in the crustal basement. The state of stress in basally welded volcanoes impedes magma ascent, ultimately

limiting edifice size. Continued magma supply to basally welded volcanoes requires reorientation of the principal stresses. This can be accomplished by superposing stresses induced by expansion of a magma chamber on the stress state in the original welded-base models. I conclude that a balance between stresses induced by lithospheric flexure and magma chamber expansion controls the size, structure and tectonics of basally welded volcanoes.

Chapter 4 begins with an extensive survey of large volcanoes on Venus, using image and topography data returned from the Magellan mission to Venus. For a list of 145 large volcanoes on Venus, I define two characteristic radii: radius of a topographically prominent edifice, and radius of an apron of radial flows surrounding the edifice. The flow aprons tend to be flat; evidence of a topographic depression (moat) is found around only three volcanoes, or 2% of the population. Volcanoes on Venus lack the linear rift zones and basal slumps characteristic of basally detached volcanoes. These characteristics are consistent with the absence of detachment-forming low-permeability sediment on Venus. Accordingly, I calculate stresses for finite element models of incrementally grown, basally welded volcanoes. I demonstrate that the magnitude of horizontal compressive edifice stress is inversely proportional to elastic plate thickness. These horizontal compressive stresses will tend to shut off magma ascent and inhibit volcano growth. I propose that large volcano formation on Venus was inhibited until the lithosphere cooled sufficiently (after a global resurfacing event) to support volcanoes at relatively low levels of edifice stress. This proposition is consistent with the observation that the surfaces of large shield volcanoes are among the youngest on the planet [*Namiki and Solomon*, 1994; *Price and Suppe*, 1994]. I also consider the implications of the flat flow aprons for volcano structure. Assuming the flow aprons cover material filling a flexural moat, I calculate the volume of such material. For a realistic range of volcano and mantle densities, I find that the volume of the edifice plus the moat fill is 7-11 times the volume of the edifice itself. This result implies an order of magnitude correction to estimates of magmatic flux based on edifice volumes alone. Such a model also has important implications for the interpretation of surface flow units visible in the radar images.

I conclude the thesis with a chapter devoted to a discussion comparing and contrasting volcanoes on Venus, Earth and Mars. I also offer ideas for future work based on the results and interpretations of this thesis.

Chapter 2

State of Stress, Faulting, and Eruption Characteristics of Large Volcanoes on Mars

This chapter is presented as a reprint of an article that appeared in the December 1993 issue of *Journal of Geophysical Research (Planets)*.

JOURNAL OF GEOPHYSICAL RESEARCH, VOL. 98, NO. E12, PAGES 23,553–23,579, DECEMBER 25, 1993

State of Stress, Faulting, and Eruption Characteristics of Large Volcanoes on Mars

PATRICK J. MCGOVERN

Department of Earth, Atmospheric, and Planetary Sciences, Massachusetts Institute of Technology, Cambridge

SEAN C. SOLOMON

Department of Terrestrial Magnetism, Carnegie Institution of Washington, Washington, D.C.

The formation of a large volcano loads the underlying lithospheric plate and can lead to lithospheric flexure and faulting. In turn, lithospheric deformation affects the stress field beneath and within the volcanic edifice and can influence magma transport. Modeling the interaction of these processes is crucial to an understanding of the history of eruption characteristics and tectonic deformation of large volcanoes. We develop models of time-dependent stress and deformation for the Tharsis volcanoes on Mars. By means of a finite element code, we calculate stresses and displacements due to a volcano-shaped load emplaced on an elastic plate overlying a viscoelastic mantle. Models variously incorporate growth of the volcanic load with time and a detachment between volcano and lithosphere. The models illustrate the manner in which time-dependent stresses induced by lithospheric plate flexure beneath the volcanic load may affect eruption histories, and the derived stress fields can be related to tectonic features on and surrounding Martian volcanoes. As a result of flexure there are three regions where stresses become sufficiently large to cause failure by faulting, according to the Mohr-Coulomb criterion: at the surface of the plate just outward of the volcano, near the base of the elastic lithosphere beneath the center of the volcano, and on the upper flanks of the volcano early in its growth history. Normal faulting is the dominant mode of failure predicted for the first region, consistent with circumferential graben observed around the Tharsis Montes and with the scarp at the base of Olympus Mons, interpreted as a large-offset, listric normal fault. Normal faulting, mostly radially oriented, is predicted for the second region. Failure in the third region is predicted to consist of thrust faulting, circumferentially oriented on the upper and middle flanks and radially oriented on the lower flanks. In models simulating a growing volcano, this portion of the edifice is subsequently covered by later units which exhibit lower stresses and are not predicted to fail; this volume of early failure remains the most highly stressed area in the edifice. Concentric terraces, interpreted by some workers as thrust faults, on the upper flanks of Olympus Mons may correspond to the predicted circumferential thrust features, if the most recent increments of volcano growth were relatively large, or in the presence of local material property or stress field variations. For volcanoes detached from the plate, predicted failure in the edifice takes the form of radial normal faulting near the volcano base. The addition of a local extensional stress arising from the regional topographic slope yields a pattern of predicted faulting which closely matches that observed on the Tharsis Montes, including the development of radial rifts on the lower volcano flanks to the northeast and southwest and the asymmetric formation of circumferential flank graben. This stress state is also consistent with an interpretation of the aureole deposits of Olympus Mons as the result of gravity sliding along a basal detachment. Our models also suggest an explanation for the lack of strike-slip features, predicted by previously published flexural models, around the Tharsis volcanoes. For a given load increment, the first mode of near-surface failure for most of the area immediately outward of the load is circumferential normal faulting and graben formation. As the volcano grows and the flexural response to the increasing load proceeds, the predicted failure mode in a portion of this annular region surrounding the volcano changes to strike-slip faulting. Because normal faulting has been predicted to have taken place earlier, however, it is likely that release of later stresses will occur by reactivation and growth of these normal faults and graben rather than by the formation of new strike-slip faults.

INTRODUCTION

The major Tharsis volcanoes of Mars (Olympus Mons and the three Tharsis Montes: Arsia Mons, Pavonis Mons, and Ascraeus Mons) are among the largest known volcanic structures in the solar system. An understanding of the formation and evolution of these structures can provide important constraints on the processes that built and maintained the Tharsis Rise. In addition, the Tharsis volcanoes may be analogues to large hot-spot volcanoes on Earth, such as those of Hawaii. For instance, Kilauea and Olympus Mons have very similar ratios of volcano height to diameter and of basal scarp height to volcano height [*Borgia et al.*, 1990]. Thus studies of the evolution of large Martian volcanoes may yield insight into terrestrial volcanic processes as well. In this paper we utilize finite element models to evaluate the evolution of internal stress and deformation within and surrounding the Tharsis volcanoes, and we discuss how the time-dependent stress field may be relatable to the eruption characteristics of the volcanoes and to the formation of associated tectonic features.

To date the investigation of the evolution of stresses in large volcanoes has taken two paths: models of edifice stresses alone (usually finite element models with rigid bottom boundary conditions), and investigations of flexural stresses in the lithospheric plate supporting the volcano. As examples of the first category of study, *Chevallier and Verwoerd* [1988] used an axisymmetric planar finite element code to investigate the effect

Paper number 93JE03093.
0148-0227/93/93JE-03093$05.00

of magma chamber and external pressures on stress and eruption histories of hot spot volcanoes. *Dieterich* [1988] modeled stress in volcano rift zones by means of a two-dimensional triangular grid of elements, and *Ryan* [1988] employed a horizontal planar finite element model of the flank of Kilauea to determine displacements and stresses due to dike emplacement. In an example of the second class of study, *Thurber and Gripp* [1988] applied a flexural model to constrain the tectonics of volcano flank motions. *Ten Brink and Brocher* [1987] proposed a link between flexural stresses in the lithosphere and eruption history; in their scenario the orientation of flexural stresses beneath a given point on the volcanic chain changes with time as the volcanic load is emplaced and then eroded. Given that magma seeks to propagate along paths perpendicular to the direction of least compressive stress, magma ascent can be blocked when both principal horizontal stress deviators are compressional. Thus eruption history depends on location along the volcanic chain or on time since volcano formation.

Recent studies have also been carried out on edifice stresses of large Martian volcanoes. *Thomas et al.* [1990] investigated the tectonics of the flanks of Martian volcanoes by means of an incompressible finite element model. Volcano self-loading and magma chamber effects were included, but lithospheric flexure was not. Thomas and coworkers found that stresses on the flanks of a large volcano are sufficient to cause circumferentially oriented thrust faulting, and they suggested that such thrusting produced the concentric terraces observable high on the flanks of Olympus Mons. *Zuber and Mouginis-Mark* [1992] utilized a finite element model to calculate stresses in the summit caldera region of Olympus Mons caused by magma chambers of different locations and geometries for comparison with observed patterns of faulting.

In this paper we study the stress field within a volcano and the lithosphere upon which it rests as a unified system. With such a model formulation we can account explicitly for the interaction between edifice stresses (e.g., due to volcano self-loading) and flexural stresses (a result of the load induced by the volcano on the lithosphere). We include both growth of the volcano and viscoelastic deformation in the asthenosphere, so the problem is intrinsically time-dependent. The calculated displacements yield the subsidence history of the volcano. The orientations of principal stresses and their change with time provide important constraints on possible magma emplacement paths and eruption histories. With the computed stress fields, a failure criterion can be used to predict locations and modes of faulting within and near the volcano. After a short discussion of important geological and geophysical characteristics of the Tharsis volcanoes, we briefly describe the finite element procedure and the modeling assumptions. The results of the numerical computations are next presented, and their potential implications for the evolution of eruption characteristics and the formation of tectonic features are then compared with known constraints on the evolution of the Tharsis volcanoes.

CHARACTERISTICS OF MAJOR THARSIS VOLCANOES

The four major Tharsis volcanoes are the largest of the Martian shield volcanoes [e.g., *Greeley and Spudis*, 1981]. Each construct is composed of many overlapping flows and flow units erupted over a period of activity as much as 2-3 Gy in duration [*Tanaka*, 1986]. The approximate heights and basal diameters are given in Table 1.

TABLE 1. Dimensions of Tharsis Volcanoes

Volcano	Diameter, km	Relief, km
Olympus Mons	600*	24*
Ascraeus Mons	400†	18†
Pavonis Mons	320†	14†
Arsia Mons	420†	19‡

**Wu et al.* [1984].
†*Blasius and Cutts* [1976].
‡*Blasius and Cutts* [1981].

The largest of the major Tharsis volcanoes is Olympus Mons (Figure 1). The principal tectonic features associated with Olympus Mons are (1) the summit caldera complex, consisting of a series of circular depressions with complex patterns of faulting, (2) concentric terraces seen on the upper slopes of the volcano, (3) the basal scarp, a nearly vertical cliff surrounding the volcano at a radius of about 300 km, and (4) the aureole deposits, which occupy a vast region dominantly to the northwest of the main shield, downslope from the Tharsis rise [*Scott and Tanaka*, 1986; *U.S. Geological Survey*, 1989]. The summit caldera is likely the result of a collapse following withdrawal of magma from a high-level magma chamber [*Mouginis-Mark*, 1981; *Zuber and Mouginis-Mark*, 1992]. As noted earlier *Thomas et al.* [1990] have interpreted the concentric terraces to be thrust faults. The basal scarp has been variously interpreted as a thrust fault [*Morris*, 1981], a listric normal fault [*Francis and Wadge*, 1983], and a fault-propagation fold over a subsurface thrust fault [*Borgia et al.*, 1990]. The aureole deposits are generally held to be disrupted landslide material derived from the slopes of the volcano [*Harris*, 1977; *Lopes et al.*, 1980; *Francis and Wadge*, 1983]. *Tanaka* [1985] proposed that gravity sliding and spreading of the aureole deposits was enabled by a weak basal detachment between aureole and substrate, and that a layer containing about 10% interstitial or interbedded ice would be sufficiently weak to provide such a detachment.

Tectonic features on the flanks of Hawaiian volcanoes on Earth may provide useful analogues to the Olympus Mons scarp and aureole. Acoustic backscatter images of the Hawaiian Ridge reveal that extensive mass wasting deposits (slumps and debris avalanches) flank all of the major Hawaiian shields [*Moore et al.*, 1989]. A study of focal mechanisms of shallow earthquakes on the southern flanks of Kilauea [*Thurber and Gripp*, 1988] supports the hypothesis that a detachment surface separates the volcanic edifice and the older oceanic crust. By this hypothesis, the volcano can overthrust the underlying crustal layer, sliding on a décollement of weak oceanic sediments. The slides and slumps, driven by intrusions at the rift zones, detach from the volcano along large-offset, listric normal faults [*Lipman et al.*, 1985].

Tectonic features observed on and around the Tharsis Montes volcanoes differ somewhat from those of Olympus Mons. The principal tectonic features associated with these volcanoes are (1) circumferential graben on the lower volcano slopes and the surrounding plains, (2) linear embayments or rifts approximately bisecting each volcano along an axis trending N40°E and serving as sources for flows embaying the northeast and southwest flanks, and (3) lobe-shaped deposits to the west or northwest of the edifice [*Scott and Tanaka*, 1981; *Scott et al.*, 1981*a*, *b*, *c*]. The Tharsis Montes volcanoes exhibit an approximate bilateral symmetry about a NE-SW-trending axis coinciding approximately

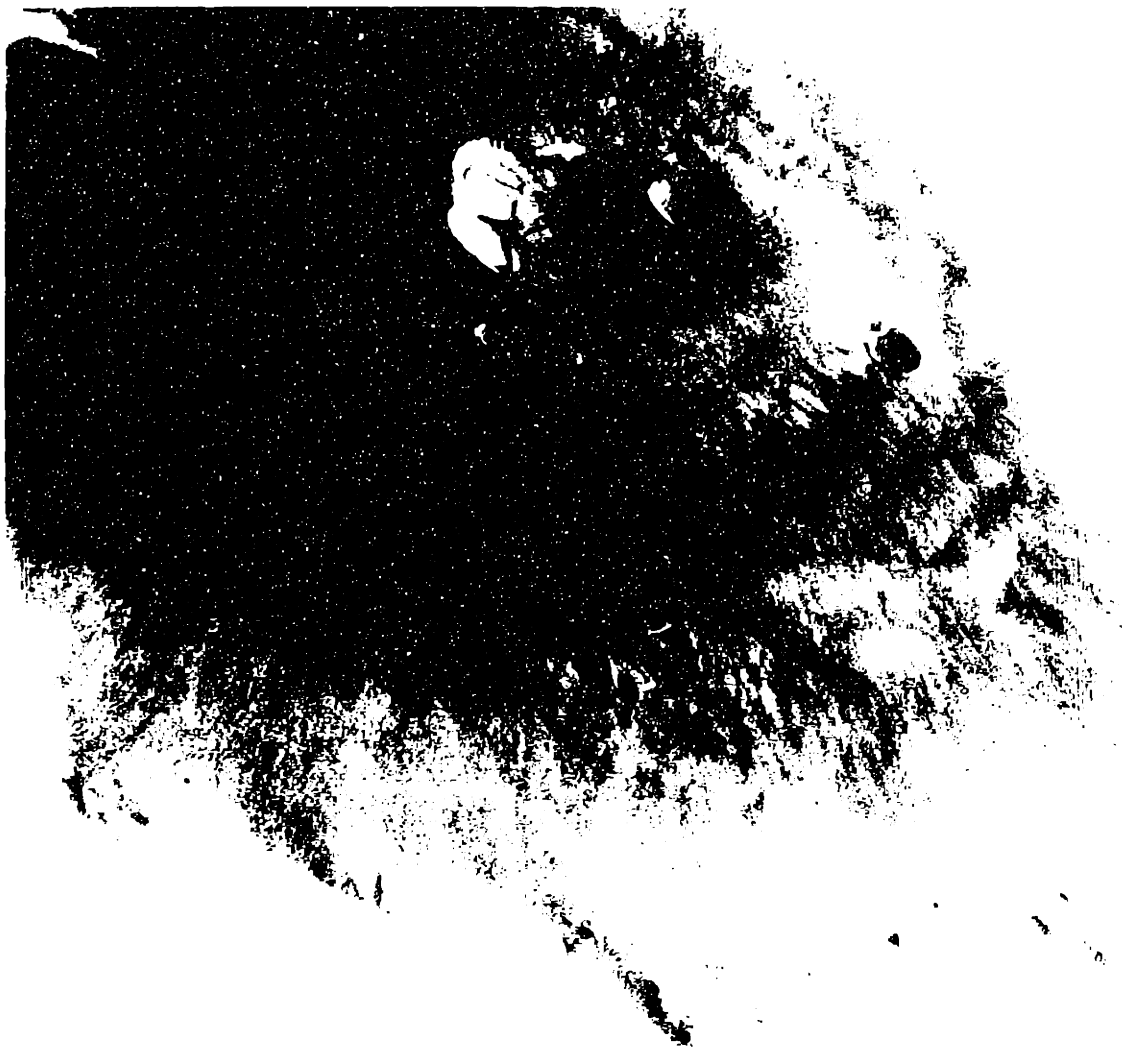

Fig. 1. Viking Orbiter view of Olympus Mons. The multiple-pit caldera and basal scarp (at bottom) are the main tectonic features visible. No graben are seen on the flanks of the volcano or on the volcanic plains immediately surrounding the structure. Frame VO641A52, width of image is 440 km.

with the line connecting their centers. Graben tend to occur on the northwest and southeast flanks of these volcanoes (Figures 2-5), i.e., perpendicular to radial directions broadly orthogonal to the line of the rifts. From photogeological study of Viking Orbiter images, *Crumpler and Aubele* [1978] proposed the following evolutionary sequence for the Tharsis Montes: (1) construction of the main shield, (2) outbreak of parasitic eruption centers on the volcano flanks along the NE-SW-trending axis, (3) subsidence of the summit and formation of concentric fractures and graben, and (4) formation of a bisecting rift along the NE-SW-trending axis, with rift eruptions leading to flooding of the summit depression and inundation of the rifted flanks. This sequence is most advanced on Arsia Mons; Pavonis Mons has reached stage (3), and Ascraeus Mons stage (2). The morphology and tectonics of the flanks of the Tharsis Montes are described in greater detail by *Zimbelman and Edgett* [1991], who propose that the lobate deposits formed by gravity sliding and were further modified by both effusive and pyroclastic volcanic activity.

Fig. 2*a*. Viking Orbiter view of western Ascraeus Mons. The complex caldera is seen at the summit, and graben with a predominantly circumferential orientation are seen along the western and southwestern margins. Graben are located on Ascraeus Mons itself and in surrounding flows (unit as, Figure 3); some graben grade into collapse pits or sinuous channels formed by magma withdrawal and downslope flow. Frame VO643A78; width of image is 420 km.

Prominent rift zones that radiate from the summit calderas are dominant structural features characteristic of Hawaiian shield volcanoes [*Peterson and Moore*, 1987]. These zones are sites of emplacement of magma drained from the summit magma chamber and indicate an environment of horizontal extension. The rift zones and landslides or slump deposits appear to be causally related, as described above. The Hawaiian rift zones may be analogues to the radial rifts of the Tharsis Montes.

The thickness of the elastic lithosphere beneath the Tharsis Montes volcanoes has been inferred from the radial distances of their circumferential graben by *Comer et al.* [1985] (see Figures 3-5). Preferred values of elastic lithosphere thickness are about 20 km. Concentric graben are not found around Olympus Mons, however, which led Comer and coworkers to conclude that the thickness of the elastic lithosphere beneath Olympus Mons must be much greater (>150 km) than beneath the Tharsis Montes. Of course, the actual lithosphere does not behave perfectly elastically; rather its strength is limited by frictional failure at shallow depth

Fig. 2b. Viking Orbiter mosaic of the western flank of Arsia Mons [*Elachi et al.*, 1991]. Note that graben extend all the way up the flank to the edge of the summit caldera.

and by ductile flow at greater depth. From strength envelope considerations for crustal and mantle material [*McNutt*, 1984], values for elastic plate thickness T_e were converted to estimates of mechanical plate thickness T_m and lithospheric thermal gradient by *Solomon and Head* [1990]. For Olympus Mons, flexurally induced curvature is small and T_m is approximately equal to T_e. The lithospheric thermal gradient was inferred to be less than 5 K km^{-1}. For the Tharsis Montes, flexural curvatures are larger, T_m exceeds T_e, and mean thermal gradients corresponding to the best fitting values of T_m were estimated to be in the range 10-14 K km^{-1}. Upper and lower bounds on T_e for the Tharsis Montes from *Comer et al.* [1985] allow a range of thermal gradients from 7-27 K km^{-1}.

METHOD

We use the finite element program TECTON [*McKenzie and Bowin*, 1976; *Melosh and Raefsky*, 1980, 1983] to model stresses and displacements in a large volcano and in the crust and mantle beneath and around the volcano. TECTON's capability for modeling viscoelastic rheology in the mantle allows us to model the time-dependent flexural response of an elastic lithosphere to each major increment of load. The program first calculates the elastic (i.e., instantaneous) response to a load. The stresses and displacements arising from load-induced viscoelastic flow in the mantle are then calculated for a specified number of time steps. The Maxwell time (τ_M) of the mantle, defined as the ratio of viscosity η to shear modulus μ, is used as a convenient reference

Fig. 2. Viking Orbiter mosaic of the eastern flank of Arsia Mons [*Eliason et al.*, 1991]. Note the lack of graben and the radial texture of flows on the upper flank. Graben are evident near the boundary between the edifice and the surrounding plain.

time scale (in subsequent discussion the term 'Maxwell time' will refer to the mantle Maxwell time). Complete descriptions of stresses and displacements were obtained at 5, 10, 15, 20, 30, 40, 70, 100, 200, 400, 700 and 1000 Maxwell times after emplacement of each load increment.

We assume that the problem is axisymmetric, with cylindrical coordinates r, θ, and z, where r and z are positive outward and upward, respectively. Out-of-plane shear stresses σ_{rz} and $\sigma_{\theta z}$ are then zero. We solve for r- and z-displacements and stress components σ_{zz}, $\sigma_{\theta\theta}$, σ_{rr}, and σ_{rz}. In axial symmetry, two principal stresses are confined to the rz plane, and $\sigma_{\theta\theta}$, the stress normal to this plane, is also a principal stress. We adopt the convention that extension is positive. An example of the finite element grid used for this study is shown in Figure 6. The displacement boundary conditions are that nodes on the side walls ($r = 0$ and $r = r_{max}$) are fixed in r but free to move in z, and that nodes on the bottom boundary ($z = z_{min} = -820$ km in the example shown) are fixed in z but free to move in r. The lower corners of the box are fixed in both directions. The volcano in the example has a radius of 200 km and is 25 km in height, the approximate present dimensions of Ascraeus Mons. In Figure 6 the volcano is the triangular region in the upper left-hand corner. The volcano rests on top of an elastic lithospheric plate of thickness T_e. All elements in the volcanic edifice and the plate have a high viscosity appropriate to the lithosphere. These elements behave essentially elastically over the time scales considered here. All elements

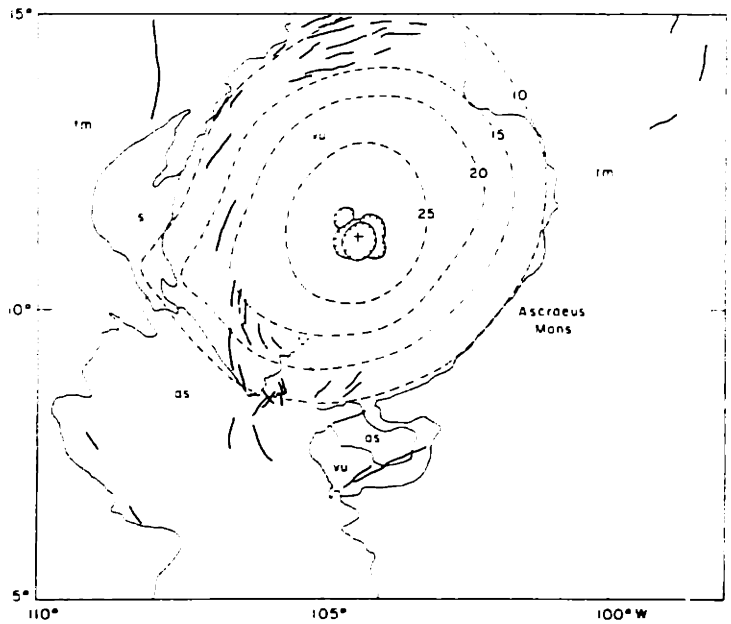

Fig. 3. Geologic map of Ascraeus Mons and surroundings, simplified from *Scott et al.* [1981*b*] by *Comer et al.* [1985]. Volcanic units shown include relatively young Ascraeus Mons flows (as), intermediate-age Tharsis Montes flows (tm), and volcanic material undivided by age (vu). Also shown as a distinct unit is slide material (s), interpreted by Scott and coworkers as landslides and debris flows. Dashed lines show approximate elevation contours, in kilometers, relative to a fourth-degree, fourth-order equipotential [*Wu*, 1978]. The summit caldera complex is indicated by inward hatched lines. Extensional faults and graben are shown as heavy lines.

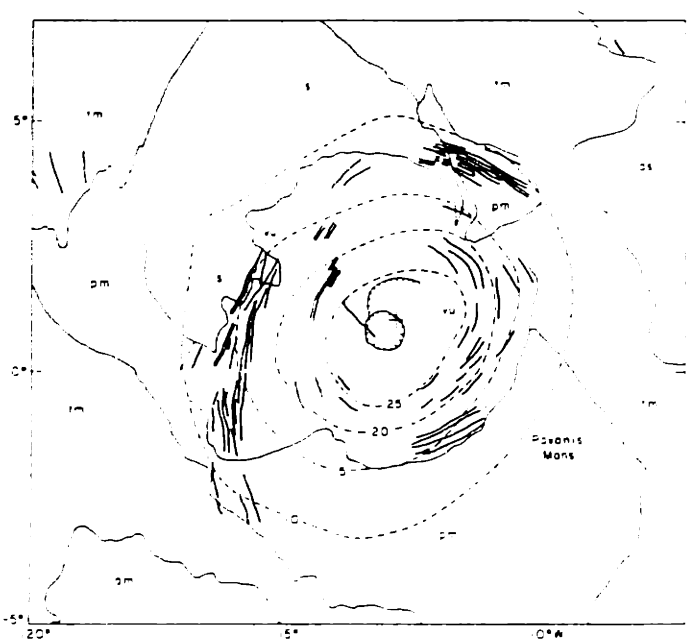

Fig. 4. Geologic map of Pavonis Mons and surroundings, simplified from *Scott et al.* [1981*a*, *b*, *c*] and *Scott and Tanaka* [1981] by *Comer et al.* [1985]. Units shown, in addition to those described in Figure 3, are relatively young volcanic flows from Pavonis Mons (pm) and Arsia Mons (am). Other information follows the format of Figure 3. Circumferential graben reach quite far up the slopes, and an approximate bilateral symmetry can be seen about an axis trending approximately NNE-SSW.

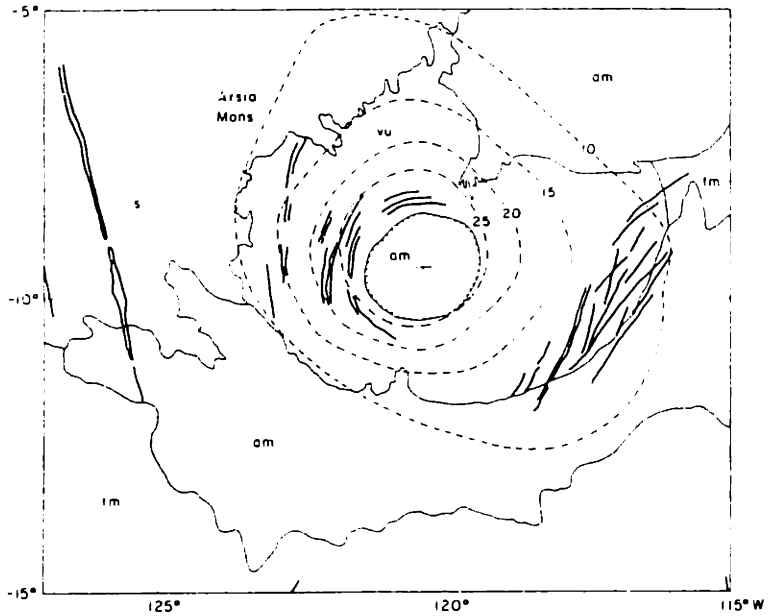

Fig. 5. Geologic map of Arsia Mons and surroundings, simplified form *Scott et al.* [1981c] by *Comer et al.* [1985]. See Figures 3 and 4 for further explanation of symbols. Circumferential graben extend almost up to the summit caldera complex.

below the elastic lithosphere have a lower viscosity value, appropriate for an asthenosphere. These elements experience viscous relaxation over the time modeled. Material property values adopted in our calculations are listed in Table 2. Parameters such as density and Young's modulus differ for the crust and mantle. Elements above depth t_c are assigned crustal values for these parameters; below this depth mantle values are assigned. For most of the models discussed here, we have chosen $T_e = t_c$. We do not mean to imply that thicknesses of the Martian lithosphere and crust coincide; this choice serves only to simplify the models. We have performed additional calculations with $T_e > t_c$ to explore the effect of a strong upper mantle on the flexural solutions. We take T_e to be variously 20, 40, and 60 km. These values fall within the range obtained by *Comer et al.* [1985] for the Tharsis Montes and Olympus Mons. The outer radial boundary of the grid is taken as $r_{max} = 1200$ km.

As a check on the use of TECTON for plate flexure calculations, we have compared the stresses and displacements calculated by the code to those from an analytic solution for thick plate flexure in axisymmetric geometry [*Comer*, 1983]. We constructed a model of the plate only, without the volcano elements, similar to analytic models. This was done to avoid local stiffening of the plate due to the added thickness of the volcano near $r = 0$, which would change the resulting flexural profile (this effect is discussed

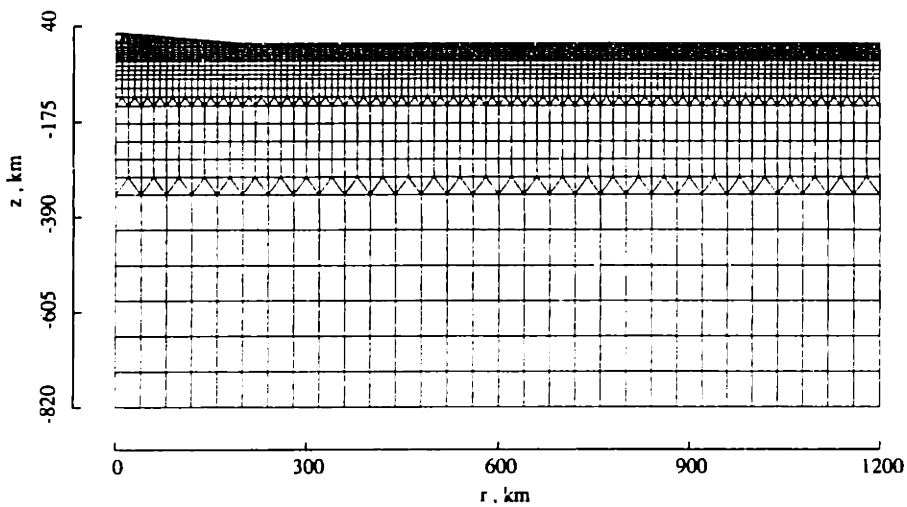

Fig. 6*a*. The finite element grid used for calculations shown in later figures. The volcano is the small triangular area in the upper left-hand corner.

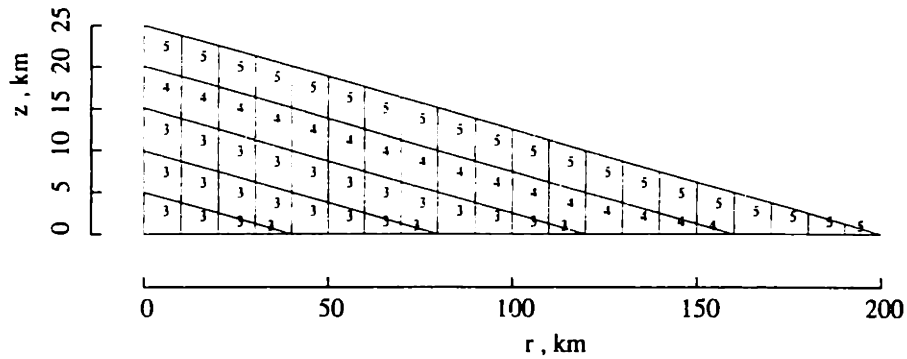

Fig. 6*b*. Plot of element types for models with incremental volcano loading, implemented by means of time-dependent element properties. Elements marked with a "3" are "on" from the start of the calculation; those with a "4" are switched "on" after 1000 Maxwell times, and those with a "5" are switched "on" after 2000 Maxwell times.

in greater detail below). The load of the volcano was simulated by applying appropriate axisymmetric forces to the nodes on the top surface of the plate. Our calculations showed that the TECTON solution closely matches the analytic solution except for errors of less than 1% near $r = 0$ and about 1.5% near the flexural arch.

An important limitation of analytic models of lithospheric loading is that the load is emplaced instantaneously. This assumption implies a growth time t_g much less than the mantle Maxwell time τ_M. For Mars, if $\eta \sim 10^{21}$ Pa s and $\mu \sim 10^{11}$ Pa, $\tau_M \sim 10^{10}$ s or 300 years. A more realistic model would allow the volcano to grow incrementally with time, simulating the superposition of many discrete lava flows to form an edifice. We have implemented a modification to the finite element code that allows us to specify the properties of a given element as a function of time. The finite element grid is set up exactly as in Figure 6*a*, except that volcano elements are initially given a density of zero and a low but finite value of Young's modulus E (the latter to prevent a singularity in the stiffness matrix used to calculate displacements). These elements are considered "off", that is, for the purposes of the simulation, such elements are considered initially unoccupied by volcano material. At the beginning of an appropriate time step, an element can be turned "on" by changing the values of the density and Young's modulus to normal crustal values. Here we have simulated the incremental growth of a volcano by switching on elements in the volcanic edifice in three stages (Figure 6*b*), at time zero and at 1000 and 2000 Maxwell times following initial load emplacement. We note here that our attempt to model a growing load is necessarily a coarse one. A typical terrestrial volcanic shield will consist of thousands of units emplaced over about 10^5 to 10^6 years (this time scale may be 10^8 to 10^9 years on Mars). Such units are much lower in volume than those we model. Further, our increments are separated by only 1000 Maxwell times (about 30,000 years for the parameters adopted here). This value was selected to be long enough to complete the flexural response to a given increment but is not meant to imply that the Tharsis volcanoes are emplaced that rapidly. Also note that use of a non-zero value of E means that small but finite stresses are generated in the elements that are "off." These stresses, however, are much lower in magnitude than those produced after the "real" values of E are implemented, and they are too small to affect significantly the stresses and displacements in the edifice and lithosphere in the early stages of flexure.

In order to explore the hypothesis that volcanoes on Earth and Mars may have similar tectonic structures, we have used special features in the TECTON code to simulate the effect of a detachment between volcano and lithosphere as described by *Lipman et al.* [1985] and others. The effects of fault slip along such a detachment on the stresses and deformation can be modeled using the slippery node method implemented in TECTON by

TABLE 2. Adopted Parameter Values

Parameter	Crust	Mantle
E, Pa	1×10^{11}	3×10^{11}
ρ, kg/m^3	3000	3500
ν	0.25	0.25
	Lithosphere	**Asthenosphere**
η, Pa s	1×10^{27}	1×10^{21}

Maximum Stress:

Symbol	Compressive	Extensional	"Predicted" Fault Type
	vertical	horizontal	circumferential normal
	horizontal	vertical	circumferential thrust
	vertical	out of plane	radial normal
	horizontal	out of plane	strike-slip
	out of plane	horizontal	strike-slip
	out of plane	vertical	radial thrust

Fig. 7. Key for stress symbols in models. These symbols denote the principal stress directions under axisymmetry. The hourglass shapes are oriented along the direction of greatest compressive stress (σ_1), the bars along the direction of least compressive stress (σ_3). Circles are meant to represent the hourglass shapes turned on their sides, such that σ_1 is perpendicular to the r-z plane. Magma is expected to ascend locally along the plane orthogonal to the least compressive stress, that is, perpendicular to the bar.

Melosh and Williams [1989]. All the nodes originally on the line $z = 0$, i.e., along the interface between the volcano and the lithosphere, are slippery nodes for such models. This modification allows the volcano to thrust outward over the flexed lithosphere.

The evolution of the stress field within and beneath the volcanic edifice in a model is depicted by means of symbols for the principal stresses within each element (Figure 7, symbols after *Melosh and Williams* [1989]). The first and second symbols denote situations where the azimuthal or hoop stress is the intermediate principal stress σ_2. The third and fourth symbols represent cases where the hoop stress is the greatest extensional stress σ_3. The fifth and sixth symbols represent cases where the hoop stress is the greatest compressive stress σ_1.

Given stress values, we use the Mohr-Coulomb failure criterion to estimate regions where faulting would occur. The Mohr-Coulomb failure equation relates shear stress τ at failure to normal stress σ_n

$$\tau_{failure} = c + \sigma_n \tan \phi \qquad (1)$$

where c is the cohesive strength of the rock and ϕ is the angle of internal friction. We adopt values for c (3.8×10^7 Pa) and ϕ (49°) appropriate for basalt [*Handin*, 1966]. Elements where the shear stress has exceeded the Mohr-Coulomb criterion are shaded to indicate failure. Once we have found where failure is expected, the orientations of principal stresses are used to determine the style and orientation of faulting, according to the criteria of *Anderson* [1951]. Given the principal stress directions, the type of faulting (normal, thrust, or strike-slip) and the orientation (radial or circumferential) can be determined. Figure 7 gives types and orientations of faulting in elements with the given orientations of the stress symbols. This classification scheme holds if the principal stresses approximately correspond to the horizontal (σ_{rr}, $\sigma_{\theta\theta}$) and vertical stresses (σ_{zz}) listed here. If the stresses are not aligned in this way, fault geometry may be less simply described. Strike-slip faults do not quite fit the usual definitions of radial and circumferential, because such faults are expected generally to strike obliquely to the principal stress directions. For most situations, strike-slip faults make smaller angles with the σ_1 direction than with the σ_3 direction. Thus, when $\sigma_1 = \sigma_{\theta\theta}$ we will consider the resulting faults approximately circumferentially oriented, and when $\sigma_1 = \sigma_{rr}$ we consider them approximately radial. Care must be taken when applying these results to regions at depth, or where principal stresses are oblique to the surface.

For a general state of stress in a plane layer constrained laterally and subjected to self-loading (before the volcanic load is applied), the orientation of the stress symbol will be as in the first line of Figure 7: maximum compression vertical and maximum extension horizontal. The magnitude of the deviatoric stress will increase with depth. This result can be derived from the equations for uniaxial strain (compaction) in the z direction [e.g., *Turcotte and Schubert*, 1982, p. 108]:

$$\sigma_{rr} = \sigma_{\theta\theta} = \left(\frac{\nu}{1-\nu}\right)\sigma_{zz} \qquad (2)$$

For Poisson's ratio $\nu = 0.25$, the factor $\nu/(1 - \nu)$ is 1/3. Thus, the vertical stress will be three times as great as the horizontal stress, and with vertical stress equal to the overburden pressure ($\sigma_{zz} = \rho_c g z$, where ρ_c is the density of crustal material and g is the gravitational acceleration), the stress difference will increase with depth. The state of stress in the terrestrial crust is still a matter of debate. *McGarr* [1988] argues that a stress state in which all principal stresses are equal to the overburden load is a better reference stress state than the "Poisson" stress state described by equation (2). However, it seems likely that the state of stress lies somewhere between the two extremes. In general, the stress state described by equation (2) is the initial state in the lithosphere for most of our models. We consider additional models, however, to determine the effects of an isotropic lithospheric prestress (with $\sigma_{rr} = \sigma_{\theta\theta} = \sigma_{zz} = \rho_c g z$). For all models, the prestress in the asthenospheric mantle is taken to be isotropic.

When applying the results of these calculations to actual geologic and tectonic features seen on Martian volcanoes, one must keep in mind the model limitations. The simplest calculations that we perform here start with the instantaneous placement, at time $t = 0$, of a significant portion of a volcanic edifice, equivalent to the condition $t_v << \tau_M$. This assumption is valid only for individual flows constituting at most a minor mass fraction of the volcano. While we have modified the finite element code to accommodate changes in element properties with time, as noted above the individual load increments are large fractions of the volcano mass. Other limitations are also noteworthy. It is difficult to determine the geometry of a given volcano load, even at the end of the last major shield-building eruptions, because of subsequent flexure and deformation that may have significantly modified the volcano's characteristics. These calculations are performed under the assumption of axial symmetry; possible effects of nonaxisymmetric loading (such as regional stress) and complex three-dimensional geometry are not incorporated. The effects of magma pressure, transport, and evacuation are not addressed in these models; these processes likely have important influences for caldera and flank tectonic evolution [*Thomas et al.*, 1990; *Zuber and Mouginis-Mark*, 1992]. Further, lateral variations in material properties (due to horizontal temperature gradients, for example) are not included. Our choice that $T_e = t_c$, while made for convenience, is not necessarily valid for the Tharsis region. Finally, it must be remembered that a viscoelastic model cannot account for relief of stress due to faulting (except for faults modeled *a priori* such as in the detached volcano models). Once faulting occurs, the stress fields calculated are no longer strictly valid, since faulting would relieve stresses locally and could thus alter the predictions for failure at subsequent times. As discussed below, some of these limitations can be relaxed in future modeling efforts.

NUMERICAL RESULTS: STRESS, DEFORMATION, AND FAULTING

Models With Growing Loads

An illustrative model for the evolution of volcano-related stresses is shown in Figure 8, which depicts the case of an incrementally grown volcano on a lithosphere with $T_e = t_c = 40$ km. At each stage in volcano growth, the base of the volcano is considered to be welded to the underlying lithosphere. At $t = 0$ (Figure 8*a*) stresses display the orientations and magnitudes expected from simple self-loading of horizontal layers everywhere but along the top layer of volcano elements, where the stresses are rotated such that the compressive axis is almost horizontal. As the effects of flexure in response to the first load increment manifest themselves with time, this rotation propagates deeper into the volcano, eventually reaching the upper part of the underlying plate (Figures 8*b*-8*d*). These figures also show predicted locations and types of faulting as functions of time. For the initial volcano of 120-km radius, faulting is predicted in two locations by about 20

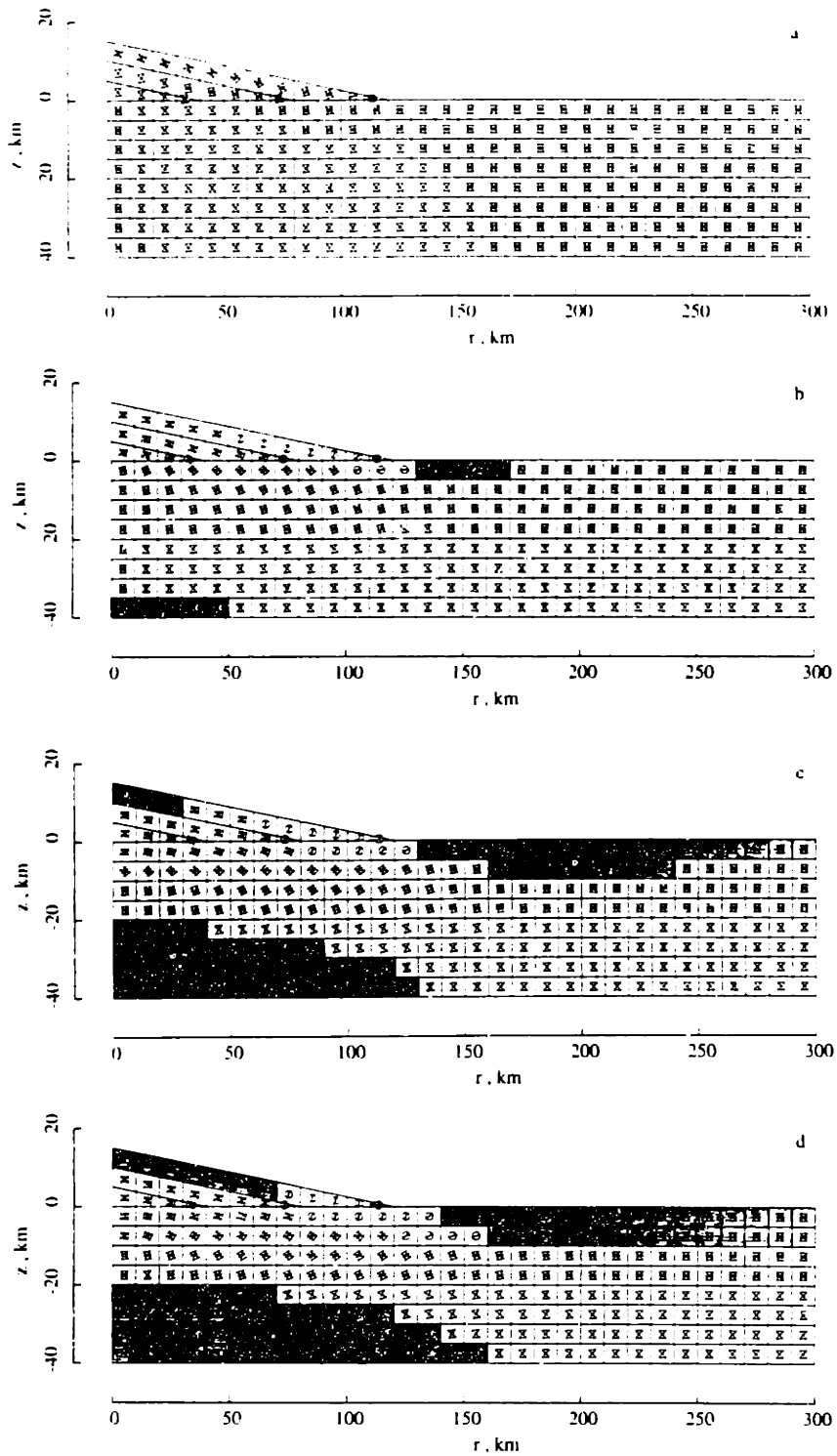

Fig. 8. Principal stress orientations and predicted failure in the vicinity of an incrementally grown volcano load on a 40-km-thick elastic lithosphere. Crustal thickness is also 40 km. See Figure 7 for the meaning of the stress orientation symbols. Elements in which stresses satisfy the Mohr-Coulomb failure criterion are shaded. Given the orientation of the stress symbol in a shaded element, the style and orientation of faulting can be inferred. (*a*) The elastic solution, (*b-d*) 20, 100, and 1000 Maxwell times after the first load increment is added, (*e-f*) 20 and 1000 Maxwell times after the second load increment is added, and (*g*) 1000 Maxwell times after the third load increment is added.

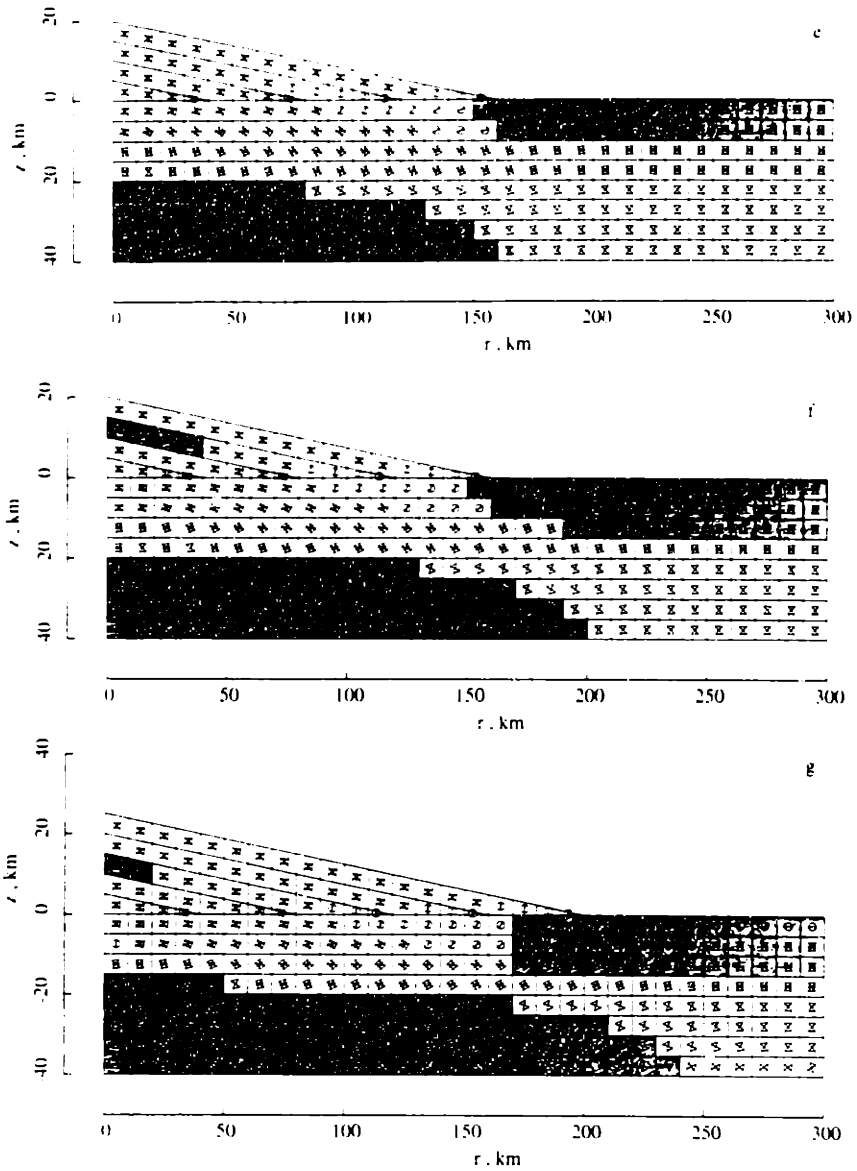

Fig. 8. (continued)

Maxwell times (Figure 8*b*). A subsurface region of normal faulting at a depth of 35-40 km (at the base of the elastic lithosphere) appears beneath the center of the volcanic load. Faulting also is predicted at the plate surface just outward of the volcano. In this region, all elements but one are predicted to experience circumferentially oriented normal faulting (the innermost element is predicted to fail by strike-slip). By 100 Maxwell times (Figure 8*c*), both of these regions of predicted failure have expanded radially and vertically, and a new zone of faulting appears along the upper volcano flanks, on which the predicted fault style and orientation is predominantly circumferential thrust faulting. Mostly radial normal faults are predicted for the subsurface failure region. By 1000 Maxwell times (Figure 8*d*), the volume of circumferential normal faulting extends up to 300-km radius (not shown in figure) and up to 10-km depth. The region of strike-slip faulting has grown in radial extent at the expense of the region of circumferential normal faulting, but each of the elements in this zone has already been predicted to fail by circumferential normal faulting at an earlier time step (see Figures 8*b*, 8*c*). The upper flanks of the volcano are predicted to fail by circumferential thrust faulting, and the lowermost element on the flank by radial thrust faulting. The failure region at the bottom of the plate now extends slightly beyond the radius of the volcano itself. Near $r = 0$, this region includes the entire bottom half of the plate (20 to 40 km below the original surface).

In Figures 8*e* and 8*f* we see the effect of the next increment of volcano growth. Notice that most elements on the volcano flank predicted to fail in Figure 8*d* are no longer predicted to be in failure in Figure 8*e*, but some of them are predicted to fail again

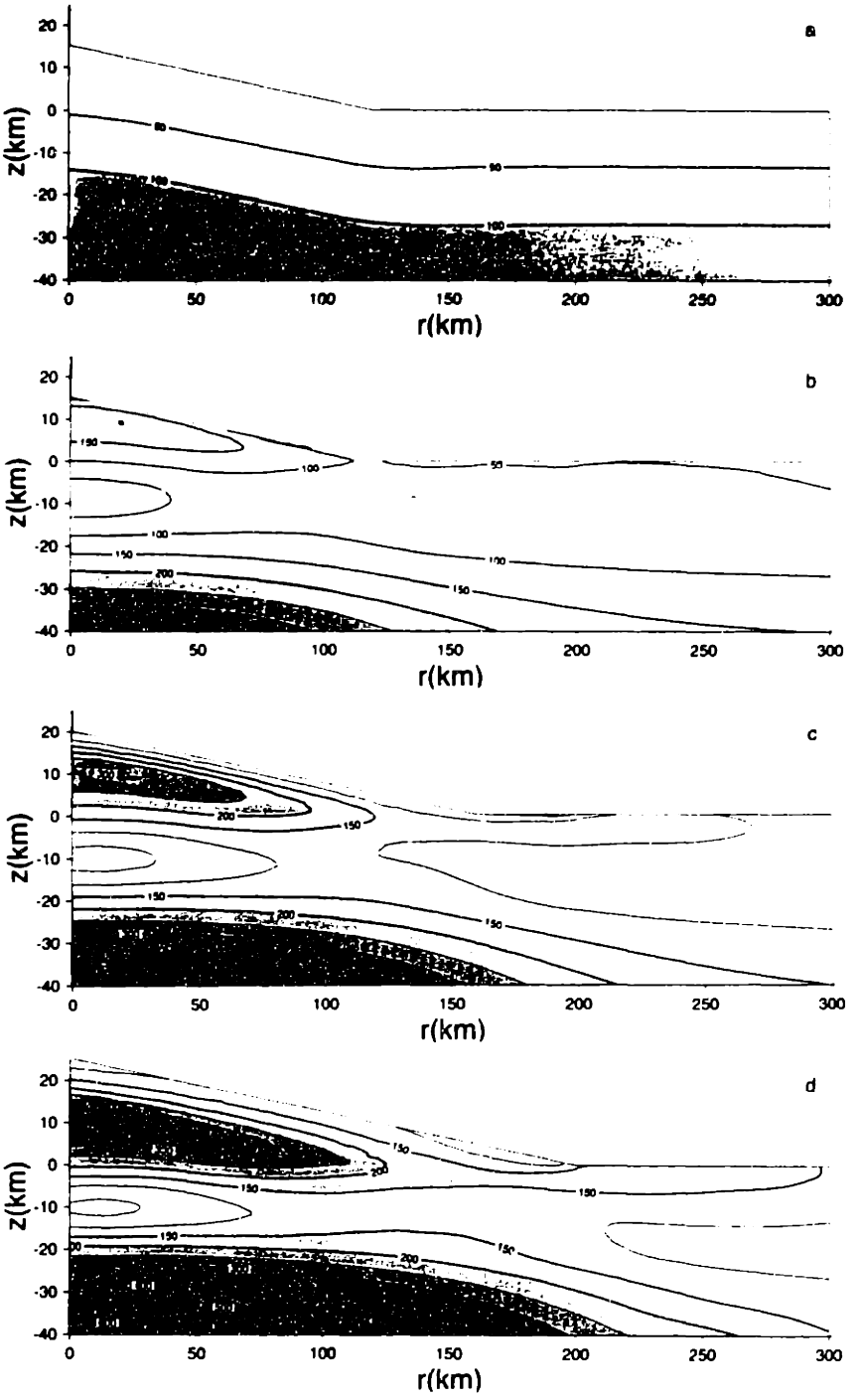

Fig. 9. Contours of maximum shear stress in the vicinity of the volcano, for the model of Figure 8. Contour interval is 50 MPa. (*a*) The elastic solution, and (*b-d*) 1000 Maxwell times after the first, second, and third load increments are added, respectively.

by the time depicted in Figure 8*f*. No failure is predicted, however, in the layer of elements constituting the new surface of the volcano. In Figure 8*g*, the effects of the final load increment can be seen. Only two elements in the entire edifice have deviatoric stresses sufficiently great to cause failure.

The maximum shear stress, which is defined as $(\sigma_1 - \sigma_3)/2$, or half the difference between the most and least compressive principal stresses, is a measure of the local deviatoric stress. The magnitude of the maximum shear stress in the vicinity of the volcano is shown versus time in Figure 9. A comparison with the

TABLE 3. Characteristics of Predicted Near-Surface Failure for Each Model

Model* and Increment		Inner Radius†, km	Outer Radius Strike-slip Faulting†, km	Outer Radius Normal Faulting†, km	First Observed Failure (Time, Radius, Type)
GW40	1	140	230	380	20 τ_M
	2	150‡	270	440	130-170 km
	3	170‡	300	490	mixed§
GW20	1	120	170	280	20 τ_M
	2	120‡	190	320	120-140 km
	3	140‡	220	360	radial normal
GW60	1	180	270	410	30 τ_M
	2	180	330	520	170-220 km
	3	190‡	360	590	mixed§
GW40/60	1	200	300	430	30 τ_M
	2	200	350	550	200-220 km
	3	210	390	630	radial normal
IW40	1	190‡	290	490	10 τ_M
					200-250 km
					radial normal
GD40	1	120	240	380	15 τ_M
	2	130‡	280	440	120-160 km
	3	150‡	310	500	mixed§
GWPS40	1	150	290	340	40 τ_M
	2	160	310	410	140-190 km
	3	170‡	320	470	strike-slip

*Model key: G, growing volcano; W, welded volcano; I, instantaneously emplaced volcano; D, detached volcano; PS, isotropic prestress applied to lithosphere; integer, crust and elastic lithosphere thickness (respectively, where two figures are given).

† Radius values given at t = 1000 τ_M after application of given load increment.

‡ Value less than the maximum radius of the volcano at a given load increment.

§ Inner part of range, strike-slip; outer part of range, radial normal.

stress orientation symbols of Figure 8 indicates the principal stresses used to calculate the maximum shear stress at a given point. In the elastic solution (Figure 9*a*), the stress difference increases with depth, as discussed above. At a given depth, the deviatoric stress is higher beneath the initial volcano load increment than outward of the volcano. At t = 1000 τ_M (Figure 9*b*) concentrations of high deviatoric stress have developed in the three characteristic regions of failure from Figure 8. Deviatoric stresses exceed 150 MPa near the volcano summit and in a wide volume near the bottom of the plate beneath the volcano. Failure is predicted in both areas. Deviatoric stresses are not as high in the near-surface region immediately surrounding the volcano, but faulting is predicted there because of the low confining pressure. There are two important regions of relatively low deviatoric stress; directly beneath the volcano summit near z = -4 to -14 km, and far from the volcano at both the top and bottom of the plate. At t = 2000 τ_M (Figure 9*c*) the region of high stress within the edifice has intensified, but it remains at about the same height as before, at the top of the first load increment. The second load increment, emplaced atop the first, shows a much lower level of deviatoric stress than deeper in the edifice. The deviatoric stress low beneath the volcano has shrunk in size and deepened slightly to about z = -10 km. By the time subsidence following final load emplacement is nearly complete (Figure 9*d*), most of the region near the volcano experiences deviatoric stress in excess of 200 MPa. The regions of high deviatoric stress have expanded to maximum size, and the deviatoric stress minimum below the volcano center has shrunk further.

Changing the plate thickness can affect the evolution of regions of failure. For $T_e = t_c$ = 20 km, the entire topmost layer of edifice elements is predicted to fail by thrust faulting after 1000 τ_M. Circumferential thrust faults on the upper flanks will be surrounded by a small annulus of radially oriented thrusts on the lower flanks. The region of failure outward of the volcano is smaller in radial extent than for the case with T_e = 40 km (Table 3). While strike-slip faulting is indicated in the inner portion of this region over most of the evolution of the stress field, initial failure for most of the affected elements is predicted to occur by circumferential normal faulting. Further, the inner annulus of initial strike-slip failure is covered by the outer edifice during later growth of the volcano. At the final stage (Figure 10, t = 3000 τ_M), the subsurface region of failure reaches through almost the entire thickness of the plate to the base of the volcano. At the radially distal edge of this region, stresses are rotated such that strike-slip faulting is expected, and the region merges with the failure zone outside the volcano to form a continuous volume predicted to be at failure. More elements (5 versus 2) in the edifice retain stresses large enough to cause failure than for the case with T_e = 40 km.

The evolution of maximum shear stress for this case follows a course similar to that for T_e = 40 km. The regions of high deviatoric stress on the volcano flanks and at the bottom of the plate closely surround a stress minimum whose center lies at about

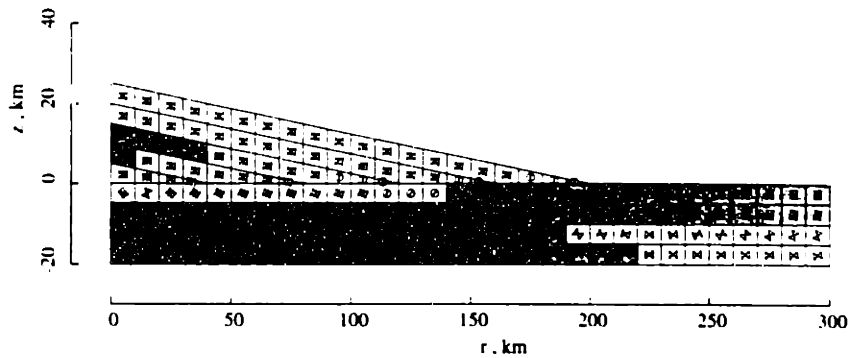

Fig. 10. Principal stress orientations and predicted failure for an incrementally grown volcano load on a lithosphere with T_e = 20 km at 1000 Maxwell times after the third load increment is added.

z = -3 km. The deviatoric stresses near the base of the plate are slightly higher in the thinner plate, and the vertical gradient of stress is greater. The peak deviatoric stress in the volcanic edifice for the T_e = 20 km case is about 110 MPa greater than for the case with T_e = 40 km.

Results for a model with a thicker elastic lithosphere and crust (T_e = t_c = 60 km) also reveal interesting changes from the first model. After the first loading increment (t = 1000 τ_M), faulting has initiated at the lithosphere base and outside the volcano, but not in the edifice itself. In the outer faulting region we again observe elements where predicted failure evolves from initial normal to later strike-slip faulting. The area of predicted strike-slip faulting is much larger in extent than for the cases with thinner lithospheres (Table 3). After the final load increment (Figure 11, t = 3000 τ_M) the region of predicted near-surface normal faulting expands outward to 590 km from the center (Table 3), as well as down to a maximum depth of 20 km. The region of failure beneath the volcano is found at a deeper level (30-60 km depth) because of the greater plate thickness. The peak deviatoric stresses in this region are slightly lower, and the vertical gradient of stress is lower. The deviatoric stress minimum beneath the volcano is also larger in extent and centered more deeply (about -14 km) than its counterpart for T_e = 40 km. The peak deviatoric stress within the volcanic edifice is about 100 MPa less than for T_e = 40 km. No faulting of any type is predicted in the edifice during the period modeled.

To investigate the effects of different crustal and lithospheric thicknesses, we performed a calculation with a 40-km-thick crust and a 60-km-thick elastic lithosphere. The upper mantle lithosphere has a higher value of Young's modulus and should cause the plate to behave more stiffly than if the plate consisted entirely of crustal material. Figure 12 shows plots of stress orientation and failure for this case; compare with Figure 8 for a case with crust and lithosphere both 40 km thick and with Figure 11 for a case with crust and lithosphere both 60 km thick. The evolution of the stress field and zones of predicted failure is qualitatively similar to those discussed above. One effect of the stiff upper mantle lithospheric layer is to concentrate into a narrower depth interval the zone of failure beneath the volcano, seemingly shielding the less rigid crust above from failure. In Figure 11, this zone extends from 30- to 60-km depth, whereas in Figure 12 only elements in the mantle portion of the lithosphere (40- to 60-km depth) show stresses that satisfy the failure criterion. We also observe that the size of the zone of near-surface

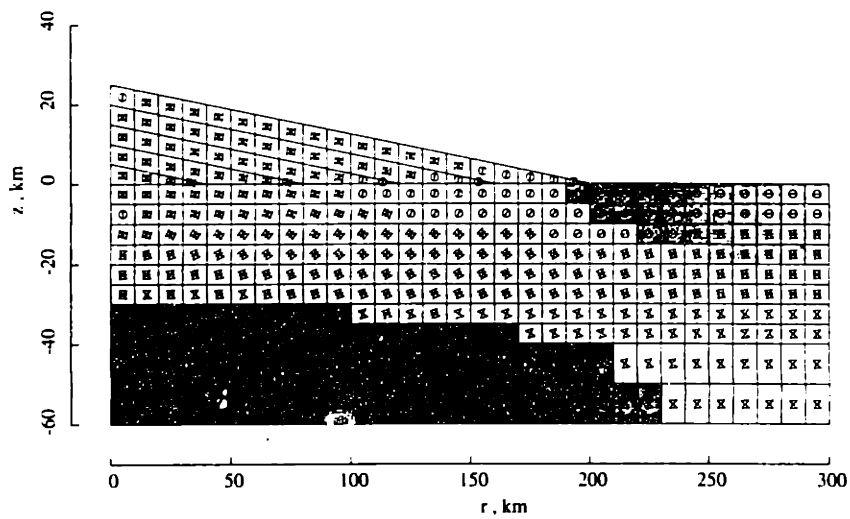

Fig. 11. Principal stress orientations and predicted failure for an incrementally grown volcano load on a lithosphere with T_e = 60 km at 1000 Maxwell times after the third load increment is added.

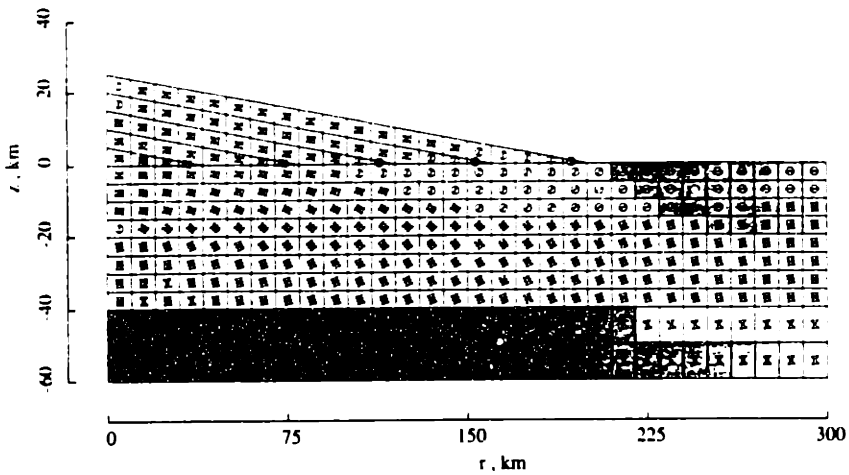

Fig. 12. Principal stress orientations and predicted failure for an incrementally grown volcano load on a lithosphere with T_e = 60 km and with a crust 40 km thick at 1000 Maxwell times after the third load increment is added.

failure outward of the volcano, and the amount of stri' ɔ faulting within it, are both greater for the plate with a strong upper mantle lithospheric layer (Table 3).

Models With Instantaneous Loads

It is instructive to consider a model with an instantaneously emplaced load, both as a comparison with analytic models and as a reference to study the effects that incremental volcano growth have on the evolution of stresses in volcanoes. Figure 13 shows stress orientations and failure for this case at the conclusion of flexure (t = 1000 τ_M). The patterns are qualitatively similar to those for the case with incremental loading (Figure 8*g*) except for the volcano flanks, which are predicted to have failed along the entire surface and to 15-km depth near the summit. Circumferential thrust faults are predicted on the upper flanks, and an annulus of radially oriented thrusts is predicted on the lower flanks. This state is similar to that predicted for the first load increment of a growing volcano (Figure 8*d*). The maximum shear stresses for this case (Figure 14) resemble those for the incrementally loaded case (Figure 10*d*) except for the concentration of stresses at the top of the edifice. In this respect the model behaves like an analytic plate flexure model, in which deviatoric stresses are a maximum at the top and bottom of the plate, with a minimum at mid-plate. The volcano serves effectively to stiffen the plate near r = 0, thus elevating the midplane from z = -20 km (for a 40-km-thick plate) to z = -8 km (for a plate effectively 65 km thick at r = 0).

Models With Detached Loads

The evolution of stress orientations for an incrementally grown volcano detached from the lithosphere is shown in Figure 15. Immediately after loading, stresses in almost the entire edifice are oriented with maximum compression vertical and maximum extension out of the plane (Figure 15*a*). This geometry may be compared with that in Figure 8*a*, where both the maximum and minimum principal stresses are in the r-z plane in the upper flanks of the volcano, and the maximum compressional direction has rotated toward the horizontal. In Figure 15*a* the onset of faulting is predicted in two areas: at the plate surface just outside the volcano (as observed in most of the other models) and near the

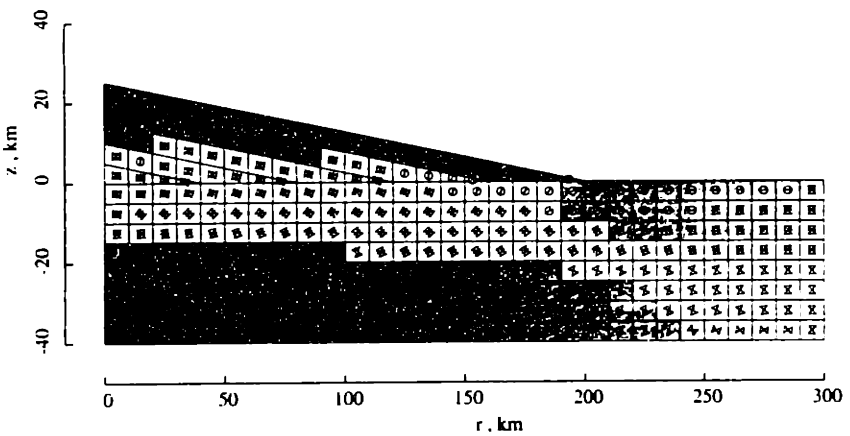

Fig. 13. Principal stress orientations and predicted failure for an instantaneous volcano load on a lithosphere with T_e = 40 km, after 1000 Maxwell times.

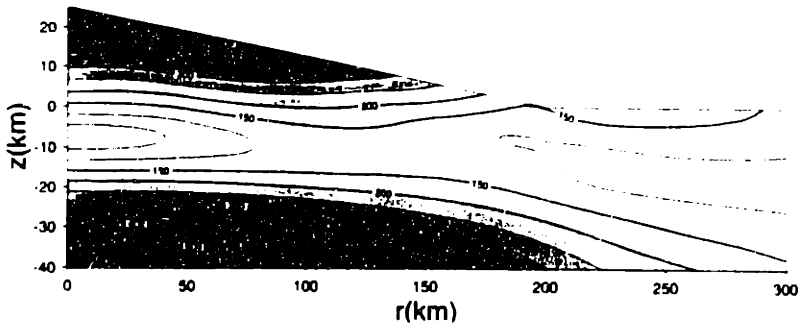

Fig. 14. Contours of maximum shear stress for the model of Figure 13, after 1000 Maxwell times.

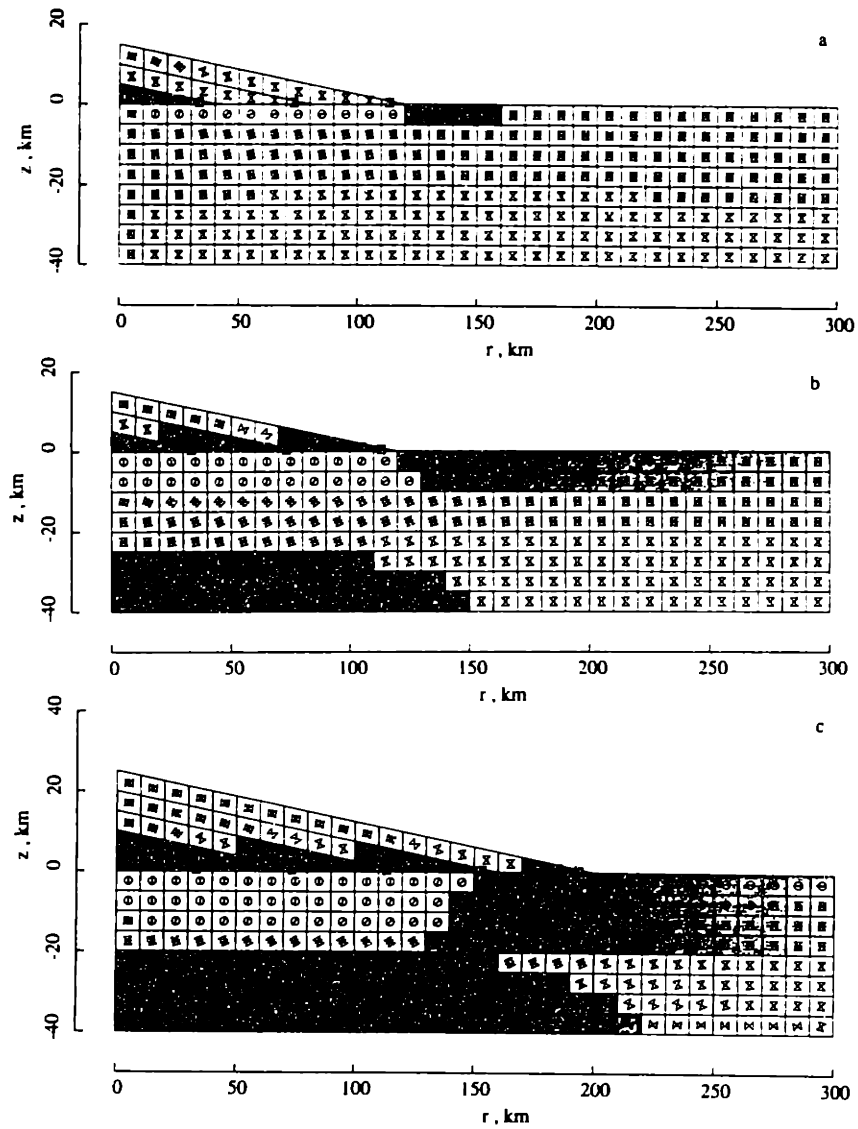

Fig. 15. Principal stress orientations and predicted failure for a model with a growing volcano load, a basal detachment between lithosphere and volcano, and crust and elastic lithosphere 40 km thick (*a-b*) 15 and 1000 Maxwell times after the first load increment is added, and (*c*) 1000 Maxwell times after the third load increment is added.

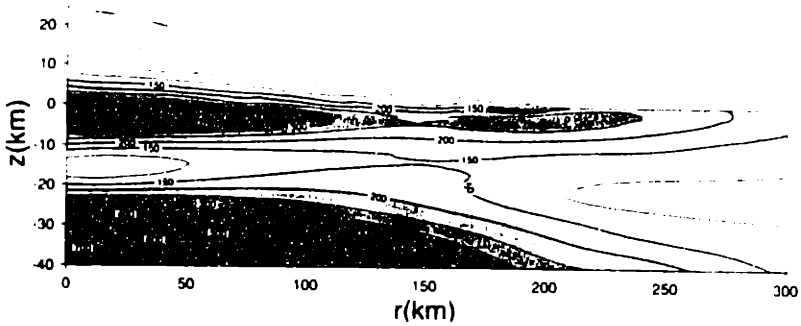

Fig. 16. Contours of maximum shear stress for the model of Figure 15, 1000 Maxwell times after the third load increment is added.

base of the volcano near $r = 0$. Radial normal faulting is predicted for this second region; the entire lower part of the volcano (near the detachment) exhibits horizontal extensional stress and vertical compressive stress, in contrast to the environment of generally horizontal compression in the models with welded volcanoes. This environment persists as the calculation proceeds (Figures 15*b*-15*c*). In Figure 15*b*, after 1000 Maxwell times, the area of radial normal faulting reaches outward through the edifice, above the detachment, to the surface at the volcano edge. Also note that stresses near the summit of the volcano have rotated to a state of horizontal compression. By the time the flexural response to final volcano growth is complete (Figure 15*c*, 3000 Maxwell times), an annulus (with inner radius 170 km and outer radius 200 km) of radial normal faulting has formed on the lower flanks. Elsewhere, the stress state depicted in Figure 15*c* is similar to the final result of the welded case (Figure 8*g*), except that the volume of predicted faulting outside the volcano extends deeper, and the faulted region beneath the volcano does not extend as far vertically. These effects may be related to local stiffening of the plate by the welded volcano, which acts to raise the midplane of the plate.

A plot of maximum shear stress for this case (Figure 16) shows how the distribution of stresses is changed by the detachment. Deviatoric stresses in the volcano tend to increase from top to bottom, the reverse of the pattern for the welded volcano (Figure 9*b*). A region of high deviatoric stress forms beneath the detachment (with a slightly higher magnitude than the high-stress region at the top of the edifice in Figure 9*d*). After completion of loading and flexure (Figure 16), stresses in the edifice are greatest at the bottom, directly above the detachment. The upper parts of the edifice have low levels of stress, except for a small volume of slightly elevated stresses near the summit. The stresses there are oriented in horizontal compression, as in the welded models, but the magnitude of compression is greatly reduced because of slip on the detachment.

In order to address the role of the initial stress state of the lithosphere in determining the time-dependent evolution of stresses and displacements, we consider a lithosphere with an isotropic prestress equal to the overburden pressure. For a model otherwise similar to that of Figure 8, the first faulting in the region outside the volcano is predicted to occur in a region five elements wide, exclusively by strike-slip mechanisms (Table 3). These elements are entirely contained within a zone of elements with stress orientations that favor strike-slip faulting. As flexure due to the first load increment continues, more elements are predicted to fail first in strike-slip mode, out to 280 km in radius, in contrast to the model of Figure 8, in which strike-slip faulting is limited to one element very near the edge of the first increment. The zone of initial strike-slip failure extends beyond the edge of the final load increment, and such faults could be visible after completion of volcano growth if not obscured by moat-filling flows. Thus the initial stress state of the lithosphere prior to volcanism can affect the observed distribution of near-surface faulting surrounding the volcano.

DISCUSSION: IMPLICATIONS FOR VOLCANO EVOLUTION

The time-dependent displacement and stress fields calculated in our models can be used to predict the type and orientation of tectonic features that would result from loading of the lithosphere by a volcanic edifice. We may compare these predictions to observed tectonic features on and around the Tharsis volcanoes. The evolution of tectonic deformation is also constrained by the model results, an advantage of the finite element method over analytical flexure and other lithospheric loading models which consider an instantaneously emplaced load. We may then evaluate the validity of each model and the applicability of terrestrial analogues for some tectonic and volcanic features.

Flank Tectonics: Circumferential Graben and Predicted Strike-Slip Faulting

As noted earlier, circumferential graben are observed on the lower flanks and the surrounding plains for all three of the Tharsis Montes (Figures 2-5). Formation of these circumferential graben requires an environment of radial horizontal extension at the top of the crust surrounding the volcano and in the near-surface region of the volcano flank. Almost every model predicts circumferential normal faulting in an annulus around the volcano. Models in which the volcano is welded to the underlying plate give near-surface horizontal compression in the edifice after lithospheric flexure, while models which include a detachment between volcano and plate show horizontal extension in the lower volcano flanks. At the base of the detached volcano, the hoop stress $\sigma_{\theta\theta}$ is extensional, and the radial normal stress σ_{rr} is compressional but small compared with the vertical normal stress σ_{zz}. In order for circumferential extensional features to form, σ_{rr} should be the least compressive stress. However, since the magnitudes of σ_{rr} and $\sigma_{\theta\theta}$ are small in this region, a small perturbation due to local or regional nonaxisymmetric stresses may determine the orientation of failure features [*Nakamura*, 1977]. The Tharsis Montes are located slightly below the crest of the Tharsis Rise, on a broad slope downward to the northwest [*U.S. Geological Survey*,

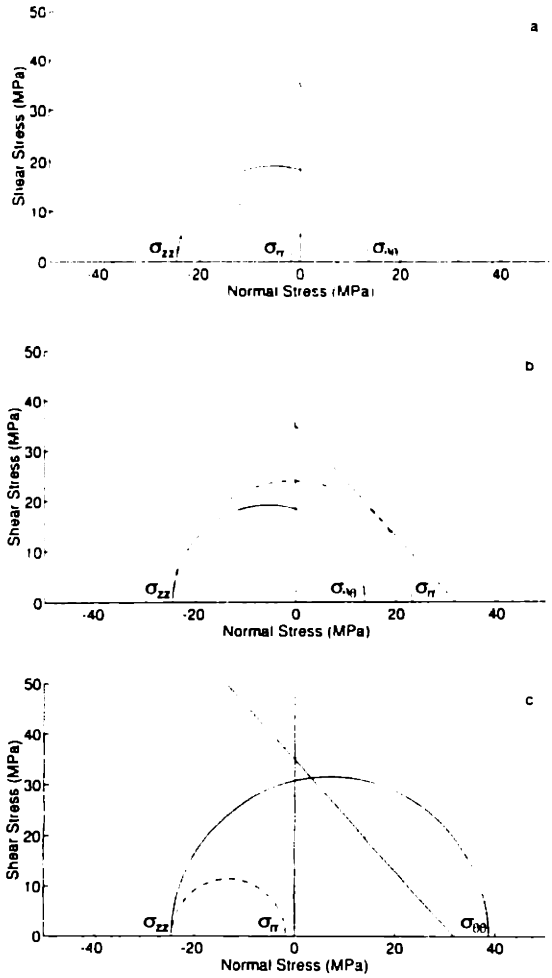

Fig. 17. Mohr diagrams for an element at the top of the volcanic edifice (element center: r = 165 km, z = 2.4 km), for the case where the volcano is detached from the lithosphere along a basal fault (Figure 15). The diagonal line is the Mohr-Coulomb failure envelope for basalt [*Handin*, 1966] with an angle of internal friction $\phi = 49°$ and cohesion c = 38 MPa. The circles represent the stress state at 70 τ_M after emplacement of the third load increment. Principal stress axes for this figure are approximately coincident (to within less than 2°) with the r and z axes (in axisymmetry, the θ axis is a principal axis by definition). A solid arc connects $\sigma_{\theta\theta}$ and σ_{zz}, a dotted arc connects $\sigma_{\theta\theta}$ and σ_{rr}, and a dashed arc connects σ_{rr} and σ_{zz}. (*a*) Original stress state calculated by TECTON; $\sigma_3 = \sigma_{\theta\theta}$, $\sigma_2 = \sigma_{rr}$, and $\sigma_1 = \sigma_{zz}$. (*b*) Stress state after the addition of 25 MPa to σ_{rr}, simulating the effect of a regional-slope-induced local stress field. Now, $\sigma_3 = \sigma_{rr}$ and $\sigma_2 = \sigma_{\theta\theta}$. Element is now on the verge of failure with a circumferential normal faulting mechanism. (*c*) Stress state after the addition of 25 MPa to $\sigma_{\theta\theta}$; $\sigma_3 = \sigma_{\theta\theta}$ and $\sigma_2 = \sigma_{rr}$ as in Figure 17*a*, and stresses satisfy the failure criterion for radial normal faulting.

1989]. This long-wavelength slope of Tharsis, in the presence of a detachment, would be expected to add a northwest-southeast extensional stress; superposition with the axisymmetric model stress field would result in radial extensional features in the northeastern and southwestern quadrants (and, at sufficiently high strains, a NE-SW trending rift), and circumferential graben on the northwestern and southeastern flanks.

We can quantify this suggestion by adding a local stress arising from long-wavelength topographic slope to appropriate components of the stress tensor generated by TECTON. Mohr circle diagrams for an element at the surface of the lower flank for the model of the volcano over a detachment are shown in Figure 17. The stress state predicted on the lower flanks in the absence of a local stress, as noted above, has $\sigma_1 = \sigma_{zz}$ and $\sigma_3 = \sigma_{\theta\theta}$ (Figure 17*a*). This yields a prediction of radial normal faulting (although at the time step given in the figures, stresses do not yet satisfy the failure criterion). If we add a stress increment of 25 MPa to σ_{rr} (in order to simulate a regional-slope-induced NW-SE extensional stress on the northwestern and southeastern flanks), that component becomes the least compressive stress, the element is on the verge of failure (Figure 17*b*), and the predicted normal faulting orientation is circumferential. If instead we add the same stress increment to $\sigma_{\theta\theta}$ (in order to simulate the stress state on the northeastern and southwestern flanks), the orientation of stresses remains the same as in the absence of a regional topographic slope (Figure 17*a*), but the additional stress puts the element into predicted failure (Figure 17*c*). Since the deviatoric stresses caused by flexure increase with time, the element in Figure 17*c* would have failed first at an earlier time step than that in Figure 17*b*. Thus radial normal faulting on the northeastern and southwestern flanks would have occurred before circumferential normal faulting on the northwestern and southeastern flanks.

On Arsia Mons, graben are prominent on the half of the volcano centered on the northwestern azimuth (all the way up the flank to the caldera rim, Figures 2, 5), but are generally absent on the upper flanks of the half centered on the southeastern direction. Several graben are evident at the southeastern edge of the edifice, but these graben are likely the result of extensional stresses at the surface of the lithosphere surrounding the volcano, as described above, and not edifice stresses. The graben on the northwestern half of the volcano terminate near the northeast-southwest-trending rift that bisects the volcano. We suggest that a portion of the northwestern half of the volcano was able to slide down the slope of the Tharsis rise, creating a stress state that led to the formation of the numerous graben (Figure 17*b*). In the southeastern half, however, the volcano was buttressed by the rising slope in that direction and thus unable to move, and the stress state remained stable (horizontal compression at the surface, as in Figure 8*g*). This scenario would account for the substantial difference in faulting character on the two "halves" of the volcano. Stresses associated with caldera formation and magma chamber evolution may have had a strong effect on the stress field near the summit [*Zuber and Mouginis-Mark*, 1992], but the effects of such stresses should be approximately symmetric about the caldera, and thus cannot explain the asymmetry in graben distribution on the flanks of Arsia Mons.

The above reasoning can be generalized to Pavonis and Ascraeus Montes. The northern and western flanks of Pavonis Mons contain a few wide (5-10 km) graben and many narrower (< 2 km) ones [*Zimbelman and Edgett*, 1992]. The widest graben on the edifice are on the western and northwestern flanks. There are fewer of these wide graben than those on the northwestern flank of Arsia Mons, although some graben on the north-northwestern flank of Pavonis Mons may be obscured by a young flow unit [*Zimbelman and Edgett*, 1992]. The significant number of (generally narrow) graben on the northeastern, eastern, and southeastern flanks of Pavonis Mons (Figure 4), however, indicate that the stress state in the edifice is too complex to be well-described by the scenario described above for Arsia Mons. Perhaps the flanks of Pavonis Mons experienced mass movement in directions other than to the northwest earlier in the evolution of

the edifice. An axisymmetric distribution of stresses associated with caldera subsidence [*Zuber and Mouginis-Mark*, 1992] could also contribute to the wider azimuthal distribution of graben. Ascraeus Mons shows the least normal faulting on its flanks; the few concentrations of graben lie on the lower slopes, far from the summit caldera, but as with Arsia Mons the graben are best developed to the west, in the direction of regional downslope. *Crumpler and Aubele* [1978] suggested that Ascraeus Mons is at an earlier stage in its development than the other two volcanoes. We cannot confirm this suggestion from the models, however, since the characteristic time for evolution in stress state is much less than the probable age of the volcano surface.

Stresses from both analytic flexure theory and our models with instantaneous volcano loads predict strike-slip faulting at the surface of the plate, immediately outside the load. Evidence for strike-slip faulting around any of the Tharsis volcanoes, however, is lacking. The absence of such features has been discussed by *Golombek* [1985] and *Schultz and Zuber* [1992], in the general context of large axisymmetric loads on planetary lithospheres. Examination of the plots of stress orientation and failure from our models (Figures 8, 10, 11, 12, 13, 15, 17), however, reveals that the predicted failure modes for elements in the region surrounding the volcano can change with time. In this region, every element that eventually fails (except the innermost) is predicted to do so first by concentric normal faulting. This can be seen more clearly in a Mohr diagram of the stresses in a typical element in this area (Figure 18). The Mohr circles grow in size as flexure proceeds, until the failure envelope is exceeded at about 70 τ_M after first loading. The largest circle shows stresses at the conclusion of flexure, the stress state corresponding to that given by analytic plate models (in which flexure occurs instantaneously).

Applying a failure criterion simply to the final stress state can be misleading. Consideration of the stress history in our models indicates that at the time of first failure, the shear failure criterion is satisfied in the surface elements immediately outside the volcano, and the principal stress directions predict circumferential normal faulting. These first-formed faults, and the antithetically dipping normal faults that would be expected to initiate near them so as to form graben [*Melosh and Williams*, 1989], would tend to relieve extensional stresses in their vicinity and would serve as preferred planes of weakness for the relief of stresses accumulated later. We suggest that as the result of this stress release, strike-slip features would tend to be prevented from forming. We also note that any strike-slip faults formed in an inner annulus of failure early in the evolution of the volcano would be buried by the volcano later in the growth of the edifice. Further, for the lower range of values of lithosphere thickness considered here (20-40 km), the zone of strike-slip faulting predicted from the late-stage stress models lies at the edge of the volcanic construct, which has the lowest surface elevation (Figure 19). This annulus of low elevation could accumulate lava flows and erosional deposits which would tend to cover deformational features (circumferential graben as well as strike-slip features).

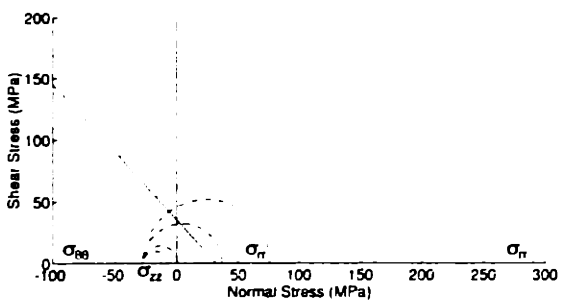

Fig. 18. Mohr diagram for an element at the top of the lithosphere (element center: r = 265 km, z = -2.5 km). The diagonal line is the Mohr-Coulomb failure envelope for basalt, as in Figure 18. Principal stress axes for these figures are approximately coincident with the r and z axes. In order of increasing radius, the arcs represent the stress state at t = 0 (elastic solution), 20, 100, 1000, 2000, and 3000 τ_M. When the failure envelope is first exceeded (t = 70 τ_M), $\sigma_3 = \sigma_{rr}$ and $\sigma_1 = \sigma_{zz}$ (this stress state is denoted by dashed arcs). At the final time shown, $\sigma_3 = \sigma_{rr}$ and $\sigma_1 = \sigma_{\theta\theta}$ (this stress state is denoted by dotted arcs).

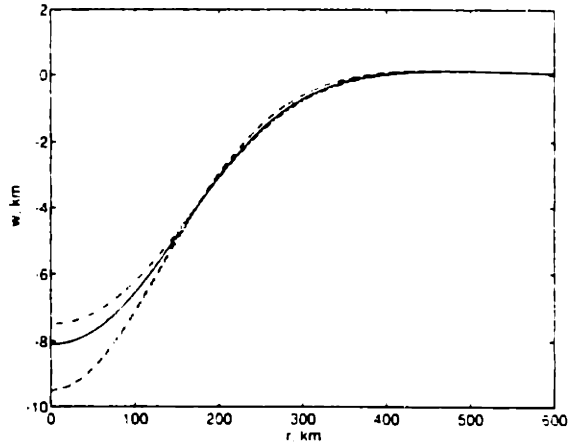

Fig. 19*a*. Vertical displacement of the upper surface of the plate for models with T_e = 40 km: dashed line is for an incrementally grown, detached volcano; dotted line for nodal loads simulating a volcano; solid line for incrementally grown, welded volcano; and dash-dot line for an instantaneously emplaced welded volcano.

Horizontal Compression in the Edifice

Circumferential terraces high on the flanks of Olympus have been interpreted as concentric thrust faults by *Thomas et al.*

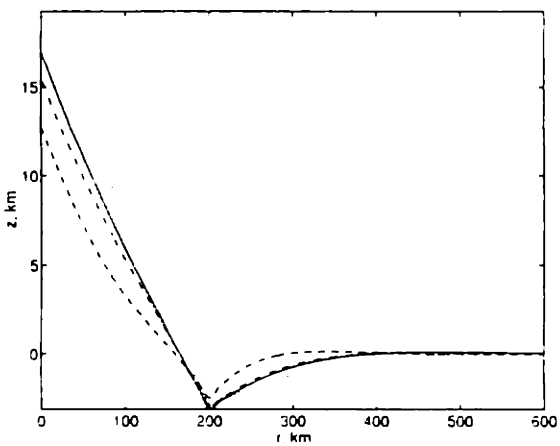

Fig. 19*b*. Surface topography for several models: solid line for an incrementally grown, welded volcano with T_e = 40 km; dotted line for the same volcano with T_e = 60 km; dashed line for same volcano with T_e = 20 km; and dash-dot line for an incrementally grown, detached volcano with T_e = 40 km.

[1990], who applied elastic finite element models to investigate edifice stresses and deformation. Our simplest model (a welded, instantaneously emplaced volcano) predicts a similar stress state, with circumferential thrust faulting on the upper flank and radial thrusts on the lower flank (Figure 13). Plate flexure models also predict large horizontal compressive stresses in the area of the load, which increase with height above the mid-plane of the plate, reaching a maximum at the surface, where thrust faulting is predicted.

Models with growing loads, however, display a different distribution of stress. The maximum horizontal stress occurs in the lowest (first) load increment and decreases upward with each later load increment (Figures 8-10). Each successive load increment "feels" tectonic stresses from itself and all later load increments. The last units emplaced are sensitive only to the effects of their own loading and therefore exhibit a low degree of horizontal compression. Thus, thrust faults (predicted by simpler models) associated with such stresses would be expected to occur either early in the evolution of the volcano or not at all and, if formed, would be covered by later units which remain unfaulted because the failure criterion is not satisfied (Figures 8, 10). We note, however, that stresses in these elements are close to failure (Figures 20, 21). Local stress perturbations and/or variations in internal friction ϕ could result in some failure visible at the surface. On the other hand, if loading increments are smaller than those adopted here (which is likely), then the degree of horizontal compression from such elements would be smaller than those shown here, and faulting would not be expected to initiate at the surface. It is evident from a comparison of Figures 8 and 9 with Figures 13 and 14 that the larger a given load increment, the larger the amount of horizontal compression in that increment at the end of flexure. If a relatively large load increment is the last unit emplaced, evidence of compressional faulting might still be found on the surface. This implies that volcanoes that exhibit compressional faults on their flanks may have experienced greater magma flux late in their growth than volcanoes that lack such flank thrust features.

The presence of graben high on the flanks of the Tharsis Montes

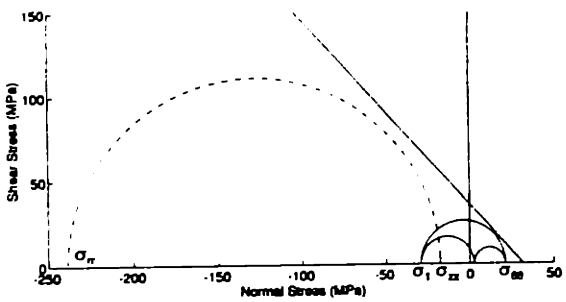

Fig. 20. Mohr diagram for an element on the surface of the volcanic edifice, at the summit (element center: $r = 5$ km, $z = 21.9$ km), representing the stress state at the conclusion of flexure from the last load increment. The diagonal line is the Mohr-Coulomb failure envelope for basalt, as in Figure 18. Large dashed arc represents original stress state: σ_1 is approximately σ_{rr} (to within 4°), and σ_{rr} is only slightly greater than $\sigma_{\theta\theta}$. The solid arcs represent the stress state after the addition of stress increments 260 MPa to $\sigma_{\theta\theta}$ and 230 MPa to σ_{rr}, to represent the effects of magma chamber pressurization near the center of a future caldera. The resulting σ_1 is inclined at 35° to the z axis, and $\sigma_3 = \sigma_{\theta\theta}$. The element is on the verge of failure, with predicted fault mechanisms a mix of strike-slip and radial normal.

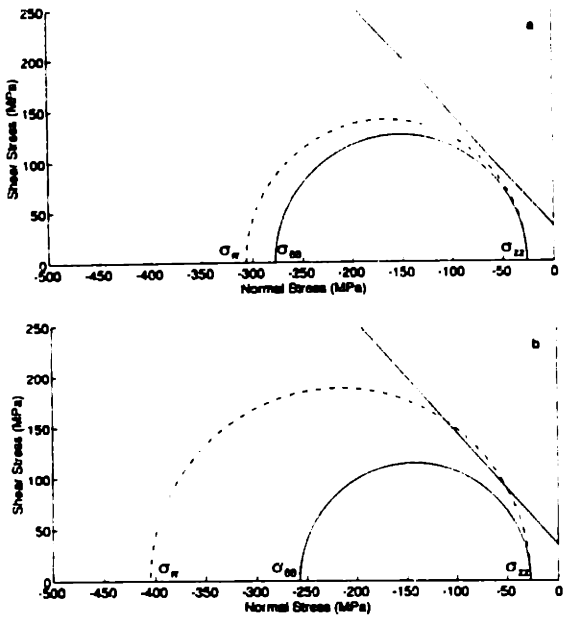

Fig. 21. Mohr diagram for an element on the surface of the volcanic edifice, near the summit (element center: $r = 45$ km, $z = 16.9$ km), representing the stress state at the conclusion of flexure from the last load increment. The diagonal line is the Mohr-Coulomb failure envelope for basalt, as in Figure 18. Principal stress axes for this figure are approximately coincident (to within 6°) with the r and z axes. A solid arc connects $\sigma_{\theta\theta}$ and σ_{zz}, a dotted arc connects $\sigma_{\theta\theta}$ and σ_{rr}, and a dashed arc connects σ_{rr} and σ_{zz}. (*a*) Stress state in the absence of a near-summit magma chamber; $\sigma_3 = \sigma_{zz}$, $\sigma_2 = \sigma_{\theta\theta}$, and $\sigma_1 = \sigma_{rr}$. (*b*) Stress state after addition of stress increments -100 MPa to σ_{rr} and 20 MPa to $\sigma_{\theta\theta}$ to simulate the effect of superposition of magma chamber pressurization. Stress orientations are the same as in Figure 21*a*, and the failure criterion for circumferential thrust faulting is satisfied.

is not consistent with the state of horizontal compression in the edifice found in the welded volcano models. Other factors, such as a basal detachment, lithospheric rifting, or caldera stresses must be invoked to explain the presence of these faults on the upper flanks. We have suggested above that pervasive extensional faulting of a volcanic edifice is evidence for the existence of a detachment beneath the construct, because the stress field in models with such a detachment favors the formation of such faults. Conversely, the orientation of stresses in welded models favors the formation of thrust faults on the upper flanks. Thus, the existence of compressional faults on the flanks of a volcano implies a welded contact between edifice and lithosphere of similar radial extent as the thrusts themselves. The absence of either type of faulting on an edifice is probably more consistent with a welded model, because surface stresses in welded, incrementally grown volcano models do not satisfy the failure criterion. An extra increment of radial compression is required to initiate faulting in such models.

Effects of a Magma Chamber

Our models have not included effects resulting from the pressurization or depressurization of a near-summit magma chamber. *Zuber and Mouginis-Mark* [1992] utilized a finite element model and observations of faulting within the caldera of Olympus Mons to constrain the geometry and depth of the magma

chamber whose evacuation led to summit collapse and caldera formation. Results of these calculations can be superposed with the stresses in our models to determine what effects magma chamber pressure has on our conclusions. Figure 3 of *Zuber and Mouginis-Mark* [1992] displays stresses as a function of radius resulting from an instantaneous pressure drop in a chamber of radial extent equal to the radius of the largest caldera crater. Horizontal stresses σ_{rr} and $\sigma_{\theta\theta}$ are large (of order several hundred MPa) and compressive near the center of the caldera. σ_{rr} makes a transition from compression to extension at some fraction of the caldera radius; $\sigma_{\theta\theta}$ remains compressive but approaches zero. To consider the effect of magma chamber pressurization, we must invert the sign of the stresses given: at small r, σ_{rr} and $\sigma_{\theta\theta}$ are large and extensional, with σ_{rr} making a transition from extension to compression at intermediate radius.

The stress state at the summit of the volcano, in the absence of a magma chamber and after subsidence from the last load increment is complete, is shown in Figure 20. Stresses are close to the failure limit, and the given orientation of stresses would predict circumferential thrust faulting. If we superpose on these stresses those due to magma chamber pressurization (the negative of the stresses given in Figure 3 of *Zuber and Mouginis-Mark* [1992]), we find that stress states and predicted faulting geometry change. On the surface near the center of the caldera, pressurization can lead $\sigma_{\theta\theta}$ and σ_{rr} to become large and extensional, while σ_{zz} remains compressive. The superposition of stress increments $\Delta\sigma_{\theta\theta}$ = 260 MPa and $\Delta\sigma_{rr}$ = 230 MPa simulate the early stages of magma chamber pressurization. The magnitude of $\Delta\sigma_{\theta\theta}$ brings the element to the verge of failure; $\Delta\sigma_{rr}$ is slightly lower following Figure 3 of *Zuber and Mouginis-Mark* [1992] for a magma chamber centered at a depth three fourths of the caldera radius.

The combined stress state is depicted in Figure 20. The summit element is on the verge of failure, with $\sigma_3 = \sigma_{\theta\theta}$. Magma from the chamber can propagate upward through the volume represented by this element, perpendicular to the tensile hoop stress. Thus, summit eruptions are enabled by stresses accompanying pressurization of a high-level magma chamber. However, σ_1 is rotated 35° from the vertical; the predicted faulting is thus intermediate between radial normal faulting and strike slip faulting. Presumably, faults of both types would occur, as well as mixed-mechanism faulting. Evidence for such activity is lacking inside the caldera. However, such faulting is likely to be accompanied or followed by eruption of magma from the chamber, which would cover such faults. Later deformation resulting from magma chamber depressurization [*Zuber and Mouginis-Mark*, 1992] will also obscure these faults. Changing the ratio of stress increments changes the angle between σ_1 and the vertical; increasing $\Delta\sigma_{rr}/\Delta\sigma_{\theta\theta}$ decreases this angle (favoring radial normal faulting), while decreasing the ratio increases the inclination (favoring strike-slip faulting). Note that if pressurization stresses are similar or less in magnitude than the maximum shear stress in the absence of a near-summit magma chamber, then they will not be sufficient to cause failure. As pressurization stresses grow from zero, proximity to failure will actually be reduced until the pressurization stresses are in excess of the original stress difference.

At larger values of radial distance, near the edge of the caldera and beyond, magma chamber pressurization produces a stress state with compressive values of σ_{rr} (Figure 3 of *Zuber and Mouginis-Mark* [1992]). The hoop stress $\sigma_{\theta\theta}$ remains tensile, but approaches zero, and σ_{zz} is unaffected. Superimposing such a stress state on that of a typical element of the mid-flank (Figure 21) will increase the tendency toward failure but will not affect the relative orientations of σ_1 and σ_3. For such an element, an increment $\Delta\sigma_{rr}$ = -100 MPa would be sufficient to cause faulting (with a circumferential thrust mechanism). Thus, pressurization stresses lead to an increase in likelihood of thrust faulting at the edge of the caldera and beyond. Of course, such faults formed within the radius of the future caldera will probably be rendered unrecognizable by caldera collapse resulting from magma withdrawal, but faults at greater radius values would be evident if not obscured by summit flows. Given sufficient pressurization, stresses could be high enough to contribute to the formation of circumferential thrust faults near the caldera, faults resembling the circumferential terraces on the flanks of Olympus Mons.

Magma Transport

The volcanic edifice stress fields calculated here have important implications for magma transport and eruption. Magma propagates through the lithosphere along fractures that form perpendicular to the direction of least compressive stress. Immediately following emplacement, the stresses in a given load increment are characterized by σ_3 horizontal (e.g., Figure 8*a*), a geometry that tends to favor vertical propagation of magma to the summit region. As a result of flexure in a volcano with a welded base, however, the principal stresses induced in that load increment rotate such that σ_1 is horizontal and σ_3 is vertical (Figure 8). Horizontal propagation of magma, outward from the summit to the flanks, should then tend to be favored. Thus within an interval of shield building there may be an evolution in favored eruption location from summit to lower flank. Such an evolution is consistent with the first two stages in the sequence of major events for the Tharsis Montes determined by *Crumpler and Aubele* [1978]. We note that while the principal stresses rotate in the most recently emplaced increment, stresses in earlier load increments remain in horizontal principal compression. Thus in the core of the edifice stress orientations favor flank eruptions or subhorizontal intrusions throughout most of the history of the edifice, in the absence of magmatic overpressure or a basal detachment.

The stress evolution of a growing volcano may affect the location of magma collection zones or chambers. Maximum horizontal compression is achieved within the earliest load increments, near the bottom of the final load. This stress pattern contrasts with that from analytic flexure calculations, where stresses increase linearly with distance from the plate midplane. A region of high compressive stress at lower levels in the edifice could inhibit ascending magma from reaching the summit, and could thus lead to the pooling of magma. A possible consequence of a stress barrier is lateral propagation of magma into sheet dikes or sills. On the other hand, high stresses in this region will likely be relieved by faulting, until the failure criterion is no longer satisfied. This region may thus be the most pervasively faulted and fractured zone, and thus perhaps a favored location for significant volumes of magma to collect. The location of this zone (as delineated by, say, the 350 MPa contour in Figure 9*d*) is broadly consistent with the depth to the Olympus Mons magma chamber estimated by *Zuber and Mouginis-Mark* [1992].

The issue of compressional versus extensional horizontal stresses in the volcanic edifice is important when considering the geometry of volcano growth. In order for the volcano to grow, there must be a path for magma to reach the surface (or near the

surface in the case of growth by intrusion). Large horizontal compressive stresses within the edifice may inhibit summit eruptions, as noted above. Flank eruptions, however, result in an added flank load, not modelled here, to which the lithosphere will respond with additional flexure. Subsidence and additional flexure near the flanks of the volcano may at least partially relieve the compressional stresses near the summit, thus enhancing the possibility of additional summit eruptions. By this scenario, the preferred site for eruptions could alternate between summit and flank, on time scales on the order of 100-1000 Maxwell times. When the effects of time-dependent loading during volcano growth are included, the magnitude of horizontal stresses in the later stages of evolution are greatly reduced compared with stresses at the equivalent level in instantaneously loaded models. When both time-dependent loading and a basal detachment are included, horizontal compressive stresses in the edifice are reduced further, and a state of extensional hoop stress is reached in the lower part of the edifice, adjacent to the detachment (Figure 15). Summit eruptions are then more easily accommodated. As noted above, the effect of magma chamber pressurization stresses is to create a state of horizontal principal tension in the rocks above the magma chamber, such that magma ascent to the summit caldera region is allowed. If these stresses are of sufficient magnitude and of the form predicted by *Zuber and Mouginis-Mark* [1992], they may allow summit eruptions even in the absence of the stress-modifying factors described above.

Flank Tectonics: Aureoles, Lobes, and Scarps

Results from our models also provide a basis for understanding the flank tectonics of the Tharsis volcanoes, in particular the downslope motions of material in the form of large slides or slumps. As noted above, the Olympus Mons aureole has been interpreted as a large landslide deposit resulting from slip along large-offset listric normal faults [*Francis and Wadge*, 1983], the upper reaches of which are postulated to coincide with the basal scarp. Aureole material is most prominent to the north and west; there is an aureole lobe to the southeast, however, suggesting that the Tharsis rise did not fully buttress the southeastern flank of Olympus. The basal scarp has greatest relief on the northwestern and southeastern flanks. Evidence for similar mass movement activity on a smaller scale is seen on the northwestern flanks of Ascraeus, Pavonis, and Arsia Montes [*Zimbelman and Edgett*, 1992].

As discussed above, the interaction between the axisymmetric stress field from volcano loading and local stresses due to regional topographic slope may influence the location, orientation and extent of scarps and of landslides triggered by fault slip on the Tharsis volcanoes. Models with a detachment predict that at the edge of the edifice $\sigma_3 = \sigma_{\theta\theta}$. This can account for radial normal faulting but not for the scarps and aureole deposits, which in the above scenario require that $\sigma_3 = \sigma_{rr}$. The addition of a northwest-southeast extensional stress, induced by the regional gradient in elevation, however, would provide the necessary orientation of stresses in the northwestern and southeastern quadrants of a Tharsis volcano. The prominent aureole deposits to the north and west of Olympus Mons could then be a result of large landslides analogous to those off the Hawaiian chain but on a larger scale, and the basal scarp could constitute the coalesced head scarps of these landslides. By this interpretation, the lobate features to the northwest of each of the Tharsis Montes would be similar in origin but smaller in scale, with accompanying basal scarps either greatly reduced in scale (on Arsia and Ascraeus Montes) or absent (Pavonis Mons) [*Zimbelman and Edgett*, 1992]. Slide deposits tend to be more prominent on the northwestern side of these volcanoes, since this is the regional downslope direction. Note that the NW-SE extensional stress field is postulated to be present throughout the evolution of the volcano in this scenario. This assumption contrasts with the view of *Francis and Wadge* [1983] that proto-Olympus Mons was elongate to the northwest because early NE-SW extension allowed preferential effusion along a NW-SE axis. The lobate features are progressively smaller from Arsia to Pavonis to Ascraeus. This variation is consistent with the view of *Crumpler and Aubele* [1978] that these volcanoes constitute an evolutionary sequence in which Arsia Mons represents the most evolved end-member and Ascraeus the least. This sequence is consistent with the prediction from our models that linear rift formation due to detachment tectonics will occur earlier than circumferential graben formation (which are ubiquitous on the northeastern flank of Arsia and largely absent on Ascraeus.)

Large landslides and slumps, triggered by extension on the flanks, may be a second important mode of volcano growth, in that mass movement clears the way for more volcanic material to be emplaced behind it. In championing this view for the Hawaiian volcanoes, *Lipman et al.* [1985] emphasize the role of dike intrusion along rift zones, arguing that the subvolcano detachment passively takes up the resulting strain. Our results suggest that without such a detachment, radial rift zones may be suppressed by horizontal compression. As a welded volcano grows, an ever increasing horizontal compressive stress near the base of the edifice would eventually choke off magma supply to the summit. Thus, the Hawaiian rift zones may owe their existence to the presence of the detachment, and volcanoes lacking such a detachment may exhibit important structural and evolutionary differences from those in Hawaii. For example, *Nakamura* [1980] has suggested that the lack of rift zones in the Galapagos shields is attributable to a paucity of oceanic sediments on the young oceanic lithosphere beneath the volcanoes.

Linear Rift Zones

Linear symmetries observed in all the Tharsis Montes volcanoes may be indirect evidence for failure in the sub-volcano region. The second stage in the *Crumpler and Aubele* [1978] sequence of volcano evolution involves the development of a linear rift bisecting the volcanoes, with eruptions emanating from this rift. Radially oriented normal faulting under a volcano might be thought at first to tend to divide the volcano into radial sections, much like pie slices. The existence of the linear rifts on the Tharsis Montes, however, suggests that this mode of failure may be concentrated into one large linear feature that bisects the volcano. Our calculations predict radially oriented normal faulting in a broad zone beneath a volcano. For the case with T_e = 20 km (Figure 10), this zone extends beyond the volcano radius and reaches within 5 km of the surface. Such a zone, if concentrated into a linear feature and if continued to the surface by sustained faulting, may give rise to the linear rifts and bilateral symmetry. Stresses contributed by the long-wavelength topography of Tharsis should add a component of northwest-southeast extension (the direction of greatest slope), which could act to concentrate the radial faulting into a rift zone striking northeast-southwest, as is observed. This mechanism is plausible only for volcanoes welded to the lithosphere, however, in order that lithospheric stresses can be transmitted to the edifice. A

problem with this idea is that the rifting has to propagate upward to the surface of the lower volcano flanks. For high values of T_e, the faulted region at the base of the lithosphere is unlikely to propagate upward through the entire plate thickness. Thus, this mechanism is plausible at most only for low values of T_e.

The prediction of radially oriented normal faulting on the lower flanks for the model with a subvolcanic detachment (Figure 15) suggests an alternative mechanism for forming the observed rifts. By this scenario, rifts may originate as radially oriented graben across which strain becomes concentrated because of the superposed regional-slope-induced stress field and movement along the detachment of the downslope half of the edifice. This mechanism has the advantage that rift formation would initiate early in the evolution of the volcano, a timing more consistent with the chronology of *Crumpler and Aubele* [1978]. Thus the rift zones on the Tharsis Montes, as with those in Hawaii, favor the presence of a detachment surface beneath the edifice.

The stress state in the lower edifice for the model of a growing volcano over a detachment surface resembles that determined seismically for western Hawaii by *Gillard et al.* [1992], with σ_1 vertical (or nearly so), and both σ_2 and σ_3 horizontal and similar in magnitude. The model stress state also resembles that of a tectonic model for the base of Hawaii proposed by *Wyss and Koyanagi* [1992] (based in part on the results of *Gillard et al.* [1992]). The model of *Wyss and Koyanagi* [1992] has σ_3 parallel to the direction of slip along the basal detachment, whereas in our model σ_3 is perpendicular to the basal slip. However, since σ_2 and σ_3 are similar in magnitude [*Gillard et al.*, 1992], local perturbations and departures from axisymmetry may determine the orientations of these stresses in actual volcanoes.

The evolution of Pacific hotspot volcanoes may provide further insight into the formation and influence of a bisecting rift zone. For instance, *Holcomb* [1985] has suggested that the island of Molokai in the Hawaiian chain resembles a volcano cut almost exactly in half, with one part transported downslope in one or more massive submarine slides, and the other part remaining to form the present island. Bathymetry of the ocean floor north of Molokai [*Moore*, 1964] supports this conclusion. We earlier conjectured that a similar but less extreme mechanism could explain the presence of graben on the upper slopes of Arsia Mons and Pavonis Mons, in that as the volcano halves slide apart from each other, an extensional environment may be created near the summit. To investigate this possibility quantitatively, a fully three dimensional model is required.

Detachment Tectonics

The flank tectonic characteristics of the Tharsis volcanoes, combined with the observations of and modeling results for terrestrial volcanoes with detachments, strongly suggest that detachments analogous to those of Hawaii-type volcanoes [*Lipman et al.*, 1985] exist on Mars. Such a detachment cannot arise from the presence of a thick oceanic sediment layer as for Hawaii. It has nonetheless been demonstrated that liquid water existed in moderate quantities at the Martian surface earlier in the history of the planet [e.g., *Carr*, 1987]. While liquid water is now unstable at the surface, large quantities of water are believed to be buried as ground-ice. *Tanaka* [1985] proposed that gravity sliding and spreading could account for the Olympus Mons aureole (and basal scarp) providing that a basal detachment zone of material with low shear strength was present. He calculated that a layer of material with about 10% interstitial or interbedded ice could provide the necessary detachment. The pre-volcanic upper crustal layer may have consisted dominantly of an impact breccia regolith produced by repeated impacts. Such heavily fractured material is likely to be porous and thus may contain interstitial ice. Even in the absence of an excess ice content, the mechanical weakness of such a layer could contribute to the formation of a detachment between a strong lower crust and a volcanic edifice. While *Tanaka* [1985] states that such a structure is unique to Olympus Mons, *Zimbelman and Edgett* [1992] mapped lobate deposits on the northwestern flanks of all three Tharsis Montes that may be smaller-scale analogues of the Olympus Mons aureoles, so some form of detachment beneath all four constructs appears to be indicated.

Plate Thickness and Volcano Size

The ratio of elastic plate thickness to volcano diameter has a significant effect on the evolution of the subsidence, stress, and regions of predicted failure in our computations. We note several trends as plate thickness increases relative to volcano diameter. Study of the patterns of stress orientations and predicted failure in Figures 8, 10, and 11, shows that the outer region of failure, at a given time, increases in horizontal (and vertical) extent with increasing plate thickness (Table 3). The magnitude of deviatoric stress within the volcanic edifice, and in particular the magnitude of maximum horizontal compressive stress, decreases with increasing plate thickness. For the largest plate thickness considered here, stresses in the edifice never exceed the failure limit (Figure 11). Volcanoes on thick plates are thus less likely to experience compressional faulting, either at the surface or below (compare Figures 10 and 11). This condition also requires greater magma chamber overpressure values to allow summit eruptions for volcanoes on thinner plates. For a given value of peak overpressure, the choking effect of horizontal stresses could set a limit to the size of volcanoes welded to thin plates. As noted above, the zone of large horizontal compressive stress at middepths in the edifice may affect the propagation of magma from its mantle sources through the edifice. Elastic plate thickness may thus play a role in determining the location of magma storage areas.

We note that for cases in which the volcano is solidly attached to the lithosphere, the deflection given by TECTON at the final time step is less than that of the analytic solution near $r = 0$. Radial distances of the zero crossing and flexural bulge are also greater than those for the analytic solution. These effects result from a stiffening of the plate by the volcanic load itself. Near $r = 0$, the elements that make up the volcano take up some of the horizontal compressive flexural stresses that would otherwise be taken up by the top half of the plate. This effect is demonstrated in Figure 19*a* for volcanoes on a lithosphere with $T_e = 40$ km. The two curves with the greatest deflection at $r = 0$ are for a simulated volcano load and for a volcano detached from the lithosphere. For these models, the load does not contribute to the strength of the lithosphere, in the first case because point loads contribute no stiffness, and in the second case because the detachment allows no shear stress to be transmitted between the volcano and lithosphere. The curve with intermediate deflection at $r = 0$ is for an incrementally grown volcano. The growing volcano adds a stiffness to the plate that increases with time. The curve with the least displacement at $r = 0$ is for an instantaneously emplaced volcano. This is the stiffest case, because the entire 25-km-high volcano is present from the start of flexure. The peak of the

flexural arch moves outward in radius (by about 15 km) as the edifice-contributed stiffness increases. This increase in flexural wavelength may be important when analytic thin-plate flexure models are compared with topographic profiles for the purpose of estimating elastic plate thicknesses (especially for high values of the ratio of volcano height to lithospheric thickness). For volcanoes welded to the underlying lithosphere, T_e would be overestimated. Figure 19*b* gives surface topographic profiles for several of the models. Note that the model with a detached volcano predicts a final volcano height lower than that for an equivalent welded volcano.

Future Directions

While the calculations presented here are limited in their ability to model accurately the behavior of large volcanoes, we hope to be able to relax some of these limitations in future models. In our models, the crust and mantle are perfectly viscoelastic; within an element, no provision is made for stresses that exceed reasonable failure limits (such as in all the shaded elements in Figures 8, 10, and 11). The inclusion of localized yielding can be presumed to have important effects on the geometry and magnitudes of the calculated stress and deformation fields in adjacent material, encouraging or inhibiting the formation of further faulting. A finite element code that incorporates plastic yielding will allow us to account more realistically for the effects that failure will have on predicted fault locations and styles. Further, the effect of thermal stresses has been ignored. Thermal stresses can play an important role in the evolution of the volcano, both through stresses accumulated by cooling after emplacement of each layer, and through the time-dependent thermal stresses in regions reheated by the later passage or storage of magma.

CONCLUSIONS

In this paper we have used finite element calculations to simulate the deformational and stress response of the lithosphere to a volcano load. The results of these calculations are compared with observed tectonic features and inferred eruption characteristics of large Martian volcanoes. Some of the zones of failure and faulting predicted in our models have direct analogues in observed features; others may be indirectly related to observed structures. Three regions of failure, each with characteristic stress geometry, are predicted in our models . Flexural stresses in the lithosphere immediately surrounding the volcano can result in circumferential graben. Flexurally induced normal faulting in a wide zone beneath the center of a large volcano may play a major role in the development and modification of the edifice. Thrust faults are predicted on the upper flanks of the volcano early in its growth, but such structures will be covered by later summit flow units not predicted to fail after emplacement.

The relative timing of events in our models is generally consistent with the chronology set forth by *Crumpler and Aubele* [1978] for the Tharsis Montes. After construction of the main shield, rift formation and flank eruptions along this rift occur in the second stage of evolution. Models of welded volcanoes predict rotation of the principal stress axes in the upper edifice from vertical to horizontal principal compression during the flexure that follows the addition of each major load increment. Given that magma ascending through the lithosphere propagates along fractures oriented perpendicular to the direction of least compressive stress, such a rotation in the principal stress orientations in the models tends to favor eruption sites shifting from the volcano summit to the flanks as flexure proceeds. After a few tens of Maxwell times the failure zone beneath the volcano (which could favor formation of the rift) has begun to grow. In models that include a detachment, radial normal faults are predicted on the flanks (these can occur very early if stresses due to regional topography are included). The third stage in the chronology of *Crumpler and Aubele* [1978] involves summit subsidence and formation of concentric fractures and graben. After about 100 Maxwell times, our computations show increased subsidence as well as the growth of the region of normal faulting outward of the volcano. In our detached volcano models, the superposition of stresses due to regional topographic slope has the effect of allowing circumferential graben to form on the flanks. The fourth stage of *Crumpler and Aubele* [1978] involves further eruption along the rift, flooding the summit and flanks. Late stage flank eruptions are consistent with the stress fields in our calculations. Summit eruptions, however, would not be favored by the computed stress fields. It is likely that the stress field is influenced by the effects of previous stages of the evolution. After sufficient flank eruptions, loading on the flanks might lead to relief of compressive stresses near the summit, re-opening the path to the summit caldera. Also, the effect of sections of the volcano sliding away from the bisecting rift may result in an extensional environment near the summit, once again favoring summit eruptions. Stress fields near the summit region may favor summit eruptions, even in welded volcanoes, if stresses from magma chamber pressurization are of sufficient magnitude to counteract flexurally-induced horizontal compression.

Previous models of lithospheric loading have been used to predict a zone of strike-slip faulting surrounding large loads, on the basis of the faulting criteria of *Anderson* [1951]. When the effects of time-dependent flexure and incremental loading are taken into account, however, a different prediction is reached. The initial faulting mechanism in this region is almost always circumferential normal faulting. The influence of these first-formed faults is likely to encourage further faulting with a similar orientation and to inhibit the formation of strike-slip faults in the area. Those limited portions of the model that do first fail by predicted strike-slip faulting are those closest to the growing load and are likely to be buried by later flows and edifice growth. Thus, the likelihood of observing such faults around large volcanoes is small.

An origin by mass movement has been suggested for the vast aureole deposits surrounding Olympus Mons [*Harris*, 1977; *Lopes et al.*, 1980; *Francis and Wadge*, 1983] as well as smaller lobate deposits to the northwest of each of the Tharsis Montes [*Zimbelman and Edgett*, 1992]. Analogy with large slumps and slides off of the Hawaiian islands [*Lipman et al.*, 1985; *Moore et al.*, 1989] suggests that a detachment between volcano and lithosphere may play a role in the evolution of volcanoes on Mars as well as Earth. Models that include such a detachment, in contrast with models of volcanoes welded to the lithosphere, predict a state of horizontal extension in the edifice (and eventually radial normal faulting on the lower flanks). When the effects of nonaxisymmetric local stresses due to regional topographic slope are considered, predicted patterns of faulting can match observed structures on the Tharsis Montes. The results of our calculations are consistent with the formation of aureole deposits as slides triggered by slip on listric normal faults. Under this interpretation, the large basal scarp of Olympus Mons, and smaller scarps on Ascraeus and Arsia Montes, are the upper

reaches of these faults at the head of these mass movements. The radial rifts on the Tharsis Montes are zones of radial extensional faulting, whose orientation may be controlled by motion along a detachment down the regional topographic gradient of the Tharsis rise. The presence of the rift zones, lobate deposits, and extensive circumferential normal faulting on the flanks of Arsia and Pavonis Montes imply the existence of a detachment beneath these constructs. Ascraeus Mons lacks the extensive normal faulting but retains a bisecting rift and lobate deposit, perhaps indicating a detachment of lesser extent that for the other Tharsis Montes. Olympus Mons exhibits extensive aureole deposits, indicative of a detachment in distal sectors of the volcano. However, the presence of apparently compressive features on the upper and mid flanks, combined with the absence of rift zones and circumferential graben, imply a welded contact between volcano and lithosphere for most of the Olympus Mons edifice. The above observations imply the existence of at least a partial detachment beneath all four constructs. We find that the model which best matches the observed tectonic features and inferred evolution of the Tharsis Montes is an incrementally loaded edifice, basally detached from the lithosphere.

Future improvements in measurements of topography and gravity as well as high-resolution imaging and geochemical mapping of the surface will help sharpen our view of the geological evolution of the Tharsis region and of the Tharsis volcanoes in particular. Models of the type presented here provide a basis for integrating new information into a quantitative understanding of the deformational and magmatic history of large volcanoes on Mars and on other terrestrial planets.

Acknowledgments. We thank Jay Melosh for generously providing us a copy of the TECTON code and for instructing us in its use, and Rob Comer for his thick-plate flexure code. Bob Grimm, Buck Janes, Paul Thomas, Ken Tanaka, and an anonymous reviewer offered helpful comments on earlier drafts. This work benefited greatly from discussions with Brad Hager, Marcia McNutt, and Jim Zimbelman. P.J.M. would like to thank the convenors of the NASA Field Volcanology Workshop of July 1992 for the opportunity to study an active volcano. This research was supported by the NASA Planetary Geology and Geophysics Program under grants NAGW-1077, NAGW-1937, and NAGW-3276.

REFERENCES

Anderson, E. M., *The Dynamics of Faulting and Dyke Formation With Applications to Britain*, 2nd ed., 206 pp., Oliver and Boyd, Edinburgh, 1951.

Blasius, K. R., and J. A. Cutts, Shield volcanism and lithospheric structure beneath the Tharsis Plateau, Mars, *Proc. Lunar Planet. Sci. Conf., 7th*, 3561-3573, 1976.

Blasius, K. R., and J. A. Cutts, Topography of Martian central volcanoes, *Icarus, 45*, 87-112, 1981.

Borgia, A., J. Burr, W. Montero, L. D. Morales, and G. E. Alvarado, Fault-propagation folds induced by gravitational failure and slumping of the Central Costa Rica volcanic range: Implications for large terrestrial and Martian volcanic edifices, *J. Geophys. Res., 95*, 14,357-14,382, 1990.

Carr, M. H., Water on Mars, *Nature, 326*, 30-35, 1987.

Chevallier, L., and W. J. Verwoerd, A numerical model for the mechanical behavior of intraplate volcanoes, *J. Geophys. Res., 93*, 4182-4198, 1988.

Comer, R. P., Thick plate flexure, *Geophys. J. R. Astron. Soc., 72*, 101-113, 1983.

Comer, R. P., S. C. Solomon, and J. W. Head, Mars: Thickness of the lithosphere from the tectonic response to volcanic loads, *Rev. Geophys., 23*, 61-92, 1985.

Crumpler, L. S., and J. C. Aubele, Structural evolution of Arsia Mons, Pavonis Mons, and Ascraeus Mons: Tharsis region of Mars, *Icarus, 34*, 496-511, 1978.

Dieterich J. H., Growth and persistence of Hawaiian volcanic rift zones, *J. Geophys. Res., 93*, 4258-4270, 1988.

Eliason, E., R. Batson, and A. Manley, Mars Mosaicked Digital Image Model (MDIM) and Digital Terrain Model (DTM), *CD VO 2003*, U.S. Geol. Surv., Flagstaff, Ariz., 1991.

Francis, P. W., and G. Wadge, The Olympus Mons aureole: Formation by gravitational spreading, *J. Geophys. Res., 88*, 8333-8344, 1983.

Gillard, D., M. Wyss, and J. S. Nakata, A seismotectonic model for western Hawaii based on stress tensor inversion from fault plane solutions, *J. Geophys. Res., 97*, 6629-6641, 1992.

Golombek, M. P., Fault type predictions from stress distribution of planetary surfaces: Importance of fault initiation depth, *J. Geophys. Res., 90*, 3065-3074, 1985.

Greeley, R., and P.D. Spudis, Volcanism on Mars, *Rev. Geophys., 19*, 13-41, 1981.

Handin, J., Strength and ductility, in *Handbook of Physical Constants, Mem. 97*, edited by S.P. Clark, Jr., pp. 223-289, Geological Society of America, Boulder, Colo., 1966.

Harris, S. A., The aureole of Olympus Mons, Mars, *J. Geophys. Res., 82*, 3099-3107, 1977.

Holcomb, R. T., The caldera of East Molokai volcano, Hawaiian Islands, in *National Geographic Society Research Reports (for 1980-1983), 21*, 81-87, 1985.

Lipman, P. W., J. P. Lockwood, R. T. Okamura, D. A. Swanson, and K. M. Yamashita, Ground deformation associated with the 1975 magnitude-7.2 earthquake and resulting changes in activity of Kilauea volcano, Hawaii, *U.S. Geol. Surv. Prof. Pap., 1276*, 45 pp., 1985.

Lopes, R. M. C., J. E. Guest, and C. J. Wilson, Origin of the Olympus Mons aureole and perimeter scarp, *Moon Planets, 22*, 221-234, 1980.

McGarr A., On the state of lithospheric stress in the absence of applied tectonic forces, *J. Geophys. Res., 93*, 13,609-13,617, 1988.

McNutt, M. K., Lithospheric flexure and thermal anomalies, *J. Geophys. Res., 89*, 11,180-11,194, 1984.

Melosh, H. J., and A. Raefsky, The dynamical origin of subduction zone topography, *Geophys. J. R. Astron. Soc., 60*, 333-354, 1980.

Melosh, H. J., and A. Raefsky, Anelastic response of the Earth to a dip slip earthquake, *J. Geophys. Res., 88*, 515-526, 1983.

Melosh, H. J., and C. A. Williams, Jr., Mechanics of graben formation in crustal rocks: A finite element analysis, *J. Geophys. Res., 94*, 13,961-13,973, 1989.

Moore, J. G., Giant submarine landslides on the Hawaiian Ridge, *U.S. Geol. Surv. Prof. Pap., 501-D*, D95-D98, 1964.

Moore, J. G., D. A. Clague, R. T. Holcomb, P. W. Lipman, W. R. Normark, and M. E. Torresan, Prodigious submarine landslides on the Hawaiian ridge, *J. Geophys. Res., 94*, 17,465-17,484, 1989.

Morris, E. C., The basal scarp of Olympus Mons (abstract), Reports of the Planetary Geology Program-1988, *NASA Tech. Memo., TM 84211*, 389-390, 1981.

Mouginis-Mark, P. J., Late-stage summit activity of Martian shield volcanoes, *Proc. Lunar Planet. Sci. Conf., 12th*, 1431-1447, 1981.

Nakamura, K., Volcanoes as possible indicators of tectonic stress orientation - Principle and proposal, *J. Volcanol. Geotherm. Res., 2*, 1-16, 1977.

Nakamura, K., Why do long rift zones develop in Hawaiian volcanoes - A possible role of thick oceanic sediments, *Bull. Volcanol. Soc. Jpn., 25*, 255-269, 1980.

Peterson, D. W., and R. B. Moore, Geologic history and evolution of geologic concepts, island of Hawaii, *U.S. Geol. Surv. Prof. Pap., 1350*, 149-189, 1987.

Ryan M. P., The mechanics and three-dimensional internal structure of active magmatic systems: Kilauea volcano, Hawaii, *J. Geophys. Res., 93*, 4213-4248, 1988.

Schultz, R. A., and M. T. Zuber, Why are strike-slip faults that are "predicted" by lithospheric deformation models rarely observed on planetary surfaces? (abstract), *Lunar Planet. Sci., 23*, 1247-1248, 1992.

Scott, D. H., and K. L. Tanaka, Map showing lava flows in the northeast part of the Phoenicis Lacus quadrangle of Mars, *Map I-1277*, U.S. Geol. Surv., Reston, Va., 1981.

Scott, D. H., and K. L. Tanaka, Geologic map of the western equatorial region of Mars, *Map I-1802A*, U. S. Geol. Surv., Reston, Va., 1986.

Scott, D. H., G. G. Schaber, K. C. Horstman, A. L. Dial, Jr., and K. L. Tanaka, Map showing lava flows in the southwest part of the Tharsis quadrangle of Mars, *Map I-1268*, U.S. Geol. Surv., Reston, Va., 1981*a*.

Scott, D. H., G. G. Schaber, and K. L. Tanaka, Map showing lava flows in the southeast part of the Tharsis quadrangle of Mars, *Map I-1269*, U.S. Geol. Surv., Reston, Va., 1981*b*.

Scott, D. H., G. G. Schaber, K. C. Horstmann, A. L. Dial, Jr., and K. L. Tanaka, Map showing lava flows in the northwest part of the Phoenicis Lacus quadrangle of Mars, *Map I-1272*, U.S. Geol. Surv., Reston, Va., 1981*c*.

Solomon, S. C., and J. W. Head, Heterogeneities in the thickness of the elastic lithosphere of Mars: Constraints on heat flow and internal dynamics, *J. Geophys. Res.*, *95*, 11,073-11,083, 1990.

Tanaka, K. L., Ice-lubricated gravity spreading of the Olympus Mons aureole deposits, *Icarus*, *62*, 191-206, 1985.

Tanaka, K. L., The stratigraphy of Mars, *Proc. Lunar Planet. Sci. Conf. 17th*, Part 1, *J. Geophys. Res.*, *91*, suppl., E139-E158, 1986.

ten Brink, U. S., and T. M. Brocher, Multichannel seismic evidence for a subcrustal intrusive complex under Oahu and a model for Hawaiian volcanism, *J. Geophys. Res.*, *92*, 13,687-13,707, 1987.

Thomas, P. J., S. W. Squyres, and M. H. Carr, Flank tectonics of Martian volcanoes, *J. Geophys. Res.*, *95*, 14,345-14,355, 1990.

Thurber, C. H., and A. E. Gripp, Flexure and seismicity beneath the south flank of Kilauea volcano and tectonic implications, *J. Geophys. Res.*, *93*, 4271-4278, 1988.

Turcotte, D. L., and G. Schubert, *Geodynamics*, 450 pp., John Wiley, New York, 1982.

U.S. Geological Survey, Topographic maps of the western, eastern equatorial and polar regions of Mars, *Map I-2030*, U.S. Geol. Surv., Reston, Va., 1989.

Wu, S. S. C., Mars synthetic topographic mapping, *Icarus*, *33*, 417-440, 1978.

Wu, S. S. C., P. A. Garcia, R. Jordan, F. J. Schafer, and B. A. Skiff, Topography of the shield volcano, Olympus Mons on Mars, *Nature*, *309*, 432-435, 1984.

Wyss, M., and R. Y. Koyanagi, Seismic gaps in Hawaii, *Bull. Seismol. Soc. Am.*, *82*, 1373-1387, 1992.

Zimbleman, J. R., and K. S. Edgett, The Tharsis Montes, Mars: Comparison of volcanic and modified landforms, *Proc. Lunar Planet. Sci.*, *22*, 31-44, 1992.

Zuber, M. T., and P. J. Mouginis-Mark, Caldera subsidence and magma chamber depth of the Olympus Mons volcano, Mars, *J. Geophys. Res.*, *97*, 18,295-18,307, 1992.

P. J. McGovern, Building 54-521, Department of Earth, Atmospheric, and Planetary Sciences, Massachusetts Institute of Technology, Cambridge, MA 02139.

S. C. Solomon, Department of Terrestrial Magnetism, Carnegie Institution of Washington, 5241 Broad Branch Road, N.W., Washington, DC 20015.

(Received May 4, 1993;
revised September 30, 1993;
accepted November 2, 1993.)

Chapter 3

The Roles of Flexural Stresses and Basal Boundary Conditions in the Structural Development of Large Volcanoes

Introduction

Long linear chains of large volcanoes on the ocean floor are believed to be the surface manifestations of hot plumes rising from deep in the Earth's mantle [*Wilson*, 1965; *Morgan*, 1972]. Large edifices form from magma erupted on the lithosphere above the hotspot; they grow, load the lithosphere, and are subsequently removed from the magma source by the horizontal motion of the oceanic plate. Volcanoes in a given chain tend to exhibit similar sizes and morphologies, but such characteristics can vary greatly for volcanoes of different chains. For example, volcanoes of the Hawaiian chain are characterized by edifice radii up to about 100 km, heights of about 9 km above basement (before erosion), and long, deep linear loci of intrusion and eruption called rift zones [e.g., *Peterson and Moore*, 1987]. In contrast,

volcanoes of the Galápagos chain are characterized by radii about 20-30 km, heights of about 3.5 km above basement, and small, sparsely distributed zones of linear fissures, believed to be shallow features [*Chadwick and Howard*, 1991]. Volcanoes in other chains have sizes and structures intermediate between these two cases. We seek in this chapter to ascertain the regional characteristics that regulate volcanic emplacment and determine the morphology and evolution of large oceanic hotspot volcanoes.

To this end, we construct numerical models of the flexural response of the lithosphere to loading by a growing volcano. We use a versatile finite element approach. We assign elements to the volcanic edifice itself, allowing calculation of the stress state and stress history within the edifice. The effects of episodic load growth are treated by implementation of time-dependent material properties [*McGovern and Solomon*, 1993]. We study the effect of several conditions on the evolution of stress and displacement in large volcanoes. The first is a subhorizontal detachment between volcano and underlying lithosphere. Seismic, geodetic, and geologic evidence point to the importance of such a detachment in controlling structure, growth, and tectonics of the south flank of the island of Hawaii [*Furumoto and Kovach*, 1979; *Nakamura*, 1980; *Dieterich*, 1988; *Thurber and Gripp*, 1988; *Li et al.*, 1992, for example]. Such a structure can be accommodated in the finite element model, while volcanoes which lack such a feature can be modeled with a base that is solidly attached (welded) to the underlying lithosphere. The thickness of the elastic lithosphere is varied to gauge its effect on the magnitude of edifice stresses. The structure of the magmatic system also plays a major role in the development of large volcanoes. To assess this role, we superpose stresses expected from expansion of a magma chamber with the loading stresses. We also consider the effect of stresses resulting from emplacement of volcanic material on the flanks of older shields. Volcanoes exhibit both circular and linear symmetries about their magmatic feeder systems. Thus, we calculate models of volcanoes in both axisymmetric and plane-strain geometries, to examine the role of structural symmetry in the evolution of the edifice stress field.

For each of several volcanic island chains, we develop a suite of models to investigate the conditions that affect volcano evolution. An edifice of appropriate dimensions is loaded on plates with a range of elastic thicknesses. Boundary conditions are varied to gauge their effect on the evolution. For each model, principal stress orientations and magnitudes are recorded after emplacment of each load increment. We use this information to infer patterns of faulting, seismicity, and magma propagation in and around a growing volcano. We then use the insight gained from the models to interpret specific features observed in each chain.

Hotspot Volcanic Chains

We have selected five of the most prominent and well-studied examples of hotspot volcanism for detailed examination: the Hawaiian, Galápagos, Marquesas, and Canary chains, and the island of Réunion. Volcanoes in each of these chains have been the subjects of detailed geological, geophysical, and geochemical studies. Conditions that may affect volcano growth and evolution (such as crustal and lithospheric properties) vary widely among these chains. Some of these properties are listed in Table 3.1. Table 3.2 lists characteristic properties of the volcanoes in these chains. There are many other chains which deserve future consideration; we believe, however, that the listed chains span a range of emplacement conditions sufficiently wide to demonstrate the effects these conditions have on volcano development.

Hawaiian Islands

The Hawaiian-Emperor chain of seamounts extends nearly 6000 km across the Pacific plate from the site of current volcanism (the island of Hawaii) to the Aleutian trench, where seamounts of age 80 Ma are being subducted [*Clague and Dalrymple*, 1987]. The eight principal Hawaiian islands are the most recent manifestations of volcanism in this chain. *Clague and Dalrymple* [1987] estimated the age of the crust and lithosphere supporting the volcanoes to be 80-90 Ma, based on observations of magnetic anomalies in the Pacific

Chain Name	Lithospheric age [a] (Myr)	T_e (km)	Swell basal depth [b] (km)	Swell height (km)	Spreading rate [c] (mm/yr)	Plate velocity [d] (mm/yr)
Canary	130 [1]	35 [1] 20 [2]	4.5 [2]	1.5 ±0.1 [3] 0 [2]	20 [4]	5-20 [5]
Galápagos	< 10 [6]	12 [7]	2.0 [8]	0.6 ±0.1 [3]	56 [9]	55 [9]
Hawaiian	80-90 [10] 110 [14]	25-35[e] [11] 33-44[f] [11] 30 ±7 [15]	6.5 [12]	1.2 ±0.2 [3]	140–200 [4]	95 ±4 [13]
Marquesas	50 [16]	18 [17]	6.0 [18]	0.95 ±0.1 [3]	90 [4]	104 ±18 [13]
Réunion	55 [19]	28 ±4 [19]	4.5 [19]	1.1 ±0.2 [3]	180 [20]	23-29 [19]

[a] at time of initiation of edifice growth.
[b] below sea level.
[c] full spreading rate at time of crustal basement formation.
[d] relative to hotspot.
[e] two-dimensional model.
[f] three-dimensional spatially variable model (T_m).

[1] *Dañobeitia et al.* [1994], [2] *Watts* [1994], [3] *Monnereau and Cazenave* [1990], [4] *Larson and Pitman III* [1972], [5] *Hoernle and Schminke* [1993], [6] *Hey* [1977], [7] *Feighner and Richards* [1994], [8] *Nordlie* [1973], [9] *Hey et al.* [1977], [10] *Clague and Dalrymple* [1987], [11] *Wessel* [1993], [12] *McNutt and Shure* [1986], [13] *Duncan and Clague* [1985], [14] *Waggoner* [1993], [15] *Watts and ten Brink* [1989], [16] *Kruse* [1988], [17] *Filmer et al.* [1993], [18] *Fischer et al.* [1986], [19] *Bonneville et al.* [1988], [20] *Schlich* [1982].

Table 3.1: Geophysical data for volcanic chains.

crust. Argon dating of basalt samples returned from Ocean Drilling Program (ODP) site 843 [*Waggoner*, 1993], however, indicate that the crustal age may be closer to 110 Ma. Pacific plate crust of ages 85–110 Ma was formed at the Pacific-Farallon spreading ridge during a burst of exceptionally rapid spreading (full rates of 140 to 200 mm/yr [*Larson and Pitman III*, 1972]). The largest and youngest island in the chain, Hawaii (Figure 1), consists of five amalgamated shield volcanoes, two of which (Mauna Loa and Kilauea) are currently active. A sixth volcano, Loihi seamount, is growing on the sumberged flank of Mauna Loa/Kilauea.

Four eruptive stages have been identified in Hawaiian volcanoes [e.g., *Clague and Dal-*

Chain Name	Volcano diameter[a] (km)	Volcano height[b] (km)	Volcano basal depth (km)	Caldera diameter (km)	Spacing (km)
Canary	100 [1]	2.4 [2]	3.0-4.5 [1]	- [c]	> 100[d] [3]
Galápagos	50-60 [4]	1.4 [4]	2.1 [4]	6 [4]	30 [5]
Hawaiian	75-210 [6]	4.2 [7]	4.5-5.0 [8]	4 [9]	72 (48)[e] [5]
Marquesas	80-120 [10]	0.4-1.2 [10]	3.0-3.5 [10]	8 [11]	54 ±10 [12]
Réunion	220 [13]	3.1 [13]	4.0 [13]	8 [14]	30 [14]

[a] including submerged part of edifice.
[b] above sea level.
[c] Canary "calderas" not considered to be magma-chamber related.
[d] estimated from map.
[e] youngest part of chain (age < 5Ma).

[1] *Watts* [1994], [2] *Ancochea et al.* [1994], [3] *Coello et al.* [1992], [4] *Nordlie* [1973], [5] *Vogt* [1974b], [6] *Moore* [1987], [7] *Peterson and Moore* [1987], [8] *Fornari and Campbell* [1987], [9] *Earthwatch Press* [1992], [10] *Brousse et al.* [1978], [11] *Filmer et al.* [1994], [12] *ten Brink* [1991], [13] *Lénat et al.* [1989b], [14] *Duffield et al.* [1982].

Table 3.2: Characteristic properties of volcanoes in given chain.

rymple, 1987]. The initial pre-shield stage is characterized by eruptions of small volumes of alkalic basalt. The shield stage consists of mostly tholeiitic basalts; these subaqueous and subaereal flows contruct more than 95% of the edifice volume in a period of perhaps 1 Ma or less. The alkalic post-shield stage covers the mature shield with a thin layer of alkalic basalt. After a hiatus of volcanic activity lasting perhaps a few million years, the alkalic rejuvenated phase of eruption produces small volumes of alkalic lava from isolated vents (this phase is also called the posterosional stage.)

The island of Hawaii is probably the most intensely studied volcanic construct in the solar system. Decades of geodetic, seismic, and geologic study have revealed the main processes and structural components that control the growth and evolution of Hawaiian volcanoes. Reviews of the physical workings of Hawaiian volcanoes are provided by *Decker* [1987]

and *Tilling and Dvorak* [1993]. Magma ascends from a zone of partial melting, inferred from geochemical studies to lie at greater than 80 km depth [*Wyllie*, 1988; *Sen and Jones*, 1990]. Seismicity in the 60–40 km depth range defines a broad belt, about 80 km long, that is a region of magma accumulation [e.g., *Ryan*, 1988]. This belt grades upwards (from the base of the lithosphere at $\approx$ 40 km) into an approximately cylindrical conduit. Magma ascends through the lithosphere in discrete planar dikes, rather than in broad blobs or continuous pipes of fluid melt [*Shaw*, 1980; *Ryan*, 1988]. The conduit enters the base of the volcano and supplies material to a subcaldera magma reservoir. At Kilauea, this reservoir is an approximately cylindrical region extending about 3-7 km below the caldera surface [e.g., *Eaton and Murata*, 1960]. Analysis and modeling of surface tilt and displacement data around the caldera [*Ryan et al.*, 1983] indicate that the reservoir is a complex network of interconnected sills and dikes, rather than a simple fluid-filled cavity. Accumulation of magma pressurizes the reservoir. This pressure eventually causes rupture of the top or sides of the reservoir, resulting in a summit eruption or rift zone dike intrusion, respectively. Rift zone dikes are centered on a level of neutral buoyancy (about 3 km deep [*Ryan*, 1987]), where the density of tholeiitic melt is about equal to the density of the surrounding rock. These dikes typically occupy the 2-4 km depth range. However, if the propagation path downrift is obstructed, magma may be forced upwards (and downwards) around the blocked area. This magma may reach the surface to supply a rift zone eruption [*Ryan*, 1994]. The surface expression of a Hawaiian rift zone is a narrow topographic ridge that is a source for flows covering the lower flanks. Several pit craters, cinder cones, and small lava shields are located along the rift zones of Kilauea.

The interaction of rift zone dike emplacement with edifice deformation and flank movement along a basal decollement is understood to be a major mechanism controlling the structure and evolution of large Hawaiian volcanoes. The intrusion of a rift zone dike compresses the seaward flank of the volcano [e.g., *Swanson et al.*, 1976; *Dieterich*, 1988; *Dvorak*, 1994]. This compression is relieved in large earthquakes such as the 1975 surface-wave mag-

nitude M_S = 7.2 Kalapana event [*Ando*, 1979; *Furumoto and Kovach*, 1979] and the 1989 M_S = 6.1 event [*Arnadottir and Segall*, 1991; *Bryan*, 1992] beneath the south flank of Kilauea. The hypocenters of these earthquakes are located near the interface between the edifice and the oceanic crust. The focal mechanism for the Kalapana event determined from teleseismic records, augmented by crustal deformation and tsunami data, has been variously inferred to indicate a thrust fault plane dipping 4° to the northwest [*Furumoto and Kovach*, 1979], or a low angle normal fault dipping 20° to the SSE [*Ando*, 1979]. The hypocenters of aftershocks to this event define a plane gently dipping to the west at depths corresponding to the inferred volcano-crust interface [*Ando*, 1979; *Crosson and Endo*, 1982; *Thurber and Gripp*, 1988]. *Ando* [1979] and *Nakamura* [1980] suggested that the Kalapana earthquake was rooted in a weak interface between the volcano and oceanic crust consisting of pelagic sediments. *Crosson and Endo* [1982] suggested that volcanic debris and breccia could also contribute to the weakness of a basal decoupling layer. *Nakamura* [1980] suggested that such a weak layer could provide a basal decollement, allowing flank movement which accommodates further rift zone intrusion. *Nakamura* [1980] also generalized this idea to other hotspot volcanoes, suggesting that volcanoes formed in areas lacking sediment cover would not be able to accommodate continued dike intrusion and would therefore lack rift zones. Models of volcanic structure by *Dieterich* [1988] demonstrated the necessity of basal faulting to allow intrusion, and to generate a dike-trapping state of stress, allowing formation of rift zones.

Seismic and geodetic data acquired since 1975 have helped to define the geometry of the decoupling layer. *Got et al.* [1994] applied a multiplet relocation technique to more than 250 small events ($1.0 < m_l < 2.5$) in a small section of the flank of Kilauea. The relocated events define a well-resolved plane dipping about 6° to the north. This value is probably too steep to represent the top of the flexed crust, which dips at about 1-2° beneath Kilauea's south flank [*Zucca and Hill*, 1980; *Thurber and Gripp*, 1988]. *Got et al.* [1994] attribute the plane's steepness to a local irregularity in the basal slip layer. Analysis of reflected phases in seismograms of small earthquakes in the Kaoiki zone within the southeast flank of Mauna

Loa [*Thurber et al.*, 1989] reveals a low velocity layer of 800 m thickness at about 11.5 km depth. Those workers attribute this layer to the marine sediments that provide the basal detachment. Geodetic data collected on Kilauea's south flank provide important constraints on the mechanics of flank deformation. The existence of a shallowly dipping planar dislocation surface (usually in conjunction with a vertical dislocation surface representing rift zone dilation) is required to model the geodetic data adequately [e.g., *Delaney et al.*, 1990; *Dvorak et al.*, 1994].

While intrusion of dikes into rift zones (from the surface to about 4 km depth) is a well-appreciated feature of Hawaiian edifice growth, recent work has examined the role that deeper rift structures play in volcano evolution. *Ryan* [1988] suggested that an aseismic region directly beneath the shallow rift zones (4-10 km depth range) he termed the "deep rift zone" was a collection site of dense picritic magma delivered directly from the mantle source, with suspended olivine crystals that precipitated from cooling magma in the shallow reservoir. Other workers attribute this aseismic region to collections of dense olivine cumulates that separated out at the base of the shallow magma reservoir [*Clague and Denlinger*, 1994]. Analysis of geodetic data collected after the Kalapana earthquake by *Delaney et al.* [1990] finds steady seaward movement of Kilauea's south flank and extension and subsidence of the summit and surficial rift zones. These workers maintain that magma chamber inflation and (shallow) rift zone intrusion alone are not sufficient to explain the the observed pattern of deformation; they suggest that the continuous and widespread nature of the deformation is instead consistent with expansion of a deep dike-like magma body in concert with slip along a low-angle basal thrust. A study of Kilauea south flank displacements from 1990–1993 by *Owen et al.* [1995] reaches a similar conclusion. On the other hand, *Dvorak et al.* [1994] argue that if the restrictive assumption of plane strain is relaxed, shallow rift widening with basal slip is sufficient to explain the geodetic observations. *Clague and Denlinger* [1994] summarize the geochemical evidence suggesting the formation of a dense olivine cumulate core beneath the rift zones. The proposed core is mostly solid (with $<$ 5-10 volume % intercumulus liquid)

but ductile (at a temperature of about 1100° C), with a rheology similar to that of ice [*Clague and Denlinger*, 1994]. Thus, the core will flow under its own weight, pushing the flank of the volcano ahead of it. Such a structure can greatly affect the stress state in the edifice, relaxing shear stresses in the region directly above [*Borgia*, 1994].

Boreholes drilled into the oceanic crust west of the Hawaiian islands (ODP sites 842 and 843 [*Dziewonski et al.*, 1992]) constrain the thickness of pelagic sediments in this region. This location, beyond the crest of the Hawaiian flexural arch, is far enough from the islands to avoid material deposited by erosion and mass wasting of the volcanoes [c.f. *Moore et al.*, 1989], although small amounts of volcanic ash from Hawaiian island eruptions is present [*Shipboard Scientific Party*, 1992a,b]. Presumably, cores at this site will give an unbiased sample of the pre-eruption sediment thickness and composition that the Hawaiian volcanoes were emplaced upon. Site 842 is located on the shoulder of a northwest-southeast-trending abyssal hill. Site 843 is 1 km northwest of site 842, at the top of the same abyssal hill. At site 842 two layers of clay were found, extending to 35.7 m below the sea floor [*Shipboard Scientific Party*, 1992a]. Beneath the clays was a layer of chert interspersed with claystone and nanofossil ooze [*Shipboard Scientific Party*, 1992a], reaching to 237.7 m below sea floor. At site 843, a layer of dark clay extended from the sea floor to 121.8 m below and was underlain by a breccia of reddish brown and red chert to a depth of 228.0 m. A layer of nanofossil limestone (with chert nodules) and a thin layer of calcareous clay lie on top of the basalt basement. The basalt was encountered at depths of 228.8 to 242.5 m below the sea floor. Note that these sites were deliberately located above elevated basement topography, in order to insure reaching basalt basement (so that a seismometer could be installed [*Dziewonski et al.*, 1992]). Sites with lower basement topography (valleys) are likely to have significantly greater depths of sediment filling them. Single channel seismic data [*Collins et al.*, 1992] suggest that sediments in the basins near the above sites are about 100 m thicker than those above the basement peaks. Thus the above measurements are lower bounds on the average thickness of the sediment layer.

A study of seismic discontinuities beneath the southeast flank of Mauna Loa [*Li et al.*, 1992] found a low-velocity layer, 1 km thick and attributed to sediments, between the volcanic pile and the underlying crust. This layer may represent the average thickness of pelagic sediments on the crust when volcano formation commenced. Alternatively (and more likely), contributions of material from the erosion and mass wasting of older shields as well as fragmented, subaqueously erupted material augments the pelagic sediments underlying a growing shield. A young volcano in the Hawaiian chain must emerge from inside the flexural depression (moat) which surrounds the islands in a 'U' shape (Figure 1). This moat is filled with sediments and slump and slide material derived from the volcanoes [*Moore et al.*, 1989; *Rees et al.*, 1993]. Thus, the young edifice will emerge on a combination of pelagic sediment and volcano-derived fragmental and disrupted material, all of which may contribute to a basal weak layer.

Galápagos Islands

The Galápagos archipelago is located just south of the Galápagos spreading center in the far eastern Pacific. The Galápagos islands rest atop a shallow volcanic platform about 1000 meters below sea level; this platform is the westernmost extension of the east-west striking Carnegie Ridge. The Galápagos hotspot contributed material to the Carnegie Ridge while it was directly beneath the spreading center; at the same time it supplied material to the Cocos Ridge to the north [*Hey et al.*, 1977]. The Galápagos spreading center has since migrated to the north of the hotspot (in the last 5-6 Ma [*Hey*, 1977]). The central part of the platform, which includes Isla Santiago, Isla Santa Cruz, Isla San Cristobal, and other smaller islands, rests on extremely young lithosphere, with elastic thickness < 6 km [*Feighner and Richards*, 1994]. West of a sharp discontinuity probably related to a lithospheric weak zone and a transform in the Galápagos spreading center, the lithosphere is older ($\approx$ 10 Ma) and stronger, with elastic thickness ≈ 12 km [*Feighner and Richards*, 1994]. Six shield volcanoes constitute the two westernmost islands of the chain (Figure 2). Volcán Fernandina

is an island unto itself (Isla Fernandina); Volcanes Ecuador, Wolf, Darwin, Alcedo, Sierra Negra and Cerro Azul are connected in a 'J' shape to form Isla Isabella (Figure 2). All the western Galápagos volcanoes except probably Volcán Ecuador have experienced eruptions in historic time [*McBirney and Williams*, 1969]. The Galápagos hotspot is currently believed to reside beneath these islands [*Hey*, 1977].

The western Galápagos volcanoes share distinctive structural and morphological features. Typical subaerial topographic profiles consist of a lower segment, starting at sea level and characterized by low slopes (the subaereal lower segment), and a steeper-sloped upper segment (the subaereal upper segment), which surrounds a flat-topped summit region, including a caldera (terms from *Nordlie* [1973]). This "overturned soup plate" topographic profile is characteristic of the Galápagos volcanoes [*McBirney and Williams*, 1969]. At the summit region, circumferential fissures surrounding the calderas are typical; radial fissures are characteristic of middle and lower flanks [*McBirney and Williams*, 1969; *Nordlie*, 1973; *Chadwick and Howard*, 1991]. Both types of fissures are sources for volcanic flows. The radial fissures are commonly aligned in zones that connect the calderas of adjacent volcanoes [*McBirney and Williams*, 1969; *Nordlie*, 1973; *Chadwick and Howard*, 1991]. There is no evidence for a basal detachment or mobile flank activity on the western Galápagos volcanoes, with the possible exceptions of a small block slide on the flank of Cerro Azul [*Naumann and Geist*, 1993], and a rift zone exhibiting Hawaiian characteristics extending to the east of Volcán Ecuador [*Rowland et al.*, 1994]. *Nakamura* [1980] proposed that the absence of sediments on the surface of the young crust at the Galápagos Islands would prevent these volcanoes from accommodating rift zone intrusions and thus inhibit the formation of such structures. *McBirney and Williams* [1969] suggested that sill complexes emplaced beneath the summit regions of Galápagos volcanoes caused domal uplifts, producing the summit platform and steep upper segment. *Cullen et al.* [1987] calculated surface displacements from pressurization of a sill-like magma chamber in a half-space, finding topographic profiles similar to those of the western Galápagos volcanoes. Other workers [*Simkin*, 1972, 1984;

Chadwick and Howard, 1991; *Geist et al.*, 1994] have proposed a constructional origin of the steep upper slopes and flat top. For example, *Chadwick and Howard* [1991] suggest construction of the steepest slopes by accumulation of short flows emanating from the circumferential fissures; the more gradual slopes of the lower flanks are built, in their view, by longer flows fed by radial vents. *Rowland et al.* [1994] propose erosion of originally low-angle slopes, with subsequent mantling by younger flows, as a mechanism to explain the steep subaereal sections.

Core samples returned from several boreholes drilled near the Galápagos spreading center enable us to infer the thickness and composition of the sediment layer upon which the Galápagos Islands were emplaced. This area is included in a broad near-equatorial belt of high productivity in the Pacific. The biogenic sediment production rate is very high (37-59 mm/yr at ODP site 677 [*Alexandrovich*, 1989]), such that even relatively young ($\approx$ 10 Ma) crust may have accumulated hundreds of meters of sediment. At ODP site 424 (0° 36' N 86° 08' W), just south of the Galápagos spreading center, oceanic crust of age 0.6-0.62 Ma is covered with about 30 m of sediment, most of which is siliceous foraminifer nannofossil ooze [*Hoffert et al.*, 1980]. At ODP site 677 (1° 12' N 83° 44' W), oceanic crust of age about 5.9 Ma [*Shipboard Scientific Party*, 1988] is covered by 200-300 m of sediment. Three major sedimentary units have been identified: Unit I consists of alternating clayey biogenic calcareous siliceous oozes and clayey biogenic siliceous calcareous oozes, Unit II consists of siliceous nannofossil ooze and siliceous nannofossil chalk, and Unit III consists of cherty limestone and nannofossil chalk [*Shipboard Scientific Party*, 1988].

Marquesas Islands

The Marquesas Islands are a 400 km long linear chain in the equatorial Pacific, in a region known as French Polynesia (Figure 3). They rest on $\approx$ 50 Ma lithosphere. These volcanoes range in age from about 6 Ma at Eiao to about 1 Ma at Fatu Hiva [*Desonie et al.*, 1993]. The chain terminates abruptly north of the Marquesas Fracture Zone Ridge, a linear volcanic

construct 20 km wide and 2 km high [*McNutt et al.*, 1989]. This hotspot is believed to reside currently beneath the fracture zone [*McNutt et al.*, 1989]. Seismic and gravity modeling indicates that the crust beneath the volcanoes is underplated by low density plume material emplaced at the Moho [*Wolfe et al.*, 1994].

The subaerial portions of Marquesan volcanoes consist of alkalic flows attributed to a late 'capping' stage of development [*Natland and McNutt*, 1987; *Filmer*, 1991]; these flows cover the tholeiitic flows of the main shield-building stage. Several islands exhibit evidence of large-volume sector collapse and mass wasting events [*Filmer*, 1991]. The islands are surrounded by an archipelagic apron [e.g., *Menard*, 1956] of sediments and debris from mass wasting of the edifices [*Filmer et al.*, 1993; *Wolfe et al.*, 1994]. This material overfills the moat caused by flexure of the lithosphere in response to the load of the edifices. The moat therefore has no bathymetric expression, but can be detected in gravity studies [*Filmer*, 1991; *Filmer et al.*, 1993; *Wolfe et al.*, 1994]. *Filmer et al.* [1994] estimated that about 400 sector collapse events of the size inferred to have occurred at Fatu Hiva would be required to form the Marquesas apron.

Surface sediments in the eastern Pacific south of the equator are principally calcareous oozes [*Davies*, 1985]. Samples returned from 2 DSDP drilling sites (74 and 75) near the Marquesas Islands help us to infer the compositions and thicknesses of the sediment layers that the Marquesas volcanoes were emplaced upon. At site 74 [*Shipboard Scientific Party*, 1971a], a layer of high-silica radiolarian ooze (0 to 23.5 m below sea floor) lies atop calcareous nannofossil ooze (23.5 to 100 m), a thin (2-m-thick) layer of calcareous nannofossil ooze containing clay, and basalt basement at 102 m. Site 75 is similar [*Shipboard Scientific Party*, 1971b], with a thin layer of red clay and foraminifera (0–1.3 m below sea floor) covering a layer of calcareous nannofossil ooze with minor amounts of red clay (2-82 m) and basalt basement at 82 m.

Canary Islands

The Canary archipelago consists of seven islands located near the coast of northwest Africa (Figure 4). Four of these islands, Tenerife, La Palma, Lanzarote, and El Hierro, are considered currently active (having erupted in the last 500 years [*Carracedo*, 1994]). The structure of these volcanoes is dominated by steep ridges that are the topographic manifestation of zones of linear dike intrusion (rift zones). These structures form islands in two configurations [*Carracedo*, 1994]: single rift (Lanzarote, La Palma, for example) or triple rift (stellate or 'mercedes'-shaped; Tenerife and El Hierro, for example). The rift zones are the principal source of the flows which constitute the islands; shallow magma chambers (and accompanying downdropped calderas) are absent [*Carracedo*, 1994]. Several horseshoe-shaped caldera-like depressions on these volcanoes are attributed to shallow, lateral collapse events [*Ancochea et al.*, 1994; *Carracedo*, 1994]. Other, broader depressions are also attributed to shallow landsliding [*Carracedo*, 1994].

Sediment production in the Atlantic Ocean is dominated by organisms that produce calcium carbonate. Thus, surface sediments in most of the Atlantic are calcareous. Deep sediment samples have been obtained from Deep Sea Drilling Program (DSDP) hole 369, on the edge of the African continental slope just south of the Canary Islands [*Shipboard Scientific Party*, 1977c]. The sediments fell into 3 principal lithologic groups; a layer of nannofossil marls and siliceous nannofossil marls to depth 346 meters below sea floor, a layer of agrillaceous nannofossil limestone, agrillaceous marls, and chalks from 346 to 422 m, and a layer of silty nannofossil marls to 489 m [*Shipboard Scientific Party*, 1977c]. Due to its location on the continental slope, the sedimentary history at this site is affected by processes that may not be typical of the deep ocean environment, such as strong erosion and an influence by continental tectonics and sediment sources. DSDP holes at deeper sites near the Cape Verde Islands (sites 367 and 368 [*Shipboard Scientific Party*, 1977a,b]) found 1144 and 985 m of sedimentary deposits, respectively. The composition of these sediments varied greatly, from nanno ooze and marls to pelagic clays, claystones and shales [*Shipboard*

Scientific Party, 1977a,b].

Réunion

Réunion Island is located in the Indian Ocean east of Madagascar. It is believed to be the youngest manifestation of volcanism from the hotspot that first produced the flood basalts of the Deccan Traps in the Cretaceous [*Morgan*, 1981; *Bonneville et al.*, 1988; *Duncan et al.*, 1989]. As the Indian Plate moved northward, the Chagos-Laccadive Ridge and the Southern Mascarene Plateau were produced; these two features were separated when spreading initiated along the Central Indian Ridge. The hotspot subsequently formed the islands of Mauritius and Réunion. The construction of Réunion began at 5 Ma, coinciding with the termination of activity on Mauritius [*Gillot et al.*, 1994]. The pattern of magnetic anomalies in the Mascarene Basin indicates the presence of an extinct ridge which ceased spreading at about 60 Ma [*Schlich*, 1982]. Réunion is located directly atop the predicted location of the crest of a segment of this ridge [*Schlich*, 1982].

Réunion Island consists of two main volcanic complexes (Figure 5): Piton des Neiges, an extinct volcano that comprises the northwest sector of the Island, and to the southeast, the currently active Piton de la Fournaise. The latter volcano is characterized by a series of nested U-shaped structures that open to the southeast (toward the ocean). *Duffield et al.* [1982] interpret these structures as faults that mark the locations of earlier rift zones and form the headwalls of rift-bounded slump blocks. The nesting would therefore indicate migration of the magma source to the southeast [*Duffield et al.*, 1982]. On the basis of stratigraphic relations and K-Ar dating, *Gillot and Nativel* [1989] and *Gillot et al.* [1994] suggest that the nested structures are calderas reflecting successive stages of magmatic activity from a central source near the current summit vent area. These calderas have experienced massive collapse/slump events directed toward their open (southeast) sides. The most current such caldera on Piton de la Fournaise, the Enclos Fouqué, contains the active vent region, including a central cone with two craters. This enclosed summit region is cut by north-south

oriented fractures; toward the edges of the caldera, these fractures trend into northeast- and southeast-oriented zones of intrusion (rift zones). These two rift zones extend down the flanks, widening downslope (to about 10 km width), ending about 5 km offshore [*Lénat et al.*, 1989b]. A third rift zone forms a ridge striking northwest, toward the summit of neighboring Piton des Neiges [*Duffield et al.*, 1982]. All three rift zones are sources of erupted material.

The distribution of surface sediments in the vicinity of Réunion Island is complex; zones of brown clay, calcareous clays and calcareous ooze form a complex pattern in this area [*Kolla and Kidd*, 1982]. Samples of deeper sediments were obtained at DSDP site 239 [*Shipboard Scientific Party*, 1972], about 400 km from Réunion and roughly halfway between Réunion and Madagascar. The sediment column at this site is 320 m deep and consists of two principal lithologic units [*Shipboard Scientific Party*, 1972]. Unit I is silty clay and clay-rich nanno ooze, extending from 0 to 158 m below sea floor. Unit II is brown clay and brown silty clay, 158 to 320 m below sea floor.

Factors Controlling the Evolution of Volcanic Islands

The observations and studies of large volcanoes discussed in the previous section offer clues to the conditions that determine the evolutionary paths of large volcanoes. We next compare and contrast observations at each of the chains cited above, seeking to identify the primary influences on and modes of volcano development. Our ultimate aim is to examine the effects of these evolution-controlling factors through numerical modeling.

Nature of the basal boundary condition

As noted above, the existence of a basal detachment beneath the islands of the Hawaiian chain is well established. Such a structure plays a vital role in the cycle of rift zone intrusion and flank movement that drives the growth of Hawaiian volcanoes [e.g., *Dieterich*, 1988]. Evidence for analogous structures in the volcanoes of the Galápagos chain is lacking, perhaps

because a lack of sediments on the young crust and lithosphere that supports these volcanoes prevents the formation of a basal decollement [*Nakamura*, 1980]. Expanding on this idea, we propose that a detailed study of the conditions affecting the volcano-crust interface can help to illuminate the processes that control the growth of large volcanoes. Additionally, such a study may allow us to infer the modes of growth of less-well-studied volcanoes, by using available information on crustal surface conditions.

We now consider the factors that control the structure of the basal interface between ocean crust and volcano. As *Nakamura* [1980] suggested, pelagic sediments may play an important role in the development of large oceanic volcanoes. The nature of sedimentation in a given location depends on several factors. Biogenic sedimentation results from the activity of microscopic organisms at shallow levels. When the organsims die, their shells settle to the ocean bottom, forming sediment layers. The sediments fall into two dominant categories: calcium carbonate and silica. Below a characteristic depth, called the carbonate compensation depth (CCD), calcium carbonate will dissolve before it reaches the seafloor. The CCD in a given area is dependent on ocean chemistry and biogenic production rate. For example, the CCD is depressed in a narrow equatorial band in the eastern Pacific, due to the high productivity of foraminifera and calcareous nannoplankton [*McCoy and Sancetta*, 1985]. The CCD also varies between oceans, being characteristically deeper in the Atlantic than the Pacific, for example. Thus, the Atlantic seafloor is characterized by carbonate sediments, while the Pacific seafloor is dominated by other materials (mostly abyssal clays and siliceous biogenic sediments). Factors that regulate growth of sediment-producing organisms include latitude, prevailing winds and ocean currents. Non-biogenic sediments are produced by erosion or mass wasting of continental and oceanic island material. These sediments are typically concentrated near their source, but the finer-grained constituents may be distributed by ocean currents to regions far from the source.

Sediments are expected to behave as a mechanically weak layer between the mechanically strong oceanic crust and the volcanic edifice. Such a layer could form a decollement, allowing

the growing edifice to thrust over the flexed crust/lithosphere. Pressurization of pore fluids in decollement layers reduces the effective normal stress across a potential fault surface, facilitating the thrusting of large intact blocks [e.g., *Hubbert and Rubey*, 1959]. One way to generate high pore fluid pressure is sediment compaction. Pore pressures generated in this way depend on the hydraulic permeability of the material; low values of permeability allow the generation of high pore pressures [*Bredehoeft and Hanshaw*, 1968]. Argillaceous rocks (rocks formed from clays) exhibit characteristically lower permeabilities than either crystalline rocks or limestones [*Brace*, 1980].

The permeability of a material depends on the mean size, size distribution and geometries of the particles constituting the material. Permeability increases with increasing grain size [e.g., *Krumbein and Sloss*, 1963]. For a given mean grain size, a wide distribution of grain sizes (poorly sorted material) will result in lower permeability than a narrow distribution (well sorted material) [*Krumbein and Sloss*, 1963]. In the former case, smaller particles will tend to fill the gaps between large particles, thus reducing the permeability. Permeability is also affected by the complexity of the connections between pores. The tortuosity τ is a measure of this complexity: it is defined as the ratio of the actual path length traversed by the fluid to the apparent path length [e.g., *Walsh and Brace*, 1984]. Permeability is inversely proportional to τ^2 [*Walsh and Brace*, 1984].

Sediments labelled "clays" are generally held to consist of particles < 2 μm in diameter [e.g., *Beiersdorf and Natland*, 1983]. Sediments labeled "oozes" consist of at least 30 % skeletal remains of pelagic organisms, with the remainder being clay minerals [e.g., *Kennett*, 1982]. Oozes may contain a significant fraction of intact and partially broken fossils of large size such as foraminifera and radiolaria (typically ranging from 50 to 400 μm in diameter [*Kennett*, 1982]) and calcareous nannofossils (ranging from 2 to 25 μm in diameter [*Kennett*, 1982]).

Anisotropic behavior of clays may play a critical role in the formation of a basal decollement. Clay particles are platelike or flakelike in shape. The arrangement of the plates

(fabric) influences the flow paths of pore fluid. Applied stresses can alter the orientations of scaly clay particles, as demonstrated experimentally by *Arch and Maltman* [1990], and as observed in core samples from basal decollements in accretionary wedges [*Moore et al.*, 1986; *Behrmann et al.*, 1988]. In both cases, strain is accommodated in narrow "shear zones" characterized by reduced porosity and clay fabric orientations sub-parallel to the zones. Permeability perpendicular to the shear zones is decreased, due to the increased tortuosity of flow paths through the zone-parallel clay fabric. Permeablility parallel to the shear zone, however, is enhanced; flow paths along the shear zone clay fabric have much lower tortuosity [*Arch and Maltman*, 1990]. This effect may cause such shear zones to become preferred paths for fluid flow [*Moore et al.*, 1986].

Numerical models of flank structure have helped to illuminate the conditions required for flank failure. *Thurber and Gripp* [1988] applied the critical taper wedge model of *Davis et al.* [1983] to Kilauea's flank, in order to determine the decollement conditions necessary for flank failure. They found that pore pressure about 50% of lithostatic pressure was required to obtain a critical wedge (i.e., a wedge on the verge of failure everywhere). *Iverson* [1995] considered the effects of external forces on the stability of a rigid wedge flank model. He found that forces from magma injection into rift zones (at the head of the wedge) were incapable of driving failure of more than a small portion of the wedge. Groundwater-related forces can reduce normal stresses across slip surfaces, thus facilitating failure. *Iverson* [1995] demonstrated that a plausible scenario for deep extensive wedge failure required a thick layer of low hydraulic diffusivity (low permeability). He suggested that a $\approx$ 200 m layer of pelagic clays could accommodate failure of the wedge.

In summary, clays have low permeabilities due to small grain sizes and high tortuosity of fluid paths through platy clay particles. Abyssal clays, when compressed, will form rocks (claystones and shales) with lower permeabilities than rocks formed from calcareous (chalks and limestones) and siliceous (cherts) material [*Brace*, 1980]. Higher pore pressures can thus be generated in the clay-derived rocks. Clays and clay-derived rocks are therefore the

volcano-base materials most likely to enable formation of a decollement. This conclusion is supported by the ubiquitous presence of clays and shales in decollements in accretionary wedges [e.g., *Moore et al.*, 1986] and large thrust sheets [e.g., *Hubbert and Rubey*, 1959].

The roughness of the basement topography also influences the character of the basal boundary condition of a volcano. High-amplitude topography at the base of the volcano will promote a welded basal boundary condition, because basement topographic highs will tend to protrude into the edifice as the volcano grows over them, helping to "lock" the edifice in place. These highs will also tend to interrupt the continuity of the sediment layers resting on their flanks, inhibiting the formation of broad basal decollements that facilitate movement of large portions of an edifice. Decollements that do form in such an environment will likely be small in extent and isolated. The processes that determine the topographic roughness of the oceanic crust therefore play a role in determining the evolutionary path of large oceanic hotspot volcanoes. Long linear topographic peaks oriented parallel to the spreading axis, called abyssal hills, are the characteristic topographic variations observed near spreading ridges. Abyssal hills form at the ridge axis through a complex interaction of tectonic and volcanic processes (see *Goff* [1991] and references therein). Analysis of abyssal hill topography indicates that topographic r.m.s. roughness increases with decreasing spreading rate [*Malinverno*, 1991; *Goff*, 1991; *Bird and Pockalny*, 1994; *Macario et al.*, 1994]. The characteristic width of abyssal hills behaves in a similar fashion [*Goff*, 1991; *Macario et al.*, 1994]. The form of the relation between r.m.s. roughness and spreading rate has been described as an inverse square root dependence [*Malinverno*, 1991] and as a strong negative correlation in a slow spreading regime, an intermediate spreading rate transition with a more gradual decrease in roughness with increasing spreading rate, and a slight positive correlation at the highest observed rates [*Goff*, 1991; *Bird and Pockalny*, 1994]. Sediment cover on older crust may obscure basement topography and alter the correlations observed above; *Bird and Pockalny* [1994], however, used single channel seismic data to determine depth to basement and found the roughness-spreading rate relation to be robust. Averaged

Ridge location	Average full spreading rate (mm/yr)	Characteristic height (m)	Characteristic wavelength (km)
MAR	35.4	197 ±13	7.1 ±1.0
PR + AI	57.6	78.5 ±6.0	4.2 ±0.5
PC	112	56.1 ±2.3	2.0 ±0.1
PN	171	79.4 ±12.2	5.4 ±0.7

MAR, Mid Atlantic Ridge; PR+AI, Pacific-Rivera and Africa-India, PC, Pacific-Cocos; PN, Pacific-Nazca,

Table 3.3: Abyssal hill parameters, from *Goff* [1991].

characteristic heights and strike-normal wavelengths for abyssal hills obtained by *Goff* [1991] are listed in Table 3.3, along with averaged spreading rates at the sites studied.

Magma chambers in large volcanoes

Accumulation and storage of magma in shallow reservoirs (at a horizon of neutral buoyancy for given magma density) is charateristic of basaltic volcanic systems such as hotspot volcanoes and mid-ocean ridges [e.g., *Ryan*, 1994]. In a volcano such as Mauna Loa or Kilauea, such a chamber is actually a network of connected dikes and sills that collects magma [e.g., *Ryan et al.*, 1983]. Magma chambers are commonly associated with an overlying caldera or caldera complex. Stresses resulting from pressurization and de-pressurization of the chamber drive caldera formation and tectonics of the upper flanks [*Chevallier and Verwoerd*, 1988; *Thomas et al.*, 1990; *Zuber and Mouginis-Mark*, 1992; *Chadwick and Dieterich*, 1995]. The currently active volcanoes Mauna Loa and Kilauea on Hawaii exhibit dynamic calderas. Despite the much smaller size of the shields, calderae on the western Galápagos volcanoes [*Chadwick and Howard*, 1991] are of comparable size to those of the Hawaiian volcanoes.

Lithospheric flexure

The lithosphere flexes in response to the load of a large volcanic edifice. The deformation of the plate induces stresses in the lithosphere that may influence the ascent of magma. *ten Brink and Brocher* [1987] proposed that such stresses may control the timing of the characteristic stages of Hawaiian volcanism [e.g., *Clague and Dalrymple*, 1987]. In this scenario horizontal compressive stresses shut off magma ascent paths in the lithosphere, terminating the primary stage of edifice growth and initiating the formation of a subcrustal plutonic complex by ponding of magma at the base of the crust [*ten Brink and Brocher*, 1987]. As plate motion carries an edifice away from the plume source, new edifices form further down the chain; flexure from these new loads releases the horizontal compression in the lithosphere beneath the older volcanoes, allowing magma ascent in the "posterosional" stage [*ten Brink and Brocher*, 1987].

Lithosperic flexure results in the formation of a topographic moat surrounding the volcanoes. These moats collect volcanic material derived from massive slope failure and mass wasting from the volcanoes [e.g., *Moore et al.*, 1989; *Rees et al.*, 1993; *Filmer et al.*, 1994; *Wolfe et al.*, 1994]. Such deposits make up a significant fraction of the total amount of material supplied by the hotspot.

Feighner and Richards [1994] found a sharp division between the western Galápagos Islands, supported by lithosphere about 12 km thick, and the central and eastern Galápagos Islands, supported by a very weak lithosphere (< 6 km thick) in a state close to Airy isostasy. They state that the smaller size of volcanoes on the central platform "is a consequence of weak lithosphere which is unable to support larger volcanic edifices." In the models described below, we seek to demonstrate a physical basis for such an assertion.

Models

Motivation

In order to understand the evolution of large volcanoes, we turn to simplified continuum models that incorporate simulations of the processes listed above. We model these processes using the finite element code TECTON [*Melosh and Raefsky*, 1980, 1983]. TECTON has already proven useful in studies of stress field evolution in large volcanoes [*McGovern and Solomon*, 1993; *Borgia*, 1994]. TECTON can model materials with a viscoelastic rheology. Lithospheric flexure can be modeled by placing a high (effectively infinite) viscosity elastic lithosphere over a low viscosity asthenosphere (as done by *McGovern and Solomon* [1993]). Basal detachments can be modeled with the "slippery node" formalism included in TECTON [*Melosh and Williams*, 1989]. Magma chamber pressurization is simulated by applying appropriate forces to the nodes of elements designated as belonging to a magma chamber.

With a suite of models, we can vary the conditions that are believed to influence volcano development. Variations in basal conditions are modeled by the presence or absence of "slippery nodes" at the base of the model edifice. The thicknesss of the elastic lithosphere is varied to gauge the effect of flexurally induced stresses in volcanoes on lithosphere of varying ages. We also test the effect of varying magma chamber configuration and overpressure on the model edifices. The time-dependent stress and displacement fields to be calculated for various models can be used to predict the type and orientation of tectonic features that would form on a large volcano subject to deformation from flexure of the underlying lithosphere. The calculated stress fields also allow us to predict the pathways by which magma ascends through the edifice to sites of intrusion or eruption. We can also superpose stress fields representing processes unrelated to plate flexure (such as pressurization of a magma chamber) to gauge the effect these stress fields have on tectonic features and magma propagation. In a later section, we compare these predictions to observed tectonic features and magma ascent and emplacement mechanisms on large volcanoes. We may then evaluate

Parameter	Crust	Mantle	Comments
Young's Modulus E [Pa]	1×10^{11}	3×10^{11}	
Density ρ [kg/m^3]	1800	2300	reduced density
Poisson's ratio ν	0.25	0.25	
	Lithosphere	Asthenosphere	
Viscosity η [Pa s]	1×10^{27}	1×10^{21}	

Table 3.4: Parameter values for volcano loading models.

the applicability of the models to specific volcanoes, and use the insight gained from the models to illuminate the processes that control the evolution of specific volcanoes. Such an approach was successfully used in a study of the tectonics of large volcanoes on Mars [*McGovern and Solomon*, 1993].

Methodology

Given a load emplaced on a viscoelastic substrate, TECTON [*Melosh and Raefsky*, 1980, 1983] first calculates elastic deformations and stresses and then determines the time-dependent viscous deformations and stresses. Time in the model scales as the Maxwell time τ_M in the asthenosphere, about 300 years for parameter values chosen (Table 3.4). We consider model edifices of a range of heights, radii, and elastic lithosphere thicknesses (parameters approximately appropriate to large oceanic intraplate volcanoes on young to intermediate age lithosphere). The asthenosphere layer was taken to extend to a sufficient depth so that a rigid lower boundary has no significant influence on the results. We adopt the convention that tension is positive: we adhere to the geological convention, however, of applying the label σ_1 to the most compressive (most negative) principal stress, and σ_3 to the least compressive (most positive) principal stress. The volcano elements are given a reduced density $\rho_{cr} = \rho_c - \rho_w = 1800$ kg/m^3, to account for the buoyant effect of the ocean. Mantle asthenosphere density is also reduced by the same amount so that the proper buoyant restoring force is provided at the bottom of the lithosphere. We take the crustal thickness T_c to equal

the thickness of the elastic lithosphere T_e for simplicity. Allowing for a mantle component of the elastic lithosphere changes slightly the stress distribution in the lithosphere, but does not change the stress state in the edifice significantly [*McGovern and Solomon*, 1993].

The effects of fault slip along a basal detachment on the stresses and deformation can be modeled using the slippery node method implemented in TECTON [*Melosh and Williams*, 1989]. We apply slippery nodes to all or some of the nodes originally on the line $z = 0$, i.e., along the interface between the volcano and the lithosphere. This modification allows the volcano to thrust outward over the flexed lithosphere.

We have implemented time-dependent material properties [*McGovern and Solomon*, 1993] in order to simulate incremental volcano growth. Each edifice has 10 layers of elements (Figure 6) that are applied in 4 or 5 sequential increments. After each increment is emplaced, the asthenosphere is allowed to relax until asthenospheric velocities are negligible. For these calculations a time interval of 1000 τ_M is sufficient to achieve this condition. The number of layers is constrained by the horizontal resolution of the finite element grid. Increasing the number of layers in a volcano of given size would allow more realistic (i.e., smaller) increment volumes, but would also greatly increase computational cost, through increasing the number of element nodes as well as the number of time steps.

The evolution of the stress field within the volcanic construct is depicted with symbols describing the orientations of the principal stresses within each element. These symbols are described in Figure 7. The orientations of the most and least compressive principal stresses are represented by the hourglass shape (or circle) and bar, respectively. Given stress values, we use the Mohr-Coulomb failure criterion to estimate regions where faulting would occur. The Mohr-Coulomb failure equation relates shear stress τ at failure to normal stress σ_n

$$\tau_{failure} = c + \sigma_n \tan \phi \tag{3.1}$$

where c is the cohesive strength of the rock and ϕ is the angle of internal friction. We adopt

values for c (3.8 $\times 10^7$ Pa) and ϕ (49°) appropriate for basalt [*Handin*, 1966]. In the stress orientation plots below, elements where the shear stress has exceeded the Mohr-Coulomb criterion are shaded to indicate failure. Once we have found where failure is expected, the orientations of principal stresses are used to determine the style and orientation of faulting, according to the criteria of *Anderson* [1951]. Given the principal stress directions, the type of faulting (normal, thrust, or strike slip) and the orientation (radial or circumferential) can be determined. Figure 7 gives types and orientations of faulting in elements with the given orientations of the stress symbols. This classification scheme holds if the principal stresses approximately correspond to the horizontal ($\sigma_{rr}, \sigma_{\theta\theta}$) and vertical stresses (σ_{zz}) listed here. If the stresses are not aligned in this way, fault geometry may be less simply described. The principal stress orientations can also yield a prediction of intrusion type and orientation, under the assumption that intrusions are emplaced perpendicular to the least compressive stress. Figure 7 thus also lists predictions of intrusion types and orientations, given the principal stress orientations shown.

For this study we will use three distinct finite element grids, varying edifice size in order to model the wide range of sizes of oceanic hotspot volcanoes. We consider three edifices with the following dimensions; radius r_v = 40 km and height h_v = 5 km, r_v = 60 km and h_v = 5 km, and r_v = 120 and h_v = 12 km (Figure 6b, c, and d, respectively). These roughly correspond to edifice sizes (accounting for flexure) in the Galápagos, Marquesas, and Hawaiian chains, respectively. All grids are modeled in axisymmetric geometry unless otherwise stated. For each family of models we calculate the effects of varying T_e and the basal boundary condition of the edifice. For selected models we also consider the effects of magma chamber expansion, regional stresses, plane strain geometry and a cumulate intrusive complex at the core of the volcano. We then interpret the characteristic features of volcanoes in each chain in light of the model predictions in order to elucidate the set of conditions that makes each chain unique.

When applying the results of the models to interpret features of real volcanoes, it is

important to keep in mind the limitations of such models. Our method of incremental volcano growth is necessarily a coarse approximation: real volcanoes consist of thousands of units emplaced at irregular timescales. The growth of large volcanoes clearly does not occur solely by repeated draping of young flows over older ones. At Hawaiian volcanoes, intrusive rift zone activity is a major contribution to edifice volume. The effects of these intrusions are not directly modeled. However, the state of stress characteristic of basally detached models ($\sigma_1 = \sigma_{zz}$, $\sigma_3 = \sigma_{\theta\theta}$) arises from the outward motion of the volcanic wedge over the flexed lithosphere, driven by the pull of gravity on the wedge. Any material emplaced anywhere in the upper part of the edifice, whether as intrusion or surface flow, contributes to the load which drives outward motion, which in turn creates the characteristic stress state. We therefore believe that our models reflect the first order processes that control the stress state in basally detached volcaones such as those of the Hawaiian Islands. The excellent agreement between modeled principal stress orientations and those determined from inversions of focal plane mechanisms in unbuttressed flanks of Mauna Loa [*Gillard et al.*, 1992] support our belief. We also apply a simple model of magma chamber expansion to the edifice stress fields in several models. This expansion has a similar effect to that of dike emplacment. Finally, we argue below that for volcanoes with a welded basal boundary condition, eruption is a substantial component of shield construction (and therefore our models are well suited to such volcanoes). Another important limitation is that the basal faults in our models are frictionless, unlike real faults. Our models are thus endmember cases; real volcanoes with detachments are likely to exhibit stress states that vary between those of welded base models and detached models. The stress field in such edifices will depend on local faulting history and earthquake cycles. Another limitation is the neglect of the effects of pore fluid pressure. Pore fluid pressure promotes faulting by reducing the effective stress normal to potential fault planes this faulting would reduce the level of differential stress in the edifice. Enhanced pore fluid pressure from dike intrusion can trigger catastrophic failure of volcano flanks [*Elsworth and Voight*, 1995]. *Wyss et al.* [1992b] determined that the differential stress

	Loading History 1		Loading History 2	
increment	levels	volume (km^3)	levels	volume (km^3)
1	1-2	6.70×10^1	1-4	5.36×10^2
2	3-4	4.69×10^2	5-7	2.34×10^3
3	5-6	1.27×10^3	8-9	3.23×10^3
4	7-8	2.48×10^3	10	2.27×10^3
5	9-10	4.09×10^3	–	

See Figure 6b for illustration of levels.

Table 3.5: Small model loading increments.

in the Kaoiki region was a few MPa, much less than the tens to hundreds of MPa typical in our models. We note, however, that the principal stress orientations in our models are similar to those determined by *Wyss et al.* [1992b,a]. We have no data on the pore pressures or stress magnitudes in other volcanoes, so it is unknown whether a similar effect applies to non-Hawaiian volcanoes.

Results

Flexurally-induced stress in model edifices

We first consider a model with edifice size appropriate for a volcano in the western Galápagos. A closeup of the part of the grid containing the edifice is shown in Figure 6b. The results of such a model, using increment set 1 (Table 3.5), and with elastic lithosphere thickness appropriate for in the western Galápagos (12 km) are shown in Figure 8. After flexure from the third load increment is complete, the most compressive principal stresses (σ_1) are oriented nearly horizontally (Figure 8a), and least compressive principal stresses (σ_3) are oriented nearly vertically. Contours of maximum shear stress and proximity to failure exhibit relatively low values (Figures 8d, g). After the fourth load increment has been emplaced, prinicipal stress orientations are similar (Figure 8b), but both maximum shear stress and proximity to failure have increased (Figures 8e, h). After emplacement of the final load

increment, maximum shear and proximity to failure increase again (Figures 8f, i). Note that maximum shear is always greatest near the base of the volcano (in the earliest, oldest load increments), and decreases with height (Figures 8d-f). Proximity to failure, however, is greatest in the middle to upper increments of the edifice (Figures 8g-i). At no time is the failure criterion exceeded: faulting is not predicted anywhere in the model edifice.

Results for an edifice of the same size emplaced on a 20 km thick elastic lithosphere, after emplacment of the final load increment, are shown in Figure 9. Principal stress orientations (Figure 9a) are similar to those of the T_e = 12 km case (Figure 8c); maximum shear and proximity to failure (Figures 9b,c) are both lower than those of the T_e = 12 km case (Figures 8f,i), although the distribution of these quantities with height is similar.

Figure 10 shows the variation of the hoop stress $\sigma_{\theta\theta}$ in a column of elements near the symmetry axis (element center radius r_c = 3 km); each curve corresponds to the end of a loading increment. In axisymmetry, $\sigma_{\theta\theta}$ is a principal stress. In these elements, $\sigma_{\theta\theta}$ is the intermediate principal stress σ_2, with the most compressive principal stress σ_1 nearly horizontal and slightly larger in magnitude than $\sigma_{\theta\theta}$. For the small edifice model, with T_e = 12 km (Figure 10a), $\sigma_{\theta\theta}$ grows as load increments are added, reaching a peak of about -260 MPa near the base after the final increment. Note that at a given time step, stress magnitudes in the youngest load increments are smaller than those in older (lower) increments. This pattern is characteristic of incrementally loaded edifices. For a model with T_e = 20 km (Figure 10b), stress magnitudes are lower than those in Figure 10a (maximum magnitude about -165 MPa). It is apparent that the details of increment emplacement influence the distribution of stress with depth (age) in the edifice. As a test of these effects, we performed the calculations with a different loading history than the models in Figures 10a and b. This alternative distribution consists of only four increments comprising 4, 3, 2, and 1 levels, respectively, from oldest to youngest (Table 3.5). The increments in this loading history are more nearly equal in volume than in the original loading history. For the new loading history (Figure 10c), stress magnitudes at the completion of loading are slightly

larger near the base of the model than in the original loading history. However, stresses in the final load increment are lower in the new history than in the old one, reflecting the smaller volume of the new final increment. A similar relationship holds between the old and new loading histories for the $T_e = 20$ km case (Figure 10d).

Results for a Galápagos-sized edifice with a detached basal boundary condition, on lithosphere with $T_e = 12$ km, are shown in Figure 11. The most compressive principal stress (σ_1) is oriented vertically at the base of the edifice (Figure 11a), in contrast with the horizontal orientation of σ_1 in edifices with welded bases (Figures 8,9). Proximity to failure and maximum shear stress levels are low in the upper edifice but higher at the base of the edifice (Figures 11b,c). The failure criterion is exceeded at the base of the volcano; stress orientations in this region predict radial normal faulting (Figures 11a,c).

The stress state in a Marquesas-sized model volcano emplaced on and welded to a 20-km-thick elastic lithosphere is shown in Figure 12. Principal stress orientations and patterns of maximum shear and proximity to failure (Figures 12a-c) are similar to those of welded Galápagos-sized volcanoes (Figures 8,9). Both maximum shear and proximity to failure (Figure 12) are greater than those for the Galápagos-sized models on the same thickness lithosphere (Figure 9). Models of a Marquesas-sized volcano emplaced on a 12 km thick elastic lithosphere are shown in Figure 13. Maximum shear (Figure 13b) and proximity to failure (Figure 13c) are subtantially greater than for the $T_e = 20$ km case (Figures 12b and c, respectively). A large region in the volcano's core is on the verge of failure (Figure 13c); the failure criterion is never exceeded in the edifice in either Marquesas-sized model, however.

We next consider a Hawaiian-sized edifice, basally detached from a 32-km-thick elastic lithosphere (Figure 14). As in the Galápagos-sized basally detached edifice (Figure 11), σ_1 is oriented vertically at the base (Figure 14a), but horizontally in a small region near the summit. Radial normal faults are predicted in the failed area at the base (Figures 14a,g). Maximum shear stress ranges from moderate values at the base to near zero in the upper edifice (Figure 14d). As later load increments are added, the basal region of predicted failure

grows outward and upward (Figures 14b, c, h, i). Near-horizontal compression ($\sigma_1 \approx \sigma_{rr}$) characterizes the proximal parts of the last load increments; the remainder of the edifice is characterized by $\sigma_1 = \sigma_{zz}$ and $\sigma_3 = \sigma_{\theta\theta}$ (Figures 14b, c). Proximity to failure and maximum shear are extremely low in the upper edifice (Figures 14e, f, h, i), with the exception of a zone of elevated proximity to failure at the summit (Figure 14i).

A model for a Hawaiian-sized edifice basally welded to a 32 km thick elastic lithosphere is shown in Figure 15. After emplacment of the final load increment, the stress state in the edifice is characterized by horizontal compression (Figure 15a). $\sigma_1 \approx \sigma_{rr}$ in the core and $\sigma_1 = \sigma_{\theta\theta}$ in distal parts of the edifice. Maximum shear stress increases with depth (Figure 15b), as is the case with the other basally welded models (Figures 8, 9, and 12), but the magnitude is much greater (Figure 15b).

All volcano models discussed so far have been axisymmetric (i.e., cones). Hawaiian shields, however, exhibit long linear rift zones which are commonly modeled as two-dimensional plane-strain structures. Accordingly, we consider a basally detached volcanic wedge in plane-strain geometry, with horizontal dimension equal to the radius of the volcano in Figure 14, and height identical to that of the model in Figure 14. The change from axisymmetric to plane-strain geometry has subtle but important effects on the stress fields produced by volcanic loading. The distribution of maximum shear stress in such a planar wedge (Figure 16b) is similar to that in the corresponding conical volcano (Figure 14h), with slightly higher peak values at the base of the planar wedge. The pattern of proximity to failure (Figure 16c) is also similar to that of the conical volcano (Figure 14i); the region of predicted failure is slightly higher and slightly more restricted horizontally in the planar wedge. Principal stress orientations in the area of predicted failure at the base of the edifice (Figure 16a,c) are such that σ_3 is horizontal and in the plane of the cross-section, in contrast to the axisymmetric case, where σ_3 in the failure region is horizontal but perpendicular to the model plane. These principal stress orientations (Figure 16a) predict the formation of normal faults paralleling the axis of the volcanic wedge.

Magma migration paths and effect of magma chamber pressurization in basally welded edifices

The models of volcanic loading of the lithosphere described above reveal the profound effect that the basal boundary condition has on the evolution of stresses and tectonics of large volcanoes. A unique pattern of distribution of stress magnitudes and orientations applies to each type of basal boundary condition (welded or detached). Edifices with welded bases are characterized by near-horizontal principal compression, with differential stress levels that increase as the edifice grows (Figure 8). Magma ascends through the lithosphere and crust via fractures which tend to open perpendicular to the direction of least compressive stress (σ_3). A stress state such as that in Figure 8, with σ_1 approximately horizontal ($\approx \sigma_{rr}$) and σ_3 approximately vertical ($\approx \sigma_{zz}$), will block magma ascent to the summit and presumably halt or greatly slow volcano growth (emplacement of subhorizontal sills is possible, but by itself is not an efficient mode of volcano growth.) Just after emplacement of a load increment, σ_1 is vertical, and magma ascent through the increment to the surface is possible [*McGovern and Solomon*, 1993]. Subsidence due to flexure horizontally (radially) compresses the top of the lithosphere beneath the load; a welded boundary condition transmits this compression to the edifice. Even in the smallest models considered, horizontal compressive stresses are hundreds of MPa in magnitude (Figure 10). Such a volcano is unlikely to grow beyond the first few load increments without modification of the stress state. The horizontal compression must somehow be neutralized in order to re-establish stress orientations that allow magma transport to the summit region.

Radially outward displacements of a pressurized magma chamber or conduit in the axial region of the volcano may provide increments of horizontal extensional stress required to reorient the principal stresses, such that a state of horizontal principal extension is achieved. This is a consequence of the strain-displacement relation of axisymmetry

$$\epsilon_\theta = u/r, \tag{3.2}$$

where ϵ_θ is hoop strain, u is radial displacement, and r is the radius of the given material element. The hoop stress generated by this strain is

$$\sigma_{\theta\theta} = \frac{(1-\nu)E}{(1+\nu)(1-2\nu)}\epsilon_\theta. \tag{3.3}$$

Thus, a positive radial displacement generates positive (tensile) stress. We note that thermal expansion of heated rock can generate similar stress states in volcanoes, as demonstrated by the models of *Chevallier and Verwoerd* [1990].

We propose that principal stress re-orientation by magma chamber expansion is required for sustained growth of basally welded edifices. This expansion creates a state of horizontal principal extension that allows ascent of magma to near-surface regions and formation of extensional tectonic features around the summit. To test this hypothesis, we model expansion of a near-summit magma chamber in a reduced grid of elements that represents only the edifice of a volcano. We apply a uniform pressure to the sides of elements designated as constituting a magma chamber. This pressure actually represents overpressurization of the chamber in excess of the lithostatic pressure gradient. We assign a reduced value of Young's modulus ($E = 1.0 \times 10^9$ MPa) in order to reflect the lowered rigidity of the fluid-filled network of dikes, sills and solidified material constituting a magma chamber. Gravity is set to zero, and lithospheric flexure is not modeled. Boundary conditions are as follows: no r or z dispacement along the basal ($z = 0$) boundary, and no r displacement but free z displacement along the axis of symmetry ($r = 0$). The fixed basal boundary is meant to correspond to the welded boundary in the full-grid flexural models above. Many workers who model the effects of magma chambers [e.g. *Chevallier and Verwoerd*, 1988; *Zuber and Mouginis-Mark*, 1992; *Chadwick and Dieterich*, 1995] extend their element grids far beyond the extent of the actual edifice, in order to avoid "artificial edge effects". We maintain that since the overall goal of this study is to gauge the effect of the basal boundary condition (welded, in this particular case), it is acceptable and even desired to apply the fixed boundary

condition to the base of our magma chamber model edifice. We acknowledge that the magma chamber models presented here are much cruder than those of previous workers [*Chevallier and Verwoerd*, 1988; *Zuber and Mouginis-Mark*, 1992; *Chadwick and Dieterich*, 1995]. They are included to demonstrate the interaction between the flexurally-generated stress field (the main focus of this study) and the stress field induced by the magma chamber (the focus of the aforementioned studies). These two different types of studies should be viewed as complements to each other.

Determination of an appropriate value for magma chamber overpressure is difficult, due to a paucity of direct constraints. *Rubin and Pollard* [1987] modeled the growth of a dike in the southwest rift zone of Kilauea and obtained an estimated excess magma pressure of 2.5 to 10.5 MPa. The observation that the magnitude of summit deflation correlated with the elevation of flank eruptions led *Decker* [1987] to conclude, through a pressure balance argument, that the maximum range of pressure change in the shallow magma reservoir system at Kilauea over the last several decades has been about 26 MPa. This figure provides an upper bound on magma chamber overpressure at Kilauea over that period. We know of no such constraints on magma chamber overpressure at other large volcanoes. We argue that magma chamber overpressure would likely be greater at a volcano with a welded basal boundary condition than at a volcano demonstrated to have a basal decollement which accommodates volcano growth through lateral motion, as at Kilauea. Accordingly, for a magma chamber applied to a model of a basally welded volcano, we use a magma chamber overpressure value of 50 MPa.

Figure 17a shows principal stress orientations resulting from simulating pressurization of a magma chamber approximately 2 km thick and 4 km in radius. The magma chamber elements, marked with a star, have a uniform pressure of 50 MPa applied to their edges. Pressurization causes a near-horizontal orientation of σ_1 within most of the edifice, but immediately above and below the chamber σ_1 is approximately vertical. σ_3 is horizontal above and below the chamber and vertical immediately outward of the chamber. At greater

r, σ_3 has a range of orientations; in several elements, $\sigma_3 = \sigma_{\theta\theta}$. However, we cannot use these orientations to predict faulting types or planes of dike propagation. We must superpose the stress field of Figure 17a with the flexurally-induced stress fields of Figure 8c (for loading of a $T_e = 12$ km lithosphere). Figure 17b shows principal stress orientations resulting from this superposition. The principal stress orientations of the resulting field show two important differences from those of the flexural field (Figure 8c): two elements directly above the chamber now exhibit sub-horizontal orientations of σ_3, and shear failure is predicted above and outward of the chamber (as well as along the innermost column of elements in the chamber itself). The results for superposition of the chamber stress field with the $T_e = 20$ km case are almost identical (Figure 17c), with slightly more horizontal orientations of σ_3 in the above-chamber elements.

Figure 18a shows principal stress orientations from expansion of a magma chamber with a horizontal/vertical aspect ratio of 4:3 (as compared to the 4:1 ratio for the chamber in Figure 17). The applied pressure is the same as in the previous model (50 MPa). Expansion of this prolate chamber causes the hoop stress to be the least compressive stress in a large zone of the upper flank (in contrast, only a few, scattered elements have such orientations in Figure 17). The much more detailed calculations of *Chadwick and Dieterich* [1995] similarly found that prolate chambers promote the establishment of the state $\sigma_3 = \sigma_{\theta\theta}$. Such principal stress orientations by themselves would favor the formation of radial dikes in the uppermost parts of the edifice. However, when the magma chamber stress field is superposed with edifice stresses from flexure of a plate with $T_e = 12$ km (Figure 18b) or $T_e = 20$ km (Figure 18c), σ_3 has a predominantly vertical orientation. In such a stress state, intrusions emanating from the chamber will be sills rather than dikes.

Discussion

We have calculated states of stress in large volcanoes subject to lithospheric flexure. These calculations allow us to predict the types and orientations of faulting on volcanic edifices and magma migration paths within them. We now compare these predictions with observed distributions of tectonic features and information on the deep structure of the volcanoes discussed in detail above, in order to constrain the conditions which have driven the growth and development of these volcanoes. We first propose scenarios describing the growth of basally welded and basally detached volcanoes. We identify volcanoes in the Hawaiian and Galapagos chains as clear examples of volcanoes in each class, respectively, on the basis of the characteristic features at each chain that indicate the basal boundary condition. We then discuss the implications of our models for volcanoes in the other chains discussed in detail at the beginning of this chapter. We examine the conditions that may have determined the basal boundary condition at each chain, examining how these conditions may relate to specific structures on volcanoes at several chains. We then compare and contrast observed features at volcanoes in the selected chains, using insights derived from the models to elucidate the processes that give volcanoes in each chain distinct modes of growth.

Growth mechanisms of large volcanoes

Basally welded volcanoes

We propose the following scenario for the growth of basally welded volcanoes. Early in the growth of a volcano, the load is small and therefore horizontal compressive stresses are correspondingly small (Figures 8, 10), allowing a magma conduit/chamber system with a connection to the summit to establish itelf in the edifice. As the volcano grows, lithospheric flexure progresses and the magnitude of horizontal compression increases. Expansion from magmatic overpressure is required to offset these stresses and keep the axial path open. The magnitude of horizontal compression is greatest in the earliest load increments at the

base of the volcano and decreases in later load increments (Figures 8, 10). This state arises because a given load increment is (approximately) stress-free when emplaced, and feels tectonic stress only from itself and subsequent load increments [*McGovern and Solomon*, 1993]. Magma chamber expansion leads to horizontal extension above the chamber and the condition $\sigma_3 \approx \sigma_{rr}$ (Figures 17, 18), allowing magma ascent to the summit and the emplacement of circumferential dikes around the summit caldera. Outward of the chamber, expansion produces extensional increments to both $\sigma_{\theta\theta}$ and σ_{zz}. In general, the extensional increment to σ_{zz} is greater than that to $\sigma_{\theta\theta}$, especially adjacent to the chamber. Such chamber stress increments do not change the principal stress orientations characteristic of flexural loading ($\sigma_1 \approx \sigma_{rr}, \sigma_3 \approx \sigma_{zz}$); in fact, they reinforce the flexural stress state. Intrusions outward of the magma chamber are therefore likely to be emplaced as sills. Emplacement of these sills and circumferential dikes above the chamber may cause positive radial displacements in the surrounding rock. As described above, such displacements will induce extensional increments of $\sigma_{\theta\theta}$. If large enough, these increments will reorient the principal stresses such that $\sigma_{\theta\theta}$ will become σ_3, allowing the intrusion of vertical dikes (as suggested by *Chadwick and Dieterich* [1995]). Since the magnitude of horizontal compressive increases with depth (age) in the edifice (Figures 8, 10), the highest levels of the edifice will require the least addition of magma chamber expansion stress to make σ_3 horizontal. The highest (youngest) layers will therefore be the sites of first intrusion from a given chamber inflation episode. These earliest intrusions will drain magma from the chamber, inhibiting further buildup of pressure in the chamber, which would be required to drive further expansion necessary to allow intrusion into lower zones of the edifice. Thus, intrusions are likely to remain at the highest level in the volcano accessible to the magma chamber (at the horizon of neutral buoyancy). We therefore predict that radial dikes in basally welded volcanoes are shallow features, restricted to the uppermost layers of the edifice. The volcano may eventually become so large that horizontal compressive stresses are too large to be countered by extensional stress from magmatic pressure and thermal expansion. A decrease in the magma supply rate from the mantle may

also interrupt growth by reducing the magmatic overpressure below that required to reorient the principal stresses in the vicinity of the chamber. When either of these conditions occurs, the volcano st. . s growing (except for perhaps minor intrusion of sills by remaining magma).

The rigidity of the lithosphere controls the magnitude of horizontal compressive stresses that build up in volcanoes with welded basal boundaries. Figure 19 shows the magnitude of radial normal stress σ_{rr}, hoop stress $\sigma_{\theta\theta}$, and maximum shear stress versus T_e for a welded volcano; all three quantities are inversely proportional to T_e. This behavior is a consequence of the direct tranmission of horizontal compressive strain from the top of the lithosphere to the edifice; for a given load, displacement increases with decreasing T_e. This result has important implications for the growth of basally welded volcanoes. Horizontal compressive stresses tend to impede magma ascent to near-summit regions and therefore inhibit edifice growth. Such stresses must be opposed by extensional stresses resulting from magma chamber pressurization. Thus, for given strength of magma chamber pressurization (presumably proportional to the magma supply rate from the deep source), volcanoes on thicker lithosphere can grow to larger size before flexurally induced stresses reorient the principal stresses and shut off magma ascent. In this way, lithospheric thickness may control volcano size through the regulation of the stress state in the volcano.

The stress state in the top of the lithosphere may also regulate the ascent of magma from the mantle source. As shown in Figures 7, 9–12, and 14 of Chapter 2, the upper lithosphere beneath the edifices is characterized by horizontal principal compression. Note that the transition between horizontal principal compression and horizontal principal tension in these Figures is not located at a depth equal to half the lithosphere thickness, as would be predicted from analytic models of plate flexure. A basally welded volcanic edifice acts as a local thickening of the lithosphere, elevating the midplane of the lithosphere-volcano "plate". Thus, the region that presents the greatest obstruction to the ascent of magma extends from the lower edifice to the uppermost lithosphere, where the condition $\sigma_3 \approx \sigma_{zz}$ allows only lateral intrusion and where high differential stresses inhibit principal stress reori-

entation. Sufficient increments of horizontal extensional stress must be added in this region to enable ascent of magma (and ultimately edifice growth). We propose several scenarios for accomplishing this reorientation. The ascending batches of magma themselves may provide part of the required stress increment, by inducing hydraulic fracture as they ascend [e.g., *Shaw*, 1980; *Ryan*, 1988]. The magma supply rate will control the amount of stress reorientation this mechanism can provide. Another possibility is that magma encountering the obstruction zone may stall and be emplaced as subhorizontal sills. Such intrusions would have lower density than the mantle lithosphere; as they accumulated they may eventually buoyantly uplift the lithosphere (and the volcano). The uplift would relieve the subsidence-induced horizontal compression, perhaps to the point of reorienting the principal stresses and enabling further magma ascent. Such intrusions may constitute "underplated" material at the base of the crust observed beneath Hawaiian [*Watts and ten Brink*, 1989] and Marquesan [*Wolfe et al.*, 1994] volcanoes. The magma chamber may provide another mechanism for magma transfer through the obstruction zone. We have proposed that expansion of a magma chamber alters the stress state in the edifice, allowing magma ascent and dike intrusion despite horizontal compressive edifice stress. This scenario will not work, however if magma ascent into the chamber itself is prevented. One way to secure a chamber magma supply is to have the base of the chamber extend below the base of the volcano into the lithosphere (as proposed by *Chadwick and Dieterich* [1995] in models of Galápagos volcanoes), perhaps as deep as the region of horizontal principal extension. Pressurization of this deeply extending magma chamber would then reorient stresses in the obstruction zone, reopening mamga ascent paths. It is likely that some combination of these proposed mechanisms operates to facilitate magma ascent to basally welded volcanoes. Finally, we note that the ease with which principal stresses can be reoriented will also depend on the stress state in the lithosphere before loading. This state depends on boundary conditions at the time of formation of the lithosphere [e.g., *McGarr*, 1988] and thermal stresses due to plate cooling [e.g., *Wessel*, 1992].

The magma supply rate to a volcano will depend on the inherent strength of the plume (melt generation rate $\dot{m}_p$). Plate motion, however, will carry a volcano away from the hotspot; an increase in plate velocity v_p will lead to a decrease in magma supply. *Filmer* [1991] gives the following expression for volume emitted per unit distance Q

$$Q = \frac{\phi}{v_p}, \tag{3.4}$$

where ϕ is the magma supply rate to the edifices. Q is an area, corresponding to the cross-sectional area of a volcano chain. Our results suggest that T_e may enter this relation through regulation of the fraction ϕ of mantle melt generation $\dot{m}_p$ that is able to ascend through the region of horizontal compressive stress to contribute to edifice growth. Thus, a balance between $\dot{m}_p$, T_e, and v_p may determine the size of volcanoes with welded bases.

Real volcanoes are constructed from flow units much smaller than the load increments in the models presented here. This distinction will affect the accuracy our predictions of the stress state in growing basally welded edifices. For example, stress profiles vs. height in model edifices (Figures 10a-d) demonstrate that stresses are similar within a load increment but jump sharply between increments. Figures 10a-d include curves that interpolate stress values at the increment centers. These curves are intended to indicate the (smoothly varying) stress state in an edifice constructed by a much finer distribution of load increments. A newly emplaced flank flow will feel essentially no subsidence-related horizontal compressive stress. Thus, profiles of $\sigma_{\theta\theta}$ vs. height (Figures 10a-d) should approach zero stress at the top of the uppermost load increment (the volcano surface). Figures 10c and d show stress profiles in a volcano for which the last load increments are the most finely resolved. Stresses approach zero at the surface more closely than for the other loading history (Figures 10a and b). Note that if the entire edifice is emplaced as one increment (Figures 12 and 14 in Chapter 2), flexurally-induced horizontal compressive stresses are greatest at the top of the edifice, and are likely great enough to induce thrust faulting.

In basally welded model volcanoes, two competing effects determine the stress state: A welded load increment acts as a local thickening of the lithospheric plate. Stresses are greatest at the top and bottom of flexing plates: thus, stresses within a volcano load increment are greatest at the top. The effects of incremental loading, however, make stresses greatest at the bottom of a pile of load increments. Thus, for an accurate depiction of the stress state in a growing basally welded edifice, load increments must be resolved finely enough such that the "plate stress effect" (stresses greatest at top) does not obscure the "incremental loading effect" (stresses greatest at bottom). As the edifice is more finely discretized, we approach the realistic case in which the lowest stresses are in the youngest increments. Figures 10a-d show that our models have sufficient resolution to crudely approximate this state.

In summary, we make the following predictions about the characteristics that distinguish basally welded volcanoes subject to lithospheric flexure. Horizontal compressive stresses will build up as the volcano grows, increasing with age (depth) in the edifice. Magma ascent will be blocked; this choking effect will severely limit volcano growth unless the stress state in the central edifice is somehow modified. The role of the magma chamber is to provide the required change in stress to allow near-surface intrusion and surface eruptions of magma which build the shield. Thus, magma chambers and their surface manifestations as calderae will be prominent features on volcanoes with welded bases. The elastic plate thickness T_e controls the magnitude of horizontal compressive stresses experienced by a given volcano (increasing T_e decreases the stresses and vice-versa). The balance between compressive flexurally-induced stresses (governed by T_e) and tensile stresses from magma chamber pressurization (governed by the magma supply rate) will determine the volume of a welded-base volcano. Welded-base volcano dimensions should increase with increasing T_e (and therefore increasing age) of the lithosphere supporting it.

Volcanoes with detached bases

Edifices with detached bases are characterized by a completely different state of stress than those with welded bases. The principal compressive stress in most of the edifice is oriented vertically ($\sigma_1 = \sigma_{zz}$), except for a small region near the summit where $\sigma_1 \approx \sigma_{rr}$. In most of the edifice σ_3 is horizontal; therefore magma can easily move upwards through the axis toward the summit in planar dikes perpendicular to σ_3. The failure criterion is exceeded at the base of such volcanoes; principal stress orientations predict radial extensional faulting. Such a stress state favors the formation of dikes radiating from the volcano's core. Sustained intrusion may result in the formation of radial intrusive zones or rift zones. Such rift zones will be favored pathways for lateral magma transport. Radial intrusions near the base of the edifice will create extensional stresses in the material above, possibly expanding the region of horizontal principal extension to the upper flanks.

In a volcano with a detached base, the role of the magma chamber is less critical. A state of horizontal principal extension already exists in such an edifice, allowing vertical intrusions to ascend through the axis of the volcano to the magma chamber beneath the summit caldera. From the magma chamber, most magma is transferred to the rift zones. Dikes intrude laterally at the level of neutral buoyancy [*Ryan*, 1994]. Such intrusions do not require substantial chamber overpressurization to drive radial displacements that alter the local stress field; basal slip beneath the flanks produces stress orientations favorable to radial dike emplacement from the start. Thus, the processes of rift zone intrusion and accommodation of this intrusion by basal slip dominate lateral transport of material in basally detached volcanoes.

Model discretization does not have a strong effect on the basally detached models. Edifice stresses are dependent on the amount of slip on the basal boundary, and stresses far from the detachment are low in all increments (Figure 14d-f). The amount of slip is likely to be similar for a basally detached volcano with fine or coarse increments. Model discretization might be more important for models with detachment friction, which would be expected to

exhibit stress states intermediate between those of a frictionless detachment and a welded base.

Application of Models to Specific Volcano Chains

The Galápagos Islands: basally welded volcanoes

The western Galápagos volcanoes exhibit characteristics that suggest the establishment of a welded boundary condition at their bases. Their small diameters and heights (compared to Hawaiian volcanoes) suggest a limitation of erupted volume by flexurally induced horizontal compression of large magnitude because of the young, thin lithosphere supporting the edifices. Prominent summit caldera depressions and large ratios of caldera diameter to (subareal) edifice diameter indicate the importance of the subcaldera magma chamber in driving growth of the Galápagos volcanoes, a condition predicted above for volcanoes with welded bases. Tectonic features indicative of detached basal boundary conditions are, with a few exceptions, conspicuously absent from the western Galápagos volcanoes. Extensional features and flow sources, such as the radial fissures, are distributed broadly on Galápagos shields, in contrast to the narrow, well-defined rift zones typical of the (basally detached) Hawaiian volcanoes.

The fundamental problem of accommodating growth of basally welded volcanoes is to maintain a viable magmatic pathway from the magmatic source at the base of the volcano to the summit region. Horizontal compression transmitted to the edifice will cause the reorientation of principal stresses such that σ_1 is horizontal and σ_3 is vertical. Such a stress state would permit only the intrusion of sub-horizontal sills into the lower part of the edifice; magma ascent into the upper parts of the edifice would be prevented. The volcanoes of the western Galápagos Islands appear to be constructed from (1) radial flows that emanate either from near-summit circumferential fissures or radial fissures that are the surface manifestations of dikes radiating from a near-surface magma chamber [e.g., *Chadwick and Howard*,

1991]; and (2) from the dikes themselves. Clearly, a magmatic pathway from base to chamber to summit caldera is available in these volcanoes, despite the presumed welded boundary condition and the relatively thin lithosphere. We propose that the establishment of shallow magma chambers and their supply conduits within basally welded volcanoes modifies the stress field near the central axis of the edifice, allowing high-level intrusive and extrusive activity. Intrusion of radial dikes will be easiest in the uppermost, youngest layers of the volcano, because these layers exhibit the lowest magnitudes of horizontal compressive stress. This inference is consistent with the observation that the radial fissures on the Galápagos Islands are the surface expression of shallow dikes [*Chadwick and Howard*, 1991].

The above-described scenario for accommodation of growth in basally welded volcanoes has further implications for volcanoes such as those of the western Galápagos Islands, and for the origins of linear eruptive features on large volcanoes. As noted above, basally welded volcanoes experience a stress state that greatly favors the emplacement of intrusions from a shallow magma reservoir as subhorizontal sills. Intrusions with this geometry would be expected to cause uplift of the surface above the intrusion. *McBirney and Williams* [1969] and *Cullen et al.* [1987] have proposed just such a mechanism for the formation of the steep-sided, flat-topped summit regions characteristic of the western Galápagos shields. Our results lead us to a similar conclusion, although we acknowledge that construction by superposition of short extrusive flows probably makes a significant contribution to summit topography (such as at Alcedo [*Geist et al.*, 1994]). The flows that constitute the lower flanks mainly emanate from radial fissures which are the surface expression of radial dikes. Emplacment of these dikes requires modification of the flexurally-induced stress field, diminishing the highly compressive tangential normal stress $\sigma_{\theta\theta}$ such that it becomes the least compressive principal stress σ_3. Magma chamber pressurization may provide part of the required tensile stress increment (Figures 17, 18), but, for reasonable values of chamber overpressure, additional sources are required. Based on finite element models of magma chamber pressurization, *Chadwick and Dieterich* [1995] proposed that the emplacment of circumferential dikes above

and around the magma chamber alters the local stress field in a way that favors later intrusion of radial dikes, and vice versa. Thus, alternating episodes of radial and circumferential diking are possible. The displacments resulting from dike expansion generate a tensile increment of normal stress perpendicular to the dike plane in a small zone surrounding and ahead of the dike tip [e.g., *Pollard*, 1987; *Ryan*, 1988]. A planar dike of width 1 m (a value appropriate for Galápagos volcanoes [*Chadwick and Howard*, 1991]) propagating upwards toward a free surface can generate tensile stress increments of tens of MPa at the propagating tip [*Ryan*, 1988]. A similar dike propagating horizontally generates tensile stress increments of several MPa at the tip. Pressurization of radial dikes that form near the caldera region can alter the stress field in front of them as they extend radially or upwards. Subhorizontal sills emanating from the magma chamber may also induce positive radial displacements, and therefore tensile increments of $\sigma_{\theta\theta}$, in surrounding regions of the edifice. If these increments are large enough, the principal stresses may be reoriented, causing propagating intrusions to reorient themselves. Under such a scenario, proximal sills may feed more distal (and shallower) dikes on the flanks.

Dike-induced stress increments of the magnitudes calculated by *Ryan* [1988] are sufficient to reorient principal stresses in the uppermost layers of the volcano, which have experienced the least flexurally-induced compression. Thus, the condition $\sigma_{\theta\theta} \approx \sigma_3$ can be established far from the caldera, enabling magma transport to distal regions. The prediction that dikes in basally welded volcanoes will be shallow features, restricted to the uppermost, youngest layers of the volcano, is consistent with the inference that the dikes feeding the radial fissure flows on the western Galápagos shields are shallow features [*Chadwick and Howard*, 1991]. These radial fissures are often concentrated in linear zones that connect the summits of adjacent volcanoes [*Nordlie*, 1973; *Chadwick and Howard*, 1991]. *Chadwick and Howard* [1991] showed that such patterns could be attributed to the superposition of stresses resulting from pressurization of adjacent shallow magma reservoirs. These workers maintained that the Galápagos shallow fissures were not analogues to the rift zones of Hawaiian volcanoes.

The results of our models lead us to the same conclusion.

The Hawaiian Islands: basally detached volcanoes

The results of our models are consistent with earlier analyses that demonstrated the importance of a detached basal boundary condition to the volcanoes of the Hawaiian Islands [*Nakamura*, 1980; *Dieterich*, 1988; *Borgia*, 1994]. Intrusions into Hawaiian rift zones are accommodated by deep slip of the edifice along a basal detachment [*Dieterich*, 1988]; the zone of shallow dikes may also be underlain by a deeper magmatic storage system [*Delaney et al.*, 1990]. The orientations of Hawaiian rift zones are influenced by the topography of and stress state in the older shields on whose flanks younger shields grow [*Fiske and Jackson*, 1972]. As a result, the rifts are oriented perpendicular to the slope of the older volcanoes, and rift zones from different volcanoes never intersect each other [*Fiske and Jackson*, 1972]. Hawaiian-style rift zones formed in this way would never exhibit the caldera-connecting geometry typical of the western Galápagos shields. Rift zones on volcanoes influenced by older shields are uncorrelated with regional stresses in the lithosphere [*Fiske and Jackson*, 1972]. Linear eruptive zones on basally welded volcanoes are much more likely to be correlated with regional stresses, since the lithosphere is directly coupled to the edifice. Thus regional alignments may also play a role in the orientation of the linear fissure zones connecting the summits of Galápagos shields [*Rowland and Munro*, 1992].

Hawaiian volcanoes may, however, experience near-welded basal boundary conditions at late stages in their development, when their flanks are buttressed by the growth of younger shields (or perhaps after sustained detachment motion has signficantly thinned the basal sediment layer). Such a situation may apply to Mauna Loa; its southern flank is partially buttressed by Kilauea, and its northern flanks are buttressed by Mauna Kea and Hualalai. This buttressing may be characteristic of the final stages of shield building. Evidence from a core sample drilled into Mauna Loa's flank near Hilo suggests that Mauna Loa is subsiding faster than it is growing, and thus is in a declining stage of its evolution [*Hawaii Scientific*

Drilling Project, 1995; *Lipman and Moore*, 1996]. The upper northern flank of Mauna Loa is cut by numerous linear fissures radiating from the summit area [*Lockwood and Lipman*, 1987]. These fissures are presumably the expression of shallow dikes, intruded from the near-summit magma chamber, that intersect the surface lower on the flank. These features are widely distributed in azimuth [*Lockwood and Lipman*, 1987], in sharp contrast to the extreme concentration of dikes and vents in the southwest and northeast rift zones of Mauna Loa. Indeed, the distributed nature of the fissure pattern on the north slopes of Mauna Loa [*Lockwood and Lipman*, 1987] is qualitatively similar to that on the western Galápagos shields [*Chadwick and Howard*, 1991]. Thus for the Mauna Loa fissures we suggest an emplacement scenario similar to that for the fissures on the Galápagos shields: magma chamber pressurization induces the intrusion of radial dikes into the uppermost layers of the edifice. Buttressing of Mauna Loa's north flank by the mature shields Mauna Kea and Hualalai prohibits relaxation of dike-induced stress by flank movement [*Rubin*, 1990]. The intrusion of a dike will increase horizontal compression perpendicular to the dike, inhibiting subesquent dike intrusion near it. The result is a diffuse system of radial dikes. We suggest that the diffuse pattern of dikes in the north quadrant of Mauna Loa is an indication that the volcano is aging gracefully into a mature stage characterized by a welded basal boundary condition. This suggestion is supported by evidence in core samples obtained from the Hawaii Scientific Drilling Project (HSDP) drill site near Hilo [*Hawaii Scientific Drilling Project*, 1995], which indicates that the lava accumulation rate of Mauna Loa is no longer sufficient to maintain its size against the rate of flexural subsidence [*Lipman*, 1995; *Lipman and Moore*, 1996]. These workers conclude that Mauna Loa is in a state of declining growth.

Loss of pore fluid (water) from the decollement zone may also contribute to a welded basal boundary condition in late stages of volcano evolution. *Clague and Denlinger* [1994] propose that a ductile dunite cumulate core beneath Hawaiian volcanoes drives flank motion ahead of it as it flows outward in response to gravity. These workers maintain that this ductile cumulate core plays a more vital role in flank motion than the sediment-rooted basal

decollement. They argue that dewatering of the decollement sediments due to loading will decrease their ductility and increase resistance to sliding. We would like to clarify possible mechanisms for decollement dewatering. Decollement-parallel permeability is often enhanced (by up to 2 orders of magnitude) by stress-induced reorientation of scaly clay fabrics [*Arch and Maltman*, 1990]. Thus, decollements often become favored pathways for fluid movement [*Moore et al.*, 1986]. If the decollement-parallel permeability is greater than the permeability of surrounding sediments and volcanic rock, dewatering will occur along the decollement. The basal decollements beneath Hawaiian volcanoes may then progressively lose water from their distal ends. These distal decollement sections will dewater last, since they will receive flow from the proximal parts. The time scale for dewatering will be controlled by the decollement permeabilities (both parallel and perpendicular). If this time scale is comparable with the lifetime of a Hawaiian volcano, removal of pore fluid from the decollement may also contribute to a transition from a detached to a welded basal boundary condition. This transition will begin near the core of the volcano (the earliest dewatered section) and propagate outwards. Mature volcanoes may have detached basal boundary conditions only in the most distal submarine flanks. A welded basal boundary condition will hold beneath the summit and rift zones due to decollement dewatering and cooling of the cumulate complex [*Clague and Denlinger*, 1994]. This scenario is also consistent with the observations at Mauna Loa described above.

We acknowledge that the detachments in our models are frictionless and thus cannot model the full complexity of flank dynamics as seen on large Hawaiian volcanoes. Cycles of intrusion, extrusive growth and flank faulting, as seen in seismic and geodetic data, are evidence for non-zero coefficient of friction μ along the detachment faults. Stresses build up from surface loading and dike intrusion. These stresses are relieved in large earthquakes along the basal detachment. Friction on the basal faults may regulate cycles of rift zone dike emplacement and flank movement, controlling the slope of the volcano flank [*Dieterich*, 1988]. However, our models do reflect stress states deep in the flanks of Mauna Loa and

Kilauea (σ_1 sub-vertical and σ_3 horizontal), as determined from inversion of fault plane solutions for stress tensors by *Wyss et al.* [1992a] and *Liang et al.* [1995]. These workers interpret their results as evidence for decollement-type faulting at the base of the edifices. If, as we propose, high pore pressures in a basal clay layer are responsible for the decollement, the detachment will act as a fault with a low effective fault friction μ_{eff} ($\approx$ 0.1–0.2 for decollements beneath accretionary prisms in Alaska [*Byrne and Fisher*, 1990], for example, as compared to typical laboratory values of μ for dry rocks 0.6–0.8 [*Byerlee*, 1978]). The value of μ_{eff} will influence the frequency and magnitude of intrusions and earthquakes and the extent to which horizontal compressive stresses build up before release. Our models with $\mu = 0$, however, give an adequate view of the long-term stress state in a basally welded volcano, which experiences much lower magnitudes of horizontal compression than a basally welded volcano.

Other chains

The dependence of linear eruptive zone style on basal boundary condition may help us elucidate the relative importance of detached-base or welded-base modes of growth on other large volcanoes.

For example, Piton de la Fournaise on Réunion Island exhibits radial rift zones and large fault-bounded slumps and submarine slides [*Duffield et al.*, 1982; *Lénat et al.*, 1989b]. The presence of such structures invites structural analogies to Hawaiian volcanoes [*Duffield et al.*, 1982]. Closer examination, however, reveals features characteristic of a welded-base style of volcanism. There are three linear zones of fissures and vents, termed 'rift zones', emanating from the central caldera of Fournaise; two of them bound the unbuttressed east flank of the edifice (to the northeast and southeast). These two narrow structures extend only about 5–10 km beyond the shoreline [*Lénat et al.*, 1989b]. The third 'rift zone' is a somewhat wider structure that extends along a constructional ridge to the northwest, directly toward the summit of the older Piton des Neiges. Such an orientation is uncharacteristic of basally de-

tached volcanoes; it is more consistent with a welded basal boundary condition that allowed transmission of a regional perturbation in lithospheric stress to the edifice (it is unlikely that the dual magma chamber pressurization scenario for the Galápagos shields [*Chadwick and Howard*, 1991] applies here, since Piton des Neiges is extinct). The orientation of the rift is similar to that of a extinct spreading ridge hypothesized to lie beneath Réunion [*Schlich*, 1982; *Gillot and Nativel*, 1989]. This potential weak zone in the lithosphere may have provided a favorable spot for upwelling material to penetrate the lithosphere and, if so, probably directed the migration of the eruptive center from Piton des Neiges to Fournaise [*Gillot and Nativel*, 1989]. The western flanks of Fournaise are stationary during rift intrusions and activity in the caldera and unbuttressed eastern sector [*Lénat et al.*, 1989a]. This behavior implies a welded basal boundary condition for the stable western sector, which would favor formation of the northwest 'rift zone' by transmitting regional stress to the edifice, not by flank movement perpendicular to the 'rift'. Such a feature would not be analagous to Hawaiian-style rift zones. The analysis of the collapse history of Réunion by *Gillot et al.* [1994] is also consistent with such a scenario. These workers describe a series of collapse events that increase in frequency but decrease in volume with time. The first postulated event (about 1.8 Ma) involved nearly the whole island, and was likely deep enough to be rooted in the weak sediment layer between volcano and crust (i.e. as postulated for Hawaii) [*Gillot et al.*, 1994]. Later events were successively smaller in volume, more shallowly rooted and more frequent [*Gillot et al.*, 1994]. The basal surface of the most recent landslide reaches down only to about 500 m below sea level [*Gillot et al.*, 1994]. The morphology of the Enclos Foque caldera resembles landslide collapse calderas on the flanks of the Canary Islands [*Ancochea et al.*, 1994; *Carracedo*, 1994]. The small volume of the currently mobile landslide material, the limited subaqueous extent of the eastern rift zones [*Lénat et al.*, 1989b], and the existence of the northwest 'rift zone', suggest that most of the edifice of Fournaise is stable and currently behaves like an edifice with a welded basal boundary.

Marquesas volcanoes lack structural features indicative of a detached basal boundary

condition. Linear rift zones are not evident on the volcanoes of the Marquesas chain [*Filmer*, 1991; *Wolfe et al.*, 1994]. The flanks of most Marquesan volcanoes exhibit failure scarps that bound sector collapse events [*Filmer*, 1991; *Filmer et al.*, 1994]. These events are believed to occur catastrophically, and are thus analogues to the Hawaiian shallow catastrophic slides and not to the much larger, deeply rooted, slow-moving slumps. The inferred shallow nature of these structures, combined with the lack of evidence for associated rift zones, makes it unlikely that Marquesan volcanoes have the kind of basal detachment/rift zone system that regulates the growth of Hawaiian volcanoes. We conclude that Marquesas volcanoes exhibit a welded basal boundary condition.

Linear intrusive/eruptive features, termed "rift zones" by *Carracedo* [1994], are found on volcanoes in the Canary chain. The surface expressions of these structures are narrow ridges which are eruptive sources. Erosive exposures and tunnel excavations reveal complexes of dense parallel dike swarms that form the inner structure of the rifts *Carracedo* [1994]. The gravitational signal of dense dikes forming the rifts can also be traced (*MacFarlane and Ridley* [1968] and others cited in *Carracedo* [1994]). These rift zones are not direct analogues to Hawaiian-style rift zones, however; for example, they do not appear to be fed from a central shallow magma chamber/caldera system [*Carracedo*, 1994]. The Canary rift zones may play a role in triggering large mass wasting events. These large landslides leave arcuate or horseshoe-shaped valleys that are bounded at their heads by a rift zone. The presence of the linear rift zones and the accompanying landslides suggests behavior similar to that of detached-base Hawaiian volcanoes, rather than welded base Galápagos volcanoes. Further, the Canary volcanoes are clearly much larger than their counterparts in the Galápagos chain. However, a careful analysis of several lines of evidence leads us to believe that Canary volcanoes are influenced by a welded basal boundary condition. The large landslides are shallowly rooted in the upper subaqueous and subareal flanks; they do not extend to the base of the volcanic pile as do the Hawaiian flank slumps. Extensive studies of La Palma by *Staudigel and Schminke* [1984] and *Staudigel et al.* [1986] reveal

dikes oriented radially to centers near the Caldera de Taburiente. A growth scenario for La Palma outlined by *Ancochea et al.* [1994] emphasizes the importance of radial dikes in the early stages of edifice growth. This scenario is consistent with the important role that radial dikes play in our scenario of welded-base volcano growth. Extensive submarine deposits now exposed in an eroded section of La Palma (the "seamount series" of *Staudigel and Schminke* [1984]) demonstrate that substantial uplift has occurred (on the order of the thickness of the seamount series section, about 1800 m). These workers ascribe this uplift to voluminous sill intrusions. Edifice growth by sill intrusion is also an indication of welded base behavior. The Canary-Galápagos size difference is probably the result of a combination of factors. First, the lithosphere is thicker beneath the Canary Islands (see Table 3.1). Under our welded-base growth scenario, volcanoes on thicker lithosphere can grow to greater size. Second, the plate velocity relative to the hotspot is much smaller in the Canary Islands (Table 3.1). Canary volcanoes will therefore be supplied with material for a longer period of time, allowing the accumulation of a greater volume of material.

We suggest that the Canary Islands exhibit a mode of welded-base behavior slightly different from that of the Galápagos volcanoes. In particular, uplift appears to play an important role in the growth of Canary volcanoes. Uplift measured on some of the Canary islands is proposed to result from intrusion of sills into the upper regions of the edifices, but deeper components of uplift from underplating of buoyant material at the base of the crust or from one of the buoyant blobs of plume material proposed by *Hoernle and Schminke* [1993] may also contribute. Such deep uplift would counteract flexural subsidence and the accompanying horizontal compressive stress increments, facilitating growth. *Carracedo* [1994] proposed a scenario of deep magmatic uplift to initiate growth of rift zones in a Canarian volcano. Canary rift zones lack a mechanism for relief of intrusion-driven compression that a basal detachment provides to Hawaiian rift zones [*Dieterich*, 1988]. Uplift from a deep source would help to relieve this compression (shallow landslides headed by the rifts probably also contribute to stress relief). Deep uplift is likely to result in the three-armed rift

Characteristic	Chain		
	Hawaii	Galápagos	Canary
basal boundary condition	detached	welded	welded
growth mechanism	flank displacment and dike intrusion	magma chamber pressurization and sill/dike intrusion	uplift and rift intrusion/eruption
Surface manifestation	rift zone (narrow)	fissure cluster	rift zone (narrow)
linear feature configuration	double linear (triple uncommon)	double or triple	single or triple (stellate) (double not observed)
orientation (control of)	stress in older shields	contemporaneous adjacent shields	stress in lithosphere
orientation (direction)	away from other summits	toward other summits	no clear relation to other volcanoes
characteristic depth	shallow and deep	shallow only	shallow and deep (?)
volcano spacing	detachment quality	lithosphere thickness [*ten Brink*, 1991]	blob spacing ? [*Hoernle and Schminke*, 1993]

Table 3.6: Interpretation of linear intrusive/eruptive features on large volcanoes.

structure observed on some of the Canary Islands [*Carracedo*, 1994], in accord with the scenario proposed by *Wyss* [1980]. The formation of rifts will be influenced by inhomogeneities and stress variations in the lithosphere, such that certain rift orientations will be favored. The growth of La Palma may provide an example of this process; in early stages of growth, the island exhibited an axisymmetric distribution of radial dikes [*Ancochea et al.*, 1994]. Later, dikes became more concentrated in the southerly direction, eventually resulting in the construction of the linear southern shield of La Palma around a prominent N-S oriented rift zone [*Ancochea et al.*, 1994; *Carracedo*, 1994].

We summarize our interpretations of linear intrusive and eruptive features characteristic of three volcanic island chains in Table 3.6. The first two columns refer to the Hawaiian and Galapagos chains, and are basically consistent with the scenarios detailed above for the evolution and growth of basally detached and basally welded volcanoes, respectively. The third column describes the linear intrusive/eruptive features, termed "rift zones" by *Carracedo* [1994], found on volcanoes in the Canary chain. These volcanoes appear to be basally welded, but influenced by uplift. We discuss controls on feature orientation and

volcano spacing in the following sections.

Origin and development of Hawaiian-style rift zones

The classic paper by *Fiske and Jackson* [1972] outlined the processes that drive the formation of rift zones on the large Hawaiian volcanoes. They modeled the development of rift zones with gelatin models of a ridge with a triangular-cross-section, resting on a flat, rigid base. Deformation of the ridge due to gravity loading induced horizontal tensional stresses in the flanks that enabled the emplacement of vertical dikes parallel to the trend of the ridge. *Dieterich* [1988], however, pointed out that these models used unrealistic values of flank slope and Poisson's ratio. Further, models with realistic values of those parameters could not produce the configuration of stresses that restrict dikes to the rift zone ('dike-trapping stresses' [*Dieterich*, 1988]). In planar volcanic wedges with realistic values of flank slope and Poisson's ratio, basal slip is required to generate dike-trapping stresses at the rift axis [*Dieterich*, 1988].

The results of the edifice models presented above demonstrate that for volcanoes subject to lithospheric flexure, a basal detachment is necessary to produce principal stress orientations favorable to rift zone formation. In the absence of a detachment, flexurally-induced compression of the upper lithosphere is transmitted to the edifice, and horizontal compressive principal stresses inhibit rift zone formation. The state of horizontal principal extension in the models of *Fiske and Jackson* [1972] is a consequence of the rigid substrate supporting the volcano without deflection. Thus, the gelatin models of *Fiske and Jackson* [1972] are not realistic models of Hawaiian volcanoes. The scenario proposed by *Fiske and Jackson* [1972] for the control of the orientation of rift zones on young shields by the topography of older shields may, however, apply to the evolution of basally-detached volcanoes subject to flexure. They noted that Hawaiian volcanoes frequently commence eruption on the flanks of older volcanoes. They proposed that rift-parallel extensional stresses in the older edifice influenced the orientation of dikes in the younger one, causing the nascent rift zone to parallel

the already established one. This idea can be applied to the results of our models, yielding a scenario for rift zone propagation in basally detached volcanoes subject to flexure.

The earliest stages in the development of an edifice are likely to be characterized by axisymmetry. The principal stress orientations in a basally detached axisymmetric edifice (Figures 11, 14; $\sigma_3 = \sigma_{\theta\theta}$) favor formation of radial dikes or rifts. These rifts are likely to extend along the full radial extent of the edifice. If the young edifice is emplaced on the flanks of an older edifice, the stress state will be influenced by the stress state in the older edifice plus the effects of the slope of the older edifice. A pre-existing slope is likely to add a component of extensional stress perpendicular to the slope direction. The superposition of slope-related stresses with the basally-detached edifice stresses results in enhanced extension perpendicular to the surface slope direction, and inhibited extension parallel to it [*McGovern and Solomon*, 1993]. Therefore, rift orientations perpendicular to the topographic slope (parallel to the rifts on the older volcano) will be encouraged, and rifts with other orientations will be inhibited [*McGovern and Solomon*, 1993].

As the slope-perpendicular rifts grow, the geometry of the volcano will shift from axisymmetric to more planar (plane-strain). Principal stresses in a basally-detached volcano in plane strain exhibit principal horizontal extension, except that $\sigma_3 = \sigma_{xx}$ (Figure 14), the normal stress in the horizontal coordinate, in contrast to the axisymmetric case. This stress state favors intrusion of dikes parallel to the growing rift axis of the young volcano. Dike propagation along the horizontal coordinate x is inhibited; assuming the magma source remains fixed with respect to the edifice axis, dikes will remain near the crest of the ridge (the rift zone). Failure is predicted in the lower flanks of a planar wedge edifice (Figure 14). In distal regions, this failure will probably take the form of listric normal faulting [see *Lipman et al.*, 1985, for example], without associated magmatism, because magma propagation paths are restricted to the vicinity of the mantle magma source, presumably beneath the summit. The edifice then continues to grow in a plane-strain geometry. Eventually, as plate motion drags the edifice away from the hotspot axis, a new magma source will emerge beneath the

lower flanks. The stress state in the lower flanks of the wedge easily accommodates the formation of a new magma conduit, which will start the growth of another new edifice. The above cycle then repeats itself. We conclude that a modified version of the scenario proposed by *Fiske and Jackson* [1972] for the development of Hawaiian rift zones applies to volcanoes subject to lithospheric flexure that exhibit a detached basal boundary condition. Our models support their idea that stresses in young edifices are influenced by stresses in the underlying flanks of older edifices. Our models describe a more realistic way to generate these structures than the gelatin analogue models of *Fiske and Jackson* [1972].

The deep normal faulting predicted in the detached-base, plane-strain volcano models will strongly influence the tectonics of the mid-to-lower flanks of such volcanoes. Displacments on normal faults at the base of the edifice will presumably transmit stress to the part of the flank directly above it. Such a process could lead to propagation of normal faults to the surface. Throughgoing faults would likely dip steeply near the surface, but flatten out at depth to accommodate basal slip, merging into the basal detachment in a listric geometry. Such a geometry was proposed by *Lipman et al.* [1985] for the structure of the Hilina fault system on the south flank of Kilauea. The depth of the zone of predicted normal faults in our models is consistent with the depth extent of the Hilina faults as visualized by *Lipman et al.* [1985].

Nature of the Crustal Surface: Foundation of Oceanic Volcanoes

Roughness of crustal surface

Given the relation between r.m.s. roughness and spreading rate (e.g., Table 3.3), and knowledge of the spreading rate at time of formation of the crust supporting large volcanoes (Table 3.1), we can predict the roughness of the interface between crust and edifice. Spreading rates were low on the Mid-Atlantic Ridge when the crust supporting the Canary Islands was formed (full spreading rate about 20 mm/yr [*Larson and Pitman III*, 1972]). We then

expect that the Canary Islands are situated on rough topography. Indeed, volcanoes in the entire North Atlantic Basin would be expected to exhibit large amplitude basement relief ($H \approx$ 150–250 m [*Goff*, 1991]). Spreading rates in the Pacific are characteristically greater than those in the Atlantic. Therefore, basal topography of crust formed at the East Pacific Rise is predicted to be small ($H \approx$ 50–100 m [*Goff*, 1991]). Both the Hawaiian and Marquesan chains should therefore be underlain by basement topography of small amplitude and wavelength. Spreading rate is somewhat lower at the Cocos-Nazca spreading ridge (Table 3.1), so basal topography beneath the Galápagos Islands will be somewhat greater than at the other Pacific chains. Based on paleomagnetic reconstructions of plate history in the southwest Indian Ocean [*Schlich*, 1982], the island of Réunion is believed to reside at the crest of an extinct spreading ridge. The spreading rate of this ridge is believed to have been about 90 mm/yr [*Schlich*, 1982], a figure which yields a prediction of low-amplitude basal topography (see Table 3.3).

Basal sediments: effects of composition and thickness

Given the constraints on sediment thickness and composition and topographic roughness discussed above, we can now predict which volcanic chains should exhibit evidence of a basally detached boundary condition. Such behavior is most likely to be found in regions with a thick clay layer and comparatively smooth (low-amplitude) basement topography. Table 3.7 summarizes these predictions.

In the Canary and Galápagos chains, predicted high amplitude abyssal hill topography (Table 3.3) and the lack of a thick clay layer make a welded basal boundary condition likely, and no evidence of basally detached behavior is observed. We note that the sediment productivity in the waters around the Galápagos Islands is very high, such that hundreds of meters of sediments can accumulate even on young ($\approx$ 10 Ma) crust. In fact, the thickness of the sediment layer in holes drilled near the Galápagos Islands is similar to that on the much older crust in the vicinity of the Hawaiian Islands, and significantly larger than that at sites

	Inferred basal topography	Thick clay layer?	Basally detached behavior	
			predicted	inferred
Canary	rough	no	no	no
Galápagos	rough	no	no	no
Hawaiian	smooth	yes	yes	yes
Marquesas	smooth	no	no	no
Réunion	smooth	probably	probably	yes, decreasing with time

Table 3.7: Predicted basal behavior

near the Marquesas Islands [*Shipboard Scientific Party*, 1983]. The Galápagos sediments are dominantly calcareous and siliceous oozes, which form high-permeability rocks (like chalks) when compressed. These rocks are unlikely to sustain high pore pressures required for the formation of a decollement. Thus, despite the thickness of this inferred basal sediment layer, the Galápagos Islands constitute a good example of a large welded-base volcano. *Nakamura* [1980] proposed that a paucity of sediments at the base of Galápagos volcanoes prevents basal slip required to accommodate rift zone formation. We support a modified version of this hypothesis. Fine-grained abyssal clay sediments are required to form a low permeability layer that allows buildup of high pore pressures which facilitate decollement formation. By this view, it is the paucity of abyssal clay sediments, not of pelagic sediments in general, that prevents the formation of a decollement beneath the Galápagos volcanoes.

The Marquesas Islands were emplaced on crust formed at a moderately fast spreading ridge; abyssal hill topography should be low in amplitude, not presenting insurmountable obstacles to basal detachment formation. The lack of a thick clay layer in the sediments near the Marquesas, however, makes it unlikely that a decollement will form. This prediction is consistent with the absence of characteristic basally-detached features like well-developed

rift zones on the Marquesas volcanoes.

The situation at Réunion is more complex. The composition of surface sediments is variable [*Kolla and Kidd*, 1982], and so presumably is the composition of the deeper sediments. Evidence from the closest Deep Sea Drilling site [*Shipboard Scientific Party*, 1972] suggests that abyssal clay layers with thickness sufficient to support a decollement layer may be present beneath Réunion. Given the low amplitude basal topography predicted by a high spreading rate at the fossil ridge beneath Réunion [*Schlich*, 1982], basally detached behavior should be possible. Such behavior is predicted to have taken place at about 1.8 Ma in the largest of a series of collapse events that have increased in frequency while decreasing in magnitude [*Gillot et al.*, 1994] and collapse basal depth. The decrease in size and depth of such activity may indicate the depletion or exhaustion of a thin or discontinuous clay layer at the base of Réunion, a layer that no longer functions as a decollement.

Among the volcanoes we have discussed in this chapter, the volcanoes of the Hawaiian chain are unique in exhibiting well-defined and long-lived structrual features indicative of a detached basal boundary condition (and are probably unique among all large subaereally-exposed oceanic volcanoes). Both the topographic and sedimentary characteristics of the basement crust near Hawaii are unambiguously conducive to the formation of a basal decollement, the only chain listed in Table 3.7 for which this is so. The uncertain and possibly variable nature of basal clay layers at Réunion seems to be consistent with the evidence for limited detachment activity. The absence of clay sediments at the Canary, Galápagos and Marquesas chains is consistent with the lack of evidence at those chains for basally detached behavior. We thus conclude that the character of oceanic basement is a useful predictor of volcano characteristics.

The effect of basal conditions on rift zone orientation

The amplitude of abyssal hill topography at the base of Hawaiian volcanoes may be insufficient to inhibit basal detachment motion, but may still influence the orientation of

structural features such as rift zones. In the early stages of growth of a basally detached, initially axisymmetric volcano, slip along the decollement produces a stress field conducive to the formation of radial dikes. In order for the volcano to maintain its axisymmetric form, radial intrusions must be equally distributed in azimuth. Any condition that favors the growth of these dikes along certain azimuths and inhibits growth along others will favor a gradual transformation to a more linear geometry, as exemplified by the linear rift zones of the Hawaiian Islands. As discussed above, the scenario proposed by *Fiske and Jackson* [1972] for control of rift zone orientation explains well the observed orientations of rift zones of volcanoes emplaced on the flank of an older neighbor. These workers divided Hawaiian volcanoes into two groups: those which formed on the flanks of older shields (the "clustered" group: Mauna Kea, Mauna Loa, Kilauea, Haleakala, Kahoolawe, Lanai, East Molokai, and Koolau), and those which developed in relative isolation (the "isolated" group: Hualalai, Kohala, West Maui, West Molokai, Waianae, and Kauai). Rift zones on these volcanoes are shown in Figure 20a (a reproduction of Figure 15 in *Fiske and Jackson* [1972]). When rift zone orientations are plotted by group (Figure 16 in *Fiske and Jackson* [1972], reproduced here as Figure 20b), those in the clustered group exhibit a wide range of azimuths, reflecting the influence of local topography and stress fields on these edifices. The isolated group show a much more restricted range of azimuths: *Fiske and Jackson* [1972] attributed the mean trend of these rift zones to the influence of regional stresses oriented along the trend of the entire archipelago (the dashed line in Figure 20b). In Figure 20b we plot the trend of the Molokai Fracure Zone: the abyssal hill trend is presumably perpendicular to the fracture zone. We observe that 11 of the 13 plotted rift zone trends fall in the $\approx 60°$ range between those of the archipelago and the abyssal hills. Only two rift zones in the "isolated" group have azimuths outside that range. Both of these "outlier" rifts belong to West Molokai volcano, which rests above, and is most likely to be influenced by, the trend of the Molokai Fracure Zone. The trend of these two rift zones is similar to that of the Molokai Fracture Zone. Thus, all "isolated" rifts not influenced by the Molokai Fracture Zone have orienta-

tions between those of the archipelago trend and the abyssal hill trend. We therefore suggest that the fabric of the abyssal hill topography also plays an important role in determining rift zone orientations in isolated shields. The interaction between regional-scale stresses induced by the linear geometry of the chain and local stresses from topographic variation encourages formation of rift zones with orientations intermediate to the two trends.

The orientation of rift zones on the young submerged edifice Loihi [*Malahoff*, 1987] is nearly parallel to the abyssal hill trend. Of course, the rift orientations of Loihi are probably influenced by the nearly north-south orientation of the southwest rift zone of Mauna Loa (although the submarine portion of this zone takes a more southwesterly trend). It is likely, however, that abyssal hill fabric will have more influence on younger, smaller volcanoes like Loihi. As such a volcano grows, it may begin to "feel" other influences, such as the topography of older volcanoes. These other influences may re-orient the rift zones, thus obscuring the effect of the basement topography.

Thurber et al. [1989] suggested that variations in the thickness of the basal low velocity layer (interpreted as the sedimentary detachment layer) could influence the stress state in the flanks of Mauna Loa. Our models demonstrate that the stress state dramatically influences the growth and development of volcanic edifices. We therefore expand the idea of *Thurber et al.* [1989] by suggesting that small-scale variations in basal topography and sediment cover influence the development of large hotspot volcanoes. Complexities in ridge geometry, such as propagating ridges or microplates, may change the conditions governing the formation abyssal hills, thus altering their characteristic height or spacing, or perhaps inhibiting their formation. Topographic variations may alter the pattern of bottom currents which affect sediment deposition or erosion. Variations in sediment thickness that reduce abyssal hill height or increase the thickness of clay layers in a given area will promote the formation of a large, basally detached edifice. Variations that increase abyssal hill height or decrease the thickness of clay layers will inhibit the formation of large, basally detached edifices, or perhaps result in formation of a small, basally welded edifice which will eventually be

engulfed by the subsequent growth of a basally detached edifice. Variations in sediment composition that decrease the integrity of clay layers (dilution of clays in biogenic oozes, for example), may have a similar growth-inhibiting effect. Thus, the spacing of basally detached volcanoes in a linear chain may depend on topographic and sedimentary conditions on the surface of the igneous crust.

Mahukona volcano [*Moore and Campbell*, 1987; *Garcia et al.*, 1990] may provide an example of the influence of basal boundary condition on volcano evolution. Mahukona is a small submerged volcano that fills a gap in one of the paired "tracks" of volcanoes that form the youngest Hawaiian Islands (the western track, which includes in order of descending age Molokai, Lanai, Kahoolawe, Mahukona, Hualalai, Mauna Loa, and Loihi). *Jackson et al.* [1972] pointed out the gap in the otherwise quite evenly spaced progression of the western track, and suggested the presence of a small volcano in the gap. Improved bathymetry [*Campbell*, 1987; *Garcia et al.*, 1990] allowed identification of a distinct seamount that Garcia and coworkers believe to be the summit of Mahukona (although *Clague and Moore* [1991] dispute this). *Garcia et al.* [1990] claim that 5-6 linear ridges emanating from the proposed summit are rift zones. Evidence from dredged rocks suggests that either Mahukona never grew tall enough to erupt subaereally [*Garcia et al.*, 1990; *Garcia and Kurz*, 1991] or only erupted a few hundred meters subaereally [*Clague and Moore*, 1991]. Explanations for the anomalously small size of Mahukona invoke variations in the strength of the underlying plume [*Garcia et al.*, 1990]. We propose that the basal boundary condition may also have played a role. Mahukona may have been emplaced on crust with rougher surface topography or a thinner clay layer than other Hawaiian volcanoes. A less efficient detachment surface would cause the edifice to behave more like a basally welded volcano. Horizontal compressive stresses, increasing with volcano size, would inhibit magma ascent to the summit region, eventually shutting down edifice construction. Such a scenario is consistent with the stunted development of the proposed Mahukona rifts when compared with those on larger Hawaiian volcanoes [*Clague and Moore*, 1991]. Conversely, areas with especially favorable detachment

conditions may experience the growth of larger than normal volcanoes (for a given plume strength). Thus, the apparently anomalously high erupted volume for the Hualalai to Kilauea segment of the Hawaiian-Emperor chain [*Clague and Dalrymple*, 1987] may partially reflect more favorable detachment conditions. When the plume track crossed the Molokai Fracture Zone, the age of the crust increased by about 15 My. Older crust will have had more time to accumulate abyssal clays; therefore, detachment conditions will tend to be more favored on the older crust, and volcano growth will be facilitated.

Volcanoes emplaced in regions lacking a thick clay layer may not exhibit the influence of abyssal hill orientation at their bases. *Filmer* [1991] analyzed the alignments of seafloor and seamount linear features in the vicintity of the Marquesas chain. He found no evidence that the alignment of seamount axes or rift zones was correlated with the direction of seafloor lineations, for seamounts greater than 500 m in height. The major axes of large volcanoes were included in this study, but rift zones were not included because none were found on these volcanoes [*Filmer*, 1991]. Assuming the Marquesas volcanoes have a welded basal boundary condition (consistent with the lack of clay sediments and absence of rift zones), the results of our models suggest that edifice growth will be regulated by a near-summit magma chamber. Magma-chamber-related stresses will be the dominant control on the emplacement and orientations of radial dikes. Without basal slip, there is no preferred orientation of these dikes; thus axisymmetric geometry is retained.

Our survey of sediment composition at several volcanic chains leads us to the conclusion that a layer of fine-grained clay sediments is required for the formation of a basal decollement between edifice and crust. This clay layer would be compacted beneath the weight of volcanic edifice to form a low-porosity shale (and perhaps metamorphosed by high temperatures near the magma conduit and intrusive complex [*Borgia and Treves*, 1992; *Clague and Denlinger*, 1994] to form slate). It would be possible to test this hypothesis by obtaining samples from the edifice-crust boundary region of a volcano possessing rift zones. Core samples returned from the the 1 km deep drill site of the Hawaii Scientific Drilling Project (HSDP)

are currently being analyzed [*Hawaii Scientific Drilling Project*, 1995]. Future extension of the Hilo hole to a depth of 4.5 km, near the base of the volcanic pile, is planned [*Hawaii Scientific Drilling Project*, 1995]. A similar drill hole 3 km deep has been drilled in the Grand Brule depression on the eastern flank of Piton de la Fournaise on Réunion [*Rançon et al.*, 1989]. Extension of these holes to the edifice-crust boundary would be an important test of the detachment hypothesis. Positioning drill core sites on the distal subaqueous flanks of these volcanoes, where the volcanic pile is thin, may be a useful alternative. *Borgia and Treves* [1992] suggested that large basally detached volcanoes like those of Hawaii would leave fossil remains that greatly resembled ophiolite complexes. They speculated that ophiolitic complexes in eastern Kamchatka could represent accreted fragments of the oldest islands in the Hawaiian-Emperor chain. If a given ophiolite complex includes the remains of an ancient basally detached volcano, we would expect to find a layer of shale or slate at the base of the volcanic pile.

The requirement of a thick abyssal clay layer for volcanic detachment places strong constraints on the location and crustal/lithospheric age of detached volcanoes. Abyssal clays are deposited at very low rates and are subject to erosion by deep currents. Deposition of calcareous and siliceous biosediments occurs at much faster rates; the much more slowly accumulating clay particles will tend to be assimilated into the biogenic sediment layers. Thus, accumulation of a thick, coherent clay layer requires tens of millions of years of accumulation, undisturbed by erosion or assimilation. At present, perhaps 30% of the oceanic crustal surface is collecting abyssal clay sediment exclusively; much of this area is in the northeast Pacific Basin [*Barron and Whitman*, 1981]. Most of the remaining seafloor is characterized by deposition of calcareous or siliceous biogenic sediments [*Barron and Whitman*, 1981]. Assuming such a pattern is typical of the paleo-distribution of sediments, the formation of basally detached volcanoes is restricted to a fraction of the Earth's oceanic crustal surface. This restriction may explain the uniqueness of the Hawaiian volcanoes as the most well-developed basally detached oceanic hotspot volcanoes.

Magma chambers in basally welded and detached volcanoes

The state of stress in a basally welded model volcano is characterized by horizontal compression: $\sigma_1 \approx \sigma_{rr}$, with $\sigma_{\theta\theta}$ slightly less compressive than σ_1 and the least compressive principal stress σ_3 nearly vertical. Intrusions are expected to propagate in a direction perpendicular to σ_3. In basally welded edifices, presuming magma supply to the base of the volcano, the stress state predicts intrusion of slightly outward-dipping sills. Such intrusions are not likely to penetrate very far in radius or to erupt (although *Cullen et al.* [1987] cite evidence for two such occurrences in the Galápagos Islands this century). Magma ascent to near summit regions, where summit eruptions and radial dikes originate, is blocked. As proposed above, the early formation of a central magma conduit and shallow sub-summit magma chamber will allow modification of the stress state by pressurization of the magma chamber and outward displacment of the surrounding flanks. The importance of such chambers is suggested by the large size of summit calderae on the western Galápagos volcanoes. Summit calderae are depressions resulting from subsidence following withdrawal of material from the underlying magma chamber. The caldera radii of Hawaiian and Galápagos volcanoes are similar. The ratio of caldera radius to edifice radius, however, is quite large for the Galápagos shields, much larger than for a basally detached volcano like Mauna Loa. Presumably the ratios of magma chamber volume to edifice volume behave similarly. The difference in ratios suggests the relative importance of the summit magma chamber in driving lateral growth. The basally detached Hawaiian volcano's growth is modulated by rift zone dike emplacement and relaxation of stress by flank movement; the relative contribution of the magma chamber is small, mostly serving as a storage area before intrusion into the rifts. The basally welded Galápagos volcano requires a large increment of horizontal extension to allow magma ascent to the surface. In such a volcano, radial expansion from magma chamber pressurization provides this stress perturbation, allowing summit eruptions and intrusion of radial dikes. The magma chamber thus dominates the lateral transport of material in these edifices. We conclude that the establishment of a shallow axial magma chamber is a critical requirement

for the sustained growth of a volcano with a welded basal boundary condition.

In basally detached volcanoes, the summit magma chamber does not play the critical role in sustaining growth that it does in welded-base volcanoes. The lower ratio of caldera to edifice radii for detached-base as compared to welded-base volcanoes supports this conclusion. The importance of magma chamber-related stresses in allowing growth is probably proportional to the degree of ease of motion along the basal weak zone. The Hawaiian basal faults have finite fault friction, so the volcanoes exhibit behavior between the idealized cases of 'welded' and 'detached' (but much closer to 'detached'). Horizontal compression from loading and dike intrusions builds up, but is relieved in large earthquakes [*Dieterich*, 1988; *Wyss and Koyanagi*, 1992]. *Rubin* [1990] suggested that the high magma supply rate to the Kilauea chamber plays a role in driving intrusions into the rift zones before relaxation of stresses from earlier intrusions occurs. We propose that magma chamber pressures enable radial dike intrusions in sectors of large Hawaiian volcanoes, such as the northern flank of Mauna Loa [*Lockwood and Lipman*, 1987], that act like basally welded volcanoes due to cessation of motion along the basal detachment. Locking of the detachment may be caused by buttressing by younger shields, dewatering of the detachment, and cooling of a deep ductile dunite core [*Clague and Denlinger*, 1994].

Lithosphere thickness and volcano size

Many have suggested that the thickness of the lithosphere controls the size of volcanoes. Such arguments commonly are based on an assumed isostatic balance in a magma column reaching from a zone of partial melt at the base of the lithosphere, through the lithosphere and crust, to the top of the edifice [*Eaton and Murata*, 1960; *Vogt*, 1974a; *Epp*, 1984]. Given the thicknesses and densities of mantle lithosphere, crust, sediment, and ocean layers, and a magma density, the height of a magma column in isostatic balance with the surrounding layers (termed the "isostatic height" by *Epp* [1984]) defines the predicted maximum height of a volcano. *Wilson et al.* [1992] describe flaws in such arguments. Most critically, magma

ascent occurs in discrete batches [e.g., *Ryan*, 1988], not in a continuously connected conduit as required in the isostatic arguments. Also, such models implicitly assume that magma erupting at the summit is positively buoyant. Ascending magma is commonly observed to stall and collect at a level of neutral buoyancy (for example in Hawaii, Iceland, and elsewhere, as summarized by *Ryan* [1994]). Further ascent of magma into regions of less dense country rock (i.e., regions of negative buoyancy) may be driven by pressure from volatile exsolution, or by the vertical growth of a horizontally propagating dike that encounters an obstruction [*Ryan*, 1994].

We suggest a further, more basic objection to the isostatic height hypothesis: the volcanoes are compensated regionally, by lithospheric flexure, rather than locally, as assumed in the models of *Vogt* [1974a] and *Epp* [1984]. As shown in the models above, flexural subsidence induces stresses in a growing volcano. Basally welded volcanoes exhibit horizontal compressive stresses of magnitude inversely proportional to the elastic plate thickness T_e (Figure 19). A tradeoff between these stresses (which tend to inhibit edifice growth), and magma chamber pressurization stresses (which drive edifice growth) determines the size of basally welded volcanoes. In other words, lithospheric thickness governs volcano size by regulating the state of stress in the edifice. The relative sizes of volcanoes in the Galapagos (r = 50 km, T_e = 12 km) and Marquesas chains (r = 100 km, T_e = 18 km) is consistent with this scenario. In basally detached volcanoes, sustained growth is easily accommodated by cycles of rift zone intrusion and flank expansion. The stress state in a given basally detached volcano is influenced by the ease of slip on the decollement and by the stress state in older abutting edifices. Thus lithospheric properties are not a direct influence on the size of basally detached volcanoes. Basal detachments require the deposition of a abyssal clay layer of significant thickness [e.g., *Iverson*, 1995]. Because the rate of clay deposition is low, it may take tens of millions of years to accumulate sufficient thickness. Thus, only older crust (lithosphere) will exhibit large basally detached volcanoes; the large size may mistakenly be attributed to some inherent property of old lithosphere.

Conclusions

The models of volcano growth described above demonstrate the importance of the basal boundary condition in determining the characteristics and evolutionary path of a given volcano. Models of volcanoes that are welded to the underlying lithosphere exhibit near-horizontal principal compression ($\sigma_1 \approx \sigma_{rr}$), and elevated levels of differential stress in the edifice. This stress state is a consequence of flexural compression of the upper lithosphere, which is directly transmitted to the edifice through the welded base. Such a stress state would tend to suppress the formation of radial rift zones, favoring only sub-horizontal intrusions at depth (perhaps leading to flank eruptions, but no well-defined rifts). Horizontal compression due to volcano growth tends to suppress magma ascent to near-surface regions, thus limiting volcano growth. These stresses are offset by magma chamber expansion from pressurization and thermoelastic effects. Volcano size may be regulated by a tradeoff between T_e, magma supply rate, and plate velocity. The axial magma chamber regulates the lateral movement of magma in the edifice; eruptions from the summit caldera and from radial fissures make up a large part of edifices with welded bases. These radial fissures are manifestations of dikes which preferentially intrude the uppermost (youngest) layers of the edifice. Radial fissures align into zones connecting adjacent calderae, influenced by magma chamber pressurization and possibly regional stresses; these shallow zones are not analogues to Hawaiian style rift zones. Therefore the ratio of extrusive to intrusive material is likely higher than for basally detached rift-intrusion dominated volcanoes like Hawaiian ones. *Nakamura* [1980] proposed that the absence of basal sediments prevents formation of a detachment beneath Galápagos volcanoes. A substantial thickness of basal sediments likely exists, however. We support a modified version of the hypothesis of *Nakamura* [1980]: the lack of a thick abyssal clay layer in the sediments on the young crust at the Galápagos Islands may account for the absence of detachments beneath, and thus well-defined rift zones on, these shields. The stress state for the welded models (Galápagos analogue) inhibits rift zone formation, whereas that for the detached models (Hawaiian analogue) encourages it. The smaller size of the Galápagos

shields is also consistent with the choking effect of edifice stresses in the welded models, an effect which is greater for younger and thus thinner mechanical lithosphere.

This behavior is in contrast to models that include a detachment, which are characterized by vertical principal compression ($\sigma_1 \approx \sigma_{zz}$) near the volcano base and relatively low values of differential stress in the edifice. Flexural stresses in the upper lithosphere are not transmitted to the edifice (or poorly transmitted, with periodic relief in large earthquakes, for basal detachments with finite frictional resistance). For these cases, radial extensional faults are predicted to form at the base of the edifice. Low differential stresses in the upper edifice could allow these faults to propagate up into the flanks, favoring the formation of linear rift zones. Intrusion of dikes into the rift zones is the major mode of detached-base volcano growth; the ratio of extrusive to intrusive material in such an edifice is small. Magma ascent to near-summit regions is easily accommodated, and large edifices are easily formed. The models with a detachment are regarded as appropriate to young volcanoes on intermediate-age oceanic crust, which likely has accumulated sufficent sediment to form a decollement.

The basal boundary condition is thus a primary influence on the structural evolution of large hotspot volcanoes. Of the chains we have studied, conditions conducive to the formation of a basal decollement exist at only two locations, the Hawaiian chain and Réunion. Conditions at Réunion may have changed over time, such that mobility of the flanks has decreased. Other chains (Galápagos, Marquesas, Canary) lack one or more of the required conditions for decollement formation, and therefore produce volcanoes exhibiting welded-base behavior. Regional variations in basal conditions may control the size and spacing of volcanoes in a chain: sites with a thick clay layer and small-amplitude abyssal hill topography will tend to develop large edifices exhibiting detached-base characteristics, whereas areas with discontinuites in the clay layer or locally rough basement topography will develop smaller, isolated edifices indicative of a welded basal boundary condition. Basal conditions also change with time in individual edifices. Large edifices that grew to maturity in a detached mode may experience a welded boundary condition in the final stages of development,

because of buttressing by other shields (as with Mauna Loa), or due to depletion or thinning of the basal clay layer (as we suggest was the case at Réunion). In such cases, the final stages of edifice development will exhibit welded-base characteristics. In summary, conditions at the interface between a volcanic edifice and the underlying crust influence the development of large volcanoes at several scales. Variations in basal conditions control differences in characteristic style between chains at the largest scale, the size and spacing of volcanoes in a chain on a regional scale, and the characteristic stages of development at the scale of an individual volcano.

FIGURE CAPTIONS

Figure 1. Map of the southeastern Islands of the Hawaiian chain. Bathymetric contours in km. Dashed line marks axis of the Hawaiian Deep trough. From *Moore* [1987] (Figure 1).

Figure 2. Map of the Galápagos Islands, adapted from a map published by Libreria Internacional, Quito, Ecuador, by *Rowland et al.* [1994]. Subaerial contours are at 50 m and then multiples of 200 m; submarine contours (dashed) are at 100 m and then multiples of 1000 m.

Figure 3. Bathymetric map of the Marquesas Islands: 500 m contour interval in Mercator projection. Bathymetry is combined from French bathymetric charts, the Digital Bathymetric Data Base 5 (DBDB5), and profiles from cruise EW 91-03 of the R/V *Maurice Ewing* [*Wolfe et al.*, 1994]. Figure 1 of *Wolfe et al.* [1994].

Figure 4. Bathymetric and topographic map of the Canary Islands (figure 1 of *Watts* [1994]. H = El Hierro, LP = La Palma, G = La Gomera, T = Tenerife, GC = Gran Canaria, F = Fuerteventura, and L = Lanzarote. Thick dashed line shows trace of Canary Island hotspot according to *Holik and Rabinowitz* [1992].

Figure 5. Bathymetric and topographic map of the Island of Réunion, from *Lénat et al.* [1989b] (Figure 1). The volcanic edifices Piton des Neiges and Piton de la Fournaise are labeled. A representative topographic cross-sectional profile across the island is shown below the map.

Figure 6. (a) Finite element grid for the "Galápagos" family of models. The volcanic edifice is the small triangular area in the upper left-hand corner. (b) Elements of the volcanic edifice from Figure 6a. The first element in each diagonal row of elements is labeled. One or more rows constitute a load increment: these increments are described in Table 3.5. (c) Edifice elements for the "Marquesas" family of models. Load increments use same element rows as in loading history 1 in Table 3.5. (d) Edifice elements for the "Hawaii" family of models. Load increments use same element rows as in loading history 1 in Table 3.5.

Figure 7. Key for stress symbols in Figures 9–10 and 12–18. These symbols denote the

principal stress directions under axisymmetry. The hourglass shapes are oriented along the direction of greatest compressive stress (σ_1), the bars along the direction of least compressive stress (σ_3). Circles are meant to represent the hourglass shapes turned on their sides, so that σ_1 is perpendicular to the $r-z$ plane. Predicted faulting types are based on the criteria of *Anderson* [1951]. Predicted intrusion types are based on the expectation that magma ascends locally along the plane orthogonal to the least compressive stress (perpendicular to the bar).

Figure 8. State of stress in an incrementally grown volcanic edifice ("Galápagos" model) emplaced on and welded to a 12-km-thick elastic lithosphere, 1000 Maxwell times after emplacement of the third, fourth, and fifth (final) load increments. Plots do not reflect deformation of the plate or volcano (stresses are plotted at the original undeformed element postitions, for simplicity). Vertical exaggeration 3:1 (a-c) Principal stress orientations and predicted failure. Elements in which stresses exceed the Mohr-Coulomb failure envelope are shaded. Given the orientation of the stress symbol in a shaded element, the style and orientation of faulting can be inferred. See Figure 7 for the meaning of the stress orientation symbols. (d-f) Contours of maximum shear stress (difference between σ_1 and σ_3) in the vicinity of the volcano. See (a-c) to determine the corresponding directions of σ_1 and σ_3. Contour interval is 50 MPa. (g-i) Contours of proximity to failure, defined as the ratio of the maximum shear stress in an element to the shear stress required to satisfy the failure criterion. Values greater than 1.0 are set equal to 1.0. Contour plots (d-i) and subsequent similar plots produced by the GMT software package [*Wessel and Smith*, 1991].

Figure 9. State of stress in an incrementally grown volcanic edifice ("Galápagos" model) emplaced on and welded to a 20-km-thick elastic lithosphere, 1000 Maxwell times after emplacement of the final load increment. (a) Principal stress orientations and predicted failure. (b) Contours of maximum shear stress. (c) Contours of proximity to failure.

Figure 10. Hoop stress $\sigma_{\theta\theta}$ vs. height (in undeformed edifice) for the column of elements with centers at $r_c = 3$ km. The jagged lines connect the stresses for each element center; the

X symbols mark the average stress in a load increment, and the smooth curves interpolate the average stresses in the increments. (a) For small edifice (Figure 6b) with $T_e = 12$ km and nominal increment application. (b) as in (a) for $T_e = 20$ km. (c) For small edifice (Figure 6b) with $T_e = 12$ km and "equal volume" increment distribution. (d) as in (c) for $T_e = 20$ km.

Figure 11. State of stress in an incrementally grown volcanic edifice ("Galápagos" model) emplaced on a 12-km-thick elastic lithosphere, with a basal detachment between volcano and lithosphere, 1000 Maxwell times after emplacement of the final load increment. Slippery nodes [*Melosh and Williams*, 1989] allow fault slip along the entire interface between volcano and lithosphere ($z = 0$). (a) Principal stress orientations and predicted failure. (b) Contours of maximum shear stress. (c) Contours of proximity to failure.

Figure 12. State of stress in an incrementally grown volcanic edifice ("Marquesas" model) emplaced on and welded to a 20-km-thick elastic lithosphere, 1000 Maxwell times after emplacement of the final load increment. (a) Principal stress orientations and predicted failure. (b) Contours of maximum shear stress. (c) Contours of proximity to failure.

Figure 13. State of stress in an incrementally grown volcanic edifice ("Marquesas" model) emplaced on and welded to a 12-km-thick elastic lithosphere, 1000 Maxwell times after emplacement of the final load increment. (a) Principal stress orientations and predicted failure. (b) Contours of maximum shear stress. (c) Contours of proximity to failure.

Figure 14. State of stress in an incrementally grown volcanic edifice ("Hawaiian" model) emplaced on 32-km-thick elastic lithosphere, with a basal detachment between volcano and lithosphere, 1000 Maxwell times after emplacement of the third, fourth, and fifth (final) load increments. The detachment extends along the $z = 0$ km line from $r = 0$ km to $r = 120$ km. (a-c) Principal stress orientations and predicted failure. (d-f) Contours of maximum shear stress. (g-i) Contours of proximity to failure.

Figure 15. State of stress in an incrementally grown volcanic edifice ("Hawaiian" model) emplaced on and welded to a 32-km-thick elastic lithosphere, 1000 Maxwell times after emplacement of the final load increment. (a) Principal stress orientations and predicted

failure. (b) Contours of maximum shear stress. (c) Contours of proximity to failure.

Figure 16. State of stress in an incrementally grown volcanic edifice ("Hawaiian" model) in plane strain geometry, emplaced on 32-km-thick elastic lithosphere, with a basal detachment between volcano and lithosphere, 1000 Maxwell times after emplacement of the final load increment. (a) Principal stress orientations and predicted failure. (b) Contours of maximum shear stress. (c) Contours of proximity to failure.

Figure 17. Principal stress orientations in an edifice subjected to pressurization of a magma chamber. (a) Pressurization stresses only. A uniform pressure of 50 MPa is applied to elements marked with an asterisk. (b) Superposition of pressurization stress field depicted in (a) with flexurally-induced stress field depicted in Figures 8 c and f (T_e = 12 km). (c) Superposition of pressurization stresses depicted in (a) with flexurally-induced stress field depicted in Figures 9 a and b (T_e = 20 km).

Figure 18. As in Figure 17, for a different magma chamber configuration (pressurized elements marked with asterisks in Figure 18a).

Figure 19. Flexurally-induced stress vs. elastic plate thickness T_e in a four elements near the axis of an incrementally grown Galapagos-sized volcano (Figure 6b). Curves for each element are marked with approximate height z above base . (a) Radial normal stress σ_{rr} vs. T_e. (b) Hoop stress $\sigma_{\theta\theta}$ vs. T_e. (c) Maximum shear stress vs. T_e.

Figure 20. (a) Map showing the southeastern part of the Hawaiian chain, from *Fiske and Jackson* [1972], Figure 15. Thick lines represent the traces of rift zones. The six volcanoes shown in the stippled pattern grew as "isolated" edifices; the eight unstippled volcanoes grew later and were buttressed by the earlier-formed edifices. (b) Rose diagrams showing orientations of Hawaiian rift zone segments. Top diagram is for rifts of isolated volcanoes, bottom is for rifts of clustered volcanoes. The dashed line marks the overall trend of the Hawaiian Archipelago. Additional trend lines for the Molokai Fracture Zone and the predicted abyssal hill trend (perpendicular to the fracture zone) have been added to the top figure. Modified from *Fiske and Jackson* [1972], Figure 17.

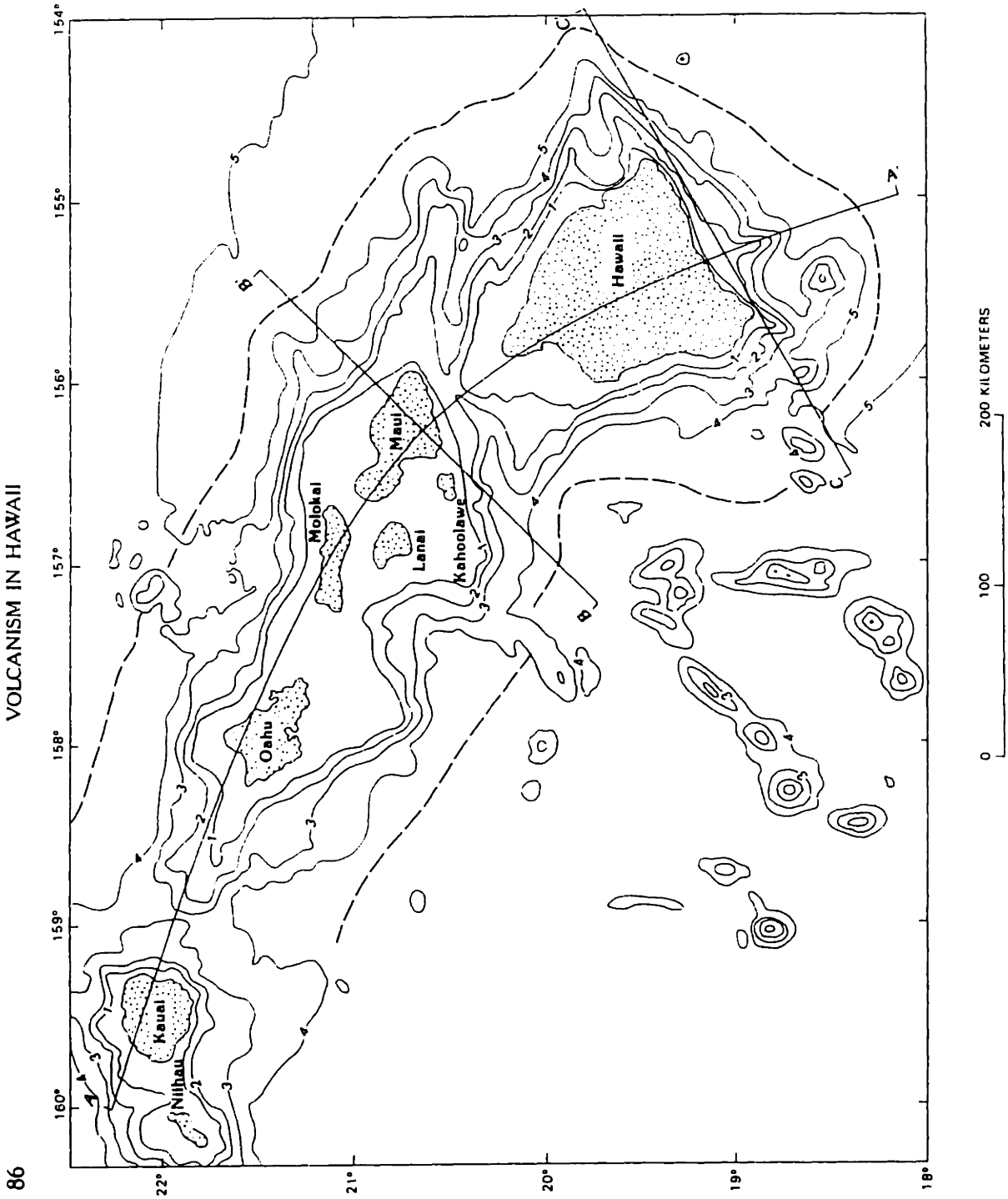
Kauai
Niihau
Oahu
Molokai
Lanai
Maui
Kahoolawe
Hawaii
A
A'
B
B'
C
C'
0
100
200 KILOMETERS
154°
155°
156°
157°
158°
159°
160°
22°
21°
20°
19°
18°

Figure 1.

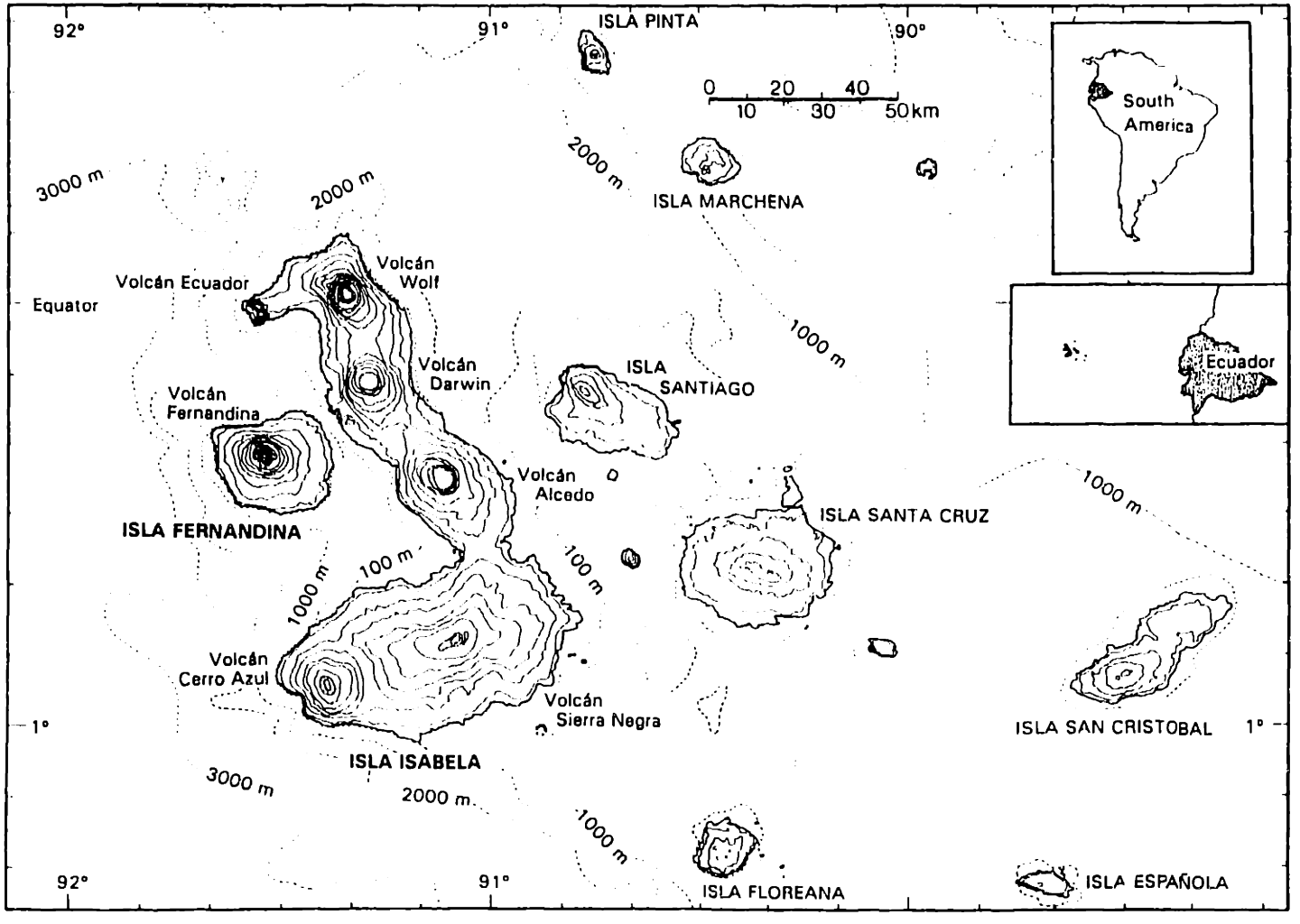

Fig. 1. Location map of the Galápagos islands (adapted from a map published by Libreria Internacional, Quito, Ecuador). Volcan Ecuador forms the northwest-most tip of Isla Isabela. Subaerial contours are at 50 m and then multiples of 200 m; submarine contours (*dashed*) are at 100 m and then multiples of 1000 m

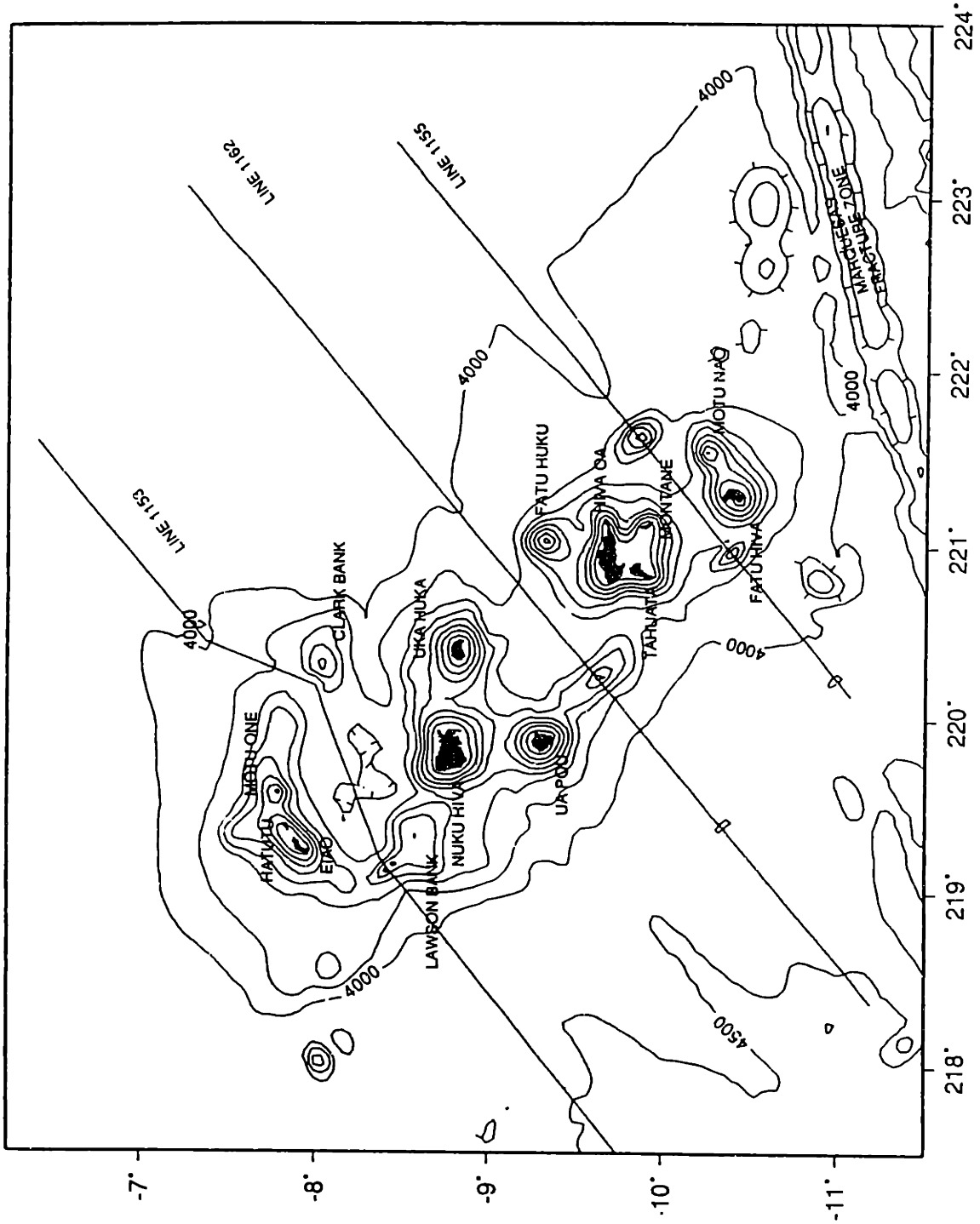
LINE 1153
LINE 1162
LINE 1155
4000
4500
CLARK BANK
HATUTU
EPAO
HOHU ONE
LAWSON BANK
NUKU HIVA
UA POU
OKA MUKA
FATU HUKU
HIVA OA
TAHUATA
MOTANE
MOTU NAO
FATU HIVA
MARQUESAS FRACTURE ZONE
-7°
-8°
-9°
-10°
-11°
218°
219°
220°
221°
222°
223°
224°

Figure 3.

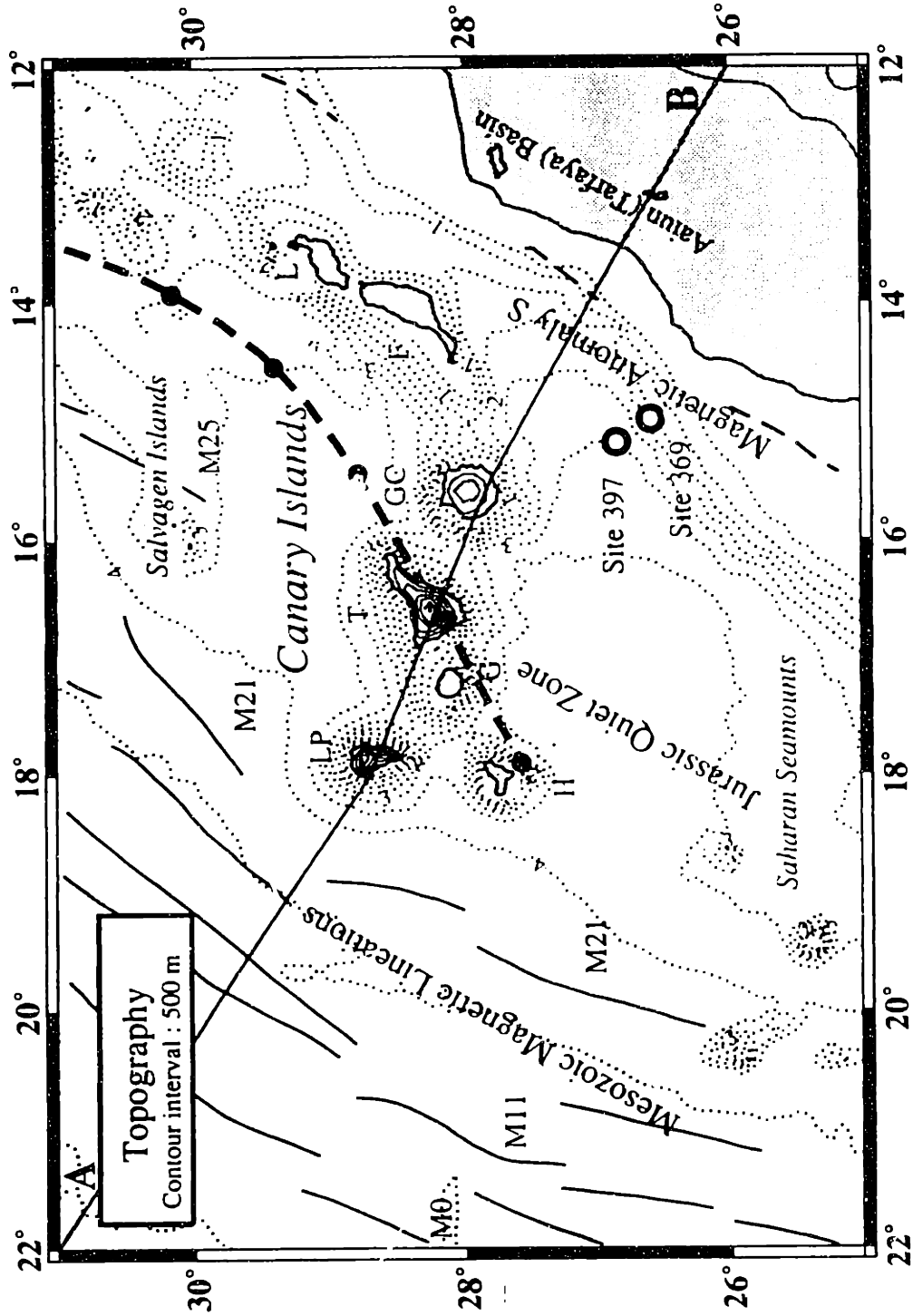
Topography
Contour interval : 500 m
Canary Islands
Salvagen Islands
Aaiun (Tarfaya) Basin
Magnetic Anomaly S
Site 397
Site 369
Jurassic Quiet Zone
Saharan Seamounts
Mesozoic Magnetic Lineations
M25
M21
M11
M0
GC
LP
H
A
B
12°
14°
16°
18°
20°
22°
30°
28°
26°

Figure 4.

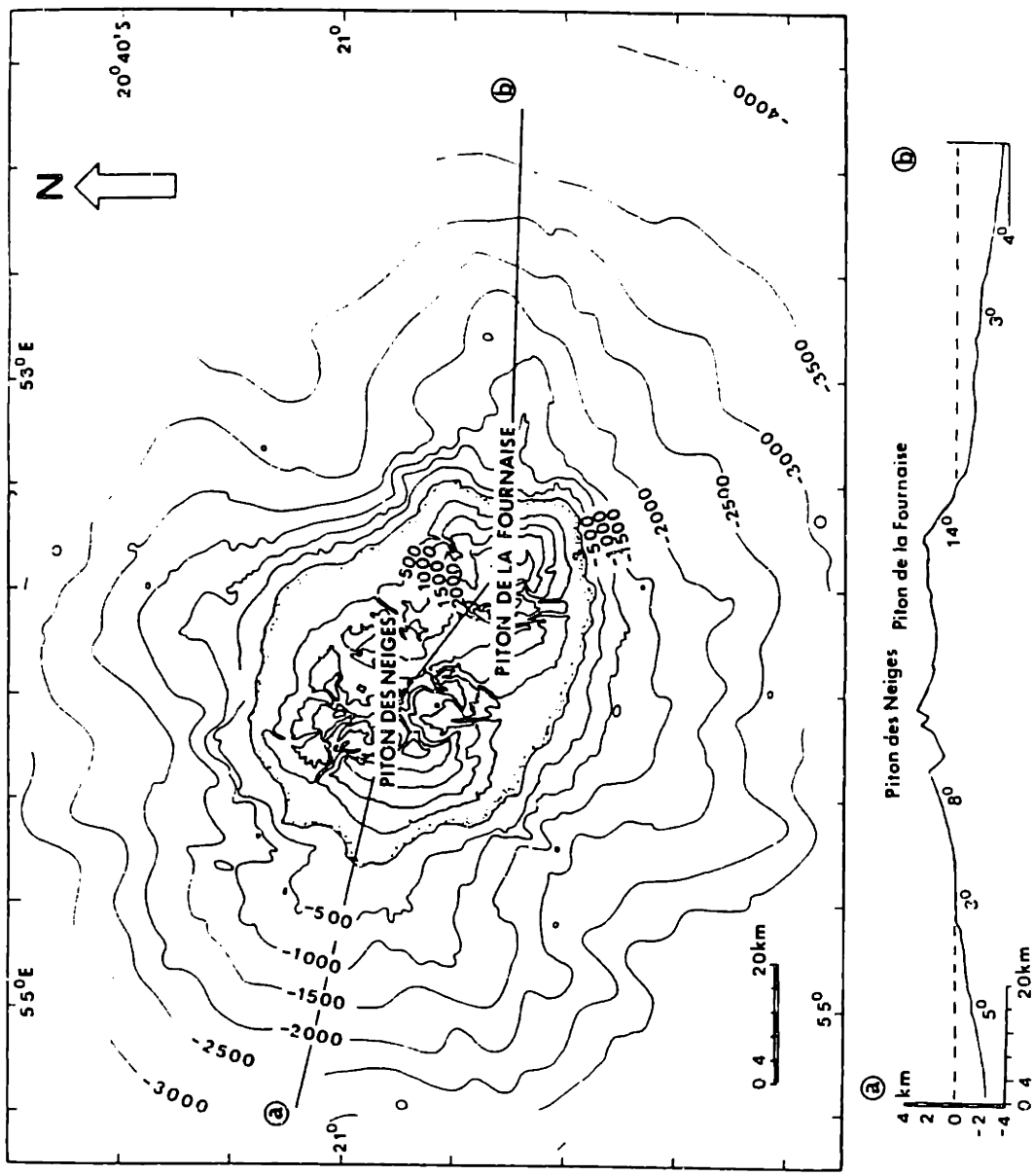
N
20°40'S
21°
53°E
55°E
55°
-21°
PITON DES NEIGES
PITON DE LA FOURNAISE
-500
-1000
-1500
-2000
-2500
-3000
-3500
-4000
0 4 20km
Piton des Neiges
Piton de la Fournaise
km
20km

Figure 5.

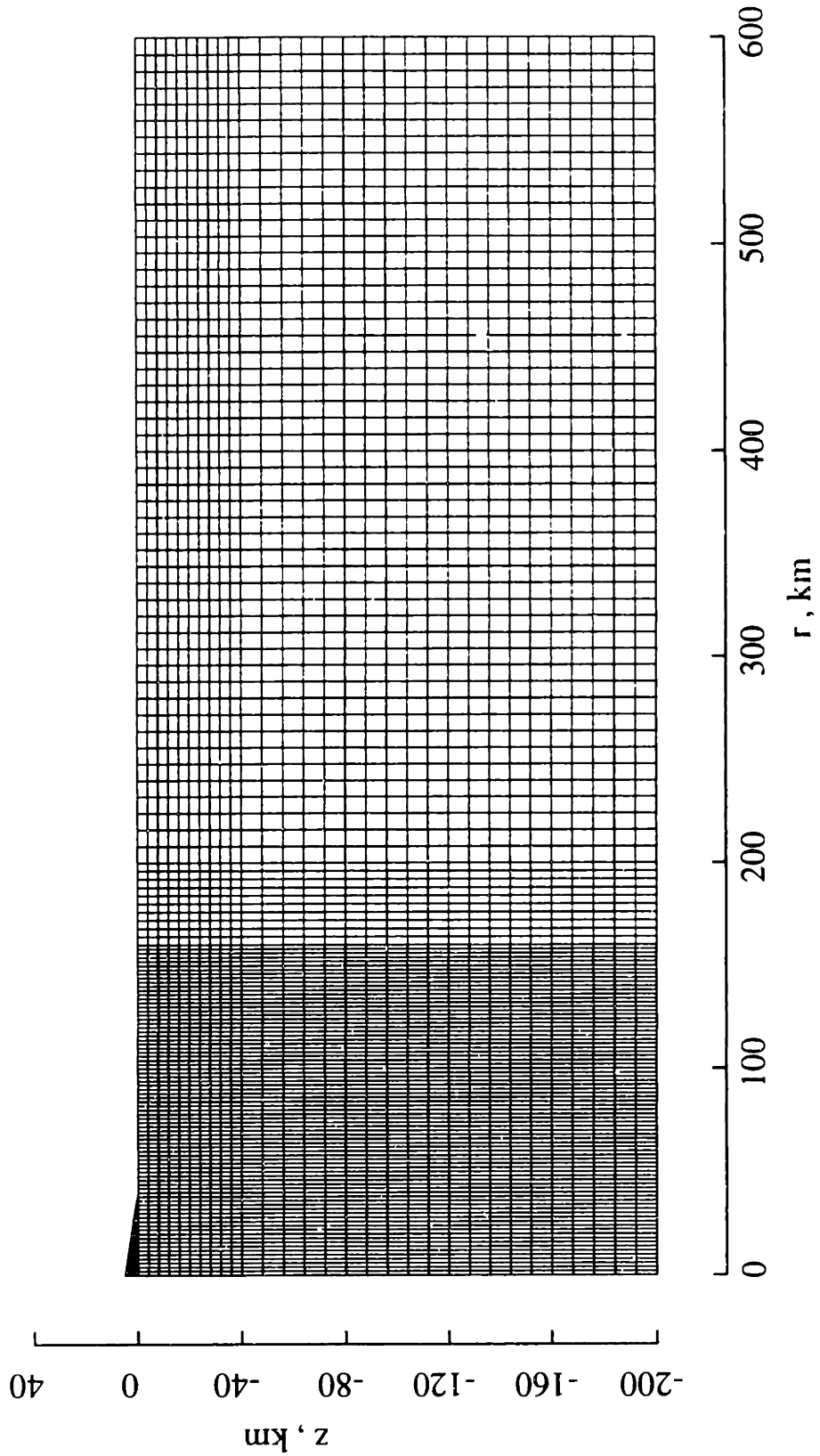

Figure 6a.

Figure 6b.

Figure 6c.

Figure 6d.

	Maximum Principal Stresses		Predictions	
Symbol	Compressive	Extensional	Fault Type	Intrusion Type
	vertical	horizontal	circumferential normal	circumferential dike
	horizonal	vertical	circumferential thrust	sill
	vertical	out of plane	radial normal	radial dike
	horizontal	out of plane	strike-slip	radial dike
	out of plane	horizontal	strike-slip	circumferential dike
	out of plane	vertical	radial thrust	sill

Figure 7.

Figure 8a.

Figure 8b.

Figure 8c.

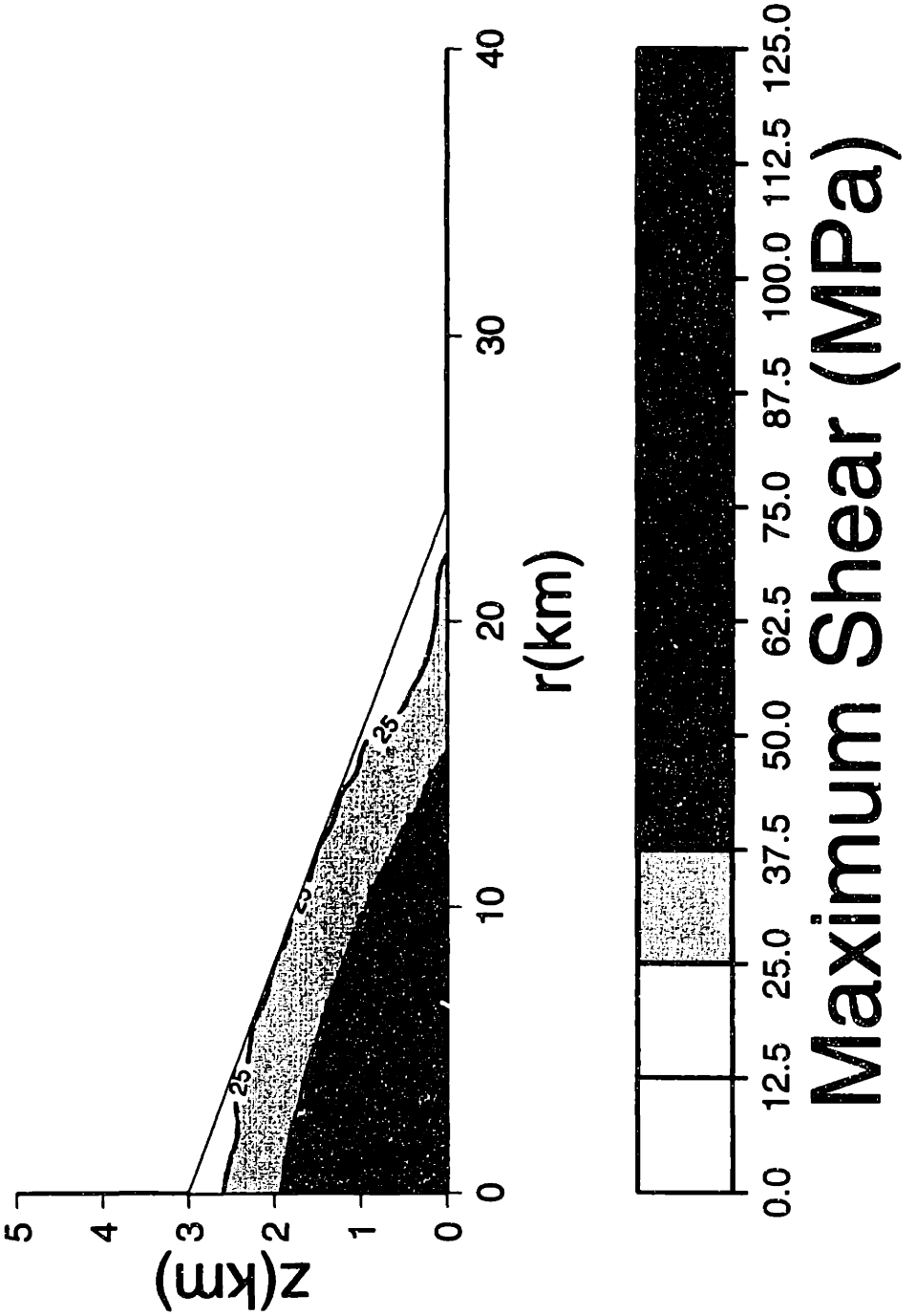
z(km)
0
1
2
3
4
5
r(km)
0
10
20
30
40
25
25
25
Maximum Shear (MPa)
0.0
12.5
25.0
37.5
50.0
62.5
75.0
87.5
100.0
112.5
125.0

Figure 8d.

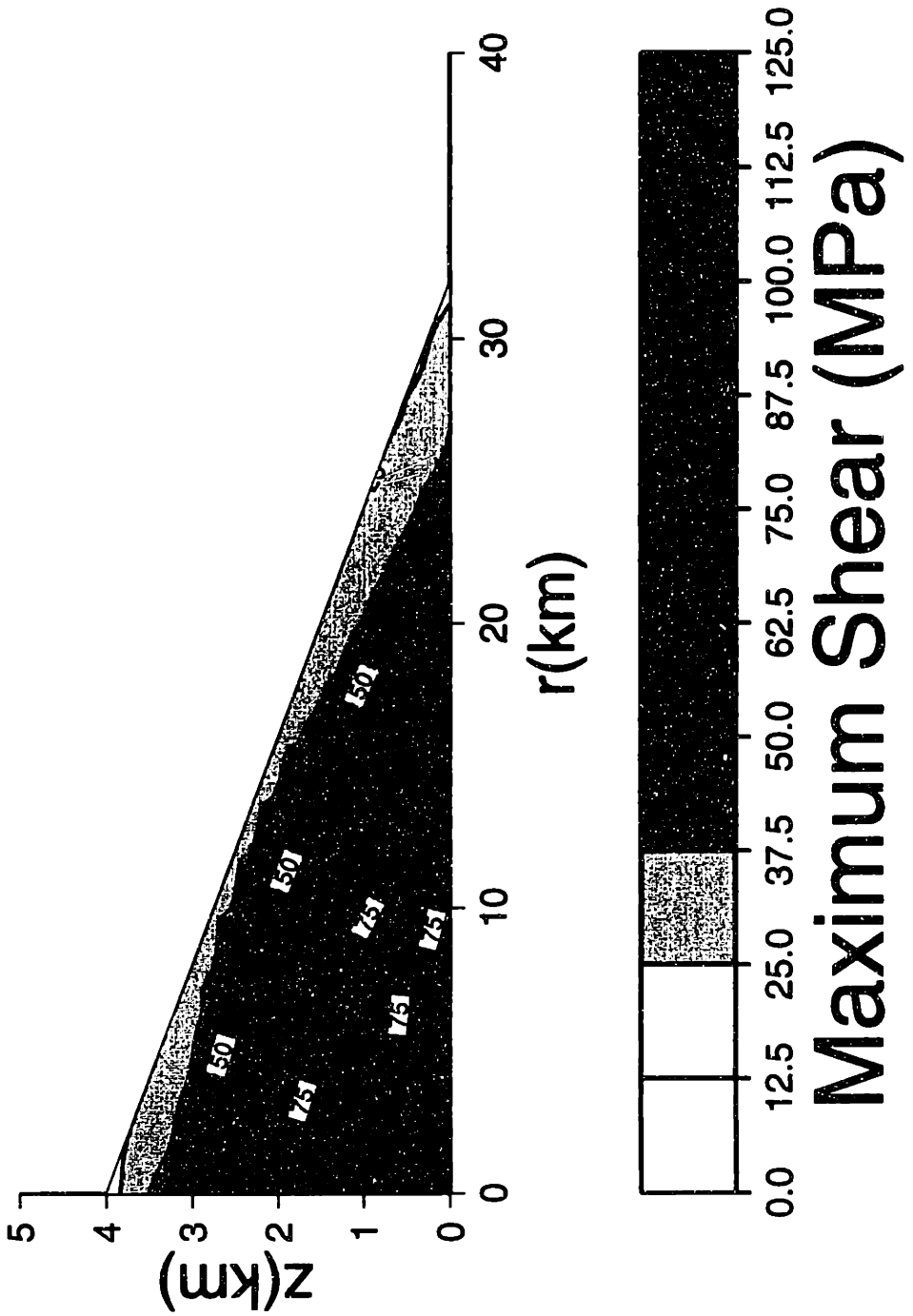
z(km)
0
1
2
3
4
5
0
10
20
30
40
r(km)
150
150
150
175
175
175
175
Maximum Shear (MPa)
0.0
12.5
25.0
37.5
50.0
62.5
75.0
87.5
100.0
112.5
125.0

Figure 8e.

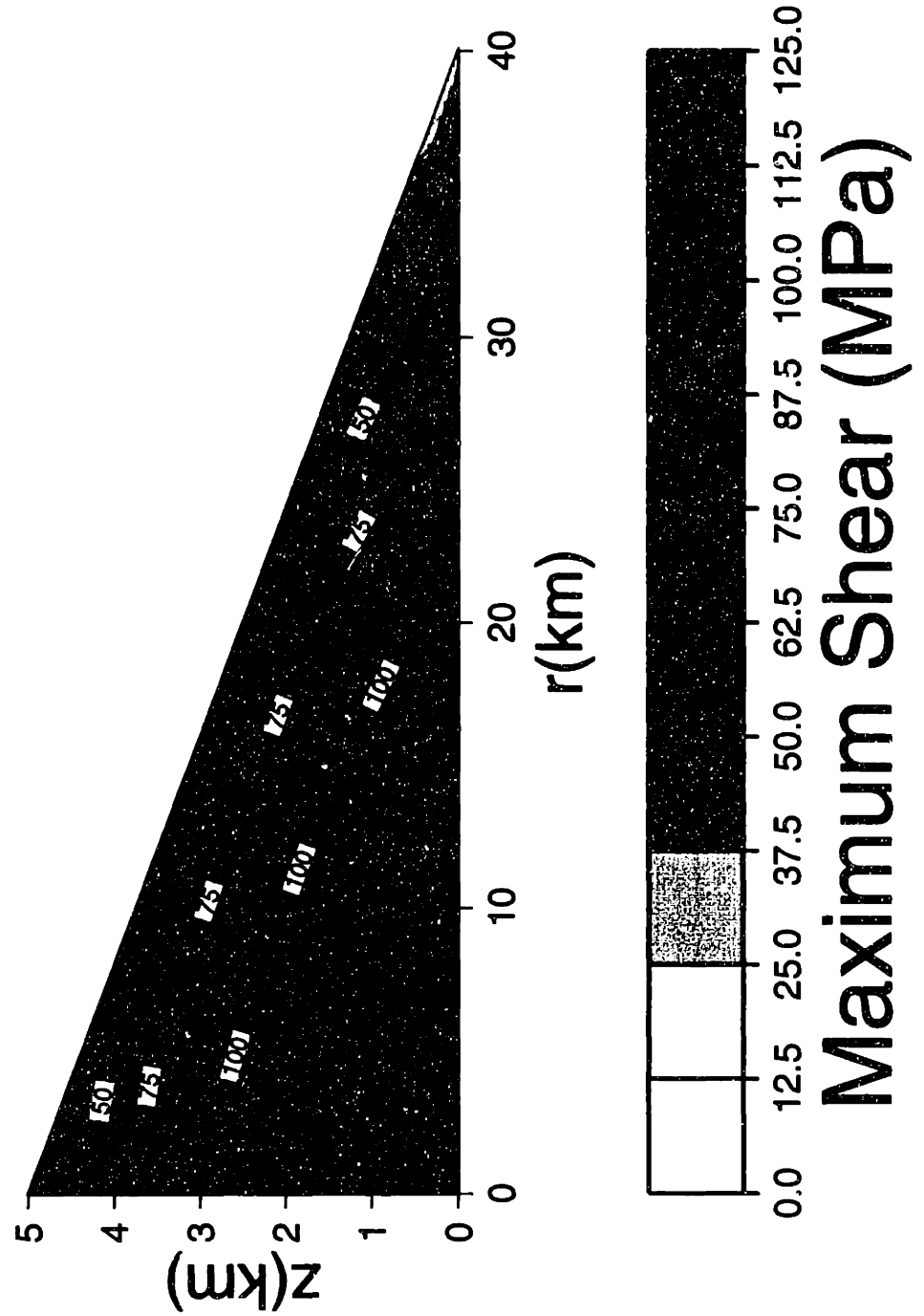
z(km)
0
1
2
3
4
5
0
10
20
30
40
r(km)
150
175
100
125
75
50
Maximum Shear (MPa)
0.0
12.5
25.0
37.5
50.0
62.5
75.0
87.5
100.0
112.5
125.0

Figure 8f.

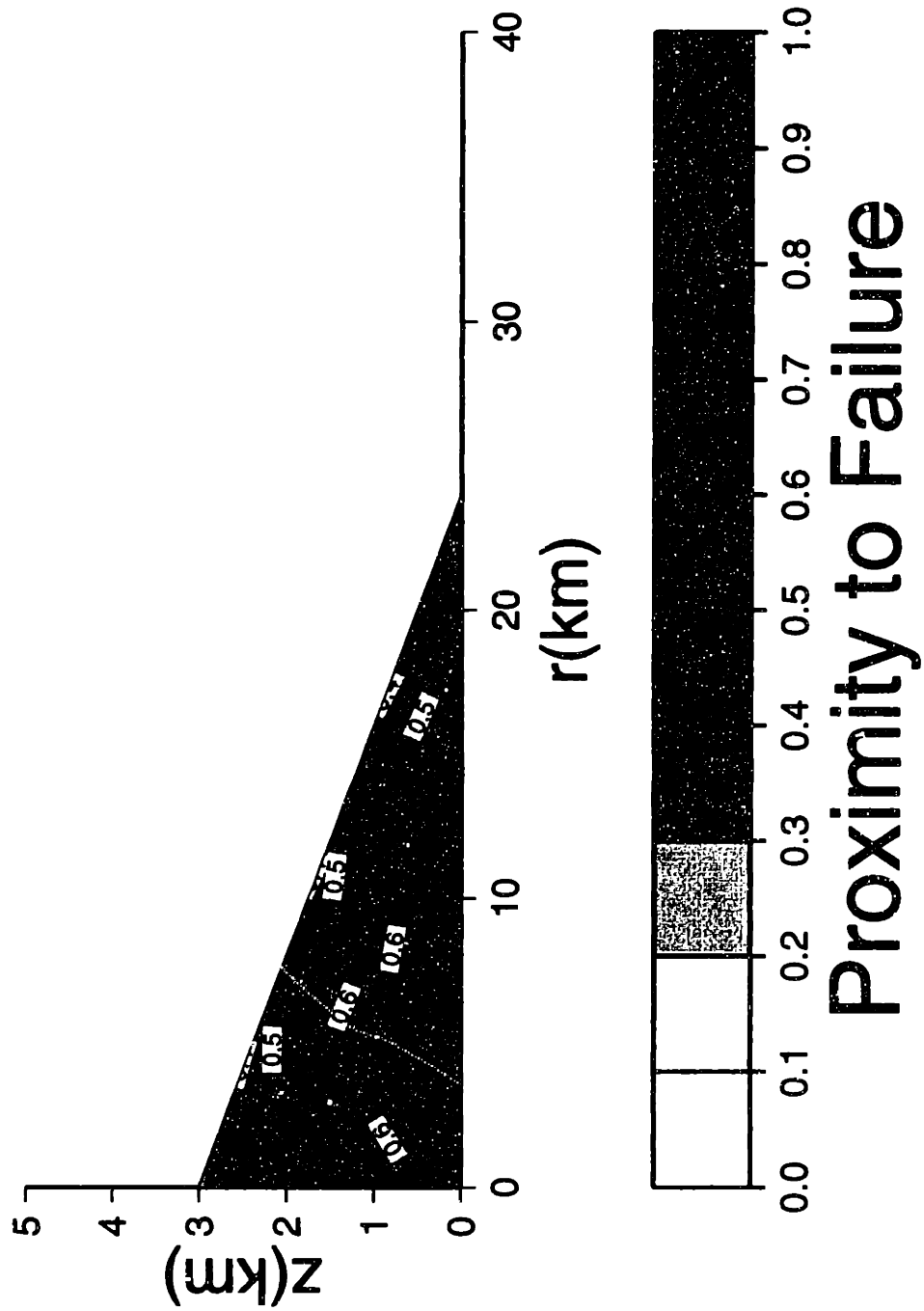
z(km)
r(km)
Proximity to Failure
0.0
0.1
0.2
0.3
0.4
0.5
0.6
0.7
0.8
0.9
1.0
0
10
20
30
40
0
1
2
3
4
5

Figure 8g.

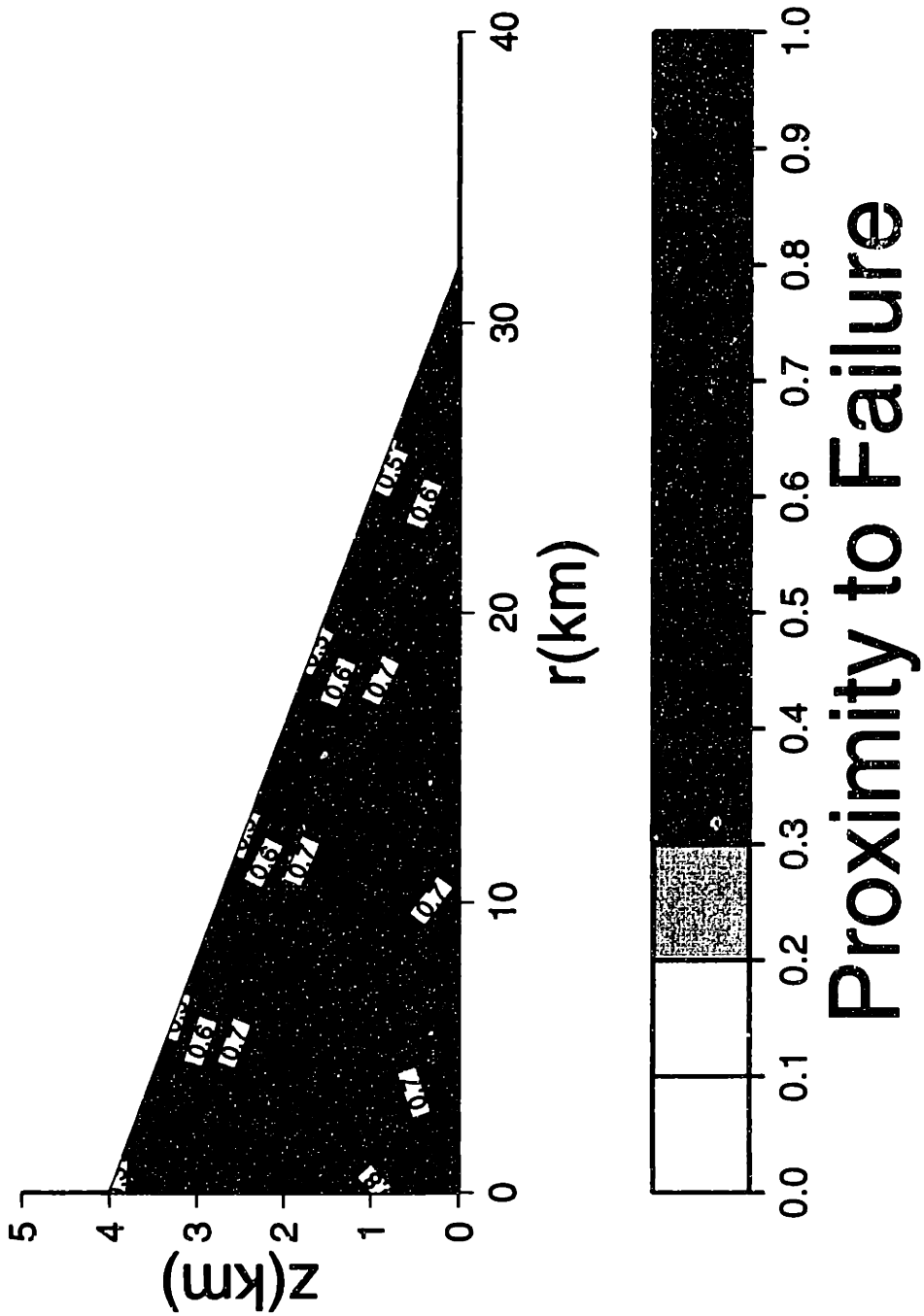
z(km)
r(km)
Proximity to Failure
0
1
2
3
4
5
0
10
20
30
40
0.0
0.1
0.2
0.3
0.4
0.5
0.6
0.7
0.8
0.9
1.0

Figure 8h.

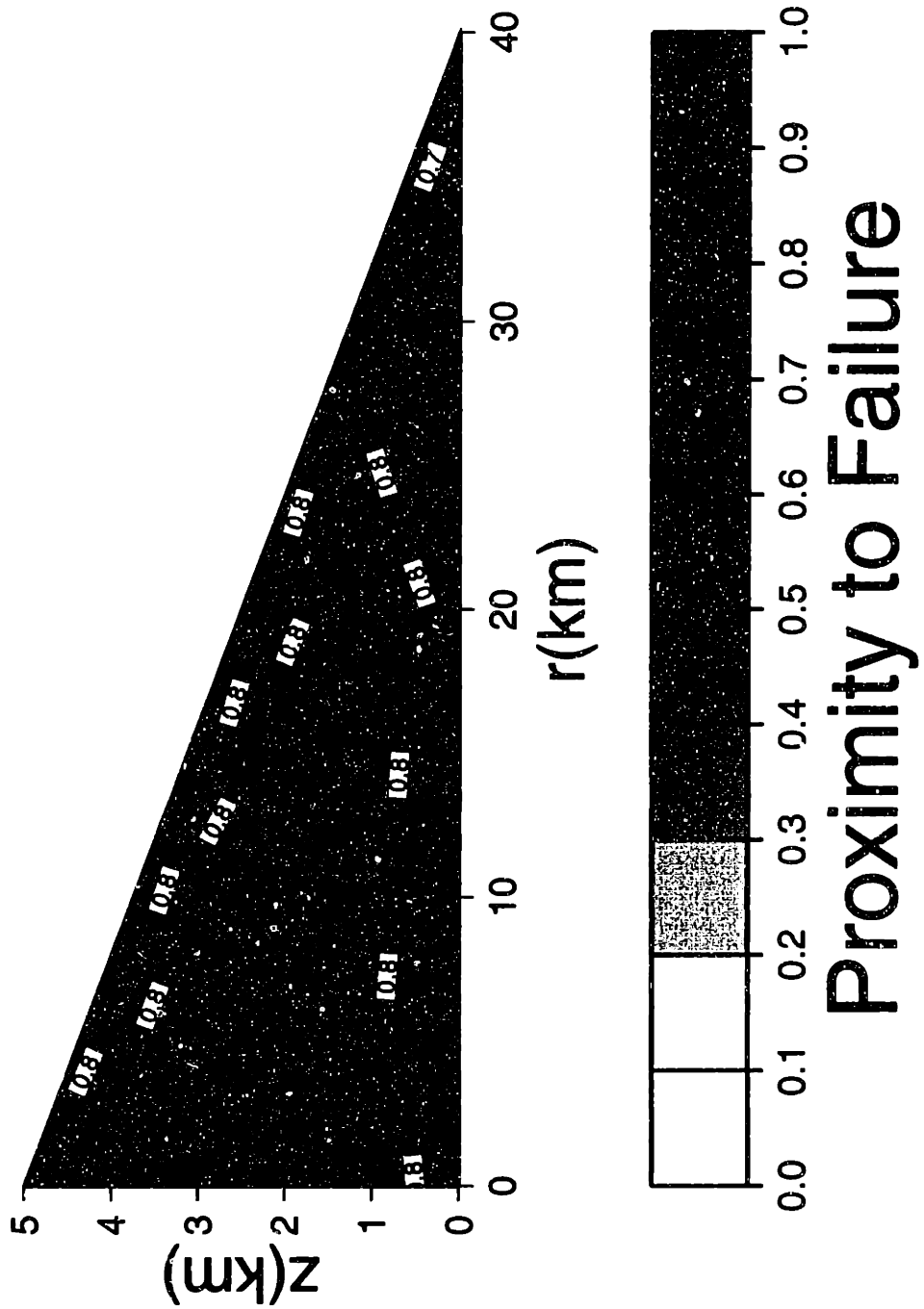
z(km)
0
1
2
3
4
5
r(km)
0
10
20
30
40
Proximity to Failure
0.0
0.1
0.2
0.3
0.4
0.5
0.6
0.7
0.8
0.9
1.0

Figure 8i.

Figure 9a.

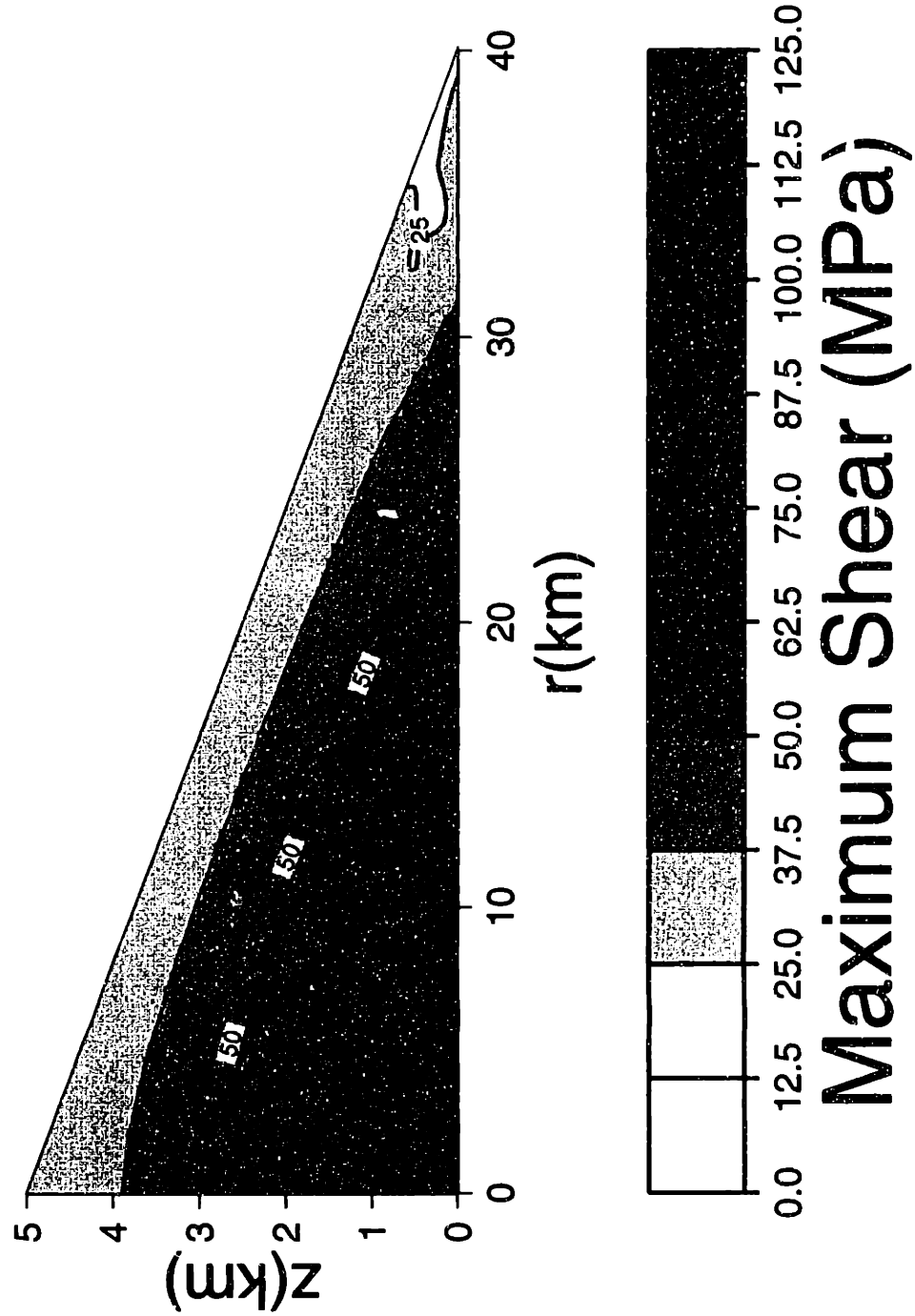
z(km)
r(km)
Maximum Shear (MPa)
0.0
12.5
25.0
37.5
50.0
62.5
75.0
87.5
100.0
112.5
125.0
25
50
50
50

Figure 9b.

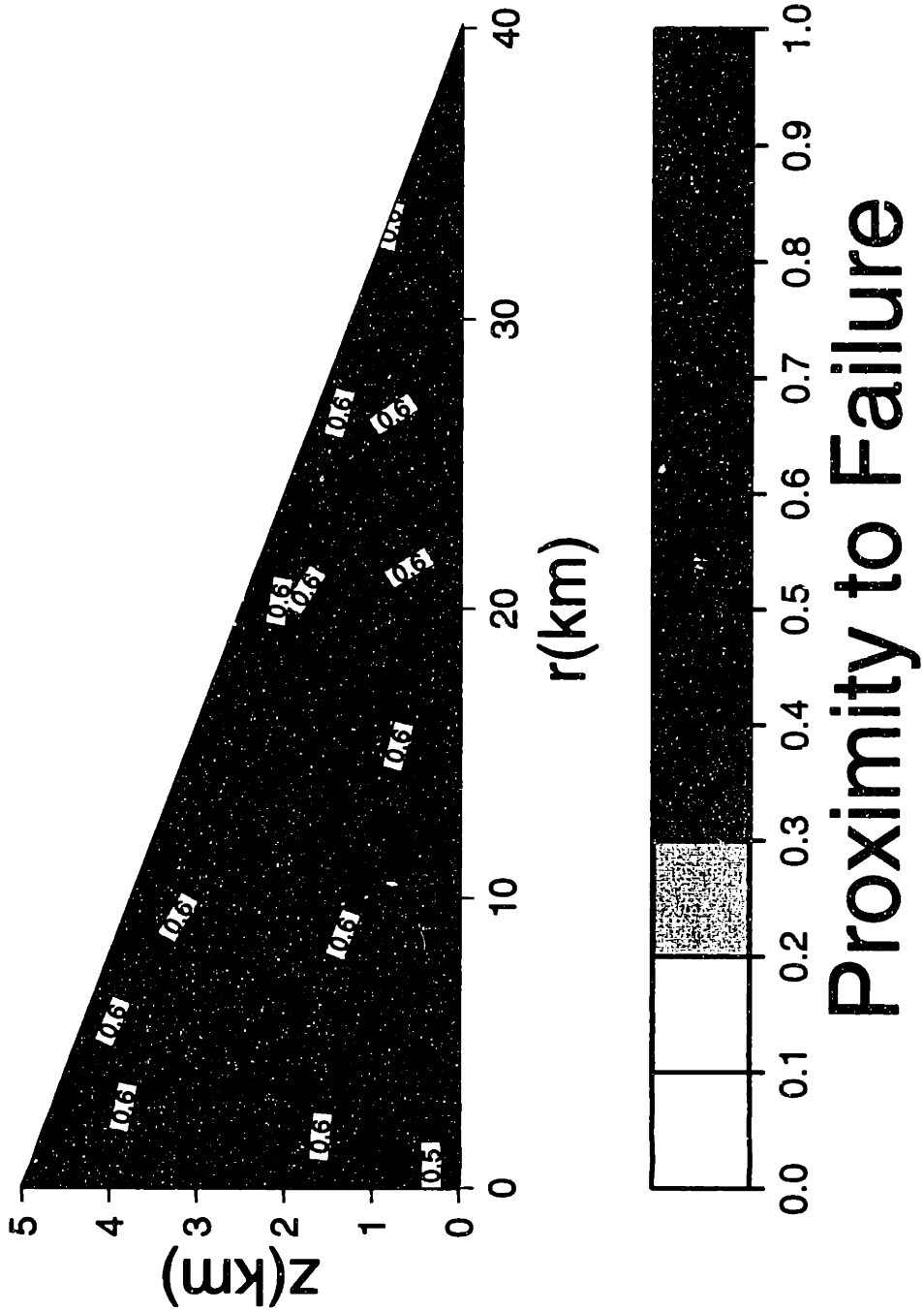
z(km)
0
1
2
3
4
5
0
10
20
30
40
r(km)
0.6
0.5
Proximity to Failure
0.0
0.1
0.2
0.3
0.4
0.5
0.6
0.7
0.8
0.9
1.0

Figure 9c.

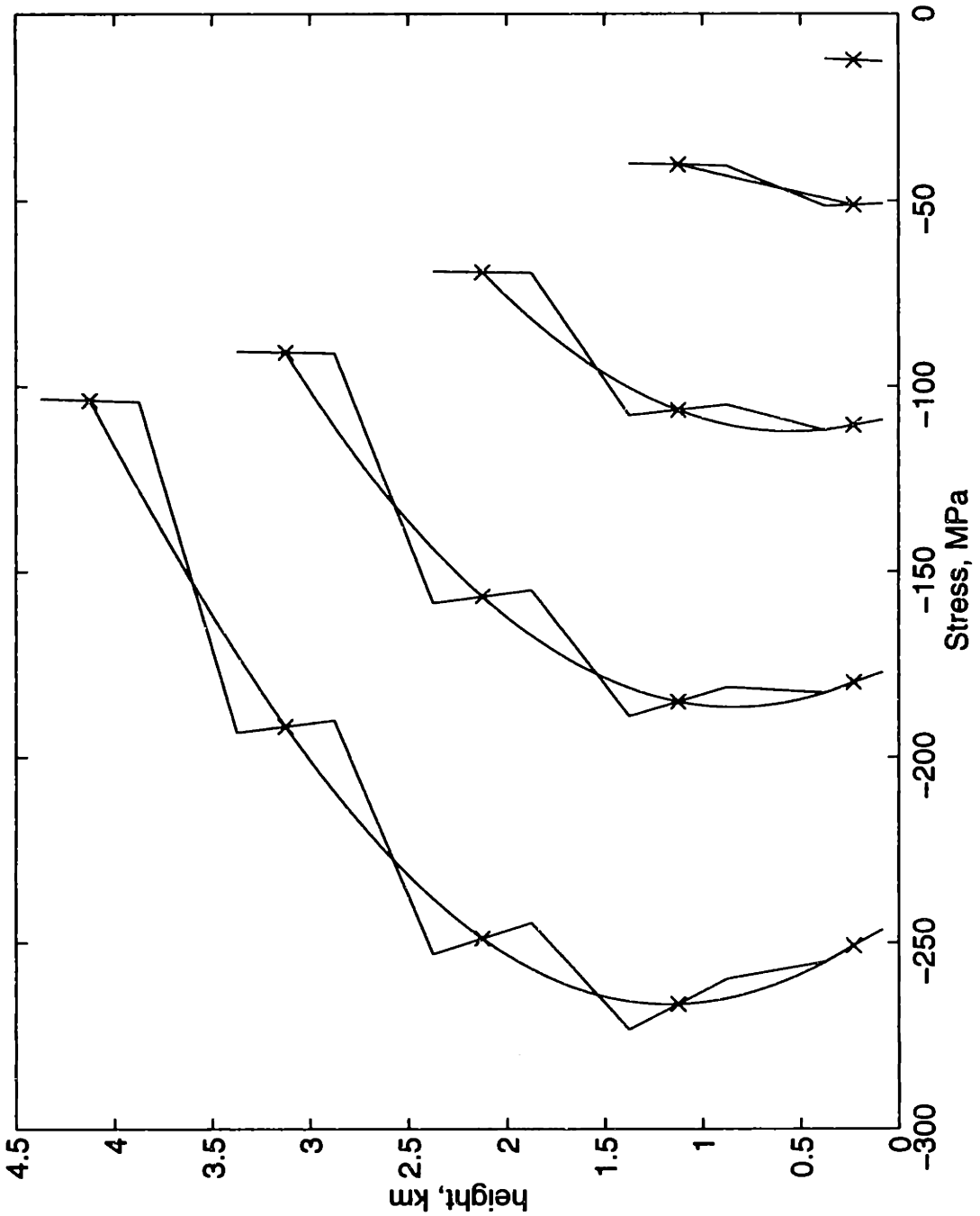
Height, km
4.5
4
3.5
3
2.5
2
1.5
1
0.5
0
Stress, MPa
0
-50
-100
-150
-200
-250
-300

Figure 10a.

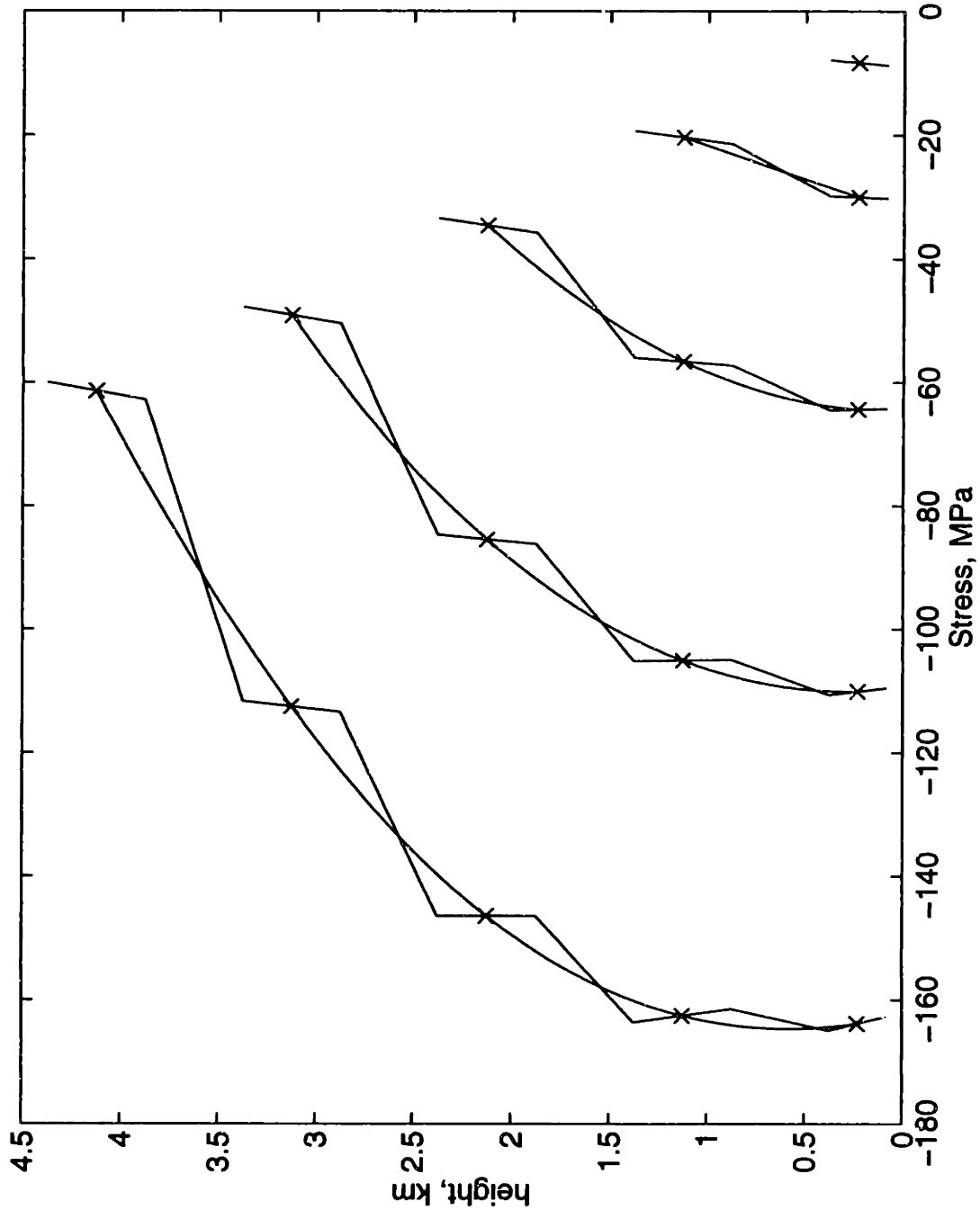
height, km
4.5
4
3.5
3
2.5
2
1.5
1
0.5
0
Stress, MPa
0
-20
-40
-60
-80
-100
-120
-140
-160
-180

Figure 10b.

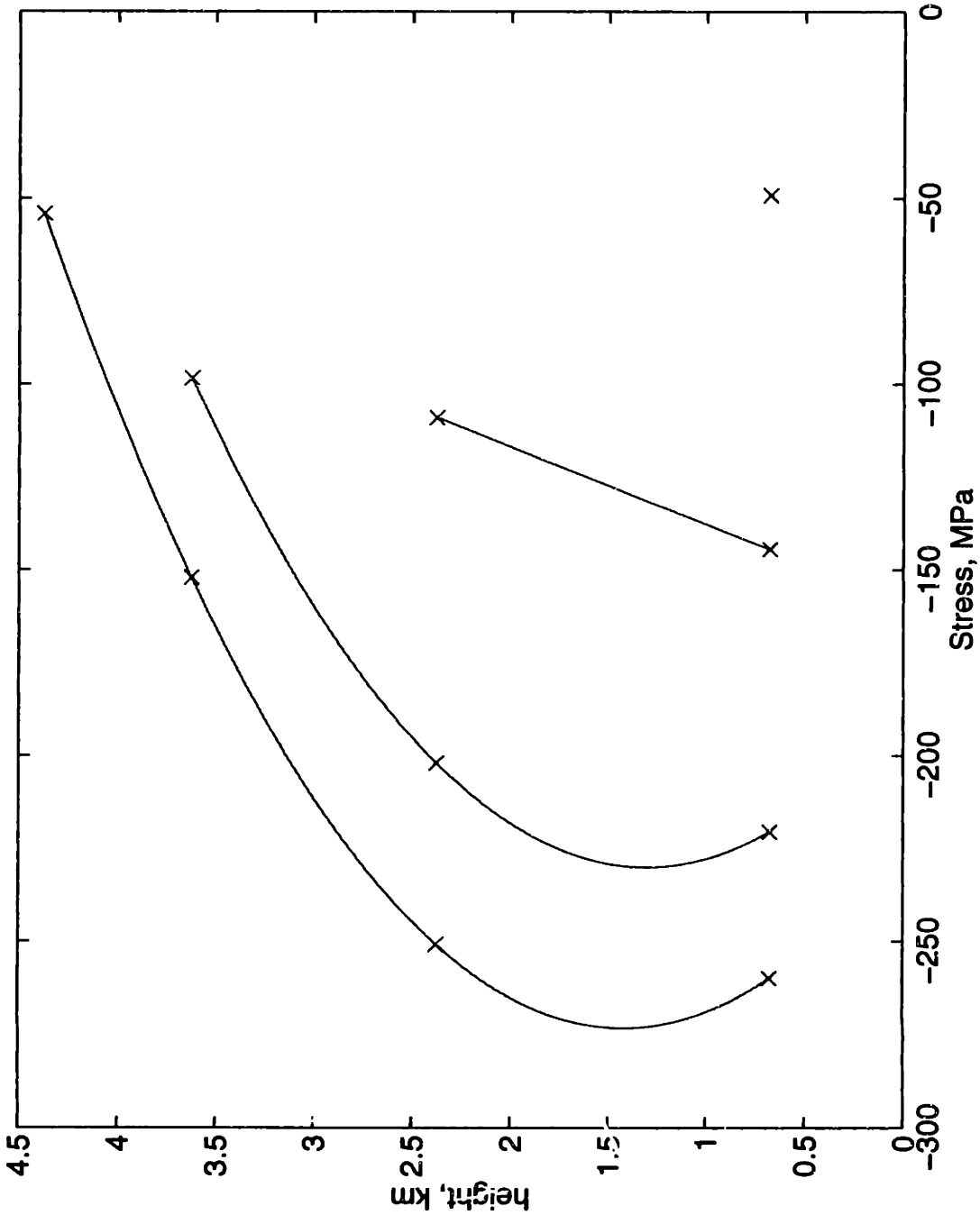
Height, km
4.5
4
3.5
3
2.5
2
1.5
1
0.5
0
Stress, MPa
0
-50
-100
-150
-200
-250
-300

Figure 10c.

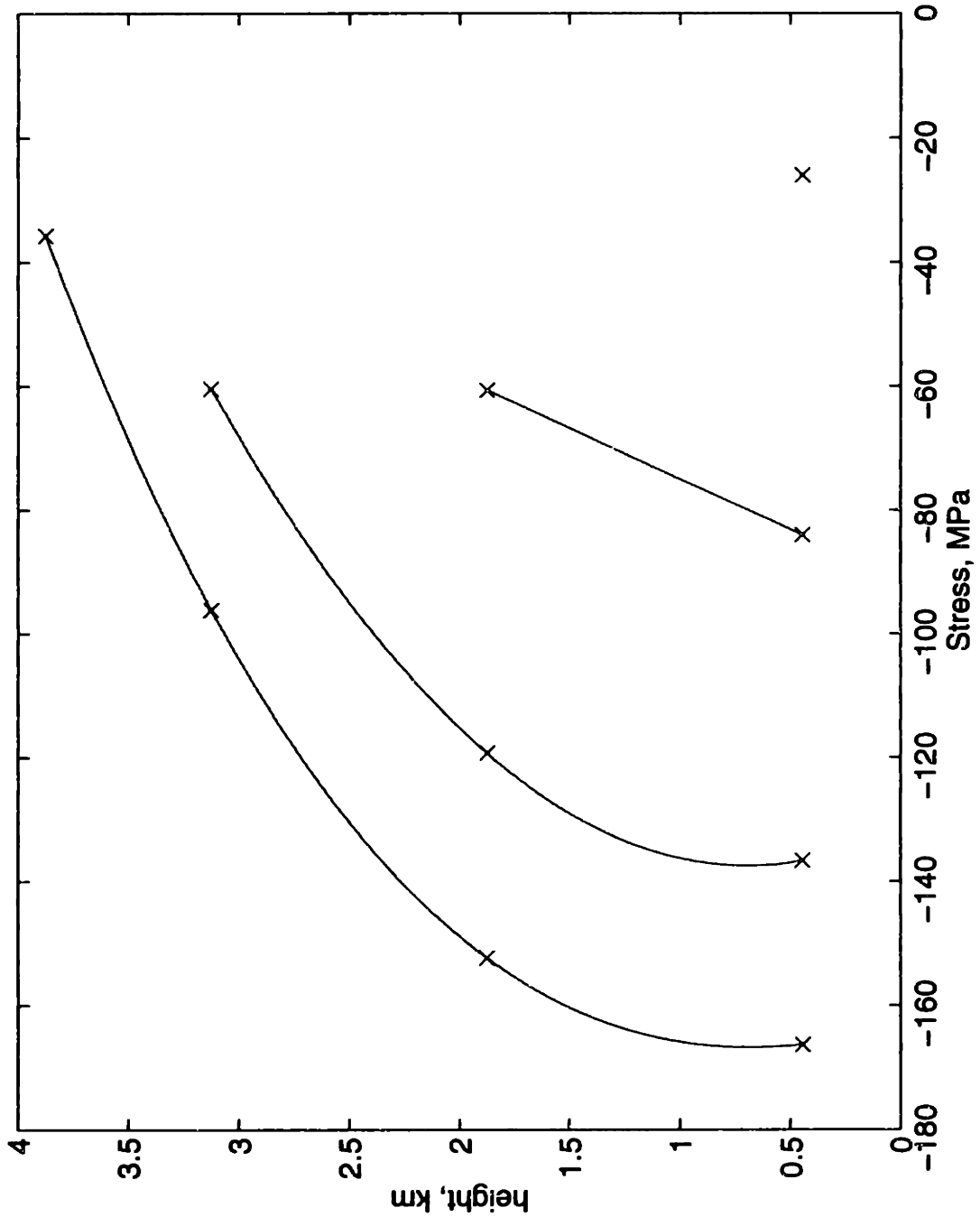
height, km
4
3.5
3
2.5
2
1.5
1
0.5
0
Stress, MPa
0
-20
-40
-60
-80
-100
-120
-140
-160
-180

Figure 10d.

Figure 11a.

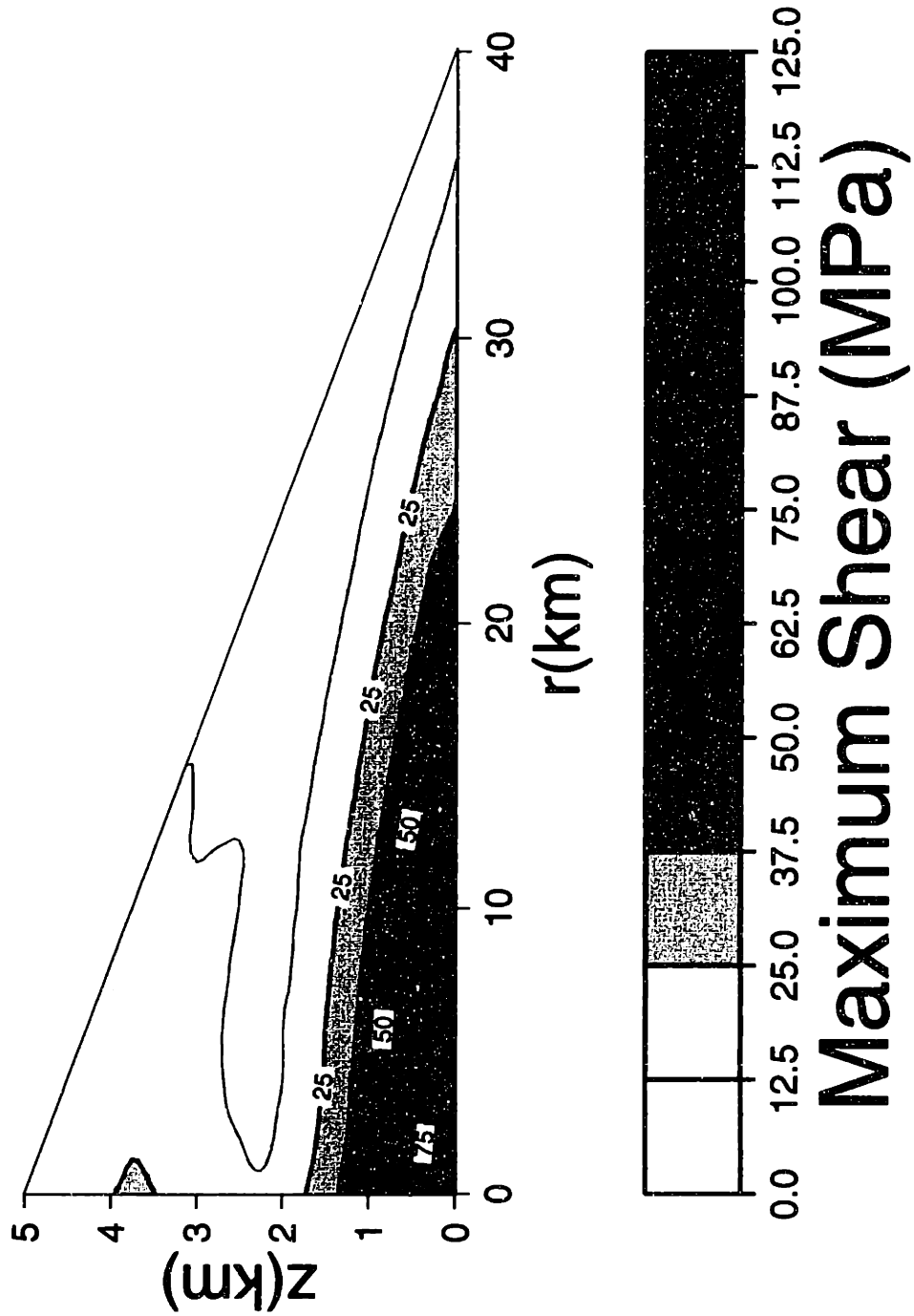
z(km)
0
1
2
3
4
5
r(km)
0
10
20
30
40
25
50
75
Maximum Shear (MPa)
0.0
12.5
25.0
37.5
50.0
62.5
75.0
87.5
100.0
112.5
125.0

Figure 11b.

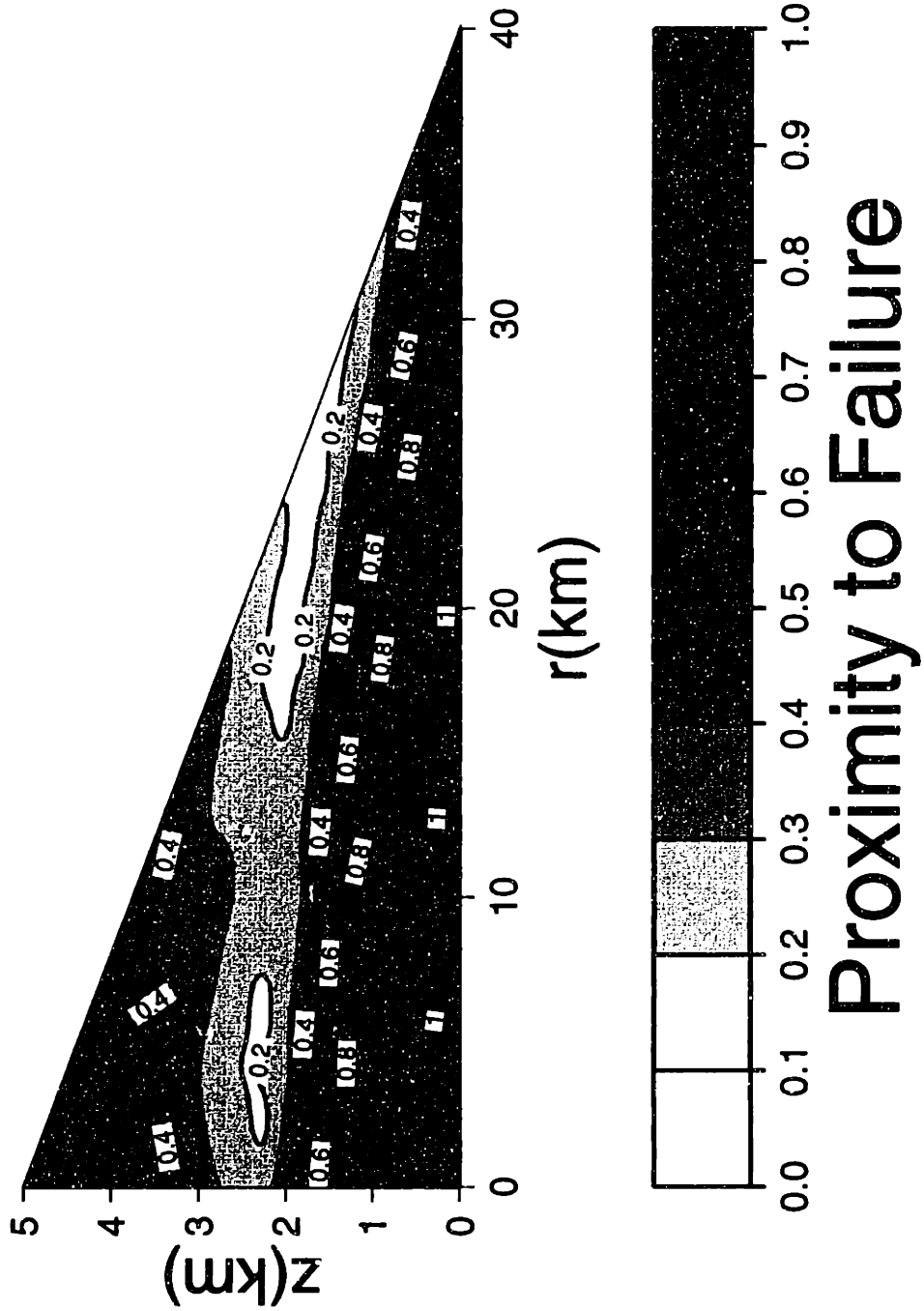

Figure 11c.

Figure 12a.

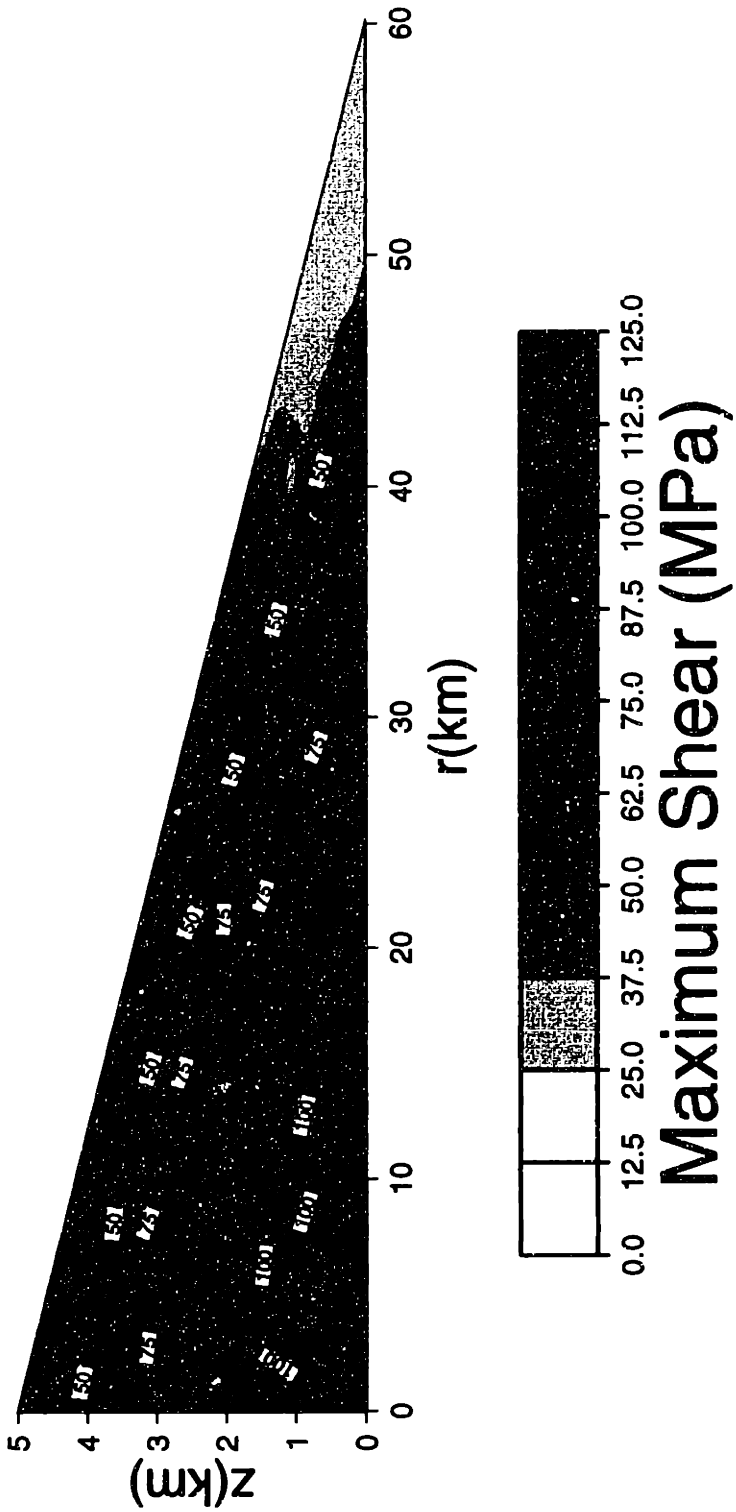
z(km)
0
1
2
3
4
5
0
10
20
30
40
50
60
r(km)
Maximum Shear (MPa)
0.0
12.5
25.0
37.5
50.0
62.5
75.0
87.5
100.0
112.5
125.0

Figure 12b.

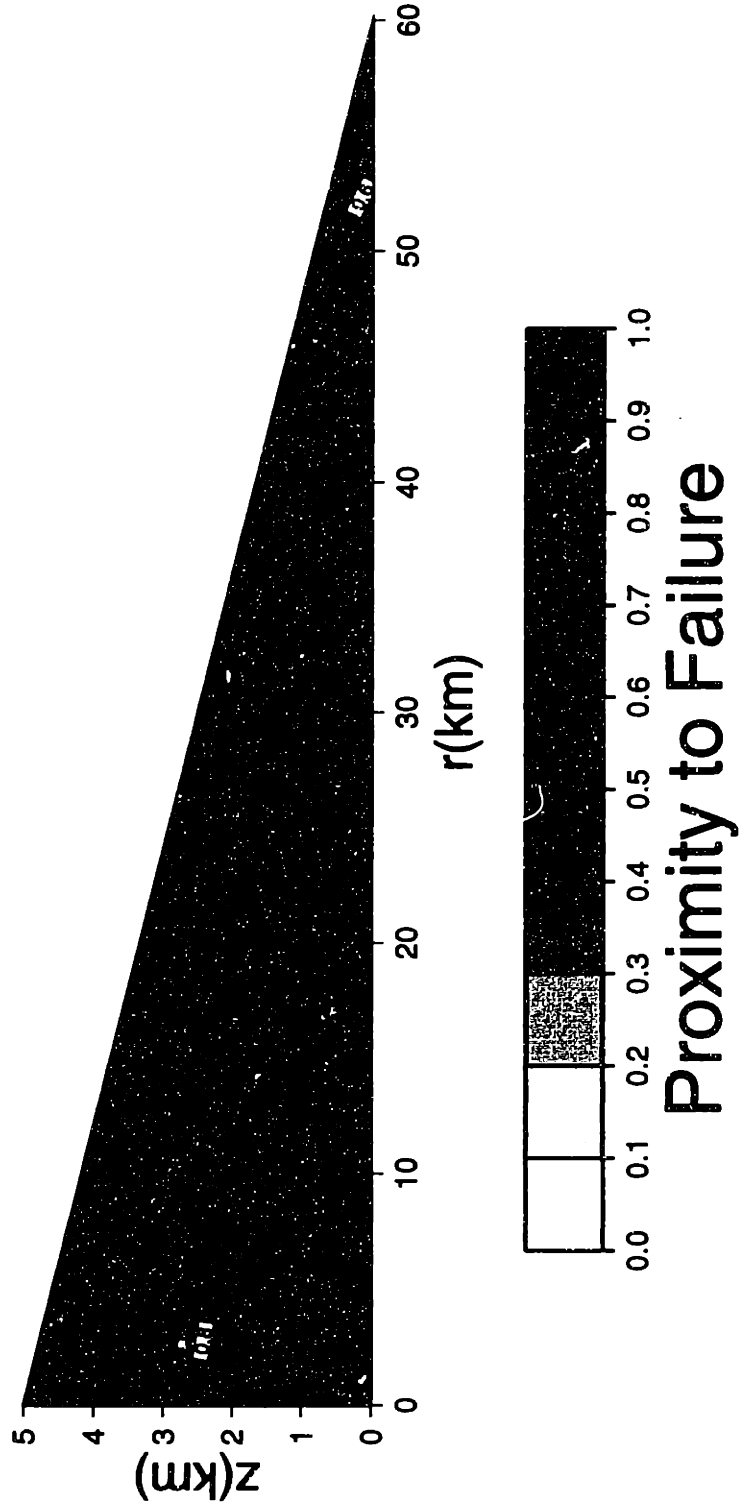
z(km)
0
1
2
3
4
5
r(km)
0
10
20
30
40
50
60
Proximity to Failure
0.0
0.1
0.2
0.3
0.4
0.5
0.6
0.7
0.8
0.9
1.0

Figure 12c.

Figure 13a.

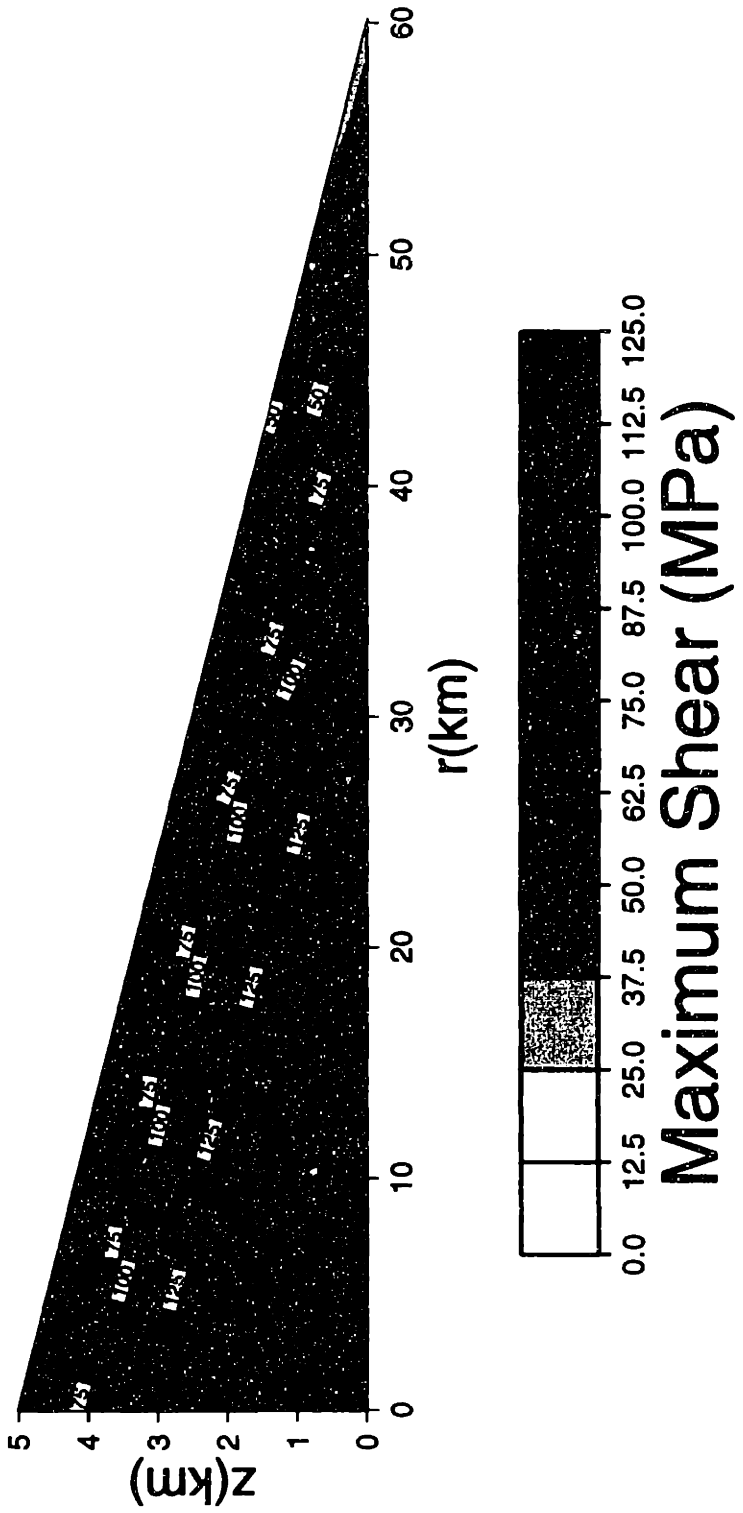
z(km)
0
1
2
3
4
5
0
10
20
30
40
50
60
r(km)
Maximum Shear (MPa)
0.0
12.5
25.0
37.5
50.0
62.5
75.0
87.5
100.0
112.5
125.0

Figure 13b.

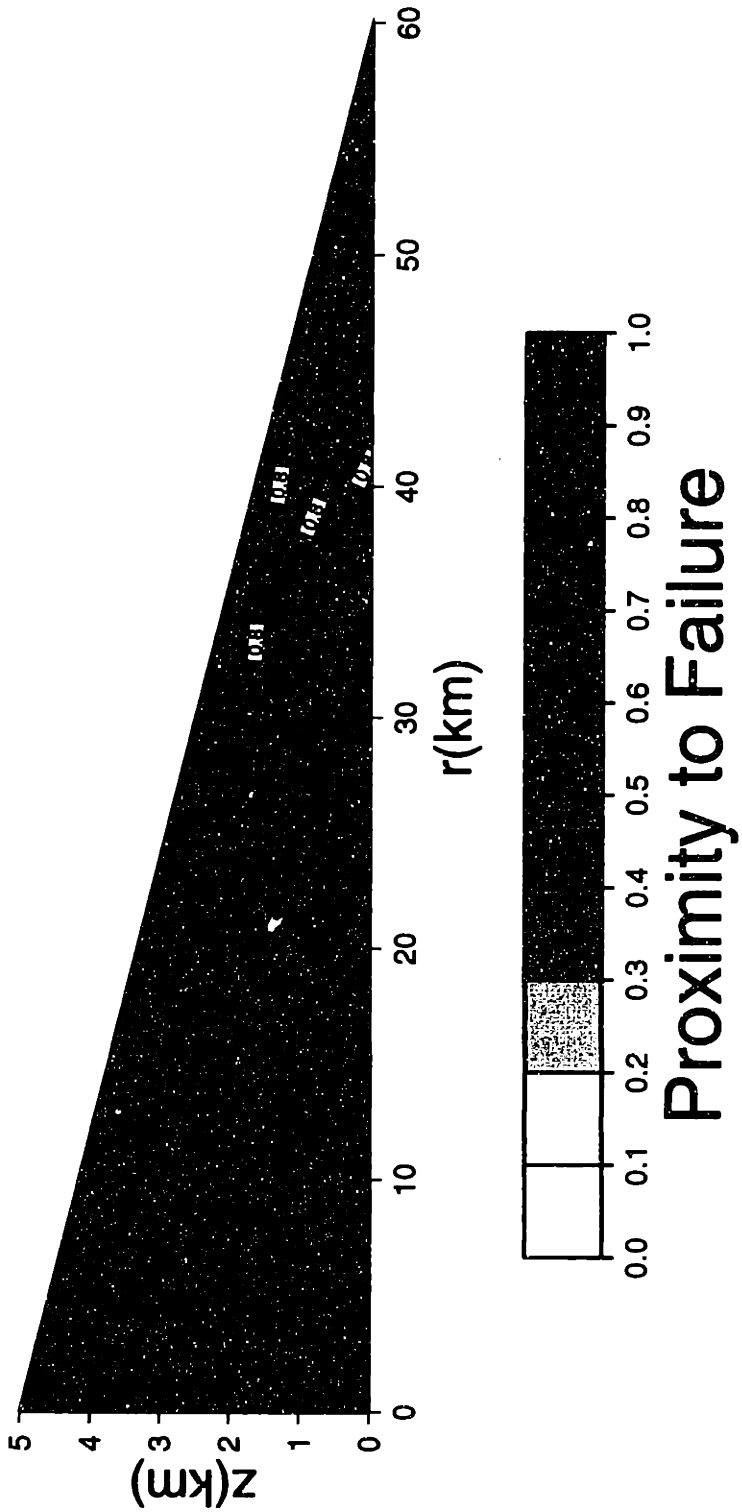
z(km)
0
1
2
3
4
5
r(km)
0
10
20
30
40
50
60
Proximity to Failure
0.0
0.1
0.2
0.3
0.4
0.5
0.6
0.7
0.8
0.9
1.0

Figure 13c.

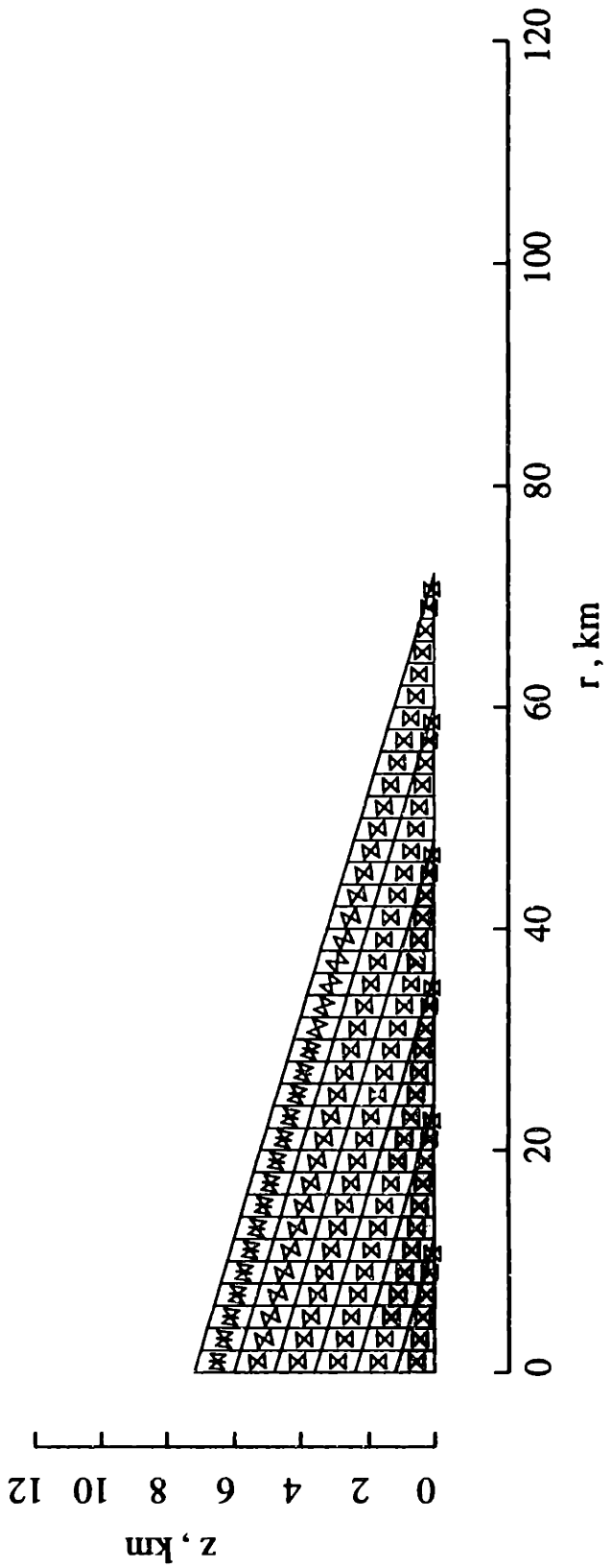

Figure 14a.

Figure 14b.

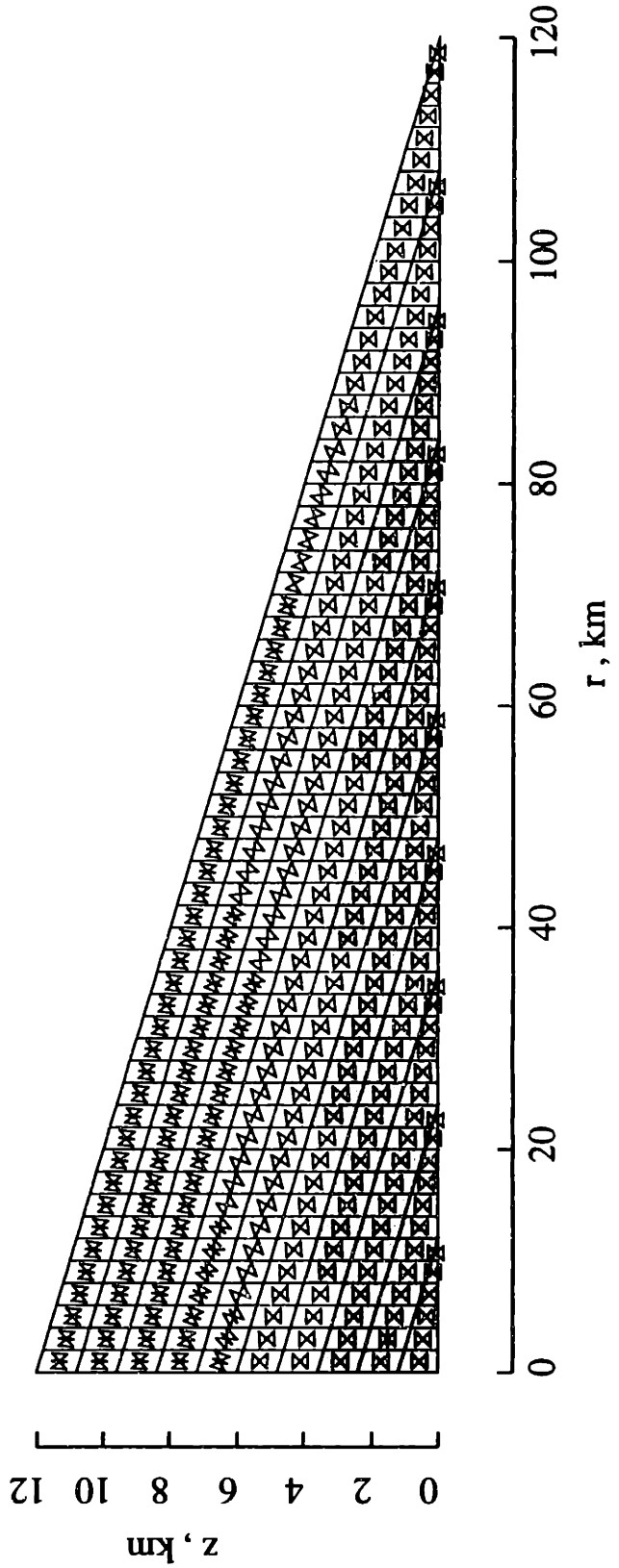

Figure 14c.

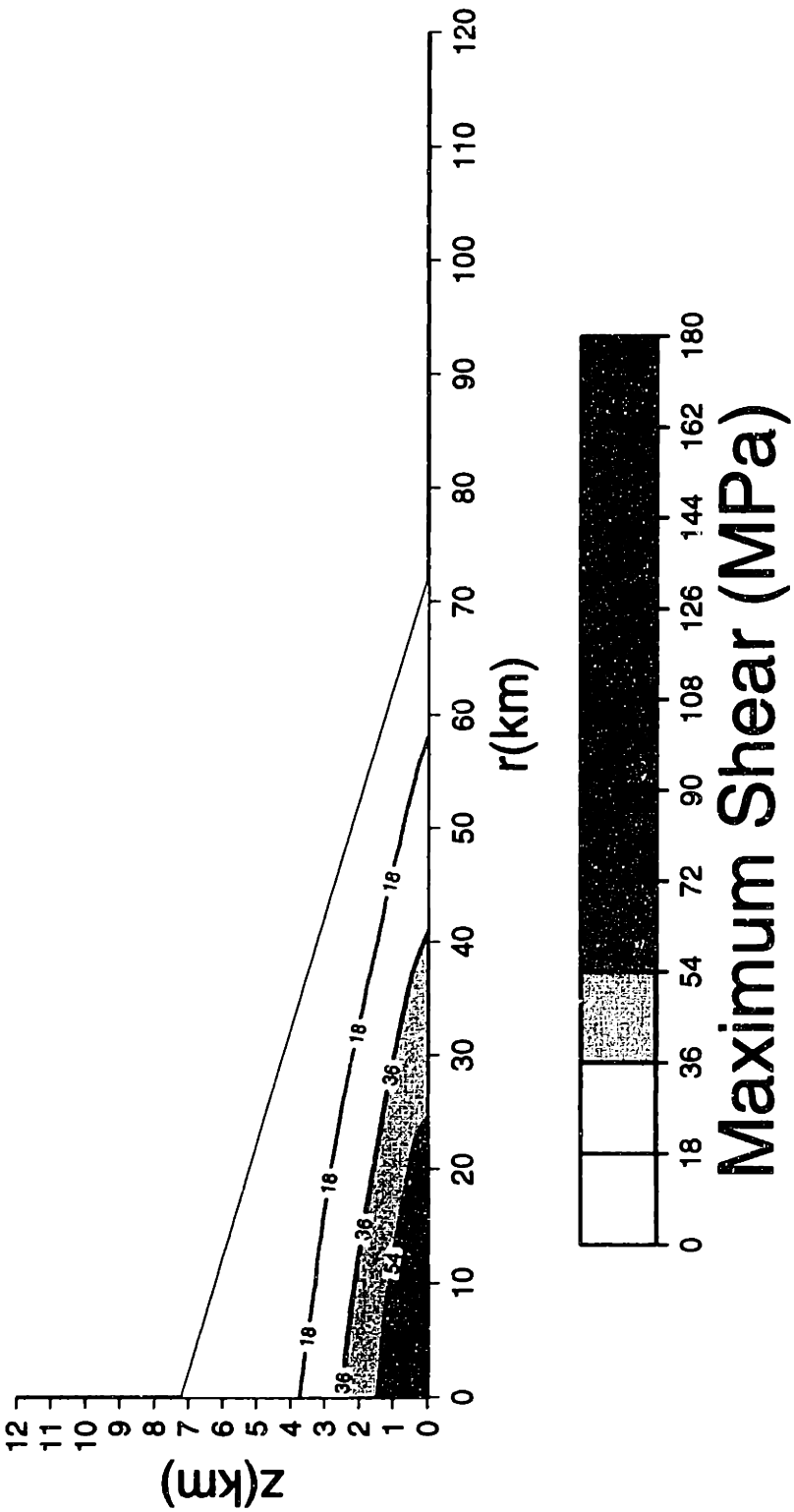

Figure 14d.

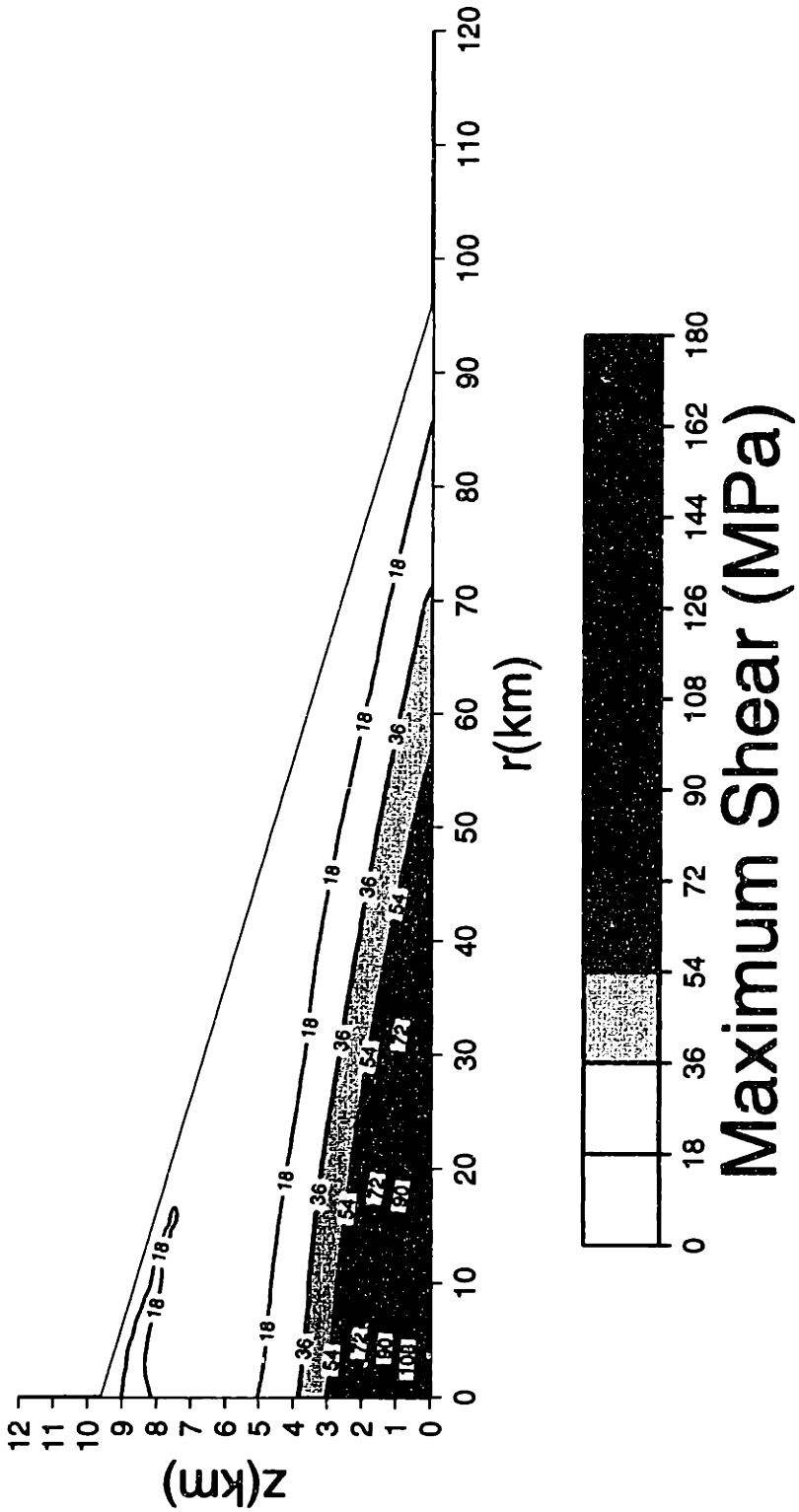

Figure 14e.

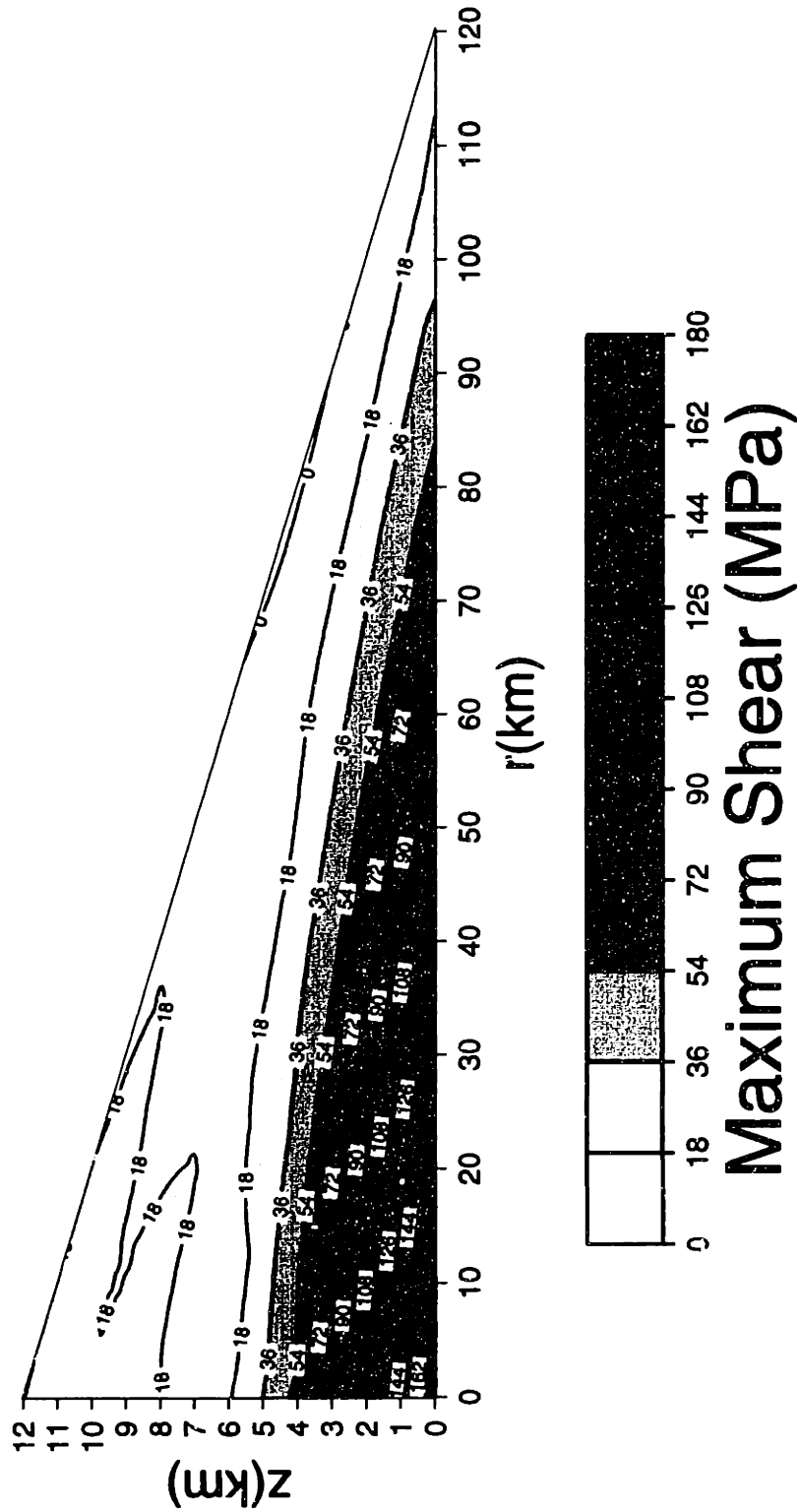

Figure 14f.

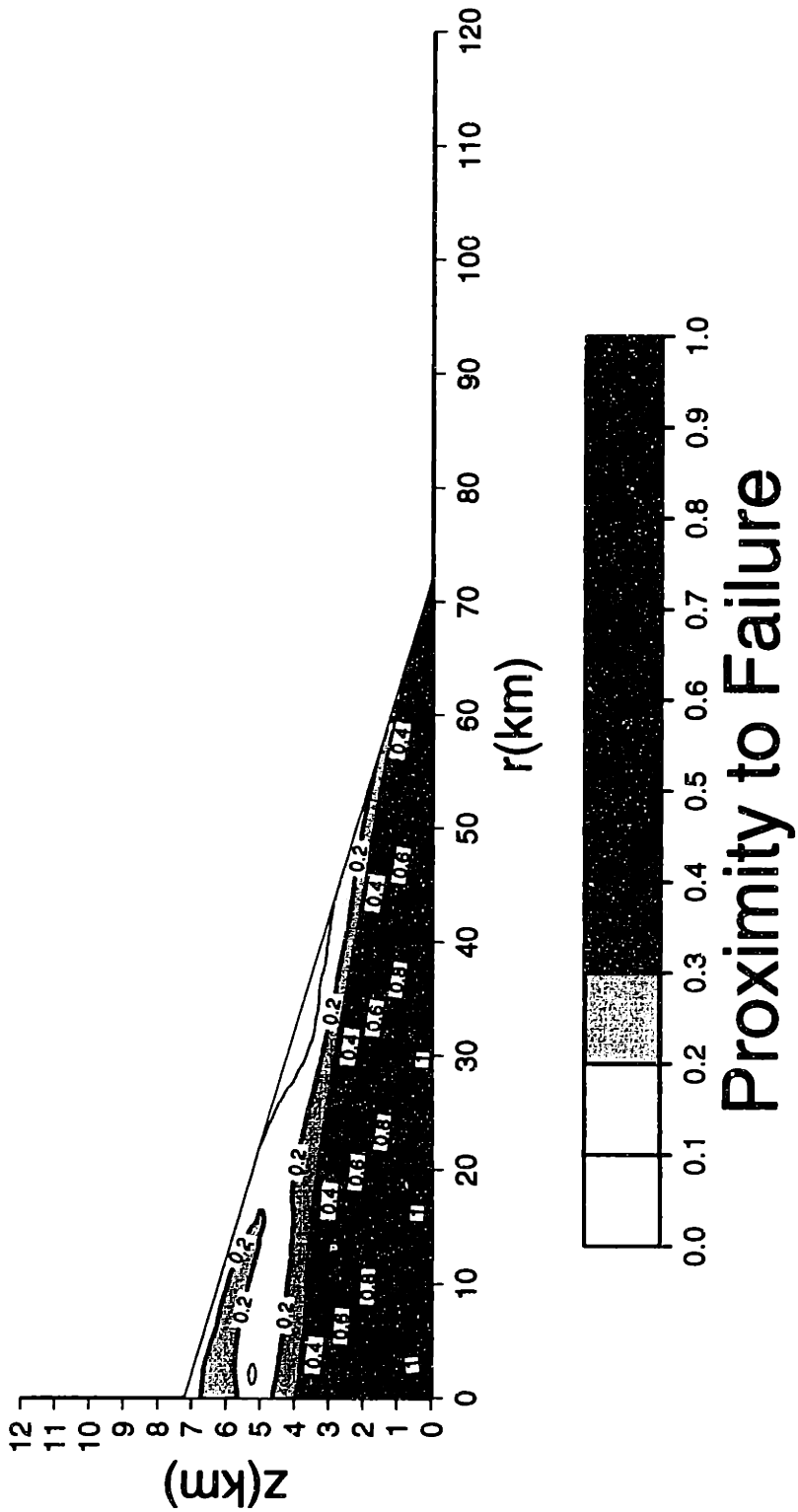

Figure 14g.

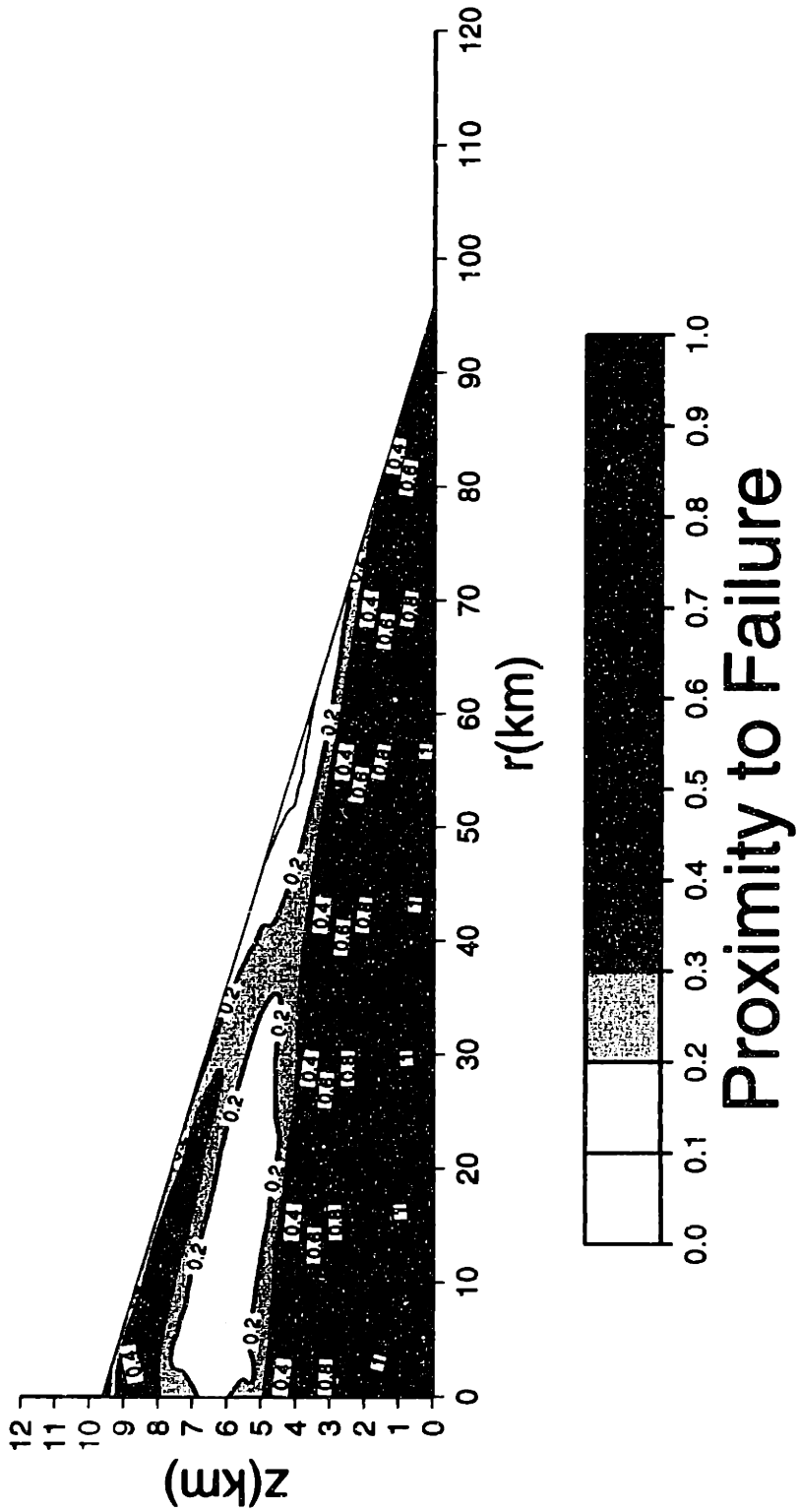

Figure 14h.

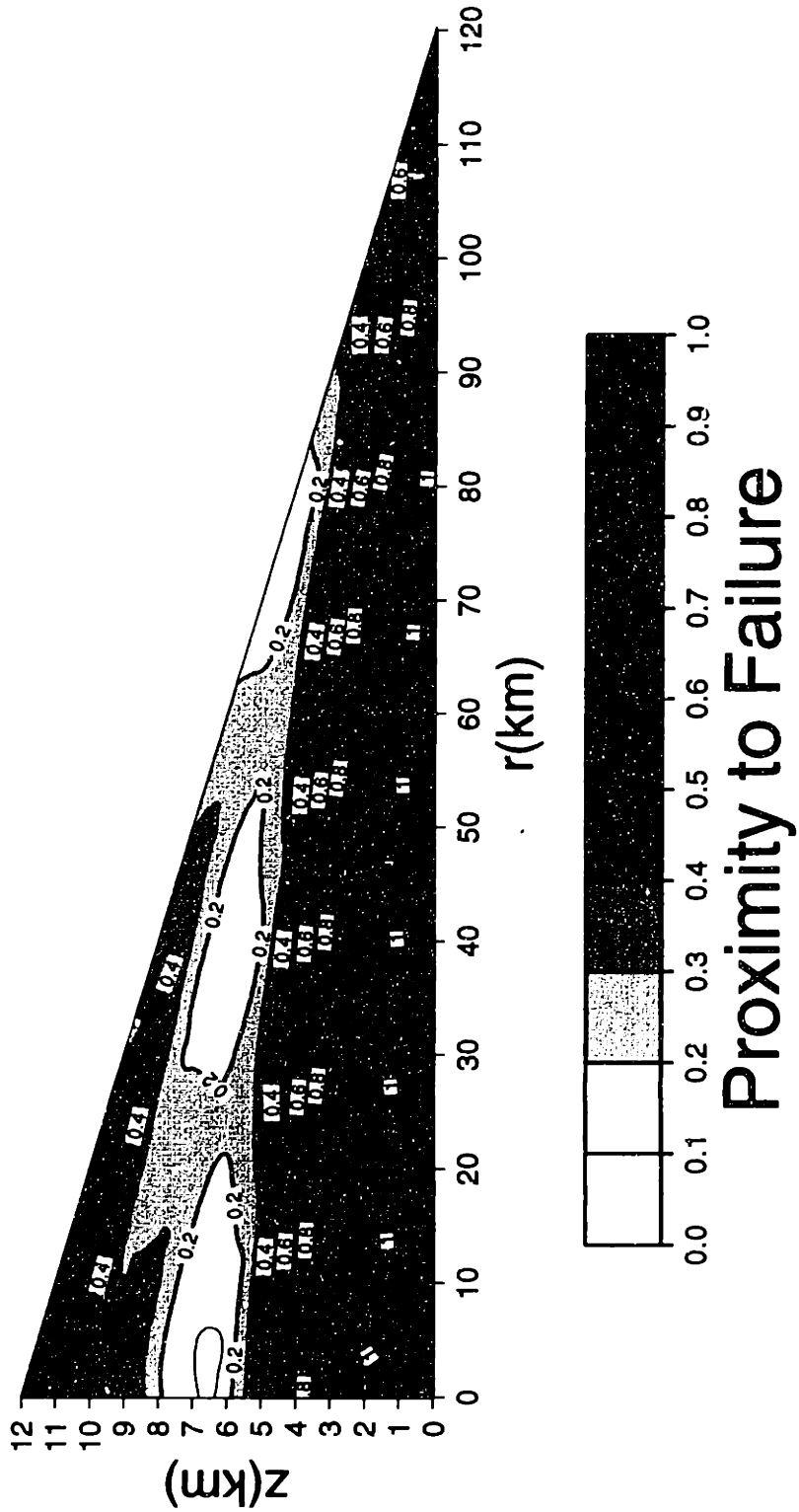

Figure 14i.

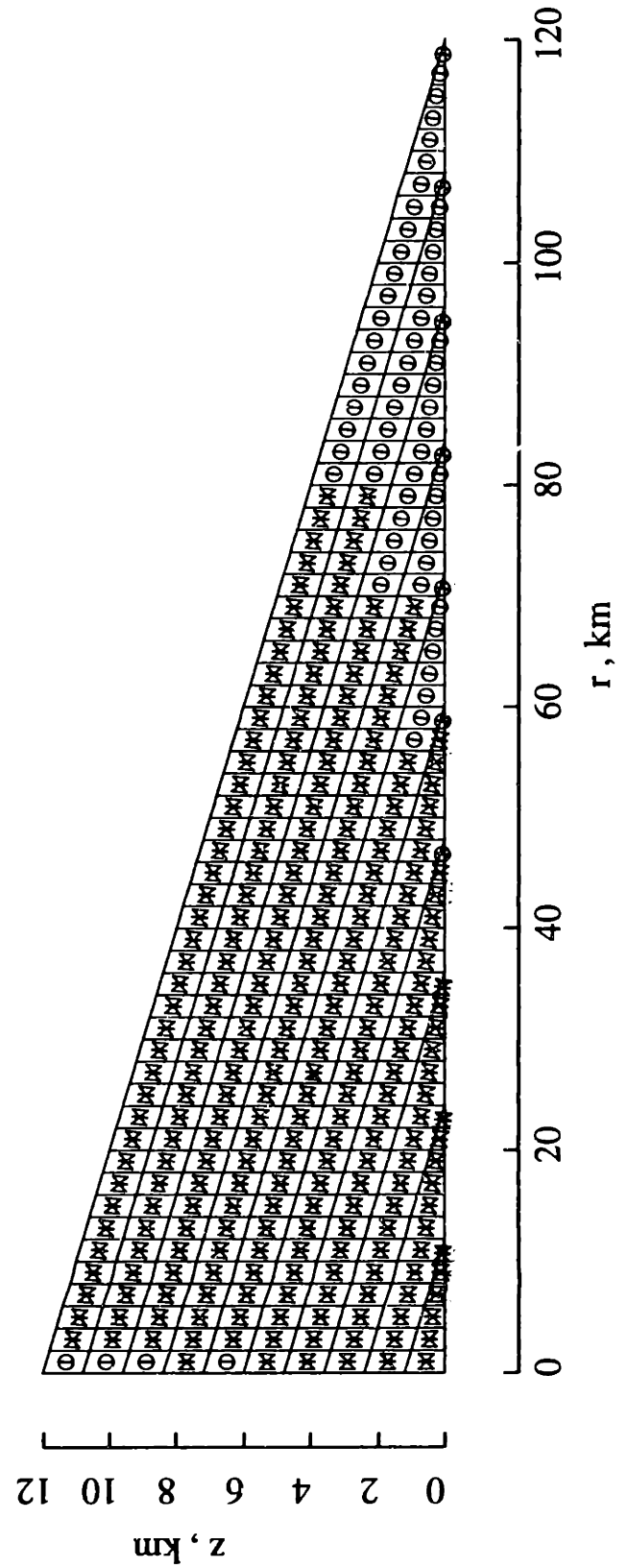

Figure 15a.

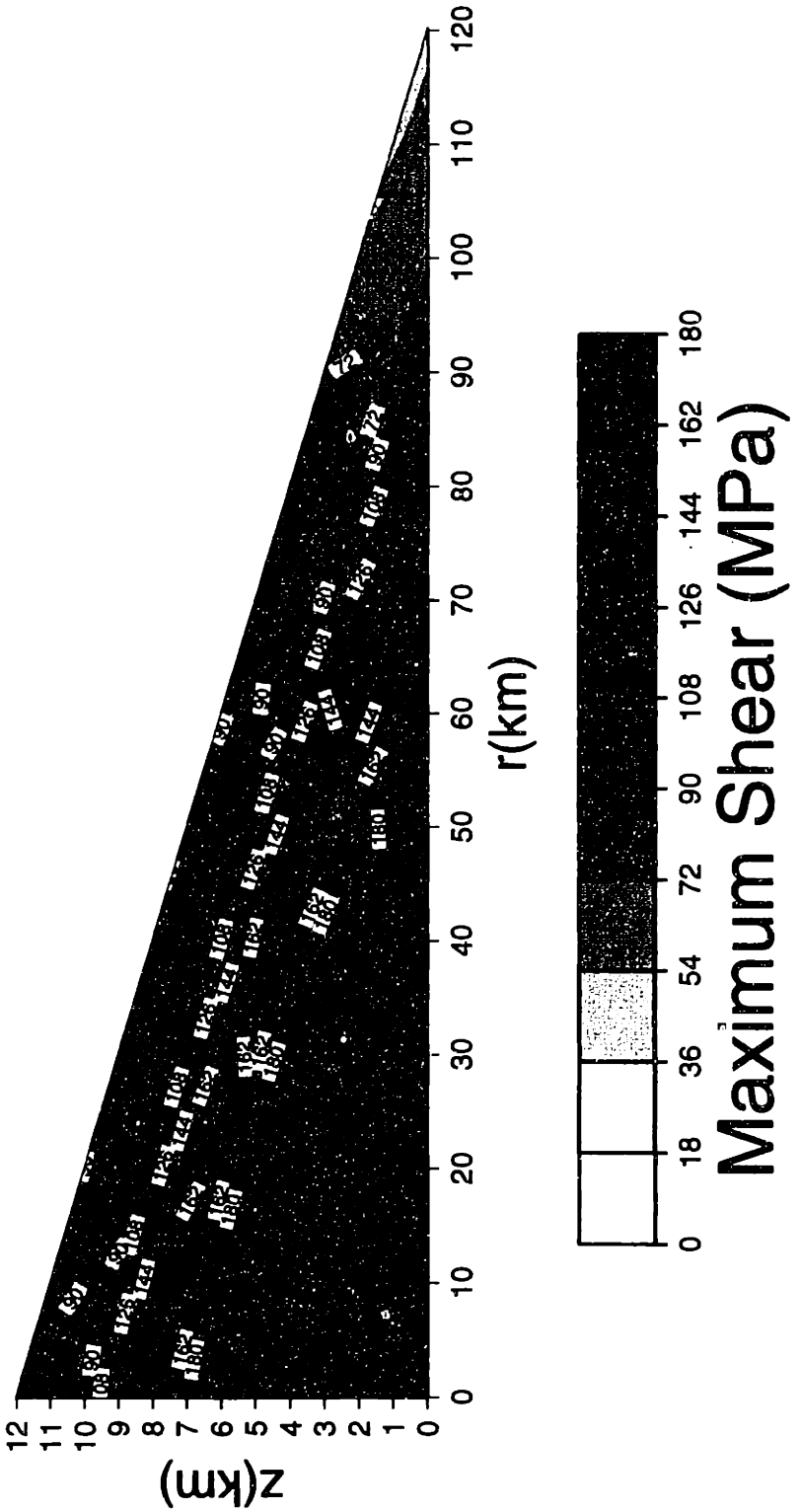
z(km)
0
1
2
3
4
5
6
7
8
9
10
11
12
r(km)
0
10
20
30
40
50
60
70
80
90
100
110
120
Maximum Shear (MPa)
0
18
36
54
72
90
108
126
144
162
180

Figure 15b.

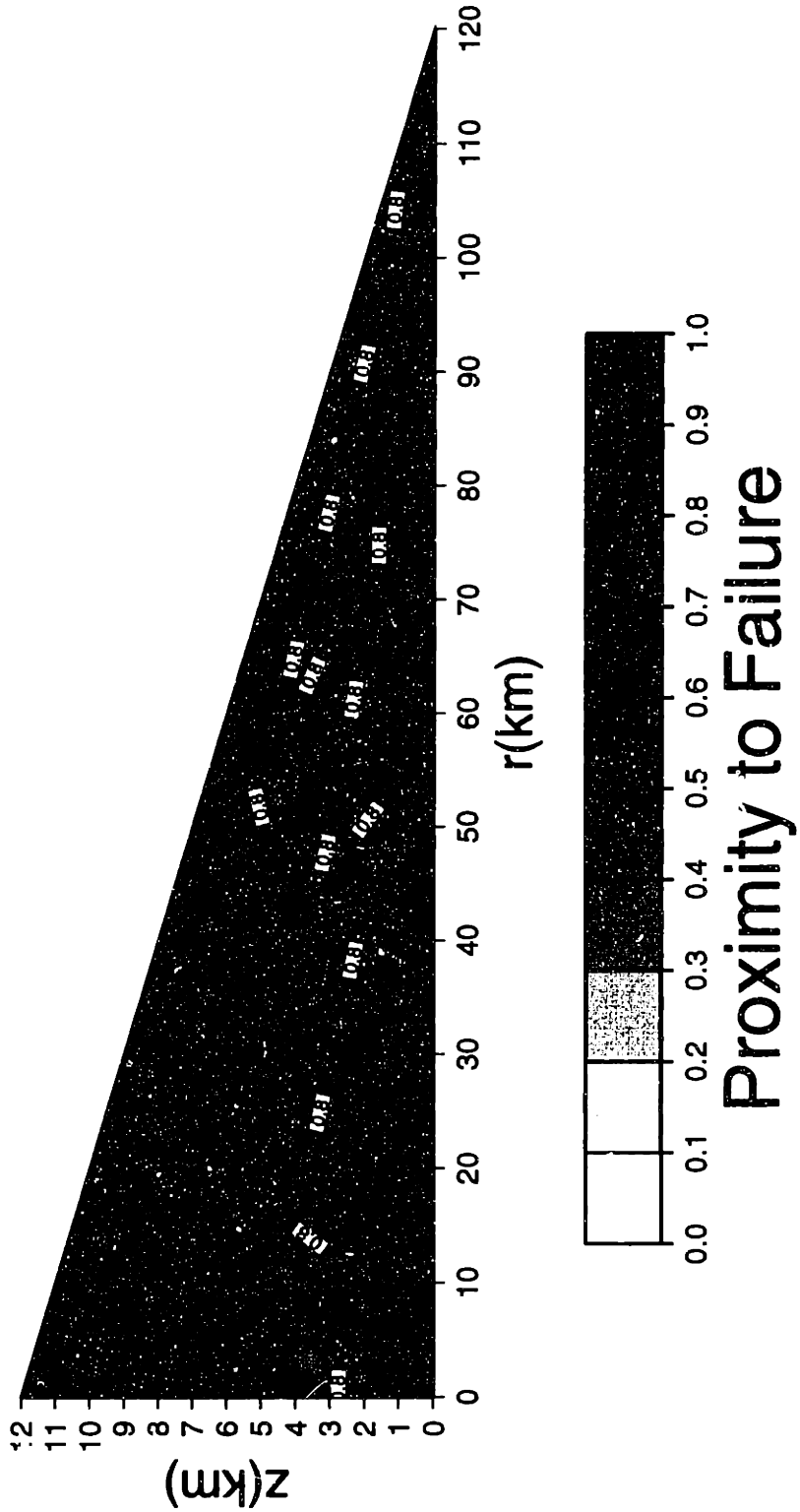

Figure 15c.

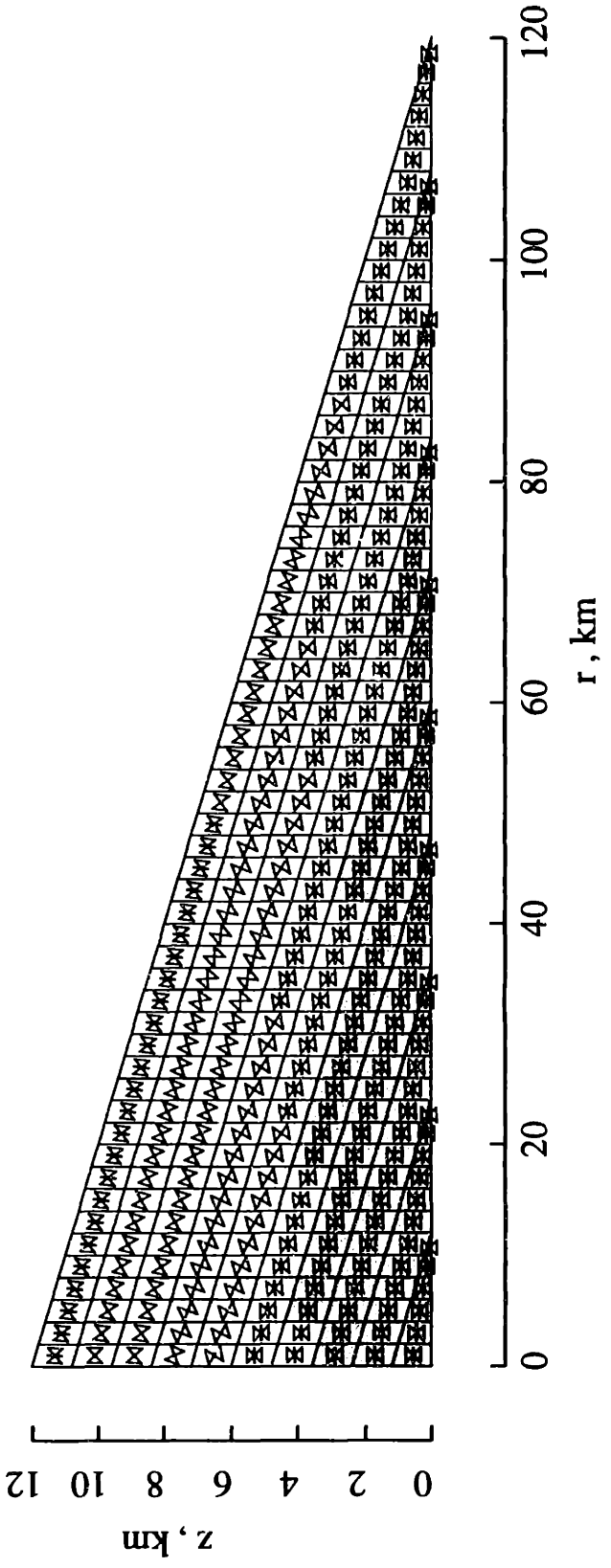

Figure 16a.

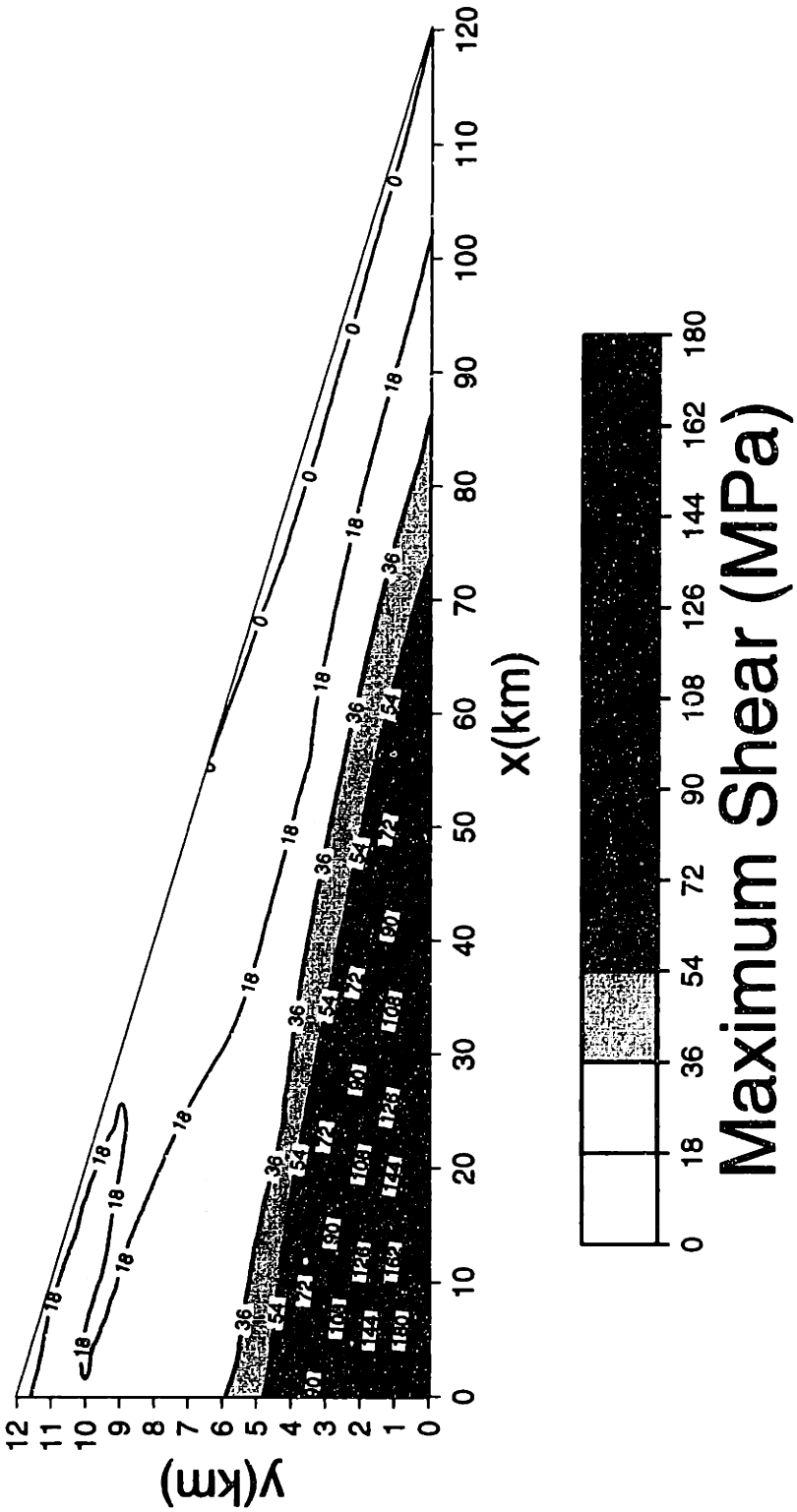

Figure 16b.

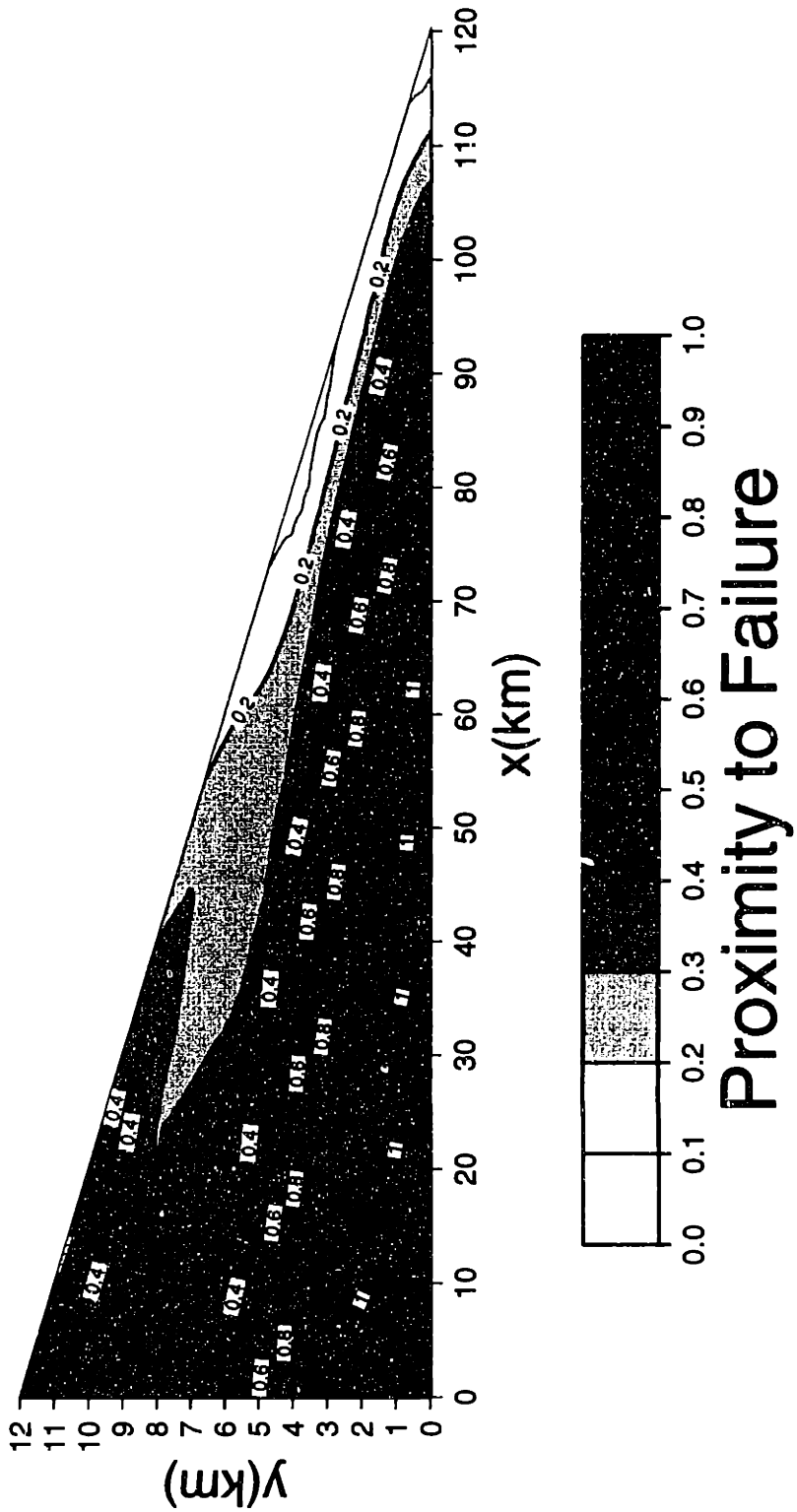

Figure 16c.

Figure 17a.

Figure 17b.

Figure 17c.

Figure 18a.

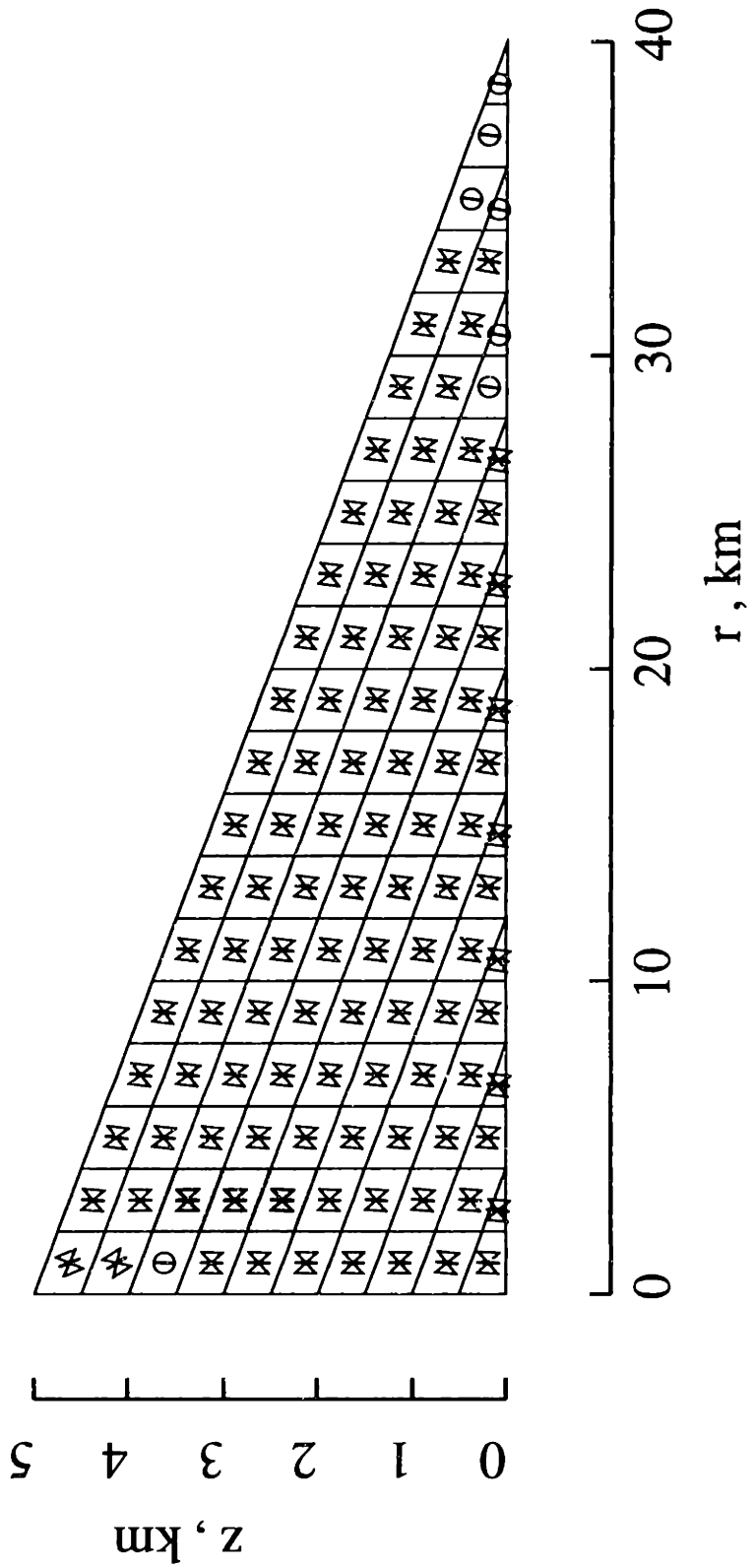

Figure 18b.

Figure 18c.

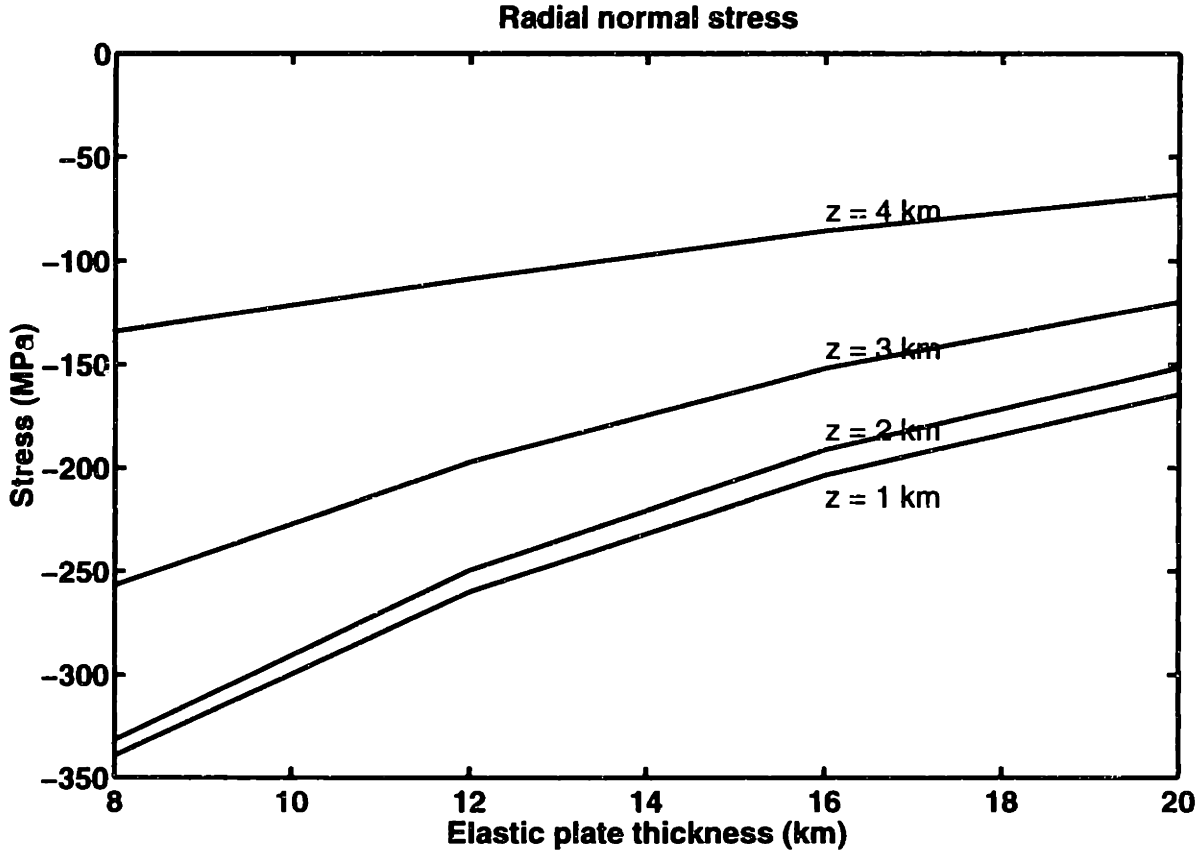
Radial normal stress
0
-50
-100
-150
-200
-250
-300
-350
Stress (MPa)
z = 4 km
z = 3 km
z = 2 km
z = 1 km
8
10
12
14
16
18
20
Elastic plate thickness (km)

Figure 19a.

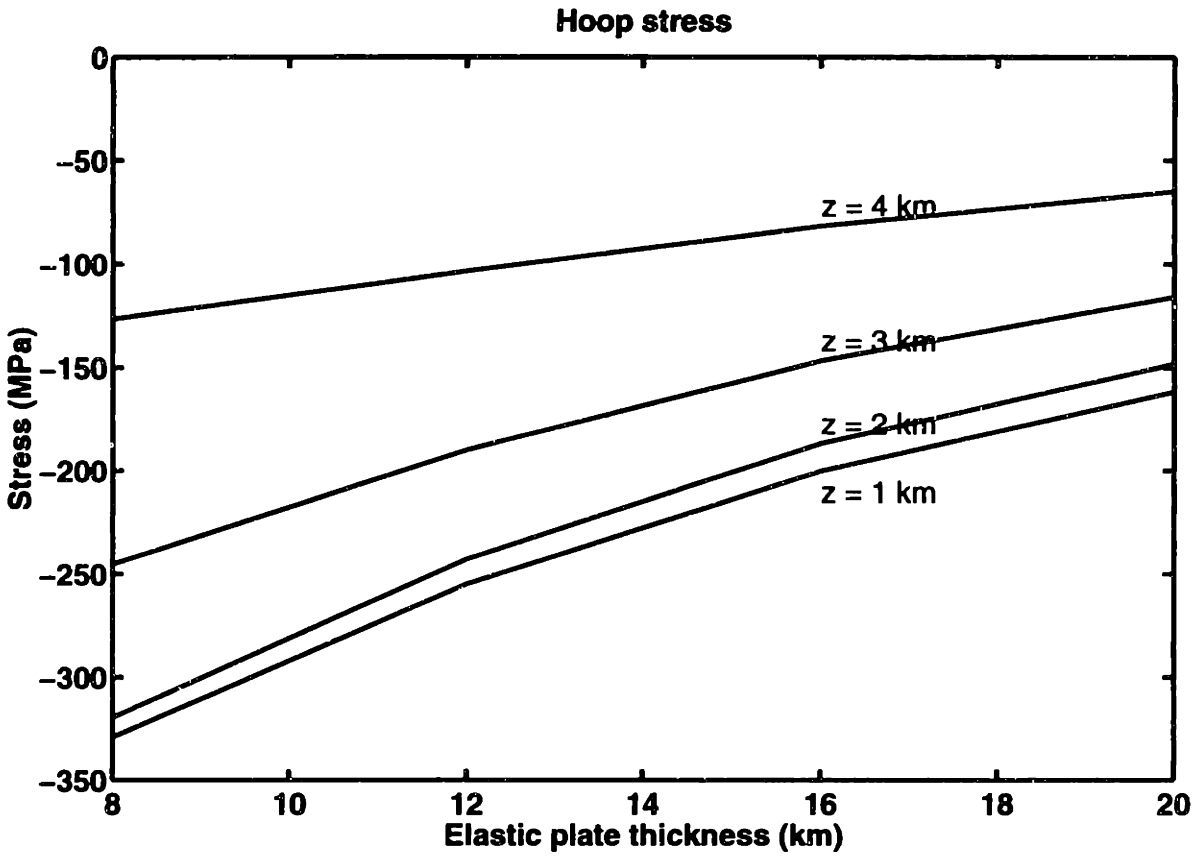
Hoop stress
0
−50
−100
−150
−200
−250
−300
−350
Stress (MPa)
z = 4 km
z = 3 km
z = 2 km
z = 1 km
8
10
12
14
16
18
20
Elastic plate thickness (km)

Figure 19b.

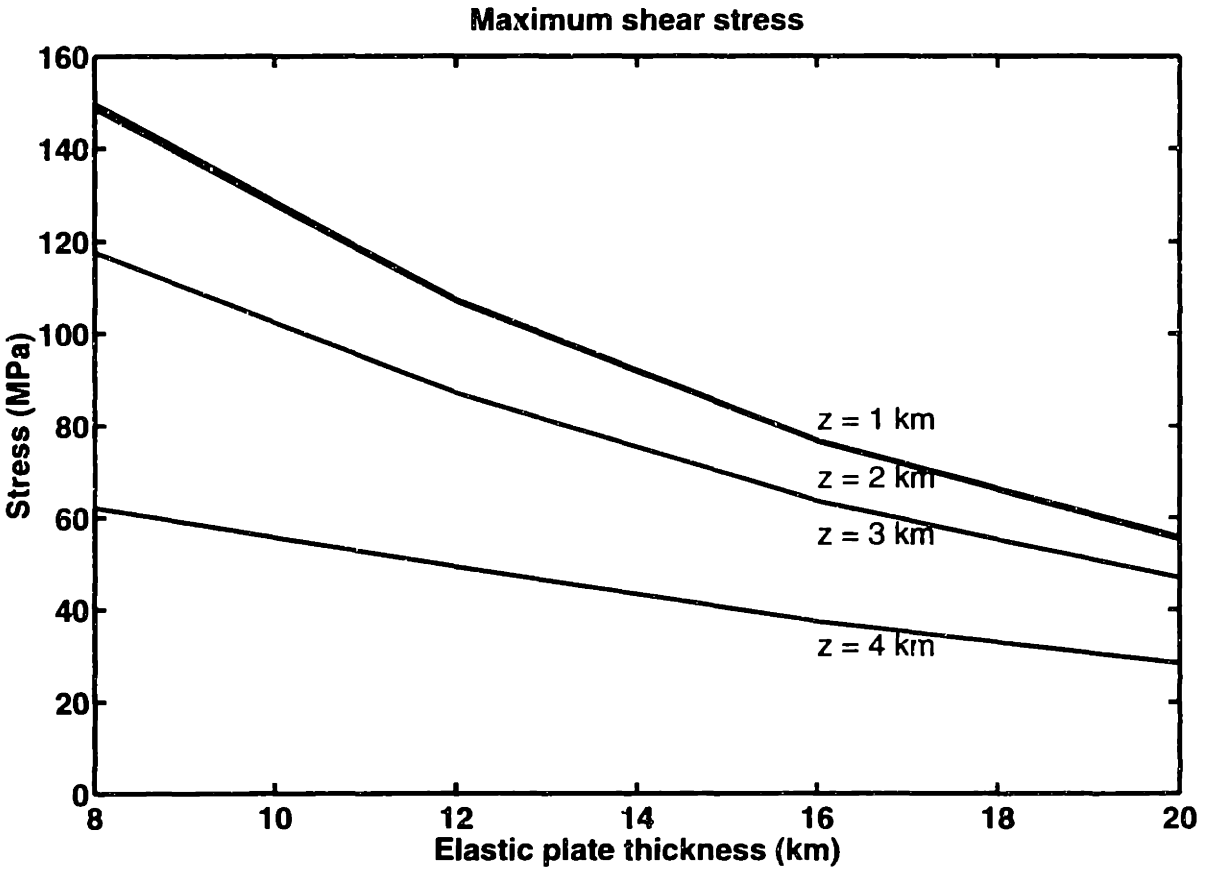
Maximum shear stress
160
140
120
100
80
60
40
20
0
Stress (MPa)
8
10
12
14
16
18
20
Elastic plate thickness (km)
z = 1 km
z = 2 km
z = 3 km
z = 4 km

Figure 19c.

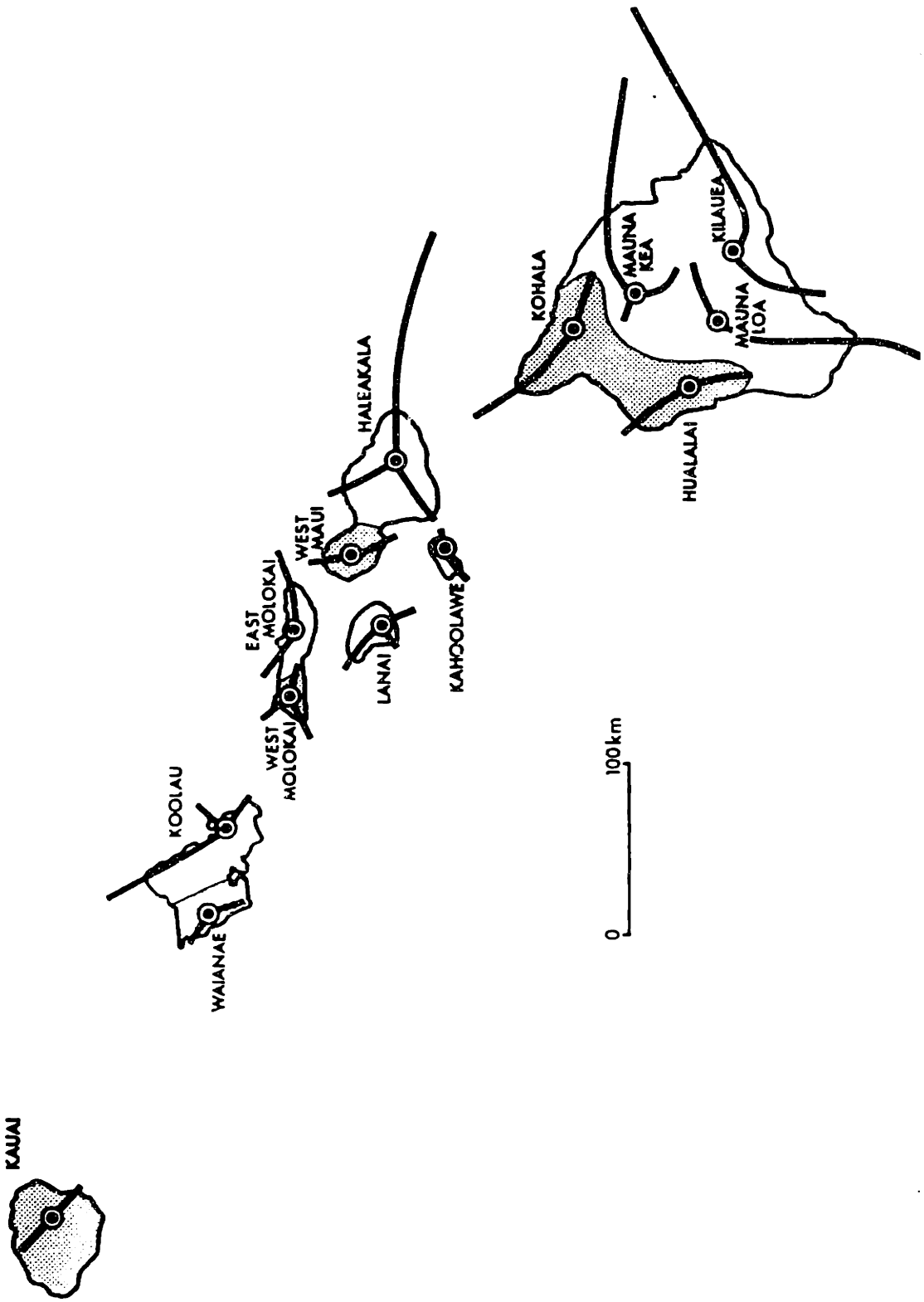
KAUAI
KOOLAU
WAIANAE
WEST MOLOKAI
EAST MOLOKAI
LANAI
HALEAKALA
WEST MAUI
KAHOOLAWE
KOHALA
MAUNA KEA
MAUNA LOA
KILAUEA
HUALALAI
0
100km

Figure 20a.

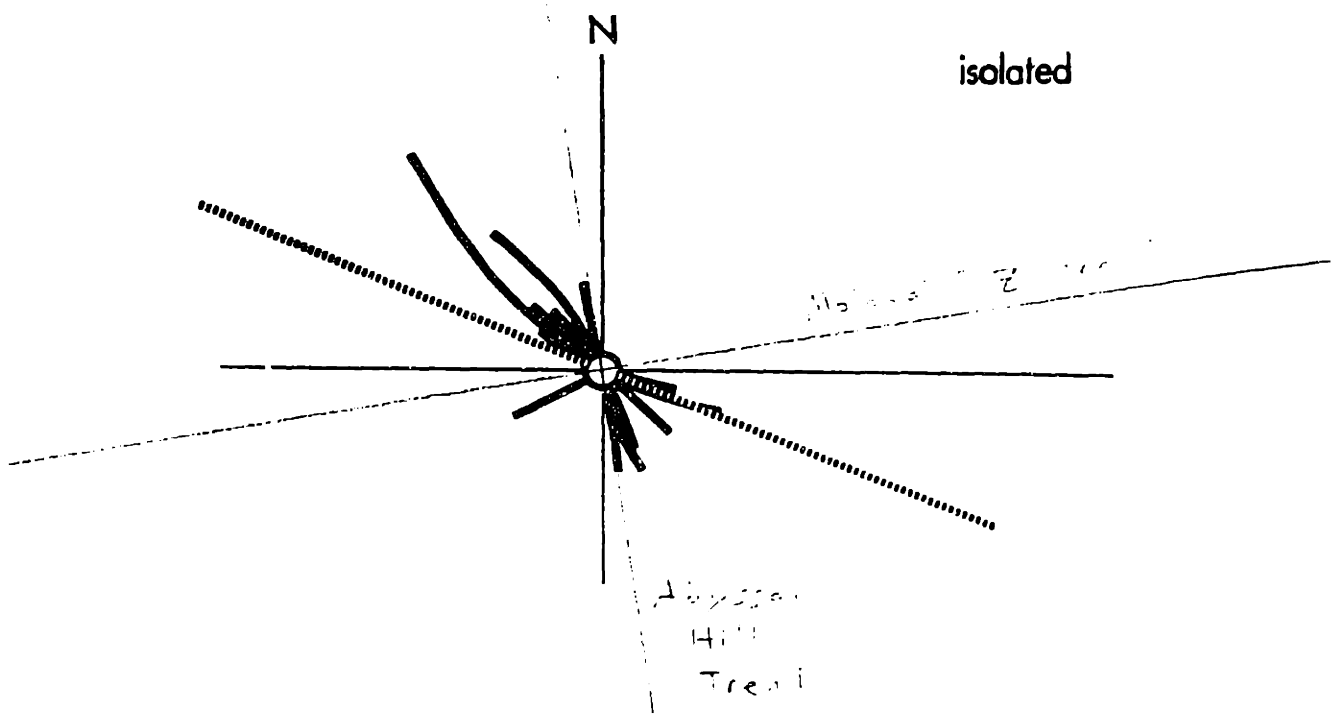

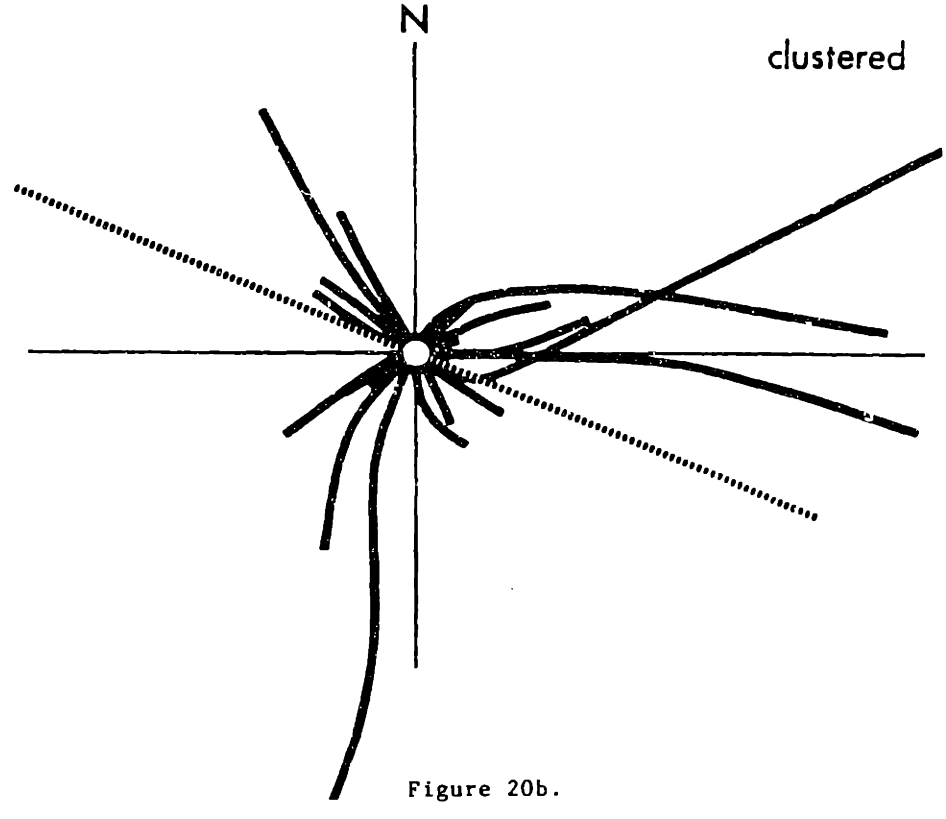

Figure 20b.

Chapter 4

State of Stress, Tectonics, and Structure of Large Volcanoes on Venus

Introduction

Large volcanoes on Venus appear to be structurally distinct from those on Earth and Mars. Studies of Magellan synthetic aperture radar (SAR) images reveal little evidence of well-defined radial rift zones or large-scale mass wasting on the flanks of large shield volcanoes on Venus [e.g., *Keddie and Head*, 1994b, 1995; *Campbell and Rogers*, 1994]. Such structures are believed to be fundamental to the development of many large volcanoes on Earth (Chapter 3), and are postulated to play a similar role on the Tharsis Montes and Olympus Mons on Mars (Chapter 2). Our goal in this chapter is to determine the conditions and processes that account for the unique style of large volcanoes on Venus. To this end, we perform an extensive survey of large volcanoes on Venus. We first compile a data base identifying 146 large volcanoes. This data base includes values of characteristic structural parameters such as edifice heights and radii, and radii of flow aprons surrounding the edifices. We point out

important characteristics common to a broad majority of large volcanoes. We then select a group of ten representative volcanoes for more detailed discussion, highlighting important tectonic and morphological features. In order to understand the forces that produced the observed structural features on these volcanoes, we model the evolution of stress and deformation in a growing volcanic edifice using the finite element method. We argue that the bases of Venus volcanoes are welded to the underlying lithosphere. The finite element calculations reveal the effects of this boundary condition on the structural evolution of large volcanoes. We then consider the mechanism by which flexural moats around large volcanoes on Venus are filled. We use the observed surface structure of the volcanoes to formulate a model of moat filling by magma flows which has important implications for global magma flux and resurfacing.

Characteristics of Large Volcanoes on Venus

The existence of large volcanoes on Venus was first revealed by the use of ground-based radar imaging. Spacecraft sent to Venus (such as Pioneer Venus and the Soviet Venera missions) returned data giving an improved view of the volcanic, tectonic, and impact processes that have shaped the surface. Data from the Magellan mission to Venus are of greatly enhanced resolution (as good as 75 meters) and completeness (about 98% of the surface of the planet has been mapped). The current data are sufficient to launch a comprehensive study of the characteristics of large volcanoes on Venus. In this section, we first briefly describe the types and quality of the available data. We then describe the compilation of a data base for the 145 large volcanoes on Venus. We then select a representative group of ten volcanoes for detailed discussion, focusing on the geologic, tectonic and topographic characteristics of the structures. Finally, we discuss the common characteristics of Venus volcanoes, and contrast these with characteristics of terrestrial hotspot volcanoes.

The Magellan mission has produced three data sets that are useful to a study of large

volcanoes. The first of these consists of SAR images of the surface. Such images provide the principal tool for studying the surficial geology of volcanoes on Venus. Tectonic structures such as calderas, fractures, rifts, and graben can be identified and mapped. Lava flows are also evident in the images; individual flow units can often be discerned and traced for long distances. Sedimentation is generally negligible on Venus, so the structure of the lower edifice, flexural moat and surface of the surrounding lithosphere is fully exposed and can be observed in the radar images. In contrast, such structures on terrestrial oceanic volcanoes are obscured by sediment cover and often by ocean.

The second data set consists of topographic measurements taken by the Magellan radar altimeter [*Ford and Pettengill*, 1992]. The horizontal resolution can be as good as 8 km along track, and 20 km across-track, but it varies with location. At the conclusion of the altimetry experiment, about 95% of the surface area of Venus had been mapped at a resolution significantly better than that available for much of the Earth. We utilize this data set to create topographic maps and cross-sections of volcanoes. As with the radar images, volcanic topography is not obscured by sediment cover or an intervening ocean.

The third data set is the global gravity field, most commonly represented by a spherical harmonic expansion [*Konopliv and Sjogren*, 1994; *Konopliv*, 1995a] to degree and order 90, generated from Doppler residuals in the tracking data from both the Magellan and Pioneer Venus spacecraft. The gravity field is useful as a constraint on interior properties, such as lithospheric rigidity. The gravity anomalies over several volcanoes are consistent with an elastic plate thickness (T_e) in the range 30–50 km [*Phillips*, 1994; *McGovern et al.*, 1995]. The expected flexural signal, however, is at the edge of resolution of the present gravity field, and other mechanisms, such as dynamic topography from an ascending mantle plume [*Kiefer*, 1994], may also contribute to the observed signal. In this study, for these reasons, we primarily rely on the radar image and topography data.

Construction of a volcano data base

The nearly global coverage of SAR image and topography data attained by the Magellan mission offers the opportunity to compile comprehensive surveys of various categories of topographic, volcanic, and tectonic features. We take advantage of this opportunity to perform such an exercise for large volcanoes. Through such a survey we can determine the characteristic morphological and tectonic styles of Venus volcanoes. These observations will constrain the processes that regulate the growth and evolution of the volcanoes; they will serve as the basis for generating models of such processes. We can also compare and contrast these characteristic properties with those of large volcanoes on other planets (see Chapter 5), to gain further insight about the conditions that regulate the growth of large volcanoes.

On the basis of the image and topography data sets we compiled a data base of 145 large volcanic edifices by means of the following procedure. A preliminary version of the data base was first obtained from a map of large volcano locations from *Head et al.* [1992]. These workers defined large volcanoes as volcanic centers with positive topography and radially oriented lava flows, with diameter (as measured across the flows) $\geq$ 100 km. We located these features on the Full-resolution and Compressed-once Magellan Image Data Record (F-MIDR and C1-MIDR, respectively) image mosaics. We then made topographic maps of the volcanoes and their surroundings from a digitized version of the Global Topography Data Record (GTDR), altimetry data in the form of a GIPS (General Image Processing System) image provided by P. Ford and G. Pettengill of M.I.T. This topography is referenced to a mean planetary radius of 6051.9 km. We deleted from the data base several features that lacked strong image or topographic evidence for the existence of a volcanic edifice. We also added several volcanoes that were found in a general reconnaissance of C1-MIDRs and global topography. Coordinates and physical parameters of these volcanoes are listed in Table 4.1, and volcano locations are marked with triangles on a topographic map of Venus in Figure 1. Volcanoes originally listed on the *Head et al.* [1992] map are marked with a "v" in the "Class" column of Table 4.1.

Name	Class	Latitude	Longitude	Edifice radius (km)	Flow Apron radius (km)	Base Altitude (km)	Summit altitude (km)	Height (km)
Unknown	v	76.00	236.00	142	225	0.0	1.8	1.8
Feronia	vc	66.00	279.00	160	225	0.0	0.7	0.7
Melia	vc	62.90	119.50	135	165	0.4	1.2	0.8
Fakohotu	vc	59.00	108.00	255	225	0.2	1.0	0.8
Mokosha	vc	57.50	255.00	255	260	-0.2	1.2	1.4
Unknown	v	56.00	216.50	150	225	0.1	0.5	0.4
Unknown	v	53.00	98.00	35	135	0.0	0.3	0.3
Unknown	v	52.25	267.50	180	252	-0.4	0.5	0.9
Unknown	v	51.50	125.00	60	125	0.0	0.2	0.2
Unknown	v	49.00	7.75	60	200	0.3	0.6	0.3
Unknown	v	48.00	97.75	35	200	-0.8	-0.4	0.4
Unknown	v	47.00	7.00	40	100	0.0	0.4	0.4
Unknown	v	46.00	213.00	30	100	-1.0	-0.2	0.8
Unknown	v	45.50	162.00	37	75	-0.9	-0.6	0.3
Unknown	v	44.75	184.80	60	60	-0.6	0.9	1.5
Sekmet	v	44.00	241.50	140	200	-0.8	2.0	2.8
Unknown	v	40.50	8.00	95	150	-0.8	0.5	1.3
Unknown	v	40.50	246.00	145	250	-0.3	0.0	0.3
Unknown	v	40.00	203.00	45	100	-0.8	0.4	1.2
Unknown	v	39.50	203.50	40	100	-0.8	0.2	1.0
Unknown	v	39.50	208.00	60	75	-0.8	-0.2	0.6
Unknown	v	38.75	55.25	165	200	-0.8	1.0	1.8
Unknown	n	38.00	223.00	350	260	0.7	4.0	3.3
Unknown	v	37.50	342.00	36	100	-1.2	-0.5	0.7
Unknown	vc	37.00	257.00	115	275	-1.0	-0.6	0.4
Nefertiti	c	36.00	48.00	260	275	0.0	2.6	2.6
Unknown	v	35.50	211.50	165	200	-0.4	1.4	1.8
Unknown	v	35.00	219.50	235	275	0.2	2.6	2.4
Unknown	v	35.00	276.50	60	75	1.4	2.6	1.2
Unknown	v	34.00	246.00	67	125	-0.5	-0.3	0.2
Unknown	v	32.00	244.50	55	75	-0.6	0.2	0.8
Unknown	v	32.00	206.00	40	100	-0.2	0.0	0.2
Unknown	n	30.00	49.00	355	500	0.0	2.5	2.5
Unknown	v	29.50	356.00	30	160	0.0	0.3	0.3
Tepev	n	29.00	45.00	125	200	-0.6	4.9	5.5
Umm Attar	vc	28.50	65.50	155	237	-0.8	0.0	0.8
Unknown	vc	28.50	241.50	90	225	-0.3	0.6	0.9
Unknown	n	28.50	326.00	35	50	-0.7	0.0	0.7
Unknown	vc	26.00	208.00	80	200	0.0	0.6	0.6
Unknown	v	24.00	3.50	40	150	-0.4	-0.2	0.2
Unknown	vc	24.00	264.00	115	225	0.4	4.4	4.0
Theia	v	23.50	280.00	230	375	3.0	4.5	1.5

Table 4.1: Locations and physical parameters of large volcanoes on Venus. Volcanoes originally listed in the volcano map of *Head et al.* [1992] or the corona table of *Stofan et al.* [1992] are marked in the "Class" column with a "v" or a "c", respectively. Volcanoes not in either list are marked with an "n". Quantities not available for a given volcano are denoted by "N.A.".

Name	Class	Latitude	Longitude	Edifice radius (km)	Flow Apron radius (km)	Base Altitude (km)	Summit altitude (km)	Height (km)
Ereshkigal	vc	22.00	84.00	200	220	-0.2	1.4	1.6
Unknown	vc	22.00	224.00	125	300	0.6	3.5	2.9
Unknown	v	22.00	344.70	45	50	-0.1	0.7	0.8
Sif	v	22.00	351.50	142	300	0.4	2.6	2.2
Gula	v	22.00	359.00	190	375	0.6	3.4	2.7
Unknown	v	21.00	20.50	20	120	-0.4	0.0	0.4
Unknown	v	21.00	342.50	50	300	-0.3	0.0	0.3
Unknown	n	19.50	344.00	35	75	-0.3	0.0	0.3
Kunhild	vc	19.30	80.10	210	300	-0.1	1.4	1.5
Unknown	n	19.00	268.00	120	120	1.2	1.8	0.6
Unknown	vc	18.00	153.00	105	600	-0.8	0.0	0.8
Unknown	v	18.00	163.00	30	75	-0.3	0.2	0.5
Unknown	n	18.50	303.00	35	80	-0.5	0.4	0.9
Unknown	n	18.00	196.00	265	320	1.4	3.0	1.6
Unknown	v	17.50	211.50	185	275	0.0	1.4	1.4
Unknown	n	17.50	303.50	65	110	-0.5	0.5	1.0
Unknown	vc	17.00	252.00	205	235	-0.2	1.6	1.8
Unknown	vc	17.00	260.00	145	180	-0.4	0.4	0.8
Unknown	v	15.50	69.50	175	235	-0.2	1.2	1.4
Sappho	vc	14.50	15.40	192	250	-0.2	1.4	1.6
Unknown	v	14.00	70.00	49	112	0.0	1.0	1.0
Unknown	vc	14.00	205.00	125	215	0.6	2.6	2.0
Unknown	v	14.00	240.50	90	250	0.0	0.4	0.4
Unknown	v	14.00	340.00	188	180	-1.2	0.0	1.2
Unknown	v	13.50	273.50	82	110	-0.4	0.0	0.4
Unknown	v	13.00	211.00	30	60	-0.2	1.5	1.7
Unknown	v	12.00	226.00	140	N.A.	0.8	2.0	1.2
Anala	vc	11.00	14.50	190	325	0.6	2.0	1.4
Unknown	v	10.00	201.00	45	80	1.0	1.8	0.8
Unknown	v	10.00	275.00	185	255	-0.6	1.6	2.2
Unknown	v	9.50	209.50	100	160	0.4	2.4	2.0
Somagalgas	v	9.30	348.50	125	300	-0.8	-0.2	0.6
Unknown	v	9.00	29.00	165	250	-0.5	2.0	2.5
Sapas	v	9.00	188.00	124	275	1.5	3.4	1.9
Unknown	v	9.00	218.50	100	100	1.8	3.2	1.4
Unknown	vc	9.00	262.00	260	300	-0.4	1.0	1.4
Unknown	v	7.00	158.00	35	90	0.0	0.6	0.6
Unknown	v	6.00	170.00	50	100	0.0	1.0	1.0
Unknown	v	4.50	206.50	75	175	1.8	2.7	0.9
Ozza	v	4.00	200.00	395	600	2.0	6.0	4.0
Unknown	v	3.50	270.00	60	250	-0.4	2.6	3.0
Unknown	n	3.00	45.50	110	140	0.0	1.8	1.8
Unknown	n	2.50	314.00	70	125	0.0	1.4	1.4
Unknown	v	2.50	301.00	70	225	0.7	1.8	1.1
Unknown	vc	1.50	222.50	200	225	0.4	3.0	2.6
Unknown	n	1.00	316.00	50	180	0.2	1.2	1.0
Unknown	v	0.50	34.50	115	175	0.4	2.7	2.3

Table 4.1: (continued). Locations and physical parameters of large volcanoes on Venus.

Name	Class	Latitude	Longitude	Edifice radius (km)	Flow Apron radius (km)	Base Altitude (km)	Summit altitude (km)	Height (km)
Maat	v	0.00	194.00	195	300	2.0	8.8	6.8
Unknown	v	0.00	288.00	210	250	0.8	2.2	1.4
Unknown	v	-2.00	194.00	145	250	2.5	6.5	4.0
Unknown	v	-2.00	256.50	60	150	-0.9	-0.6	0.3
Unknown	v	-2.25	287.50	260	300	1.0	2.6	1.6
Seia	vc	-3.00	153.00	100	175	0.5	0.8	0.3
Unknown	v	-6.25	299.00	60	140	1.5	2.6	1.1
Unknown	v	-6.50	172.00	30	100	0.4	1.0	0.6
Unknown	vc	-8.00	221.50	205	240	0.8	3.6	2.8
Unknown	vc	-8.00	243.25	175	250	-0.7	0.4	1.1
Unknown	n	-9.00	225.00	120	200	0.6	1.2	0.6
Unknown	v	-9.00	305.50	70	100	0.5	1.8	1.3
Unknown	vc	-9.00	214.00	160	190	0.4	2.0	1.6
Unknown	vc	-11.00	173.00	150	250	1.4	3.2	1.8
Unknown	vc	-11.00	211.00	60	200	0.4	1.8	1.4
Unknown	v	-11.00	355.50	50	100	-0.7	-0.6	0.1
Unknown	c	-12.00	251.00	180	275	-0.4	1.0	1.4
Unknown	vc	-13.00	261.00	155	230	-0.2	1.8	2.0
Unknown	n	-13.50	315.50	60	165	-0.7	0.3	1.0
Miralaidji	vc	-14.00	163.80	170	275	0.4	1.8	1.4
Unknown	v	-14.00	305.50	60	60	0.4	0.8	0.4
Unknown	vc	-15.00	215.00	190	215	0.1	1.2	1.1
Unknown	v	-16.50	208.00	75	100	0.4	1.8	1.4
Unknown	vc	-16.50	255.50	150	220	0.4	1.6	1.2
Unknown	n	-17.00	244.00	265	350	-0.4	1.6	2.0
Unknown	v	-18.00	285.00	145	275	1.9	4.6	2.7
Unknown	v	-18.50	259.00	155	200	0.4	1.1	0.7
Unknown	vc	-22.00	291.00	120	200	0.0	1.8	1.8
Unknown	vc	-24.50	177.50	110	170	0.8	2.0	1.2
Ushas	n	-25.00	325.00	125	245	0.2	1.4	1.2
Unknown	v	-26.00	238.00	20	75	-0.4	0.1	0.5
Unknown	n	-26.00	247.00	85	165	-0.1	0.2	0.3
Unknown	n	-26.00	297.00	55	60	-0.2	1.4	1.6
Unknown	vc	-27.50	262.00	90	240	0.5	1.0	0.5
Unknown	vc	-28.00	280.50	205	275	0.4	1.7	1.3
Unknown	v	-29.00	296.50	55	65	0.0	2.3	2.3
Unknown	n	-31.00	224.50	20	75	0.0	0.3	0.3
Unknown	v	-32.00	100.00	60	225	0.6	2.3	1.7
Kunapipi	vc	-34.00	86.00	255	325	-0.2	2.0	2.2
Innini	n	-34.00	329.00	167	220	0.0	2.2	2.2
Unknown	v	-35.00	226.00	55	60	-0.1	0.5	0.6
Unknown	n	-37.50	165.00	53	115	-0.8	-0.4	0.4
Unknown	v	-37.50	225.00	35	50	0.0	0.8	0.8
Ninhursag	c	-38.00	23.50	135	150	0.1	0.7	0.6
Unknown	vc	-38.00	270.00	145	285	-0.2	1.8	2.0
Unknown	c	-38.50	284.00	190	325	0.8	2.2	1.4

Table 4.1: (continued). Locations and physical parameters of large volcanoes on Venus.

Name	Class	Latitude	Longitude	Edifice radius (km)	Flow Apron radius (km)	Base Altitude (km)	Summit altitude (km)	Height (km)
Hathor	n	-40.00	325.00	215	310	0.2	2.2	2.0
Unknown	v	-42.50	28.00	20	50	0.1	0.2	0.1
Unknown	vc	-42.50	280.00	300	325	0.6	2.2	1.6
Unknown	v	-43.00	258.00	50	110	-0.3	0.1	0.4
Unknown	n	-43.50	321.50	N.A.	95	N.A.	N.A.	N.A.
Unknown	v	-45.00	215.00	115	225	0.6	3.4	2.8
Unknown	v	-45.00	273.00	125	155	0.2	1.8	1.6
Unknown	vc	-45.00	287.00	140	225	0.5	1.0	0.5
Unknown	v	-45.50	294.00	110	160	0.3	1.0	0.7
Jord	vc	-59.00	350.00	115	200	0.4	1.0	0.6

Table 4.1: (continued). Locations and physical parameters of large volcanoes on Venus.

Several volcanoes in the data base exhibit characteristics attributed to coronae. Coronae are structures characterized by an annulus of tectonic features [*Stofan et al.*, 1992]. Most of these tectonic features are believed to be extensional [*Stofan et al.*, 1992]. Radially oriented tectonic features also occur on many coronae; these usually predate the circumferential features. Corona topography is characterized by a raised annulus surrounding a lower central region [*Stofan et al.*, 1992]. The morphology of coronae has been attributed to deformation of the lithosphere by ascending mantle diapirs [*Stofan et al.*, 1992; *Squyres et al.*, 1992b; *Janes et al.*, 1992; *Koch*, 1994]. A class of features called novae [*Janes et al.*, 1992] are characterized by domical topography and radial tectonics, consistent with deformation predicted in the earliest stages of diapiric ascent. Thus novae are considered to be an early stage in the development of coronae [*Janes et al.*, 1992]. The large volcanoes exhibiting corona characteristics also appear in a corona data base compiled by *Stofan et al.* [1992]; these are marked with a "c" in the "Class" column of Table 4.1.

In Table 4.1, volcano radius is defined in two different ways. Topographic profiles are used to define an "edifice radius," the average distance from the center of the volcano to the break in slope at the edge of the edifice. The slope break may occur at different altitudes on opposite sides of the volcano, because of local variations in basement topography unrelated to the volcano. This difference is typically a few hundred meters. Measurement of the edifice

radius requires definition of an edifice basal height. We define this height from a topographic contour map by the lowest contour that closely conforms to the shape of the edifice for at least two thirds of the edifice circumference. This rule helps to resolve the ambiguity caused by regional topographic variations by providing an average value for the altitude of the slope break. "Flow apron radius" is defined by the maximum extent of flows identified in the image data as clearly emanating from the volcano. Volcanoes listed in this data base have flow apron radii larger than 50 km. Inasmuch as we based our volcano list on a earlier compilation of volcanoes greater than 100 km in diameter (on the basis of extent of flows), we believe that our list of such volcanoes is complete. The earlier list of *Head et al.* [1992] did not consider a topographic measure of diameter; we estimate that in our list all volcanoes with edifice radii $>$ 35 km are included.

Representative individual volcanoes

We have chosen a subset of the volcanoes in the data base for detailed study. These ten volcanoes are listed in Table 4.2. The volcanoes in this subset are representative of the ranges of morphologies, topographic profiles, and regional settings encountered in the entire set of large volcanoes on Venus. In addition, all but one of these volcanoes (the one at 36°N, 211°E) have been discussed previously in the literature. Many have been mapped, and several have been the subject of detailed geological, tectonic, and stratigraphic analysis. We use these discussions and analyses as the basis for the construction of our models.

For each volcano in Table 4.2, we have produced a local topographic map from the global altimetry data set, using the Generic Mapping Tools (GMT) mapping software package [*Wessel and Smith*, 1991]. For an adopted topographic center of the edifice, twelve topographic cross sections radial to this point are generated by sampling and interpolating the data. These cross sections are then averaged to give a mean topographic profile of the volcano. We display both the raw and averaged cross sections for each volcano; the radial extents of flow aprons are marked with bars above the cross sections.

Volcano	Flow apron radius (km)	Edifice radius (km)	Height (km)	Radial tectonic features	Circum-ferential tectonic features	Summit features	Profile morphology
Sif	300	142	2.2	yes	no	caldera, radial pits	peak
Gula	375	190	2.7	yes	no	rift, 2 calderae?	peak?
9N, 29E	250	165	2.5	yes	no	caldera, radial pits	peak
Tepev	200	125	5.5	no	yes	2 peaks, caldera?	peak
Sapas	275	124	1.9	yes	yes	steep margin domes	peak
Maat	300	195	6.8	no	no	caldera, radial pits	peak
36N, 211E	200	165	1.8	no	yes	flat, small caldera?	dome
15S, 215E	215	190	1.1	yes	yes	nova-like	intermediate
4N, 270E	250	60	3.0	no	no	bright, caldera	peak
10N, 275E	255	185	2.2	no	yes	dark, ridges	dome

Table 4.2: Characteristics of large volcanoes discussed in text.

Two major shield volcanoes, Gula Mons and Sif Mons, are located on the crest of Western Eistla Regio (Figure 2), a broad topographic rise of dimensions 3200 by 2000 km [*Senske et al.*, 1992]. Image and topography data for Sif Mons are shown in Figure 3. Sif Mons rises about 2.2 km above a basal altitude of 0.4 km above mean planetary radius. The edifice and flow apron radii are 142 and 300 km, respectively. Elongated depressions and pit chains, oriented radially to the 40 km diameter summit caldera, are evidient south of an arcuate scarp defining the southern caldera boundary. These pit chains are similar in size and orientation to those observed in the western Galápagos Islands [*Chadwick and Howard*, 1991]. The central edifice is covered by an annulus of radially textured flows. These flows are superposed on mottled bright plains consisting of 150–200 km long, 15–20 km wide flows also radial in orientation [*Senske et al.*, 1992]. The mottled bright plains unit is believed to represent an early stage of high magmatic flux, based on its broad lateral and radial extent [*Senske et al.*, 1992]. Radially oriented fractures, believed to be long, narrow graben, are seen on the northwest flank [*Senske et al.*, 1992; *Grimm and Phillips*, 1992].

The edifice of Gula Mons rises about 2.7 km above a basal altitude of 0.6 km. Edifice and flow apron radii are 190 and 375 km, respectively. Images of Gula (Figure 4) reveal a complex morphology. A simple summit caldera is not evident. Instead, a 30 by 150 km

linear deformation zone oriented northeast-southwest occupies the summit region [*Senske et al.*, 1992]; *Grimm and Phillips* [1992] interpret this feature as a rift zone connecting calderae at each end. The southeast flank of Gula Mons is cut by fractures emanating from Guor Linea (Figures 2b, 4b), a large rift zone extending several hundred kilometers along the southeastern limb of the Western Eistla rise. Additional fractures sub-radial to the summit occur in the southwest and northwest sectors of the volcano. A dense zone of fractures exposed to the northwest is believed to be an extension of Guor Linea [*Senske et al.*, 1992]. Further to the northwest, a set of annular fractures surrounds Idem-Kuva, a 225-km-diameter corona [*Stofan et al.*, 1992]. Flow deposits from Gula have been emplaced on both the east and west sides of Idem-Kuva. Gula flows have a predominantly radial orientation. The flow apron is highly asymmetric, however. Flow to the southeast is limited by Guor Linea [*Senske et al.*, 1992]. Alternatively, perhaps an early stage in the construction of Gula was later disrupted by lateral propagation of the Guor rift. Flow to the northwest is blocked by Idem-Kuva. To the west, flows from Gula meet with Sif flows along an approximately north-south boundary. In the northern part of the boundary, flows from Sif appear to postdate flows and faults on Gula; farther south, the relationship is ambiguous [*Senske et al.*, 1992].

Eastern Eistla Regio is an elevated region broader than the Western Eistla Rise but not as high. The northern part of Eastern Eistla contains a concentration of large coronae. The southern part contains several large volcanoes. One of these is located at 9°N, 29°E, in low terrain on the periphery of the Eastern Eistla rise (Figure 5). The edifice rises 2.5 km above a base level of -0.5 km. Average edifice and flow apron radii are 165 and 200 km, respectively. A summit caldera, delineated by a bright ring of fractures, is about 40 km in diameter (Figure 5d). Elongated pits and chains of craters, similar to those at the summit of Sif Mons, radiate from the caldera (Figure 5d). Several sets of paired linear fractures radial to the caldera extend to the east-northeast and west-southwest (Figure 5d). Bright flows on the southern half of the volcano exhibit radial orientations. The northern half of the volcano is significantly darker (Figure 5b), but radial flows can still be seen faintly. Flows

from the volcano at 9°N, 29°E cover bright fractured plains to the northeast and southeast, and also cover darker fractured plains to the west. A long tongue of apron flows to the northeast extends up to 400 km from the summit. A smaller offshoot from this tongue is circumferentially oriented, subtending about 30° of arc to the northeast of the edifice. A small parasitic shield on the southeast flank of the main edifice is a source of additional flows (Figure 5d).

Bell Regio is a volcanic rise located at 30°N, 45°E. Bell Regio contains five major volcanic sources; Tepev Mons, a broad shield volcano east of Tepev Mons, two small edifices in high terrain to the southeast of Tepev, and Nefertiti Corona [*Campbell and Rogers*, 1994]. Tepev Mons is located on the western flank of the Bell Regio rise (Figure 6a). It reaches 5.5 km above a mean base level of -0.6 km, with average edifice and flow apron radii of 125 and 200 km, respectively. Tepev Mons is one of three volcanoes where circumferentially oriented flows are observed in the flow apron (Figure 6b). Such flows likely fill a topographic moat caused by the flexural response to the volcanic load [*McGovern and Solomon*, 1992]. Evidence for the existence of this moat can be seen in the topography (Figures 6a, c). Note the indentation of the dashed contours in a clockwise direction to the north of the edifice, and several enclosed depressions in the area. Topographic cross sections to the northwest (Figure 6c, azimuths 330 and 0 degrees) show a small depression in the radius range of the circumferential flows. The primary source of the circumferential flows appears to be to the east, probably one of the small edifices in the high terrain to the southeast of Tepev [*Campbell and Rogers*, 1994]. The high topography to the east of Tepev blocks expansion of apron flows; apron extents are much smaller in these directions (Figure 6c). On the western flank of the edifice, a fan of radial flows extends outward to the inner edge of the circumferential flows (Figure 6b). The circumferential flow unit covers the older radial flows [*Campbell and Rogers*, 1994].

Topographic contours defining the Tepev Mons edifice are roughly elliptical, with the major axis directed east-west (Figure 6a). Twin topographic peaks are centered roughly at the foci of the ellipse. The western peak is radar bright with a small dark circular region in

the center (Figure 6b). The eastern peak has a large dark circular region at center. Both of these features have been interpreted as summit calderae [*Campbell and Rogers*, 1994], presumably associated at one time with underlying magma chambers. Radially oriented fracturing is absent; however, several sets of parallel fractures, circumferential to the eastern peak, are evident on the north flank of the edifice. Their orientations relative to the proposed summit caldera suggest that these fractures are graben, caused by extensional stress from magma withdrawal from a chamber beneath the eastern peak. North of the caldera there is a prominent circumferential tectonic feature several kilometers in width. This feature is identified as a pit crater chain by *Campbell and Rogers* [1994]. Flows from this feature may contribute to the circumferential flow unit at the base of the edifice [*Campbell and Rogers*, 1994].

Sapas Mons is a large shield volcano (275 km flow apron radius, 124 km edifice radius) located to the northwest of Atla Regio. Sapas rises 1.9 km above a base level of 1.5 km. Magellan SAR image and topography data for Sapas Mons are shown in Figure 7. In the SAR image (Figure 7b), boundaries of individual volcanic flows are easily discernible. These flows have a predominantly radial orientation to the peak area of the volcano. Figure 7a shows a topographic map of Sapas Mons and vicinity. The edifice resides atop a broad domal rise, as seen in the distal cross sections (Figure 7d). Flow units extend part way down the rise. Flows reach greater radial extents in the northwest and southeast quadrants. *Keddie and Head* [1994b] suggested that preexisting high topography to the northeast and southwest (Figure 7a) influenced the emplacement of flows, encouraging flow down steeper slopes to the northwest and southeast. A set of circumferential graben (with radius about 50 km) is evident on the upper eastern flank of Sapas Mons (Figure 7c). These graben have been attributed to stresses resulting from evacuation and/or cooling of a magma chamber beneath the summit [*Keddie and Head*, 1994b]. Radial fractures extend from the lower flank of Sapas in three groups, oriented north-northeast, south-southeast and southwest (Figure 7c). These fractures are believed to be the surface manifestation of dikes radiating from the central

magma chamber [*Parfitt and Head*, 1993; *Keddie and Head*, 1994b].

There is no topographic evidence of a moat surrounding Sapas Mons. Radial cross sections of the topography (Figure 7d) show instead profiles that slope smoothly away from the edifice, reminiscent of archipelagic aprons that surround oceanic hotspot volcanoes on Earth [*Menard*, 1956]. While such terrestrial aprons are filled mostly with debris from mass wasting of the islands [*Wolfe et al.*, 1994; *Filmer et al.*, 1994], there is no evidence of landsliding or mass wasting into the region surrounding the Sapas Mons edifice. Two scalloped-margin domes that are located in the summit region (Figure 7c) do show evidence of collapse [*Keddie and Head*, 1994b], but of very limited extent, much less than that required to contribute to moat filling. These domes have much steeper slopes than the edifice as a whole, probably due to high magma viscosity during emplacement of the domes (much higher than the fluid lavas which constitue the flanks and apron of Sapas and other volcanoes). *Keddie and Head* [1994b] attribute the high viscosity to a rhyolitic composition. *Sakimoto and Zuber* [1995], however, maintain that thermal differences may account for high viscosity; under this hypothesis magmas forming the domes are not necessarily compositionally different from magmas that constitute the edifice, but instead are emplaced at lower temperatures.

Maat Mons is the tallest volcano on Venus, rising 6.8 km above an average basal elevation of 2.0 km, with average edifice and flow apron radii of 195 and 300 km, respectively. Maat sits on the northwestern flank of Dali Chasma, one of five extensional zones that intersect in Atla Regio (Figure 8b). Another large volcano to the northeast, Ozza Mons, has been heavily fractured by intersecting rift zones (Figure 8b). Maat Mons is not cut by rifts; instead, flows from Maat cover adjacent parts of the rift. These observations indicate that Maat Mons is the youngest structure in the area [*Senske et al.*, 1992]. A summit caldera about 25 km in diameter is flanked to the southeast and southwest by several radially aligned chains of small pits ([*Keddie and Head*, 1994b], Figure 8d), similar to those observed on the flanks of the western Galápagos volcanoes on Earth [*Chadwick and Howard*, 1991]. No major tectonic features are evident on Maat [*Keddie and Head*, 1994b]. Flows on Maat Mons are radially

oriented. Flows to the south and east are confined by the topography of Dali Chasma and Ozza Mons. The flow apron reaches its greatest extent to the northwest, descending toward a topographic saddle between Maat and Sapas Mons (Figure 8).

A large volcano located at 35.5°N, 211.5°E rises 1.8 km above a basal altitude of -0.4 km. Mean edifice and flow apron radii are 165 and 200 km, respectively. The upper edifice is cut by an elongated annulus of fractures, approximately 160 (north-south) by 125 (east-west) km in extent (Figure 9b). This annulus is most strongly defined in the northwest and southeast sectors. A small circular set of fractures about 30 km in diameter is located just inside the northwest section of the annulus (Figure 9c). This structure, located on a small hill that is the highest point on the edifice, may be a caldera. The region inside the tectonic annulus is otherwise very flat, giving the volcano a domal shape (Figures 9d, e). Radially oriented tectonic features are not evident, except for two parallel sets of fractures diverging from the southwest corner of the annulus into the surrounding terrain (Figure 9b). This divergence may indicate interaction of a regional stress field with edifice stresses. Radially oriented flows extend a great distance to the north and west. High regional topography to the south and east of the edifice restricts the extent of apron flows in those directions.

A volcano at 15°S, 215°E rises 1.1 km above a base level of 0.1 km, with average edifice and flow apron radii 190 and 215 km, respectively. The distal edifice flanks and flow apron are covered with radially oriented flows (Figure 10b). This volcano has a prominent tectonic annulus surrounding a set of radial graben and fractures on the summit region. This tectonic annulus is similar to annuli observed at coronae [*Squyres et al.*, 1992b; *Stofan et al.*, 1992]. The central set of radial fractures is similar to features observed at novae [*Janes et al.*, 1992], which are believed to be precursors to coronae. This volcano is included in a list of coronae compiled by *Stofan et al.* [1992]. We note, however, that the topography (map, Figure 10a, and cross sections, Figures 10c, d) lacks the characteristic topographic signature of coronae, i.e., a raised annulus surrounding a lower center. The topographic profiles (Figures 10c,d) instead resemble those of a broad shield. *Head et al.* [1992] suggest that this volcano is

representative of a class of structures transitional between volcanoes and coronae.

A volcano at 3.5°N, 270°E has an unusually high ratio of flow apron radius to edifice radius (Figure 11). This volcano rises 3.1 km above a base level of -0.5 km, with mean edifice radius of only 60 km but mean flow apron radius of 250 km. A bright summit region may contain a very small (diameter < 10 km) caldera [*Head et al.*, 1992] (Figure 11b). Radial and circumferential fracturing is absent near the caldera. Several north-striking features, probably related to a regional stress field, cut the apron to the south and east (and possibly to the north). Very radar-dark flows are seen on the east flank of the edifice. These flows may be darkened because those slopes face away from the incidence direction of the radar. Additional patches of dark flows are seen in the north and east-northeast sectors of the flow apron.

A large volcano located at 10°N, 275°E rises 2.2 km above a mean basal level of -0.6 km, with mean edifice and flow unit radii of 185 and 255 km, respectively. The summit region is on average less steep than the outer flanks, giving the volcano a domal average profile (Figure 12). This volcano lacks major circumferential or radial tectonic lineaments. A small set of irregular ridges northwest of the summit region and a possible summit dome in the south summit region are the only visible summit structures [*Keddie and Head*, 1994b]. A dark unit on the perhiphery of the flow apron, lacking discernible individual flows, is believed to be composed of early stage eruptions from this volcano [*Keddie and Head*, 1994b]. Radially oriented flows comprise most of the flow apron and edifice. A zone roughly centered on the summit is significantly darker than the distal flanks and flow apron. Near the edge of the flow apron, to the west and northwest, several radial flows broaden circumferentially. To the northwest, one set of flows is deflected into a circumferential path [*Head et al.*, 1992; *McGovern and Solomon*, 1992; *Keddie and Head*, 1994b]. This phenomenon is rarely observed on Venus volcanoes. Only two other examples of circumferential flows have been found. One is Tepev Mons, discussed above; the other is a moderate-sized volcano at 13°S, 316°E (Figure 13); in both of these cases, the circumferential flows appear to have originated from a

source external to the volcanic edifice. Thus the volcano at 10°N, 275°E is the only volcano on Venus known to have partially filled its own topographic moat with circumferentially oriented flows.

General observations

General observations about the volcanoes in this data base can be summarized as follows. The Magellan SAR images indicate that surface flows are dominantly radial, with only three volcanoes exhibiting clear evidence of circumferential ponding of flows in topographic moats (Tepev Mons and volcanoes at 10°N, 275°E and 13°S, 316°E [*McGovern and Solomon*, 1992]). Other volcanoes lack an unambiguous topographic moat; typically a nearly flat apron of radial flows surrounds the volcanoes. There is little evidence of mass wasting on the flanks of large shield volcanoes, although some steep-sided domes and edifices less than 50 km in diameter exhibit such evidence [*Guest et al.*, 1992; *Head et al.*, 1992].

Well-developed radial rift zones, such as seen on the volcanoes of the Hawaiian chain, are not evident in the topography (as ridges) or in the SAR images (as sources of flows) of isolated, more or less axisymmetric volcanoes. Linear extensional zones, however, can occur on volcanoes strongly influenced by rifting in response to regional-scale extension (such as Theia Mons, Ozza Mons, and a volcano at 18°S, 285°E). These structures are continuations of the regional-scale rifts and are usually termed "rifts" in the literature. They are not proper Hawaiian-style "rift zones," however, in that rifts on volcanoes on Venus are related not to the edifice stress field (as in the Hawaiian case) but to the regional stress field. Moreover, Venus volcano rifts are not constructional features, but rather cut into the flanks of the volcano. They are therefore unlike Hawaiian-style rifts, which are ridges built up by magmas flowing downslope, perpendicular to the strike of the ridge.

Circumferential graben attributable to stresses from plate flexure are not generally seen around large volcanoes on Venus. Some volcanoes exhibit circumferential tectonic features near their summits, but these are most likely associated with a summit caldera (Sif Mons,

Maat Mons, 9°N, 29°E, 3.5°N, 270°E) or subsidence due to evacuation of a magma chamber (Sapas Mons [*Keddie and Head*, 1994b], and perhaps Tepev Mons). Radially oriented fractures and pit chains, observed just outside of caldera structures at the summits of Sif Mons, Maat Mons, and the volcano at 9°N, 29°E, are similar to those observed around the calderas of the western Galápagos Islands [*Chadwick and Howard*, 1991]. Evidence for thrust faulting on the flanks of large volcanoes on Venus is also lacking.

As seen the SAR images (Figures 2–13), and as graphically demonstrated in the topographic cross-section figures, the radial extent of flows can vary greatly with azimuth (even over a narrow range of azimuths). Regional topography and the presence of tectonic structures and nearby volcanic constructs greatly affect the extent to which flows radiate out from the edifice. Substantial regional topographic variablility was presumably present when the volcanoes formed. Flexural uplift may produce an arch, contributing a small (tens of meters) component of the observed topography. In theory, such an arch would manifest itself as an annulus of raised topography surrounding the edifice and flow aprons. Well-defined topographic annuli are not observed around any of the volcanoes in our database. The high amplitude and spatial variation of the pre-existing topography apparently obscure arch topography.

Finite Element Structural Models

Method

As in the preceeding chapters, we model displacements and stresses due to flexural loading of the lithosphere by a volcanic edifice using the finite element code TECTON [*Melosh and Raefsky*, 1980, 1983]. TECTON can model elastic and viscoelastic materials, and has provisions for modeling of faults (the "slippery node" method of *Melosh and Williams* [1989]). We also use here the modifications of *McGovern and Solomon* [1993] to allow incremental emplacement of the volcanic load. As discussed earlier, most large volcanoes on Venus are

isolated, axisymmetric edifices. Accordingly, we use an axisymmetric geometry and cylindrical coordinates r, θ, and z, where r and z are positive outward and upward, respectively. Out-of-plane shear stresses $\sigma_{r\theta}$ and $\sigma_{\theta z}$ are zero. We solve for displacements in r and z, and stress components σ_{rr}, $\sigma_{\theta\theta}$, σ_{zz}, and σ_{rz}. In axisymmetry, two principal stresses are confined to the rz plane and $\sigma_{\theta\theta}$, the stress normal to this plane, is also a principal stress. We adopt the convention that extension is positive.

Examples of the finite element grids used in this study are shown in Figure 14. As in the previous chapters, elements are assigned either lithospheric or asthenospheric properties. The large displacement formalism in TECTON allows such a grid to implement correctly the restoring force that the viscous mantle asthenosphere exerts on the lithosphere, necessary for a correct representation of plate flexure. Displacement boundary conditions on the side walls ($r = 0$ and $r = R_{max}$) are fixed in r but free to move in z, and nodes on the bottom boundary are fixed in z but free to move in r. These models are analogous to the models of Martian volcanoes in *McGovern and Solomon* [1993] (which is also Chapter 2 of this thesis). As for the models in Chapters 2 and 3, we use a Mohr-Coulomb failure criterion for basalt [*Handin*, 1966] to predict where faulting would occur. Unique conditions on Venus (such as lack of water and high surface temperature) may affect the mechanics of failure of basalt rock masses on Venus [*Schultz*, 1993]. Calculations of rock mass failure envelopes accounting for these differences, while exhibiting significantly lower values of tensile strength and cohesion than the Mohr-Coulomb parameters used here, yield broadly similar envelopes in the compressive region [*Schultz*, 1993].

As discussed in the previous chapter, a coherent layer of low-permeability material of substantial thickness is required for the formation of a basal decollement. On Earth, pelagic clays provide such a layer beneath large oceanic hotspot volcanoes [*Iverson*, 1995]. The formation of such a layer requires millions of years of deposition undisturbed by erosive currents or other sources of sedimentary material. High pore fluid pressures generated by the compaction of the low-permeability clay [*Iverson*, 1995] cause this layer to act as a

decollement. Conditions on Venus make the formation of a basal decollement extremely unlikely. Venus lacks liquid water at its surface [*Donahue and Pollack*, 1983], and likely has lacked it for much of its history [*Grinspoon*, 1987]. Current surface modification and aeolian dispersal rates on Venus are orders of magnitude less than terrestrial rates [*Arvidson et al.*, 1992]. Even assuming that a layer of clay-sized particles of sufficient thickness did form, there would be no pore fluid to generate the pore pressure required for decollement slip.

The roughness of the pre-existing surface also regulates the boundary condition at the base of a volcano. Rough topography on the volcano-substrate interface creates a strongly welded basal boundary condition, as demonstrated for large terrestrial oceanic volcanoes in Chapter 3 of this thesis. The most important variations in terrestrial basal topography are abyssal hills, long topographic features formed at mid-ocean ridges. Volcano-scale topographic variations are rarely formed subsequent to abyssal hill formation (in fact, topographic variation is obscured by deposition of sediment). A significant amount of topographic relief may have been present at the sites of initial construction of volcanoes on Venus. For example, rough tessera blocks are preserved as inliers to much of the lowland plains of Venus. Volcanoes constructed upon tessera terrain will feel rough basal topography at short to intermediate length scales. Analysis of crater statisitics [*Namiki and Solomon*, 1994; *Price and Suppe*, 1994] shows that volcano surfaces are substantially younger than the mean age of the entire surface of Venus. This age difference may be hundreds of millions of years [*Price and Suppe*, 1994]. Even allowing for volcano construction intervals of tens of millions of years, hundreds of millions of years worth of patchy volcanism or modest deformation could generate significant surface roughness at many length scales. If a volcano formed on smooth plains shortly after their emplacement, however, the basal interface could be relatively smooth. Thus, basal roughness will depend upon the tectonic and volcanic history of the region and the timing of edifice initiation. Thus, the topographic roughness at the base of volcanoes on Venus probably varies significantly.

Basal slip along a weak lower crustal layer is another possible mechanism for generating

a decollement beneath Venus volcanoes. Such a layer would decouple strong layers in the upper crust and the mantle, such that the upper crustal layer would deform as a separate, thinner plate. In order to function as the kind of structure observed beneath Hawaiian volcanoes, however, the transition to ductile behavior would have to occur at very shallow levels. The flow law for anhydrous crust on Venus [*Mackwell et al.*, 1995] would require a very high thermal gradient to achieve a shallow brittle-ductile transition. Such high gradients may have existed shortly after crustal formation, but are not likely to have persisted for more than a few million years thereafter. Also, a thin upper crustal plate is not able to support large volcano loads. We will show below that volcanoes on thin lithosphere develop large horizontal compressive stress levels that limit volcano growth.

Finally, as argued above, the tectonic structures and magma flow patterns observed on large volcanoes on Venus do not resemble those predicted for volcanoes with detached bases. Based on these observations and the mechanical arguments just cited, we conclude that large basal detachments of the kind observed beneath Hawaiian volcanoes do not form beneath large volcanoes on Venus. Accordingly, we will concentrate our efforts on models that are basally welded to the lithosphere.

Results of finite element calculations

In this section we show principal stress orientations and maximum shear stress magnitudes for several finite element model calculations. Symbols used to describe the principal stress orientations are described in Figure 7 of Chapter 3.

Results for an model edifice emplaced incrementally on and basally welded to a 40 km thick elastic lithosphere are shown in Figure 15. After completion of flexure from the third load increment, the most compressive principal stress σ_1 is nearly horizontal ($\approx \sigma_{rr}$) near the central axis, and exactly horizontal ($= \sigma_{\theta\theta}$) in the distal part of the edifice (Figure 15a). Maximum shear stress decreases with increasing height in the edifice (Figure 15d), characteristic of an incrementally loaded edifice ([*McGovern and Solomon*, 1993, and the preceeding

chapters]). As the fourth and fifth load increments are added, the distribution of principal stress orientations remains about the same (Figures 15b-c), but the maximum shear stress increases (Figures 15e-f). The Mohr-Coulomb failure criterion for basalt is never exceeded in the edifice.

Results for a similar model but with a 16-km-thick elastic lithosphere are shown in Figure 16. Principal stress orientations (Figures 16 a-c) are similar to those in Figure 15, but the state $\sigma_1 \approx \sigma_{rr}$ is prevalent to a greater radial distance. At the completion of each increment, maximum shear in this model (Figures 16d-f) is significantly higher than that at the corresponding increment of the T_e = 40 km case (Figures 15d-f). The Mohr-Coulomb failure criterion is exceeded only in a very small zone at the distal surface of the edifice (Figures 16 a-c). Stress orientations in this region yield a prediction of strike-slip faulting.

We also calculated models with elastic lithospheric thickness values of 8, 24 and 32 km. We plot the peak value of maximum shear in the edifice vs. load increment for five values of T_e in Figure 17 Starting at T_e = 40 km, we see that as T_e decreases, the level of maximum shear stress increases. This trend holds for all increments in the range T_e = 40 to 24 km, and for the early increments in the range T_e = 16 to 8 km. However, the later increments of the T_e = 16 to 8 km models show lower stress levels than would be expected from an extrapolation of the stresses in earlier increments. In the most extreme case (T_e = 8 km), maximum shear actually decreases after emplacement of the third increment, and the final value of maximum shear is lower than for the T_e = 24 km case. This apparently aberrant behavior can be explained by considering the characteristic wavelength of flexure (also known as the flexural parameter) at the appropriate values of T_e. The flexural parameter α is

$$\alpha = \frac{4D}{\rho_m g}^{1/4}, \tag{4.1}$$

where D, the flexural rigidity, is

$$D = \frac{ET_e^3}{12(1-\nu^2)}, \tag{4.2}$$

E is Young's modulus, and ν is Poisson's ratio. For $T_e = 40$ km, $\alpha = 94$ km, and the flexural response is broad (Figure 18). For $T_e = 8$ km, $\alpha = 28$ km, and flexure is accommodated in a very narrow region at the edge of the load (Figure 18). As the load grows laterally, this region of flexure follows the edge of the edifice. For cases with small flexural parameters, lateral growth will eventually move the region of flexure far enough from the central axis such that the lithosphere beneath the center "unflexes," releasing horizontal compressive stresses built up earlier in the sequence of growth.

Finite element model predictions

The boundary condition at the base of the volcano plays a critical role in governing the structural history of the volcano. Volcanoes that are detached from the lithosphere exhibit low levels of horizontal compressive stress and principal stress orientations that allow propagation of magma to the summit region [*McGovern and Solomon*, 1993]. The flanks of such a volcano thrust outward, thus accommodating magma emplacement behind them in a summit magma chamber or radial rift zone. Volcanoes that are instead welded to the lithosphere experience high levels of horizontal compressive stress that can tend to shut off magma propagation to the surface. Propagation of radial rifts or dikes is inconsistent with such a stress state. To allow further summit eruptions, this stress field must be altered such that the least compressive principal stress is horizontal. Pressurization of a magma chamber can induce additional stresses sufficient to allow upward magma propagation [*McGovern and Solomon*, 1993]. Viscous relaxation of stresses in an intrusive complex consisting of hot ultramafic cumulates [*Borgia*, 1994] can also re-enable summit eruptions, although this relaxation has been demonstrated only for a basally detached volcano with a plane-strain rift zone geometry already in place. In the absence of these mitigating factors, or in more distal regions of the edifice, principal stress orientations favor outward propagation of magma in subhorizontal intrusions [*McGovern and Solomon*, 1993]. *Walker* [1992] proposed that a welded basal boundary condition would lead to emplacement of a series of horizontal sills,

forming what he termed a "coherent intrusive-sheet complex". Such a mechanism may result in "cone sheet" and sill complexes described by many workers in volcanoes in Scotland, Iceland, and elsewhere [*Walker*, 1992]. The magnitude of horizontal compressive stress is inversely proportional to the effective elastic thickness of the lithosphere (T_e). For values of T_e comparable to estimates from admittance studies [*Phillips*, 1994] the maximum horizontal shear stress in the central edifice is less than 200 MPa.

In general, edifice stresses in the models described above do not satisfy the failure criterion (except for a small region at the edge of models with low values of T_e, as in Figures 16a-c). Stress orientations in all but the most distal regions of the edifices would lead to predictions of circumferential or radial thrust faulting. Failure is not predicted in these regions because of the effects of sequential emplacement of load increments. A given increment feels stresses only from its own emplacement and that of subsequent units. Thus, at any given time the surface units exhibit the lowest amount of horizontal compressive stresses in the edifice (e.g., Figures 15d-f and 16d-f). The model prediction of no edifice thrust faulting is consistent with the lack of evidence for thrust faulting on large volcanoes on Venus.

With regard to the central edifice stress state, *McGovern and Solomon* [1993] demonstrated that the addition of stresses from magma chamber expansion would be sufficient to relieve horizontal compressive stresses near the volcano axis. This addition would reorient the principal stresses such that σ_1 is vertical, thus enabling magma propagation to the summit region. This axial region will be heavily faulted by intrusions of magma from below, as well as by stresses from loading by the whole edifice [*McGovern and Solomon*, 1993], such that future parcels of magma will follow this path of least resistance to the surface. The establishment of this central conduit is essential to the continued growth of the volcano. Environmental conditions that impede the establishment of this conduit may inhibit volcano growth or stop it completely. Such adverse conditions could include emplacent on thin lithosphere (high horizontal compressive stress), high magma viscosity, or movement of the magma source relative to the volcano.

Discussion

Implications for volcano structure

Despite the prediction from the finite element models that loading-related stresses are unlikely to cause formation of radial extensional features on basally welded volcanoes, such features are commonly observed on volcanoes on Venus [*Parfitt and Head*, 1993] For example, radial fractures, believed to be the expression of near-surface dikes intruded from a central magma chamber, are observed on the flanks of Sapas Mons [*Keddie and Head*, 1994b], Sif Mons [*Senske et al.*, 1992], Ushas, Innini and Hathor Montes in Dione Regio [*Keddie and Head*, 1995], and the volcano at 9°N, 29°E (Figure 5). Radial pit chains emanate from calderae on Maat Mons [*Senske et al.*, 1992; *Keddie and Head*, 1994b], Sif Mons [*Senske et al.*, 1992], and the volcano at 9°N, 29°E (Figure 5). Similar radial fractures and pit chains on the western Galápagos Islands ([*Chadwick and Howard*, 1991]; Chapter 3) are attributed to dikes radiating from a central magma chamber. The finite element model results suggest that radial dikes propagating from a central magma chamber would encounter increasing levels of horizonal differential compressive stress, which would inhibit further propagation as a radial dike.

The distribution of stress in a growing volcano suggests a resolution to this apparent disagreement. Each load increment feels stresses only from its own load and the load of later increments. The maximum horizontal stress occurs in the lowest (first) load increment, and decreases upward with each later load increment. Thus, dikes would find it easiest to propagate through the most recent load increments, which would exhibit the least resistive stress to radial propagation. This scenario has also been proposed for terrestrial welded-base volcanoes, such as the western Galápagos Islands (see Chapter 3). The development of the radial structures is sketched in Figure 19. As the volcano grows, the magma chamber ascends in(to) the edifice. Reorientation of principal stresses will be easiest in the uppermost (youngest) flow units. These layers will be the first to assume stress orientations favorable

to radial dike propagation. Thus, radial dikes will preferentially intrude the uppermost edifice layers. The stress state in the lower layers of the edifice will still favor intrusion of subhorizontal sills from the magma chamber.

Many volcanoes on Venus lack evidence of radial dikes; additional stress perturbations (for example, from regional topographic gradients [*McGovern and Solomon*, 1993]) may be required in some cases for dike initiation and propagation. *Keddie and Head* [1994b] suggest that such topographically induced stresses cause a focusing of radial fractures along a roughly NE-SW axis at Sapas Mons, forming "proto-rift zones". These workers also note that the radial fractures are in the lower flow units, determined stratigraphically to be the oldest exposed units. This would appear to contradict our suggestion that dikes should propagate in the youngest unit. However, the currently exposed surface units span only a fraction of the age of the entire volcanic structure. The exposed units cover many older units that fill the flexural depression beneath the edifice and flow apron; we present such a structural model for volcanoes on Venus in a section below. Thus, the observations at Sapas Mons are consistent with the evolution of a basally welded volcano. The stratigraphy of exposed flows at Sapas offers additional clarification. The oldest exposed units have the greatest radial extent; younger flow units are of progressively smaller radii [*Keddie and Head*, 1994b]. These workers suggest a reduction of magma supply with time. Presumably, a reduction in supply would reduce the likelihood of radial dike propagation from the magma chamber. Thus, the dikes in the oldest (and most voluminous) currently exposed units likely formed when those units were the youngest on the volcano and magma supply was plentiful. Later, supply was reduced, resulting in flows of limited volume and radial extent. Magma chamber overpressure was not sufficient to resume radial dike propagation; thus the youngest flows on Sapas Mons are not fractured. This scenario suggests that Sapas Mons reached the last stages of edifice construction.

Implications of resurfacing and thermal histories for edifice construction

Review of proposed resurfacing and thermal histories

The record of impact cratering provides the most important constraint on the resurfacing history of Venus. Magellan radar images, providing coverage of 98 % of the planet, reveal a total of 842 impact craters, with rim diameters varying from 1.5 to 280 km [*Schaber et al.*, 1992]. This population of craters has a size-frequency distribution characteristic of asteroid and comet impacts of the post-heavy-bombardment era [*Schaber et al.*, 1992]. All evidence of a crater population from the late heavy bombardment era (3.9 Ga), as seen on the Moon, Mars and Mercury, has been removed. Given the areal distribution of craters and an estimate of the flux of impactors at Venus (for example, *Shoemaker et al.* [1991]), an average age for the surface can be calculated. Ages calculated in such a manner range from about 300 Ma *Strom et al.* [1994] to 500 Ma [*Phillips et al.*, 1992; *Schaber et al.*, 1992], with uncertainties of perhaps a factor of 2 [*Herrick*, 1994]. The global areal distribution of impact craters cannot be distinguished from a spatially random population [*Phillips et al.*, 1992; *Schaber et al.*, 1992]. *Strom et al.* [1994] also maintain that the distribution of craters with altitude is also statistically indistinguishable from random. *Herrick and Phillips* [1994], however, maintain that the crater distribution is nonrandom with respect to altitude. Specifically, the elevation range from 6052.4 to 6052.9 km (elevation above center of mass) is deficient in craters. This elevation range is strongly associated with volcanic rises, rifts and coronae; structures expected to contribute to the removal of craters.

Models of resurfacing can be grouped into two categories: catastrophic/episodic models, which invoke one or more magmatic events that resurface nearly the entire planet and cease over a relatively short time, and gradual models, which invoke processses occurring at steadily declining rates to accomplish the observed surface age distribution. *Strom et al.* [1994] present a catastrophic model, which postulates a nearly global resurfacing event which

ceased over an interval of less than 10 Ma and occurred 300-500 million years ago. In their model, this event has been followed by tectonic and volcanic near-quiescence, so that the accumulated impact craters have a random spatial distribution [*Strom et al.*, 1994]. *Herrick and Phillips* [1994] estimate that about 30% of the planet has been resurfaced with sufficient material to bury craters produced since a global resurfacing event. In contrast, *Schaber et al.* [1992] estimate less than 10% post-global-event resurfacing, and *Strom et al.* [1994] put that figure at 4–6%.

The resurfacing models discussed here place strong constraints on the thermal properties and evolution of the mantle and lithosphere of Venus. For example, *Schaber et al.* [1992] and *Strom et al.* [1994] cite a convection model for Venus [*Arkani-Hamed and Toksoz*, 1984] that predicts oscillatory heat flux and convective velocities, with a time scale for oscillations of about 500 Ga. *Parmentier and Hess* [1992] developed a parameterized convection model that tracks the growth of a depleted residual mantle layer. They found that as this layer grows and cools, its negative thermal buoyancy eventually exceeds its positive compositional buoyancy, resulting in a catastrophic mantle overturn event. *Turcotte* [1995] proposed that episodic global subduction events are required for the release of the internal heat of Venus. These events are envisioned to be of short duration and accompanied by intense tectonic and volcanic activity, analogous to the foundering of the surface crust of a lava lake [*Turcotte*, 1995]. Heat and magma flux are very high during this event, and the elastic lithosphere is very thin. The event is followed by an extended period of tectonic and volcanic quiescence; the lithosphere cools and thickens during this period. Other episodic thermal models have similar consequences for heat and magma fluxes and the state of the lithosphere.

Such thermal models have important implications for the formation of large volcanoes. The period during and immediately following the postulated resurfacing event is characterized by thin lithosphere. As demonstrated above for low values of elastic plate thickness T_e (Figures 16, 17), large lithospheric deflections result in very high levels of horizontal compressive stresses in a growing volcano. These stresses will inhibit ascent of magma to

the surface and therefore halt the growth of a proto-edifice at an early stage. After the postulated global resurfacing event, the lithosphere cools and thickens. Volcanoes emplaced during this period will experience much lower level of horizontal compressive stresses; extension produced by pressurization of a central magma chamber/conduit system should be sufficent to counteract these stresses and maintain a magmatic pathway to the surface (as demonstrated for terrestrial welded-base volcanoes in Chapter 3). Such volcanoes will then be able to grow to sizes currently observed on Venus. We thus conclude that the growth of large edifices may be inhibited until the lithosphere is sufficiently strong to support the volcanic load at low levels of horizonal differential stress. This prediction is consistent with evidence that the surfaces of shield volcanoes are among the youngest on the planet [*Namiki and Solomon*, 1994; *Price and Suppe*, 1994].

Volcano versus corona formation

Coronae are believed to be the surface manifestation of mantle plumes [*Stofan et al.*, 1992; *Janes et al.*, 1992]. Why does mantle upwelling on Venus sometimes produce coronae and sometimes produce shield volcanoes? Analysis of impact crater densities indicates that shield volcanoes, on average, have surface ages less than the mean age for the planet, and less than coronae as well [*Namiki and Solomon*, 1994; *Price and Suppe*, 1994]. Geologic mapping also reveals that shield volcanoes are stratigraphically younger than coronae, which in turn are younger than the surrounding plains deposits [*McGill*, 1994]. Calculations of gravity/topography admittances [*Phillips*, 1994; *McGovern et al.*, 1995] indicate elastic lithosphere thicknesses T_e in the range 30-50 km beneath volcanoes. For comparison, flexural models of moat topography at several coronae yield mechanical plate thickness estimates in the range 15-30 km [*Johnson and Sandwell*, 1994] (with somewhat higher but less well-constrained values for a few of the largest coronae). *Cyr and Melosh* [1993] estimated elastic plate thicknesses at coronae by comparing observed patterns of tectonics and faulting around coronae with those predicted from models of lithospheric upwarp and annular loading. They

found the tectonic patterns around several coronae were consistent with $T_e = 10 \pm 5$ km, with another corona exhibiting patterns consistent with $T_e \approx 2$ km.

The evidence that volcanoes are younger than and are emplaced on generally stronger lithosphere than coronae suggests that edifices form only when the lithosphere is thick enough to support edifice formation. In the context of an episodic thermal model, the observation that volcanoes are younger on average than coronae implies that a sufficient period of time must pass after a global resurfacing event before the lithosphere in a given region can sufficiently cool (and thicken) to support the edifice. Lithospheric cooling and thickening will make it easier for later-formed edifices to continue surface eruptions, because of a reduction of magma-obstructing horizontal compressive stresses (Figures 15, 16). Conversely, proto-edifices formed on thin lithosphere will experience enhanced horizontal compressive stresses, which will tend to inhibit extrusive flows and may restrict growth to subhorizontal intrusions only. Over an active plume, however, the stress field may be dominated by stresses due to near-surface flattening of the plume head [*Janes et al.*, 1992; *Koch*, 1994]. The predicted stresses above the plume are tensile and may counteract the compressive edifice stresses so that the principal stress orientations are permissive of magma propagation to the surface over the entire flattened plume head. Because horizontal compressive stresses due to loading are greatest near the center of the proto-edifice, ascending magma may bypass the edifice center in favor of eruption sites elsewhere over the plume head. Thus, widespread vent and sheet volcanism rather than shield construction will tend to be favored.

We are therefore led to the suggestion that coronae are the manifestation of mantle upwelling beneath thin lithosphere, while large volcanoes are the mansifestation of mantle upwelling beneath lithosphere that has reached a critical thickness. A comparison of T_e estimates for coronae [*Johnson and Sandwell*, 1994] and volcanoes [*McGovern et al.*, 1995] would place this critical value at around 30 km. This value is consistent with an upper bound for T_e of 32 km [*Janes et al.*, 1992] determined by modeling topographic profiles of novae (believed to be coronae in the earliest stage of formation). In such a scenario, volcanoes

that exhibit characteristics of coronae (such as the volcano in Figure 10) can be attributed to emplacement on lithosphere exhibiting T_e values near the critical value.

Corona formation on Earth?

The above-outlined scenario for lithospheric control of the surface manifestation of upwellings has important implications for the behavior of upwelling plumes on Earth. *Watters and Janes* [1995] suggested that coronae may have formed on Earth, although they also note that only one candidate structure in the southwestern Caribbean sea [*Christofferson and Hamill*, 1978] has been detected to date. Our scenario may help to explain the failure to detect coronae on Earth.

Our scenario predicts that coronae will only form on thin lithosphere. On Earth, such an environment is provided only in young oceanic lithosphere, near a spreading ridge. Thus, we would expect terrestrial coronae formation to be limited to young seafloor. Upwellings beneath older lithosphere will likely manifest themselves as volcanic island chains. A diapir ascending directly beneath a spreading center may produce a corona-like structure; however, this structure will be deformed and eventually split apart by plate motion, rendering it unrecognizable as a corona. Further volcanism at this ridge will be manifested as a volcanic ridge extending to either side of the plume (as at Iceland and the Carnegie and Cocos ridges formed when the Galápagos hotspot resided beneath the Cocos-Nazca spreading center [*Hey*, 1977].) Diapirs ascending off-ridge would still experience shear as they approached the moving plate, deforming the resulting annular structure, but perhaps not beyond recognition. In such a case, slower plate velocity (relative to the diapir) will lessen distortion of the annulus and therefore increase the likelihood of detection. Sedimentation will tend to obscure such structures after they form. They will eventually be removed by subduction. In addition, the scenario for corona formation discussed by *Janes et al.* [1992] and *Koch* [1994] requires deformation of the lithosphere by the flattening diapir (or plume head). Presumably the tail of the plume, which will feed subsequent hotspot volcanoes, cannot form the structures

that the head can. Thus, to find terrestrial coronae we must find the point where the plume first breaks through the lithosphere. For many hotspot volcanic chains, such as Hawaii, this point has presumably been subducted and cannot be found.

A New Structural Model for Volcanoes on Venus

Direct evidence for the existence of flexural moats surrounding large edifices on Venus is generally lacking. Topographic profiles of such volcanoes (Figures 3-13) rarely exhibit well-defined minima within the flow aprons. Ponding of flows at the edge of a flow apron or deposition of flows in a circumferential orientation would indicate the presence of a depression; as noted above, these phenomena have only been observed at three large volcanoes (Figures 6, 12, 13). Radially oriented flows cover the edifices and flow aprons of all other large volcanoes.

We presume that flexural depressions nonetheless exist around large volcanoes on Venus. In order for large depressions of the lithosphere to be absent, the lithosphere would have to behave practically rigidly ($T_e >> 100$ km), or the volcano would have to be perfectly compensated by dynamic support from below. Both of these conditions are extremely unlikely. Estimates of T_e beneath volcanoes are in the 30-50 km range [*Phillips*, 1994; *McGovern et al.*, 1995], and dynamic support from mantle tractions is more likely to produce a regional topographic swell than a short-wavelength, volcano-shaped uplift. Assuming that annular depressions once existed, they have apparently been completely filled by flows. Flexurally-induced topographic moats surrounding large terrestrial volcanoes are partially [*Rees et al.*, 1993] to completely [*Wolfe et al.*, 1994] filled by the products of catastrophic flank failure and erosion of the edifice. Moat-filling material is therefore a significant fraction of the output of terrestrial hotspots [*Wolfe et al.*, 1994]. In this section we examine the importance of material that fills flexural moats around large volcanoes on Venus, with implications for volcano structure, magmatic flux, and recent (post-global-resurfacing-event) resurfacing on

Venus.

Volcano moat structure

The structure of moat infilling around volcanoes in the Hawaiian and Marquesan chains is shown in Figure 20 [*Watts and ten Brink*, 1989; *Wolfe et al.*, 1994]. In both cases, the center of the moat is filled with "edifice volcanics." This term refers to submarine- or subaerally-erupted material that remains intact at or near its point of eruption (or intrusion), i.e., high density basalt flows that constitute the solid structure of the volcano. The surrounding topographic moats are filled with volcano mass wasting products and sediments derived from volcanics [*Rees et al.*, 1993; *Wolfe et al.*, 1994]. Note that the Marquesan moat is overfilled with sediment [*Wolfe et al.*, 1994], while the Hawaiian moat is underfilled [*Rees et al.*, 1993]. The Marquesan archipelagic apron hides all topographic evidence of plate flexure, such as distance to the flexural arch (although this information can be recovered from the gravity field [*Filmer et al.*, 1993] and seismic stratigraphy [*Wolfe et al.*, 1994]). The Hawaiian flexural arch, however, can be seen clearly in the bathymetry. The difference in moat cover is believed to stem from differences in volcano construction style and mass wasting efficiency [*Wolfe et al.*, 1994]. The basal detachment at Hawaii accommodates intrusive growth into rift zones, adjusting the volcano's slope "gracefully" such that Hawaiian edifices are less prone to sector collapse than Marquesan edifices. Despite their large size, the landslides and slumps detected on the flanks of Hawaii [*Moore et al.*, 1989] appear to be less efficient at moat filling than the less voluminous but probably more frequent sector collapse events at the Marquesas Islands [*Wolfe et al.*, 1994]. The moat-filling material has a lower density than the edifice volcanics, but nonetheless it originated as magma from the underlying hotspot [*Filmer et al.*, 1994]. This fact is not yet well appreciated by the volcanological community; hotspot output is commonly measured as the volume of the edifice volcanics only.

The mechanics of the interface between volcano and lithosphere may account for a unique mode of moat-filling on Venus. We have argued above that volcanoes on Venus develop with a

welded basal boundary condition. Such a condition inhibits large-scale catastrophic failure of the flanks, a prominent feature of terrestrial hotspot volcanoes [*Moore et al.*, 1989; *Holcomb and Searle*, 1991]. Thus, deeply rooted flank slumps and slides, as observed at Hawaiian volcanoes [*Moore et al.*, 1989] and the island of Reunion [*Duffield et al.*, 1982; *Gillot et al.*, 1994], are not present on large Venus volcanoes. Lateral volcano growth via Hawaiian-style rift zone intrusion and eruption is also prevented by the welded basal boundary. Shallowly-rooted failure of oversteepened flanks, as observed at the Marquesas [*Filmer et al.*, 1993; *Wolfe et al.*, 1994], Canary [*Carracedo*, 1994], and other terrestrial volcanic chains, is a second possible mode of moat filling. Flank instability increases with increasing flank slope [e.g., *Iverson*, 1995]. Volcano heights and slopes on Venus are much lower than on the other terrestrial planets. This is partially attributed to low viscosity of magmas emplaced at Venus surface conditions, predicted on thermal and petrological grounds. Lacking buoyancy from an ocean, a volcano on Venus will cause a greater deflection of the lithosphere than an identical terrestrial volcano; this result will also contribute to lower flank slopes on Venus volcanoes. These low-sloped flanks are likely to be stable with respect to landslides. Pore fluid pressure is another important destabilizing factor for volcano flanks. Pore fluid (water) pressure may trigger flank failure in terrestrial oceanic volcanoes [*Elsworth and Voight*, 1995; *Iverson*, 1995]. Venus lacks liquid water at its surface; there is no other likely pore fluid to destabilize the flanks of Venus volcanoes. Thus, the combination of low flank slopes and lack of a pore fluid on Venus accounts for the paucity of shallow landsliding on Venus volcanoes; only very steep structures, like the small steep-sided domes observed on the plains [*Guest et al.*, 1992] and on and near some volcanoes [*Keddie and Head*, 1994b; *Campbell and Rogers*, 1994], will generate the stresses required for failure. Volcanoes on Venus thus lack the main mechanisms by which terrestrial flexural moats are filled.

The predominance of radial flows on the edifices and surrounding aprons suggests that on Venus the moats are instead filled mostly by radial flows. Topographic profiles of Sapas (Figure 7) and Maat (Figure 8) Montes demonstrate smoothly sloping profiles that resemble

those of terrestrial archipelagic aprons described in *Menard* [1956]. We conclude that flows emanating radially from the edifice overfill the flexural moats in a manner similar to the overfilling of the Marquesas moats by mass wasting [*Filmer et al.*, 1994; *Wolfe et al.*, 1994] to produce archipelagic aprons. The low viscosity (high mobility) of the Venus magmas enables them to play the role that fragmented mass-wasted material and volcano-derived sediment play in the Marquesas moat fill. We note that the paucity of circumferentially oriented or ponded flows implies that moats are almost always filled by radial flows. Moats may be filled before they form; i.e., if the magma supply rate outstrips the flexural subsidence rate, a Marquesas-style topographic profile is maintained throughout the growth of the volcano. Alternatively, circumferential and ponded flows may contribute significantly in early stages of volcano growth, but are later hidden as the volcanoes mature. This latter scenario would require that almost all of the volcanoes currently visible are in mature stages.

Flows must travel great distances from the summit region to the moat. This observation, coupled with the low slopes typical of large volcanoes on Venus, suggests that the viscosity of magmas that constitute these volcanoes must be relatively low. Low viscosities for magmas on Venus are expected on thermal and petrological grounds. Significantly, steep-sided volcanic domes, the only volcanic features observed to experience flank instability and mass wasting on Venus [*Pavri et al.*, 1992; *Guest et al.*, 1992], are believed to consist of high viscosity magmas. These features are small, less than 50 km in diameter, and likely represent a small fraction of extrusive volcanism on Venus. Given the likelihood of welded basal boundary conditions, these steep-sided domes lack the ability to expand via intrusion and slip on a basal decollement. The domes could only accommodate further growth by mass wasting of oversteepened flanks. Such a mode of growth would be analogous to that of the Marquesas islands on Earth.

Large edifices on Venus often exhibit radial lineations, fractures, and graben, which are interpreted to be the surface manifestation of shallow dikes intruded from a central magma chamber [*Parfitt and Head*, 1993; *Keddie and Head*, 1994b, 1995; *Ernst et al.*, 1995]. These

inferred dikes are often observed to extend through the flow apron and even beyond, into the surrounding terrain. Such dikes could not propagate through the fragmented material that fills terrestrial moats and remain recognizable as a dike. If a dike were to reach the bottom of such a moat, the magma would simply take advantage of plentiful paths of weakness through the fragmented moat fill, eventually erupting. The resulting deposit would not resemble a linear dike; it would in fact obscure the deep source of the magma. The existence of radial dikes in the flow aprons of Venus volcanoes is therefore further evidence for the solid nature of the moat fill. To our knowledge, linear dikes have never been observed (or even proposed to exist) in the moats or flexural arches of terrestrial oceanic volcanoes. In addition, no such throughgoing dikes have been detected on Martian volcanoes. From these observations, we suggest that Venus volcanoes are structurally unique among terrestrial planet volcanoes.

Synthetic stratigraphy for Venus volcanoes

To help visualize and quantify the importance of moat-filling flows, we construct a synthetic stratigraphic cross section of a volcano on Venus by superposing the results of several plate flexure calculations (Figure 21). We use an axisymmetric thick-plate flexure solution [*Comer*, 1983], and we assume that the moats are filled to the pre-existing surface level by flows of final density equal to that of the central edifice. To account for this infill, we set the buoyant restoring force proportional to the density contrast between volcanic material and mantle. We perform the calculation for a progression of edifice sizes that represent equal-volume conical loading increments on a lithosphere with elastic thickness $T_e = 40$ km. These conical increments have the same slope as the final edifice. In Figure 21a, the upper solid line represents the final topography of the edifice and moat fill; the lower solid line is the deflection of the top of the lithosphere, and dashed lines denote surfaces at intermediate growth stages. The dashed lines should be viewed as schematic indications of the volcano stratigraphy and not as indications of the thicknesses of actual flow units: Each increment in Figure 21a would in reality be made up of thousands of individual flows. Note that the

volume of the edifice is only a small fraction f_e (14% for the model in Figure 21a) of the total volume of erupted material. This fraction not a strong function of volcano size or elastic plate thickness; however, it depends on the density of the volcanic load and the density contrast at the crust-mantle boundary (2800 and 500 kg/m^3, respectively, in the model of Figure 21a). Reducing mantle density to 3100 kg/m^3 (and thus reducing the density contrast to 300 kg/m^3) reduces f_e to about 9% (Figure 21c).

The topographic moats around large volcanoes on Venus are predicted to contain 7–11 $\times$ the volume of the apparent edifice. If the moats are indeed filled with flows rather than mass-wasted material, we can infer that a significant fraction of the total volcanic volume (edifice and moat) is extrusive, as opposed to intrusive, in origin. This fraction is difficult to estimate but is likely to be significantly higher than that estimated for for Hawaiian volcanoes (extrusive/intrusive volumetric ratio in the 1:3 to 1:9 range [*Borgia and Treves*, 1992]). Thus, even though welded-base volcanoes might be expected to grow mostly by sub-horizontal intrusion, the inability of the edifice to expand laterally, coupled with the relaxation of compressive stresses near the central axis (to allow magma propagation to the summit region), may result in an volcano that consists of a greater proportion of extrusive flows than a volcano with a detached base. This apparent paradox is partially resolved by recalling that thrusting of the edifice over the detachment creates a stress state favorable to further intrusions [*Dieterich*, 1988; *McGovern and Solomon*, 1993; *Borgia*, 1994].

The model of moat filling described above has important implications for the interpretation of flows at the edge of the flow apron. The distance to the edge of the moat (defined here as the intersection of the flexural curve with the altitude of the original surface) is dependent on two parameters. The most important of these, the characteristic flexural wavelength, is a function of elastic plate thickness T_e, but independent of edifice size. Moat edge radius would be constant during volcano growth (assuming constant T_e) if the flexural wavelength were the sole influence on moat edge radius. Lateral growth of the volcano, however, pushes the flexed region of the lithosphere outward in radius. Thus, the characteristic wavelength

of the volcanic load also influences the radius of the moat edge. In Figure 21b, a close up of the region near the flexural arch shows that the moat edge migrates outwards about 20 km between emplacement of the first and last model increments. Load increments onlap the flexural arch; the increment visible at the surface is thus predicted to be the youngest. Older flows near the arch are predicted to be buried.

Care must be taken when applying the predictions of our idealized models to the interpretation of structures on actual volcanoes, however. We note that the difference in height between the surfaces of the earliest and latest model load increments in Figure 21b is less than 25 meters. Heights of individual flow units are a significant fraction of this value. A sufficiently thick group of early flow units at the moat edge may present a topographic obstacle to later flows and may not be covered by them. The first flows to reach the moat edge could then remain visible there throughout the growth of the volcano: moat edge units would then be the oldest exposed units on that volcano. Units at the edge of flow aprons have been identified as the oldest units at Sapas Mons and the volcano at 10°N, 275°E [*Keddie and Head*, 1994b]. These early flows may be difficult to distinguish from the surrounding terrain, for several reasons. A contrast in tectonic fabric is one method used by photogeologists to distinguish flow units and structures. A volcanic flow exhibiting tectonic fabric similar to that of external terrain may be assigned to the external unit. If such a flow is one of the earliest from the volcano, it could have accumulated tectonic features over the lifetime of the volcano. This lifetime could be a signficant fraction of the age of the external surface; thus, both external terrain and moat edge flows may have time to accumulate similar tectonic fabric. The oldest volcano flows will not resemble younger flows tectonically and may be incorrectly assigned to regional units. Another difficulty in determining the origin of flows is that the substrate on which the volcano is formed is also likely to be made up of erupted magma. Many workers have described the units underlying volcanoes as regional plains, rapidly deposited over a broad area during the postulated global resurfacing event. While such units did not originate from a centralized shield, they may have flowed from their vents

over distances and slopes similar to those of the apron flows. Plains flows could thus resemble apron flows in morphology and radar return. The plains units thus are not necessarily easily differentiated from volcano-derived flows in the SAR images.

The model presented in Figure 21 makes several predictions regarding the relative importance of edifice and apron material. A diagonal solid line in Figure 21a denotes the edge of the edifice during growth of the volcano. Material to the left of this line was emplaced on or intruded into an edifice that projected above base level. Material to the right of this line was emplaced as part of a flow apron. The edifice material forms a complex with a triangular cross-section. Figure 21a has a high vertical exaggeration; when projected without exaggeration, the edifice complex will resemble a disk with a pointed external edge. We see (Figure 21a) that the radial extent of the edifice increases with time, while the radial extent of the flow apron, which depends most strongly on T_e (but slightly dependent on load radius), remains roughly constant (increasing by only 20 km between the first and last load increments). Thus, this model of moat structure predicts that the ratio of edifice radius r_{ed} to flow apron radius r_{fa} will increase with time. A volcano with a small r_{ed}/r_{fa} relative to other volcanoes is likely to be at an earlier stage of development than the other volcanoes. The volcano at 3.5°N, 270°E (Figure 11) has a very small edifice in relation to the size of the flow apron. We suggest that this volcano either is currently at an early stage of development (and perhaps still active) or was arrested at this stage by an interruption of the mantle magma source. If one of these interpretations is correct, the lack of circumferential or ponded flows in the apron of this volcano suggests that radial flows fill flexural moats throughout the growth of large volcanoes on Venus.

Synthetic stratigraphy models have similarly been calculated for several terrestrial oceanic hotspot chains. Onlap of the flexural arch is similarly predicted in models of moat filling for the Hawaiian Islands calculated by *ten Brink and Watts* [1985] and *Watts and ten Brink* [1989]. In moat-filling models for the Marquesas Islands calculated by *Wolfe et al.* [1994], early layers onlap the flexural arch but subsequent layers overfill the moat and offlap the

arch. In the Hawaiian models of *Watts and ten Brink* [1989], a series of loads are emplaced successively along a line, simulating the growth of a chain of volcanic islands. In a cross section perpendicular to the direction of load propagation, the stratigraphic layers onlap the flexural arch. The burial of early layers by later ones emanating farther down the chain produces the onlapping pattern. In our models, the onlap results from the radial expansion of a single volcanic load with time. Seismic reflection studies at the Hawaiian chain [*ten Brink and Watts*, 1985; *Rees et al.*, 1993] reveal a characteristic pattern of onlap of the flexural arch in lower moat sections, but offlap in upper moat sections, with ponding of the youngest units in the deepest part of the moat.

Volcano volume and Venus resurfacing

Common assumptions about volcano structure can yield erroneously low volumes. Typically, workers determine edifice heights and radii and use a conical approximation to determine volcano volumes [e.g., *Keddie and Head*, 1994a], ignoring the volume of moat-filling material beneath and around the edifice. Such values are then used to estimate a flux integrated over all the volcanoes of Venus [*Head et al.*, 1992], which then forms a basis for discussions of resurfacing rates [e.g., *Strom et al.*, 1994]. Such a procedure may seriously underestimate the volcanic flux on Venus.

We estimate the volcano magmatic flux on Venus as follows. For each of the 145 large volcanoes in Table 3.0 we measured an "edifice radius" R_t, defined by a break in slope at the edifice edge. Height is then measured from the summit to the elevation of the slope break. Approximating the edifice as a cone ($V = \pi R_t^2 h/3$), the total volume of edifices $V_{te} = 6.0 \times 10^6$ km^3. The total volume of material erupted at large volcanoes (V_{tv}) is then V_{te}/f_e. A simple conical model underestimates volcano volume by a factor $1/f_e$. For the values of density contrast described above, this factor is in the range 7–11. Thus, $V_{tv} = 4$–7×10^7 km^3. Given V_{tv} and an assumed duration τ_v for the period during which large volcanoes formed on Venus, the volcano magmatic flux is $\dot{m}_v = V_{tv}/\tau_v$. This quantity is shown in Figure 22

vs. τ_v for V_{te} equal to 4 and 7 $\times 10^7$ km^3. For comparison, bounds on the present terrestrial intraplate magmatic flux $\dot{m}_t$ (the sum of oceanic intraplate and intracontinental volcanic rates [*Crisp*, 1984]) are also shown.

We have suggested [*McGovern and Solomon*, 1995] that volcano construction on Venus occurred after the postulated global resurfacing event, once the lithosphere had become sufficiently thick to support large volcanic loads. If so, the age of the resurfacing event t_{gr} provides an upper bound on τ_v and thus a lower bound on $\dot{m}_v$. Estimates of t_{gr} range from 300 to 500 Ma [*Strom et al.*, 1994; *Phillips et al.*, 1992]. Under the assumption that the long-term eruption rate at large volcanoes has been approximately constant since that time, we set $\tau_v = t_{gr}$. This assumption yields magmatic flux estimates of 0.1 to 0.2 km^3/yr, about a quarter to half of the current intraplate volcanic flux $\dot{m}_t$ on Earth [*Crisp*, 1984]. Evidence from stratigraphy [*McGill*, 1994] and crater counts [*Namiki and Solomon*, 1994; *Price and Suppe*, 1994] indicates that large volcanoes are significantly younger than the global mean surface age. While a crater retention age for large volcanoes of 0.5 t_{gr} [*Namiki and Solomon*, 1994] is consistent with $\tau_v = t_{gr}$, a younger crater age [*Price and Suppe*, 1994] would favor a lesser value of τ_v. With τ_v = 150 Myr, for instance, the implied volcano magmatic flux (Figure 22) is 0.3 to 0.4 km^3/yr, comparable to $\dot{m}_t$.

Alternatively, if volcanoes were produced during a burst of activity of duration $\tau_b < t_{gr}$, centered in time about the mean volcano age, we can define a paleo-magma-flux $\dot{m}_p = V_{tv}/\tau_b$. If the duration of this burst was small, $\dot{m}_p$ may have substantially exceeded the current terrestrial flux $\dot{m}_t$ (but then the current value of $\dot{m}_v$ may be small).

The quantity $\dot{m}_v$ is a lower bound on the overall planetary magma supply rate $\dot{m}_p$ because it ignores contributions from other volcanic features such as shield fields, small- and intermediate-sized shields [*Head et al.*, 1992], extensive flow fields [*Magee Roberts et al.*, 1992], rift-related volcanism, and recently active coronae, as well as intrusive emplacement of intermediate-density material within or at the base of the crust (underplating), as observed at terrestrial hotspot volcanoes [*Wolfe et al.*, 1994; *ten Brink and Brocher*, 1987]. Of these,

rift volcanism, coronae, and intrusion are probably the largest contributions. Rift and corona volcanism may increase $\dot{m}_v$ by a factor of 2; intrusion may increase it by a factor of 2–10 [*Stofan et al.*, 1995]. However, any intruded or underplated material that compensates the volcanic load would reduce the required amount of moat fill, and can be considered to be accounted for in the above calculation.

This proposed structure for Venus volcanoes has important implications for scenarios of global resurfacing and the estimation of planetary volcanic fluxes. From the spatial distribution of impact craters and the paucity of deformed and externally embayed craters, *Strom et al.* [1994] have argued for a global resurfacing event of short ($\approx$ 10 Ma) duration, followed by a 300 to 500 Ma period of low rates of volcanism (0.01–0.15 km^3/yr). These workers contend that these low rates of volcanism are required to avoid crater embayment as craters accumulate on the surface. These volcanic flux estimates are well below the estimated terrestrial intraplate flux [*Crisp*, 1984], as well as our best estimates of $\dot{m}_p$. The rates cited in *Strom et al.* [1994], however, are based on the assumption that resurfacing occurs by the emplacment of thin ($<$ 1 km) flow units. Moats for typical-sized Venus volcanoes will be several kilometers deep, violating this assumption. Moat filling limits the areal extent of flows, while accommodating a significant flux of magma (and interior heat) to the surface. Moat filling increases the ratio of volume to surface area for the volcanism that occurred after the global resurfacing event and provides a mechanism for reconciling the observed decrease in areal resurfacing rates after plains emplacement [*Price and Suppe*, 1994] with the existence of a steady, significant magma flux to the surface. This model relaxes the constraint on magma flux proposed by *Strom et al.* [1994]; it further suggests a less extreme episodicity to the thermal history of Venus than previously proposed. If volcanoes were created in a burst at the mean volcano age, we still have an era of large magma flux after global resurfacing. This burst is large enough to provide volcano material but evidently not large enough to thin the lithosphere (which would inhibit volcano formation).

Venus thermal history

Our estimates of magma flux provide a new constraint on the thermal evolution of Venus. The planet must have been able to produce at least 4–6 $\times 10^7$ km^3 of erupted or shallowly intruded magma sometime after the global resurfacing event. In one class of models for the global resurfacing event [*Turcotte*, 1995], a period of widespread lithospheric recycling and high magmatic and thermal flux is followed by an extended period of lithospheric stability, low magmatic flux, and low heat flow, and a present thermal lithosphere thickness of 300 km or more. The amount of melt produced by a plume increases with increasing plume potential temperature and decreasing lithosphere thickness [*White and McKenzie*, 1989]. Models in which a very thick lithosphere underlies recently active large volcanoes on Venus may require unrealistically high plume potential temperatures. Such thick lithospheres, however, are not required by the current set of geophysical observations [*Simons et al.*, 1995]. If lithospheric thicknesses and plume potential temperatures are similar on Venus and Earth, similar magmatic fluxes imply similar plume-delivered heat fluxes.

Conclusions

Large volcanoes on Venus exhibit a tectonic style distinct from that of large volcanoes on Earth and Mars. Surface conditions likely preclude a detached basal boundary condition for volcanoes on Venus; instead the bases are welded to the lithosphere. The observed tectonics on Venus volcanoes are consistent with those predicted for a basally-welded volcano with an active magma chamber. A basally-welded boundary condition encourages intrusions in the form of sub-horizontal intrusive complexes (sills); inflation of a magma chamber modifies the stress state to allow magma ascent to the summit caldera and intrusion of radial dikes. Flexural depressions beneath and surrounding the edifices are filled with extruded flows, unlike terrestrial moats which are filled with fragmented mass-wasted material and volcano-derived sediment. The fraction of extrusive flows comprising volcanoes may be significantly

greater on Venus than on terrestrial volcanoes. When the volume of moat filling material is accounted for, the magmatic flux from large volcano construction on Venus is similar to the terrestrial intraplate magma flux. Large edifices may have formed on Venus only after the planet cooled sufficiently to thicken the lithosphere past a threshold value (around 30 km) sufficient to allow magma propagation to the surface.

Figure Captions

Figure 1. Global topography of Venus from a degree and order 360 spherical harmonic expansion [*Rappaport and Plaut*, 1994], truncated at degree and order 90 and tapered from degree and order 85 Locations of large volcanoes (as listed in Table 4.1) are marked with shaded triangles.

Figure 2. Magellan data for Western Eistla Regio. (a) Topographic contours, from Magellan Global Topography Data Record (GTDR) 3.1. Contours are referenced to mean planetary radius of 6051.9 km. Dark solid reference contour roughly outlines the volcanoes Sif Mons and Gula Mons. Light solid contours and dashed contours denote elevations above and below the reference contour, respectively. Reference contour 0.6 km above mean planetary radius. Contour interval is 0.2 km for both dashed and solid contours. Sinusoidal projection, with projection longitude 355° E. (b) Synthetic aperture radar (SAR) image of the southern flanks of Sif and Gula Montes. A portion of Magellan Compressed-once Magellan Image Data Record 15N352 (C1-MIDR15N352), browse image. East-west extent of image is about 1350 km. The image was stretched using the histogram equalization command in the imaging software package xv. The following features are labeled: Sif Mons (1), Gula Mons (2) and Guor Linea (3).

Figure 3. Magellan data for Sif Mons. (a) Topographic contours. Dark solid reference contour roughly outlines the volcanic edifice. Light solid contours and dashed contours denote elevations above and below the reference contour, respectively. Reference contour 0.6 km above mean planetary radius. Contour intervals 0.2 km (solid), 0.1 km (dashed). Lines radiating from summit indicate cross section tracks. (b) SAR image (F-MIDR20N351, browse image) with superposed topographic contours. Histogram equalization applied as above. (c) Topographic cross-sectional profiles for four quadrants. The horizontal bar denotes the radius range of the edge of the flow apron in the given quadrant. (d) Average of the twelve profiles from (c).

Figure 4. Magellan data for Gula Mons (a) Topographic contours, as in Figure 3. (b)

SAR image (F-MIDR20N357, browse image) of summit region and southern flank. East-west extent of image is about 700 km. Custom image stretch applied. Labeled features: summit linear deformation zone (1), westernmost section of Guor Linea rift (2). (c) Topographic profiles of Gula Mons. (d) Mean topographic profile of Gula Mons.

Figure 5. Magellan data for volcano at 9° N 29° E. (a) Topographic contours, as in Figure 3. Reference contour -0.2 km above mean planetary radius. Contour interval 0.2 km (for both solid and dashed). (b) SAR image (cropped from C1-MIDR15N026 browse image, histogram equalization applied to cropped region) of edifice and most of flow apron. East-west extent of image is about 1050 km. (c) Contours of topography superposed on image in (b). (d) Close up of summit and southern flank, framelet 54 of C1-MIDR15N026. East-west extent of image is about 225 km. Labeled features: Summit caldera complex (1), radial fracture zones to east-northeast (2) and west-southwest (3), and western part of parasitic shield (4). (e) Topographic profiles. (f) Mean topographic profile.

Figure 6. Magellan data for Tepev Mons (a) Topographic contours, as in Figure 3. Reference contour 0.0 km above mean planetary radius. Contour interval 0.4 km (solid), 0.2 km (dashed). (b) SAR image (special product MRPS 43148 produced by JPL). East-west extent of image is about 500 km. (c) Topographic profiles. (d) Mean topographic profile.

Figure 7. Magellan data for Sapas Mons (a) Topographic contours, as in Figure 3. Reference contour 1.6 km above mean planetary radius. Contour interval is 0.2 km for both dashed and solid contours. (b) SAR image (F-MIDR10N188, browse image) of Sapas Mons. Histogram equalization applied. East-west extent of image is about 610 km. (c) Close up of summit region. Image cropped from (b); histogram equalization applied to cropped image. East-west extent of image is about 450 km. Labeled features: Summit scalloped-margin domes (1), flank circumferential graben (2), radial dikes (3). (d) Topographic profiles. (e) Mean topographic profile.

Figure 8. Magellan data for Maat Mons (a) Topographic contours, as in Figure 3. Reference contour 2.0 km above mean planetary radius. Contour interval 0.4 km (solid),

0.2 km (dashed). (b) SAR image (C1-MIDR00N197, browse image, histogram equalization), showing both Maat (label 1) and Ozza (label 2) Montes, as well as Dali Chasma (label 3). East-west extent of image is about 1850 km. (c) SAR image (F-MIDR00N194, browse image, histogram equalization) of Maat Mons. East-west extent of image is about 610 km. (d) SAR image (framlet 21 of F-MIDR00N194, histogram equalization), showing summit region of Maat Mons. East-west extent of image is about 75 km. (e) Topographic profiles. (f) Mean topographic profile.

Figure 9. Magellan data for volcano at 35.5° N 211.5° E. (a) Topographic contours, as in Figure 3. Reference contour -0.2 km above mean planetary radius. Contour interval 0.2 km for both dashed and solid contours. (b) SAR image (F-MIDR35N210, browse image, histogram equalization), showing edifice and south and west portions of flow apron. East-west extent of image is about 610 km. (c) SAR image (framlet 22 of F-MIDR35N210, histogram equalization), showing northwest caldera complex. (d) Topographic profiles. (e) Mean topographic profile.

Figure 10. Magellan data for volcano at 15° S 215° E. (a) Topographic contours, as in Figure 3. Reference contour 0.4 km above mean planetary radius. Contour interval 0.2 km for both dashed and solid contours. (b) SAR image (F-MIDR15S214, browse image, histogram equalization), showing all but easternmost section of flow apron for this volcano. East-west extent of image is about 610 km. (c) Topographic profiles. (d) Mean topographic profile.

Figure 11. Magellan data for volcano at 4° N 270° E. (a) Topographic contours, as in Figure 3. Reference contour -0.2 km above mean planetary radius. Contour interval 0.2 km for both dashed and solid contours. (b) SAR image (cropped from C1-MIDR00N266, browse image, histogram equalization applied to cropped region). East-west extent of image is about 750 km. (c) Topographic profiles. (d) Mean topographic profile.

Figure 12. Magellan data for volcano at 10° N 275° E. (a) Topographic contours, as in Figure 3. Reference contour -0.2 km above mean planetary radius. Contour interval 0.2

km for both dashed and solid contours. (b) SAR image (F-MIDR10N273, browse image, histogram equalization), of edifice and western flow apron of volcano. East-west extent of image is about 610 km. Labeled features: distally broadening flows on western flank (1), flows deflected into a circumferential path (2, extending to southwest). (c) contours of topography overlaid on image in (b). Reference contour -0.4 km above mean planetary radius. (d) Topographic profiles. (e) Mean topographic profile.

Figure 13. Magellan data for volcano at 13° S 316° E. (a) Topographic contours, as in Figure 3. Reference contour -0.6 km above mean planetary radius. Contour interval 0.1 km for both dashed and solid contours. (b) SAR image (C1-MIDR15S317, browse image, histogram equalization), of edifice and circumferential moat filling flows. The source for these flows is in the high terrain to the west. East-west extent of image is about 650 km.

Figure 14. (a) Complete finite element grid for Venus volcano models. (b) Close up of volcano edifice elements, with numbers identifying load increment. Elements marked with a "3" are switched "on" after the initial elastic calculation, those marked with a 4 are switched "on" after completion of relaxation from the previous increment, and so on until completion of relaxation from the final increment ("7").

Figure 15. Stress state in edifice welded to underlying lithosphere, T_e = 40 km. (a) Principal stress orientations in the edifice after completion of relaxation from the third load increment. Symbols describing principal stress state are defined in Figure 7 of Chapter 3. Elements are plotted in their original (undeformed) positions. (b) As in (a) after relaxation from the fourth load increment. (c) As in (a) after relaxation from the fifth load increment. (d) Contours of maximum shear stress (difference between σ_1 and σ_3) in the edifice after completion of relaxation from the third load increment. Edifice is shown in its original (undeformed) configuration. (e) as in (d) after relaxation from the fourth load increment. (f) as in (d) after relaxation from the fifth load increment.

Figure 16. Stress state in edifice welded to underlying lithosphere, T_e = 16 km. (a) Principal stress orientations in the edifice after completion of relaxation from the third load

increment. (b) As in (a) after relaxation from the fourth load increment. (c) As in (a) after relaxation from the fifth load increment. (d) Contours of maximum shear in the edifice after completion of relaxation from the third load increment. (e) as in (d) after relaxation from the fourth load increment. (f) as in (d) after relaxation from the fifth load increment.

Figure 17. Maximum σ_{rr} vs. load increment for five models with T_e values from 8 to 40 km.

Figure 18. Surface topography for finite element models with T_e = 8 km and 40 km.

Figure 19. Schematic diagram of preferred paths of intrusion in a large volcano on Venus. Unmodified, principal stress orientations favor intrusion of subhorizontal sills. Such sills may intrude into any of the layers regardless of age or differential stress magnitude. Magma chamber pressurization, however, adds a stress perturbation which may reorient the principal stresses to favor radial dike intrusion. This reorientation is easiest in the uppermost layers, in which differential stresses are the least. Intrusion of radial dikes is therefore restricted to the uppermost layers of the edifice. Remnants of older dikes remain in the lower, buried parts of the edifice. These buried structures may eventually be intruded by sills. Magma chamber pressurization also changes principal stress orientations in the region connecting the chamber and the surface caldera (marked with a "c"), allowing magma ascent into the caldera. Note: magma chamber is drawn to be roughly spherical; vertical exaggeration of figure is about 10:1.

Figure 20. Flexural moat structure and moat filling at volcanoes in two different terrestrial chains. (a) Flexure and moat filling at the Hawaiian chain on a cross section taken across the Island of Oahu, from *Watts and ten Brink* [1989]. Top line in both figures is bathymetry. Jagged line at bottom of bottom figure is crustal basement, determined from seismic reflection data [*Watts and ten Brink*, 1989]. Elastic flexure models are shown as solid, dashed and circle curves on bottom figure. Note depression in bathymetry flanking the central edifice. (b) Three sections of seismic stratigraphy at the Marquesas chain, from *Wolfe et al.* [1994]. Dashed and solid lines at base of seismic sections represent deflection of

the lithosphere calculated from surface loading and surface plus underplating loading elastic flexure models, respectively. Note the absence of a bathymetric depression flanking the central edifice volcanic complex.

Figure 21. Proposed stratigraphy of a large volcano on Venus. Flexural displacements are calculated for five equal-volume conical load increments (flexural profiles computed using the thick-plate formulation of *Comer* [1983].) Each increment has the deflection from all later increments applied to it. Dashed lines denote the top surface of each increment. The top solid line is the final topography; the bottom solid line is the base of the volcanic pile. The diagonal solid-dashed line denotes the edge of the incremental edifices: all material to the left of this line was emplaced on or intruded into an edifice; all material to the right was emplaced on or intruded into a flow apron. (a) T_e = 40 km, ρ_c = 2800 kg/m^3, ρ_m = 3300 kg/m^3. Total erupted volume is 7 × edifice volume. (b) closeup of (a) near zero crossing of flexural profile. (c) T_e = 40 km, ρ_c = 2800 kg/m^3, ρ_m = 3100 kg/m^3. Total erupted volume is 11 × edifice volume.

Figure 22. Estimated volcano magmatic flux on Venus versus volcano formation time scale. Solid curves represent volume estimates for two values of edifice volume fraction f_e (14% for lower curve, 9% for upper curve). Dashed lines are estimates of the terrestrial intraplate volcanic flux from *Crisp* [1984].

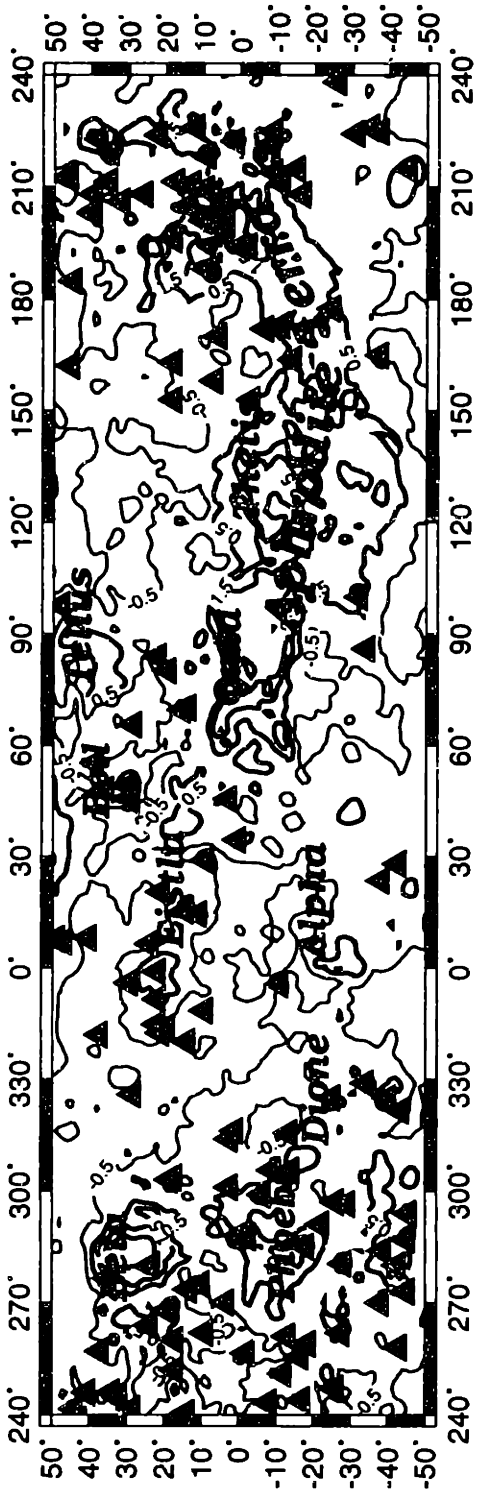
50°
40°
30°
20°
10°
0°
-10°
-20°
-30°
-40°
-50°
240°
210°
180°
150°
120°
90°
60°
30°
0°
330°
300°
270°
240°

Figure 1.

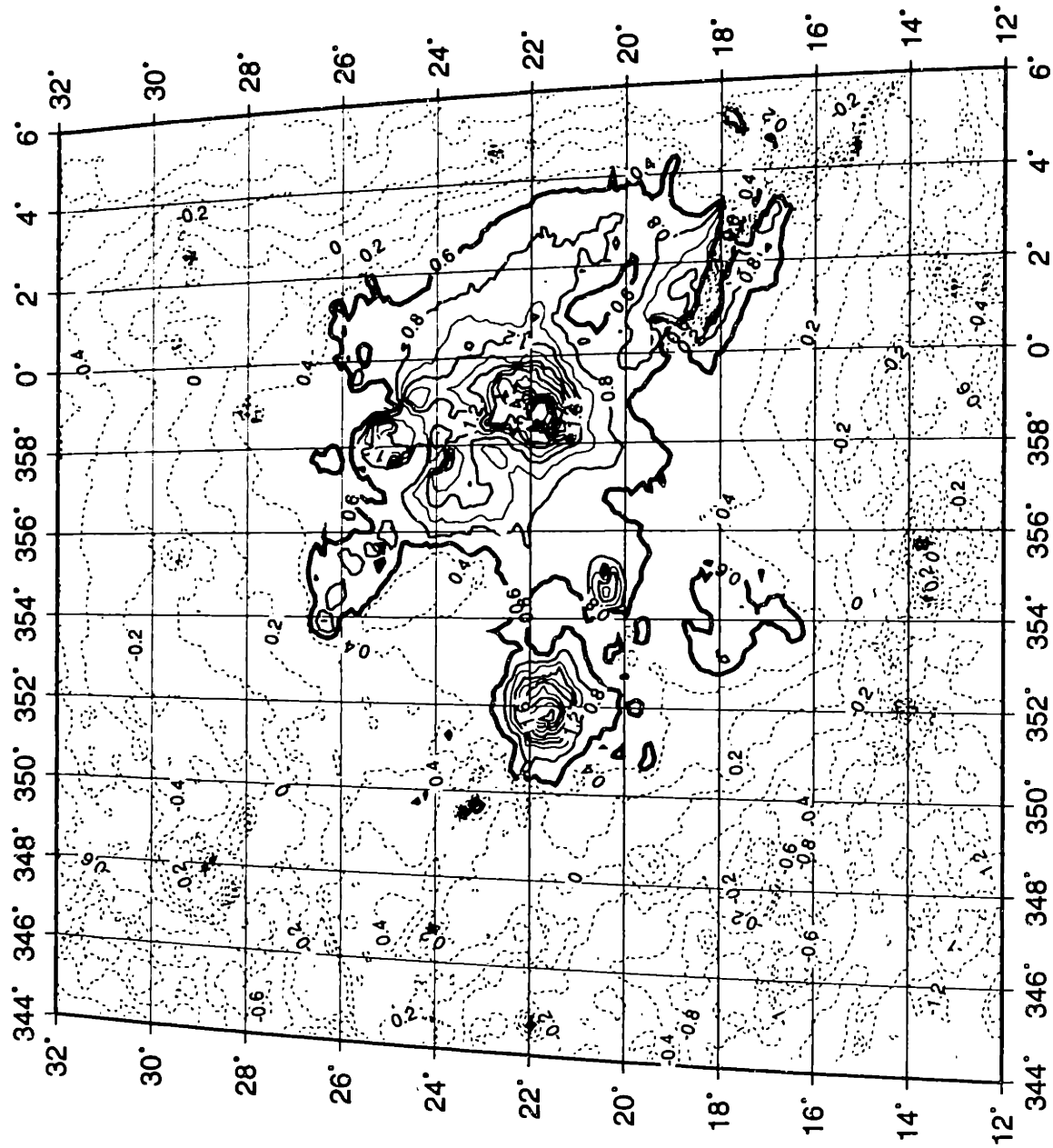
32°
30°
28°
26°
24°
22°
20°
18°
16°
14°
12°
6°
4°
2°
0°
358°
356°
354°
352°
350°
348°
346°
344°

Figure 2a.

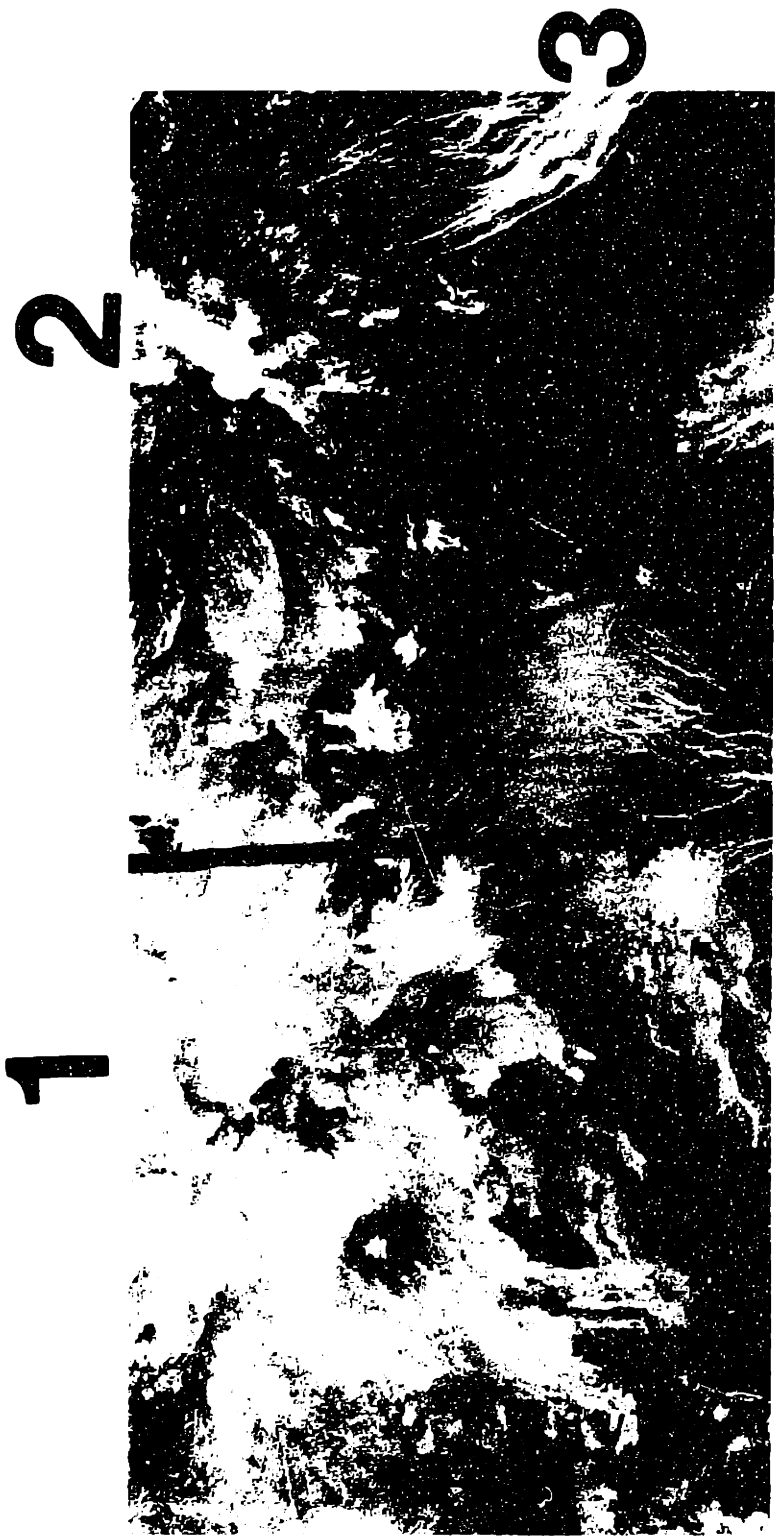

Figure 2b.

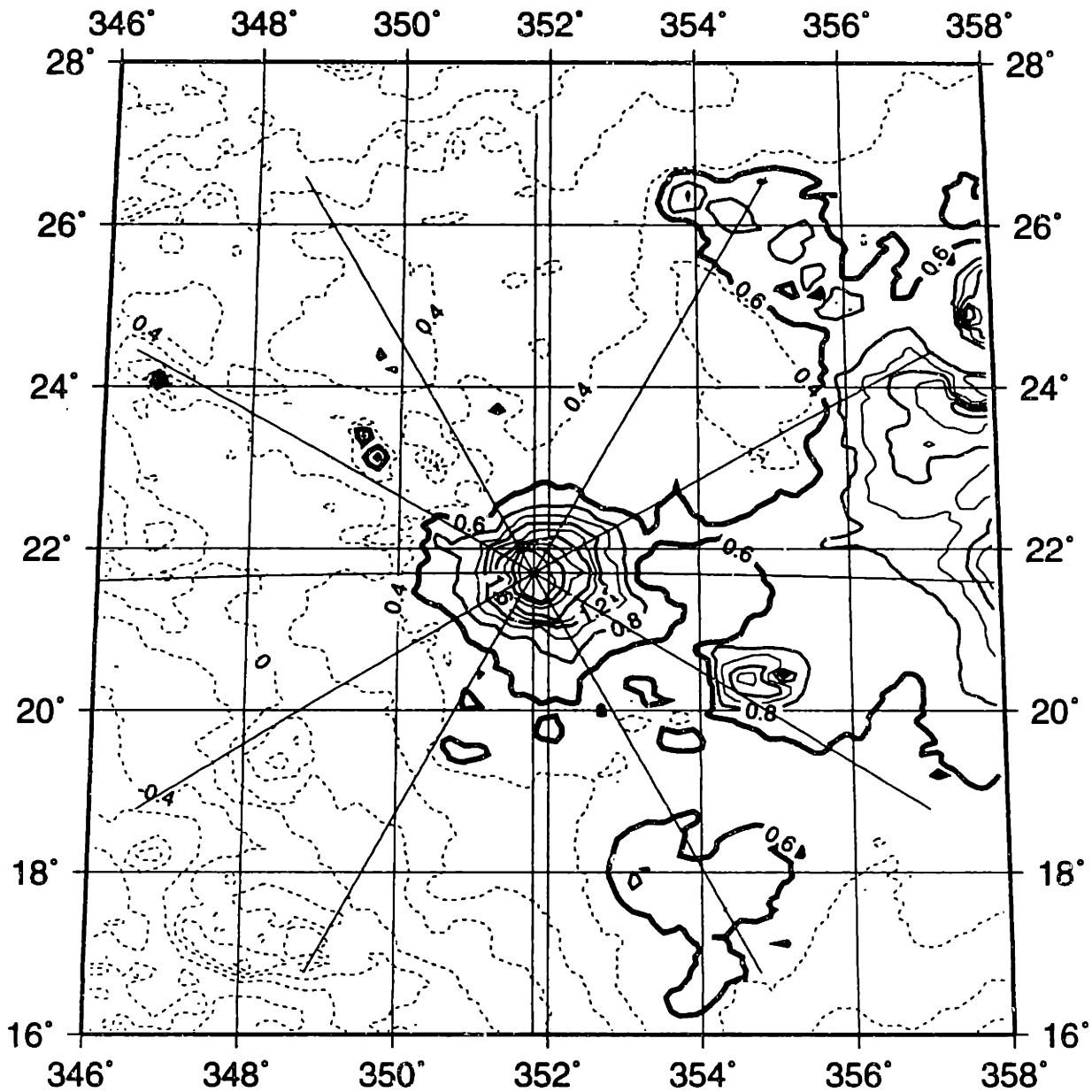

Figure 3a.

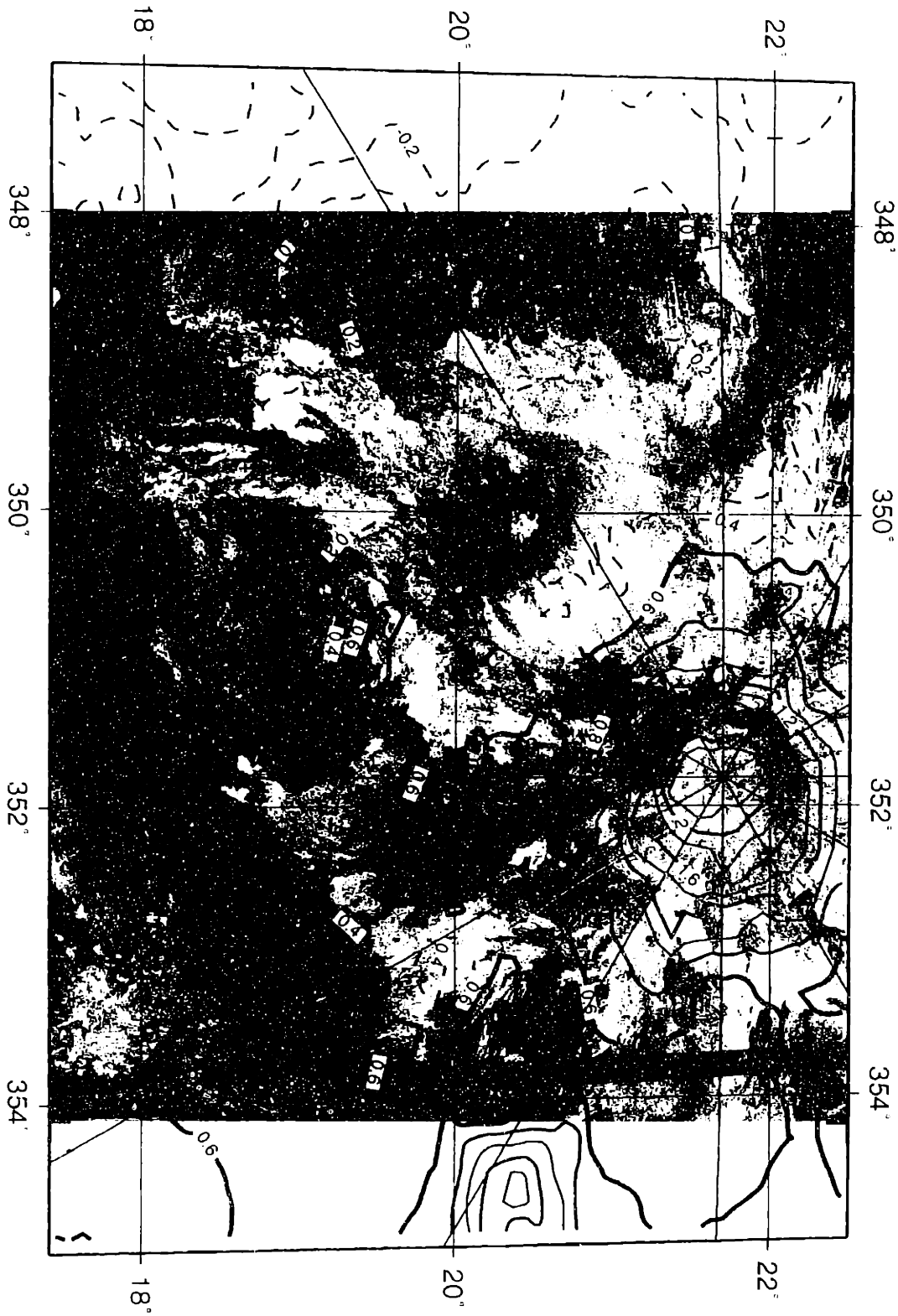

Figure 3b.

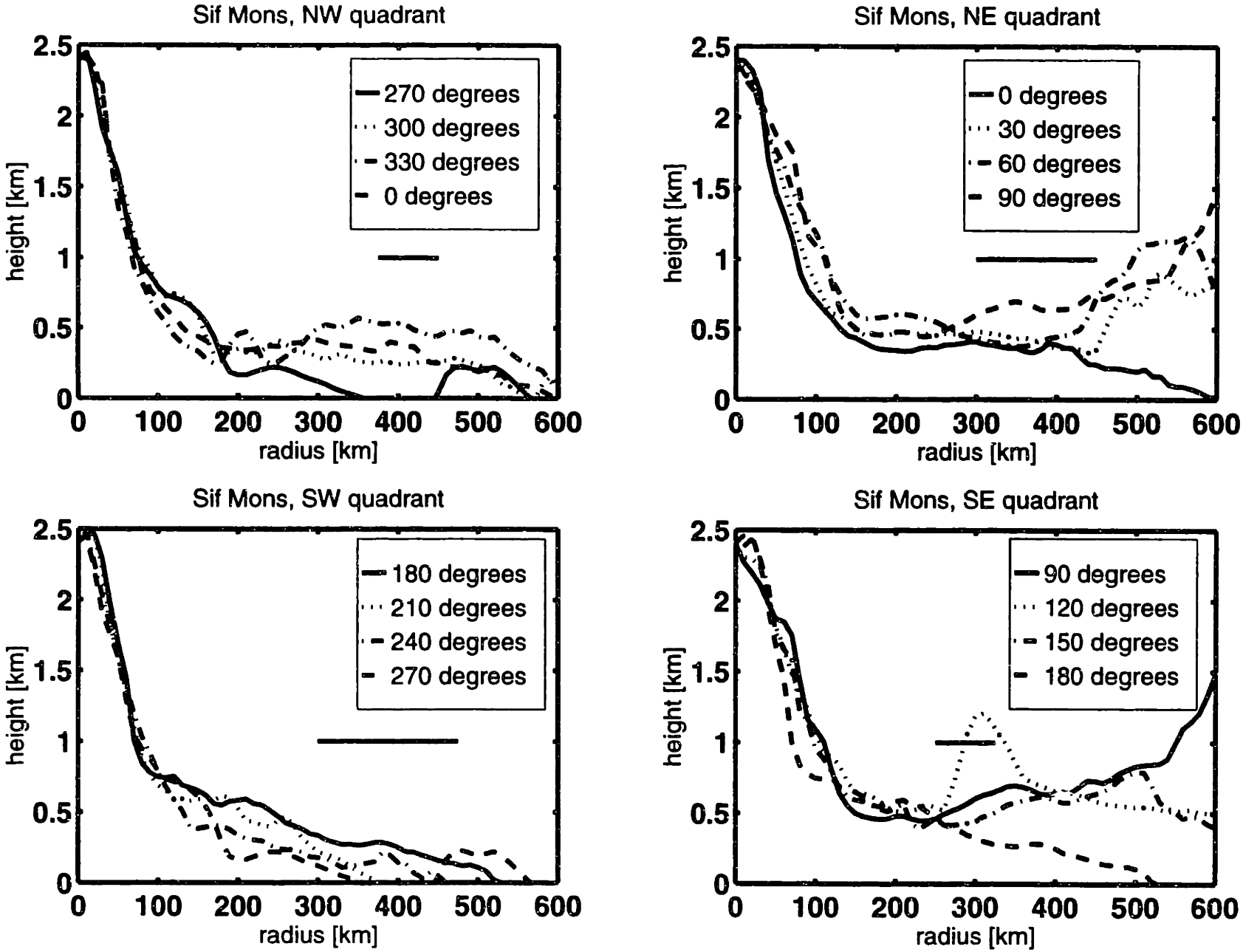
Sif Mons, NW quadrant
270 degrees
300 degrees
330 degrees
0 degrees
height [km]
radius [km]
Sif Mons, NE quadrant
0 degrees
30 degrees
60 degrees
90 degrees
height [km]
radius [km]
Sif Mons, SW quadrant
180 degrees
210 degrees
240 degrees
270 degrees
height [km]
radius [km]
Sif Mons, SE quadrant
90 degrees
120 degrees
150 degrees
180 degrees
height [km]
radius [km]

Figure 3c.

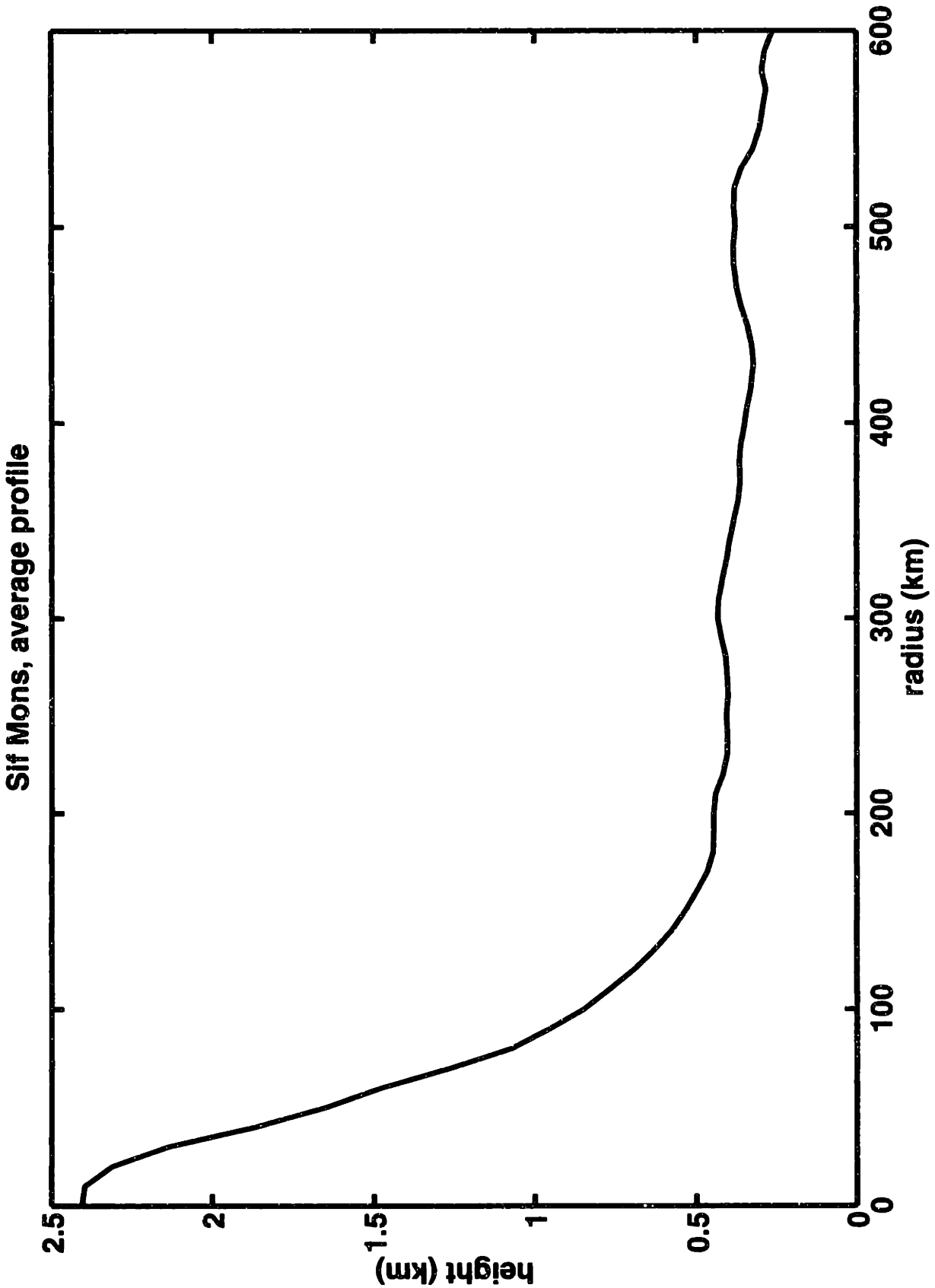
Sif Mons, average profile
height (km)
radius (km)
2.5
2
1.5
1
0.5
0
0
100
200
300
400
500
600

Figure 3d.

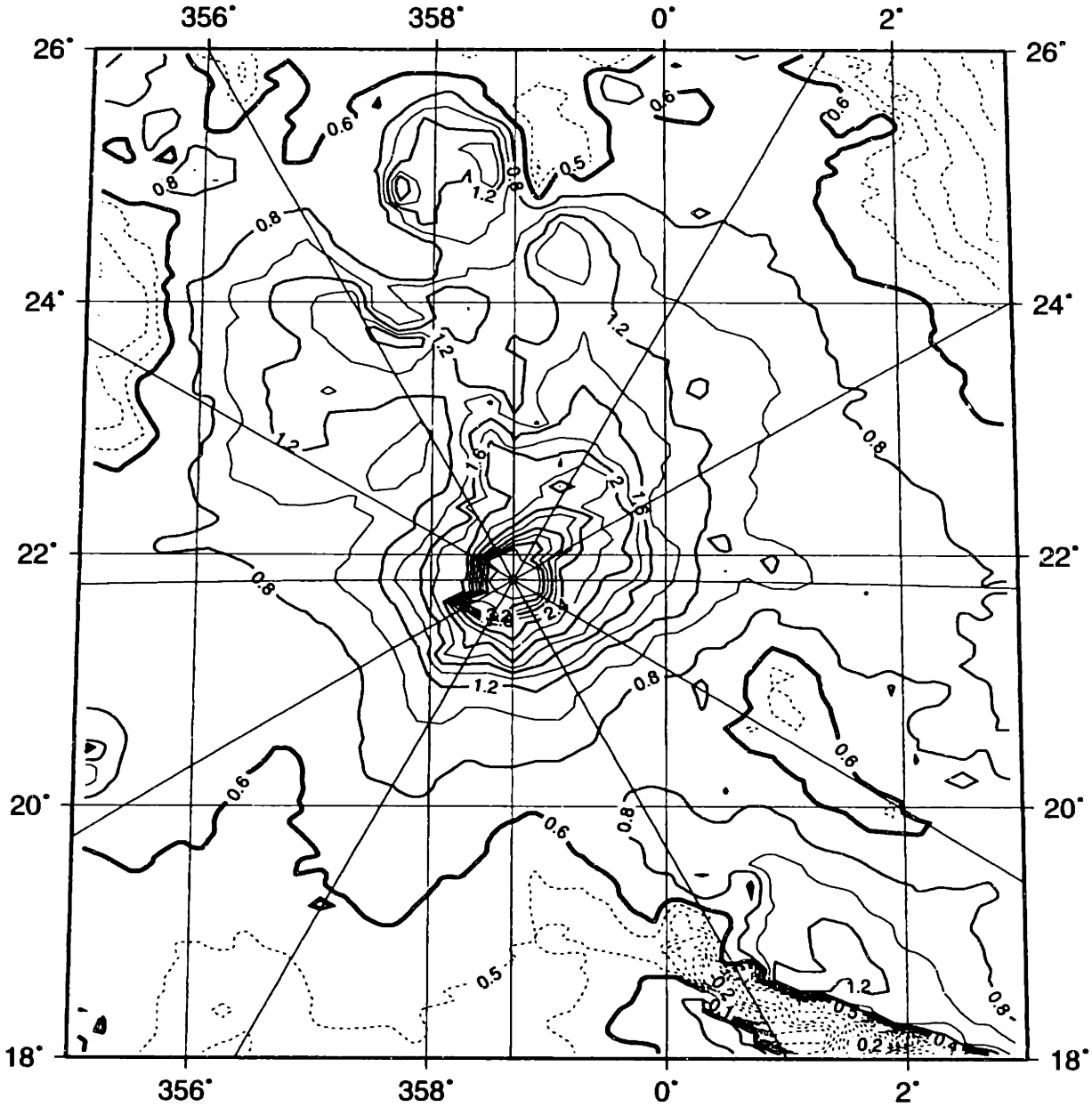

Figure 4a.

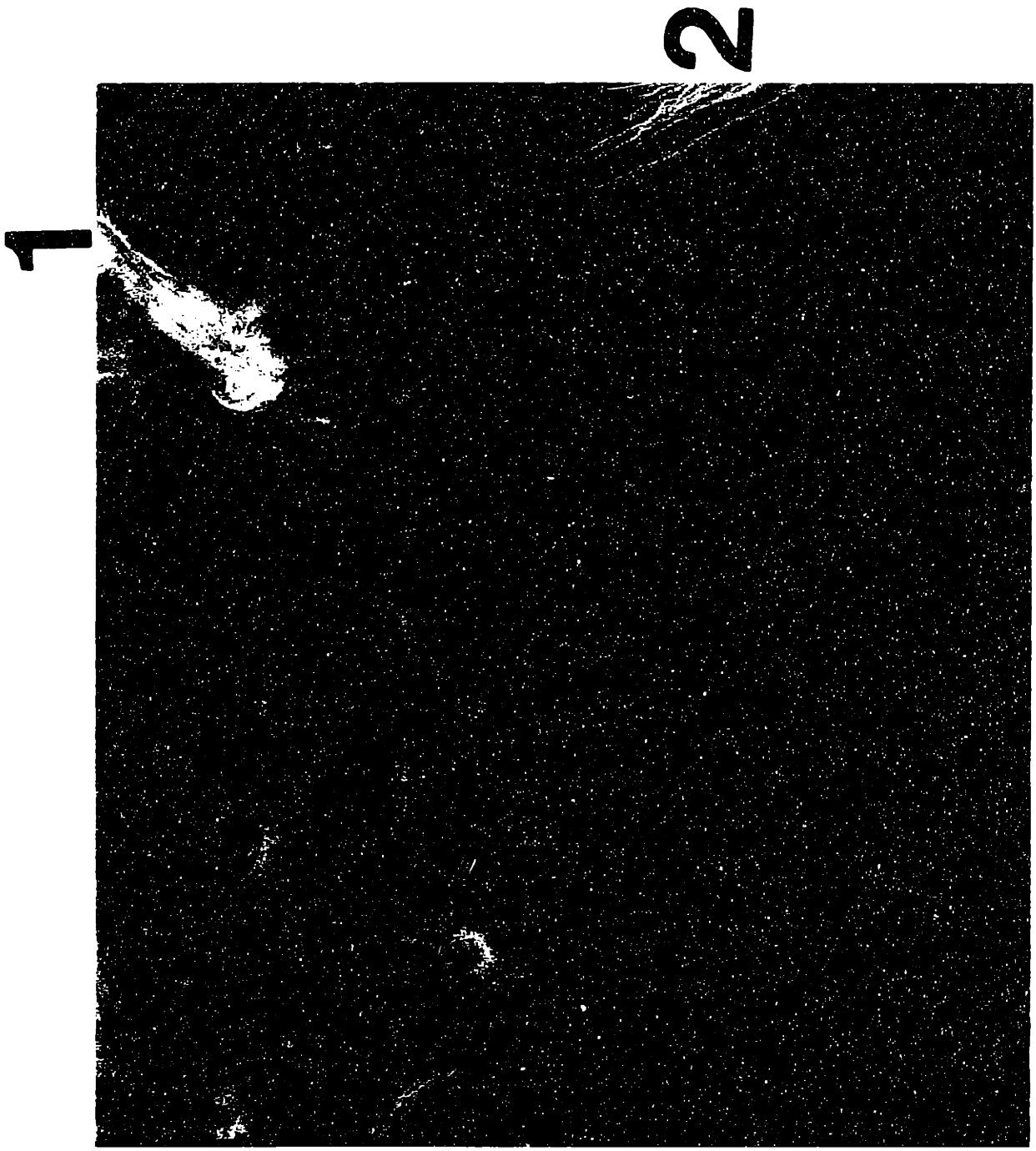

Figure 4b.

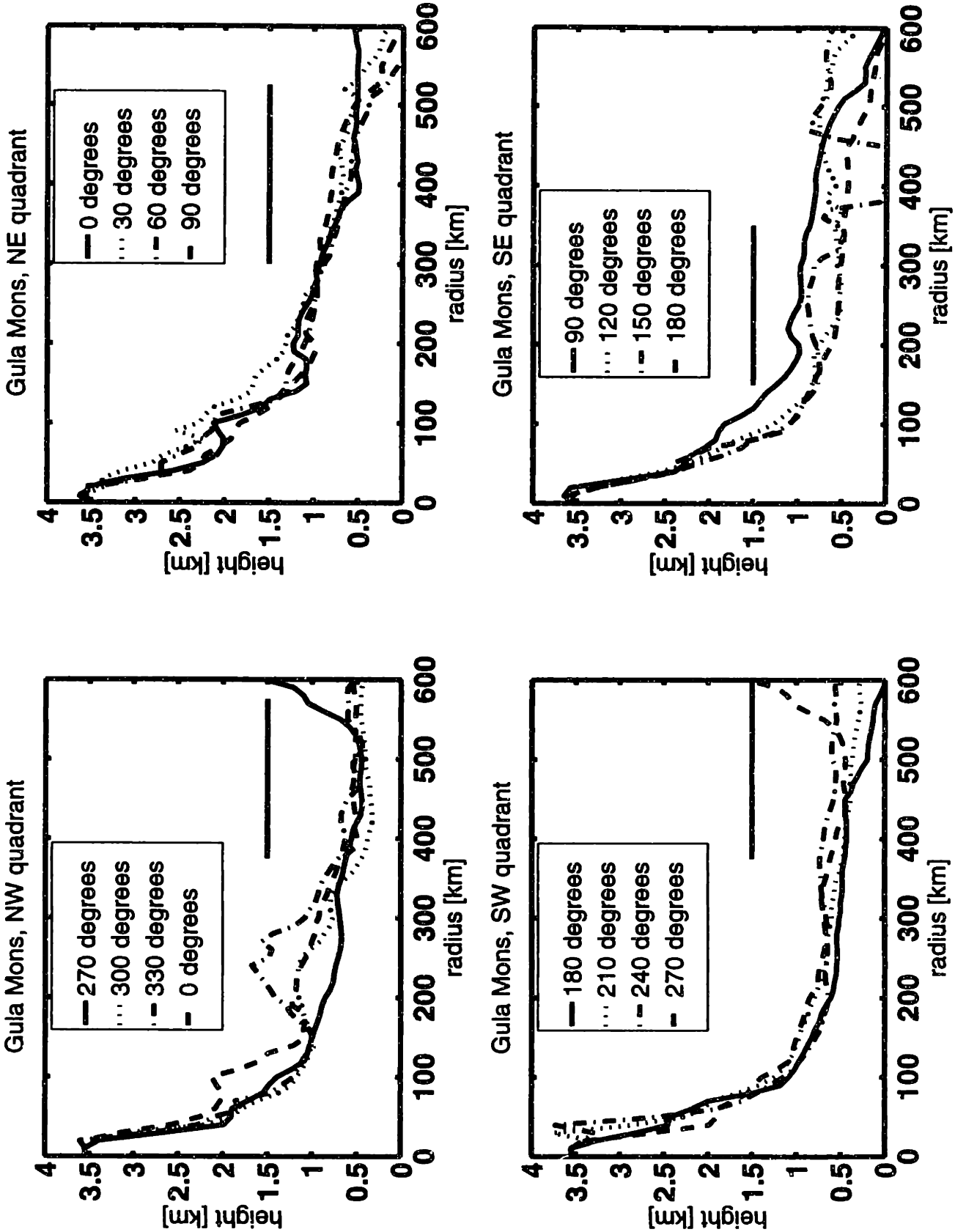
Gula Mons, NE quadrant
0 degrees
30 degrees
60 degrees
90 degrees
height [km]
radius [km]
Gula Mons, SE quadrant
90 degrees
120 degrees
150 degrees
180 degrees
height [km]
radius [km]
Gula Mons, NW quadrant
270 degrees
300 degrees
330 degrees
0 degrees
height [km]
radius [km]
Gula Mons, SW quadrant
180 degrees
210 degrees
240 degrees
270 degrees
height [km]
radius [km]

Figure 4c.

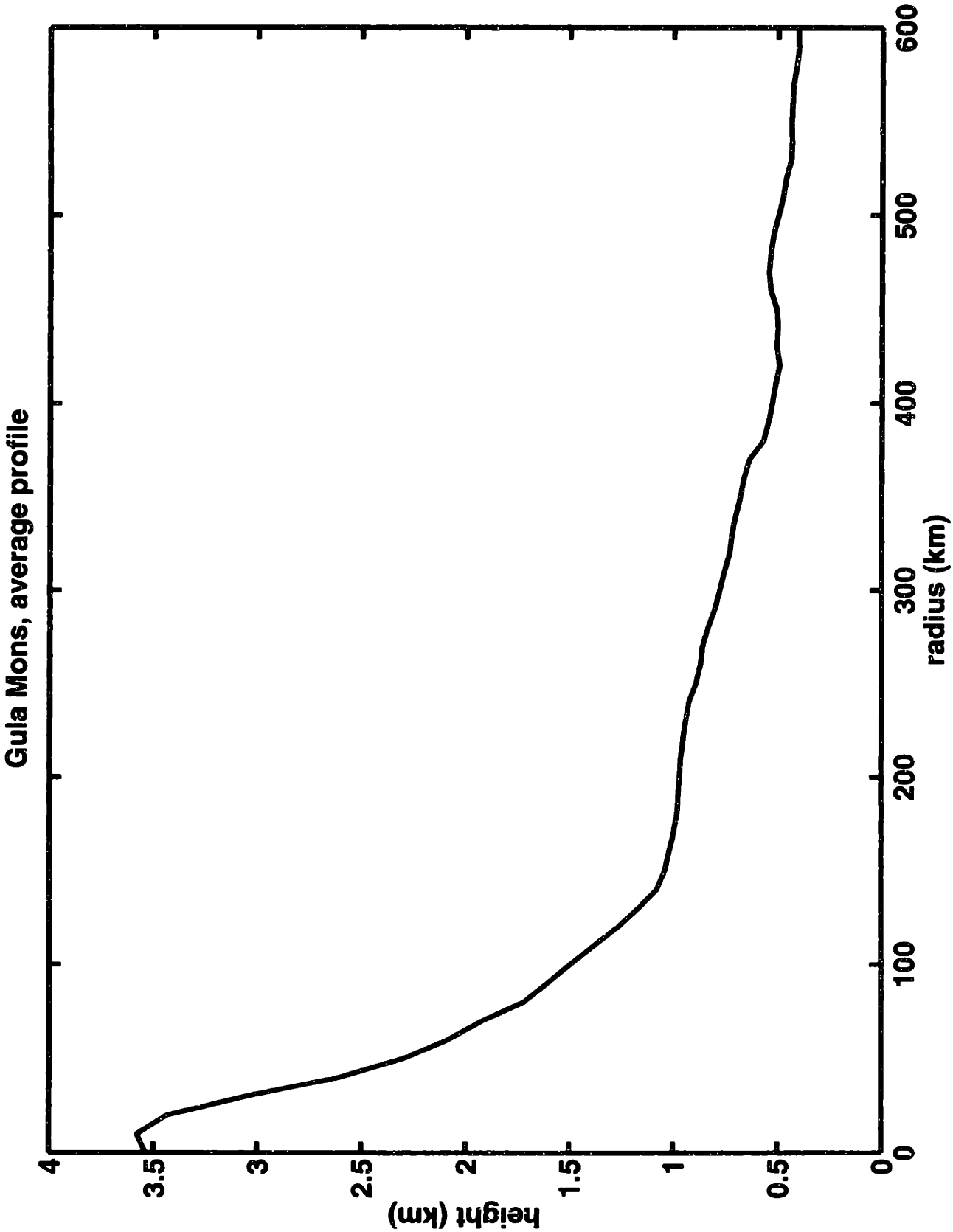
Gula Mons, average profile
height (km)
radius (km)
0
0.5
1
1.5
2
2.5
3
3.5
4
0
100
200
300
400
500
600

Figure 4d.

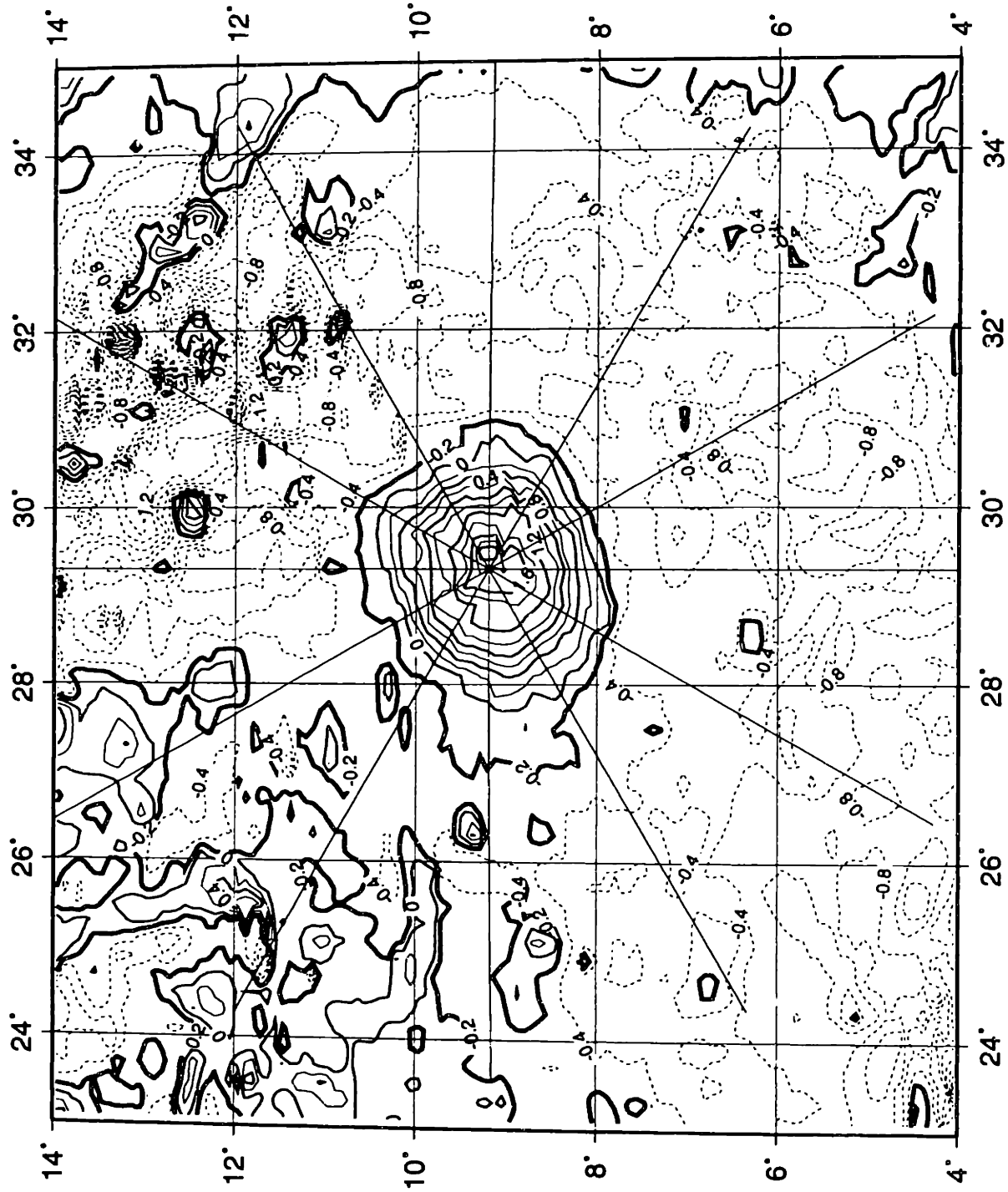

Figure 5a.

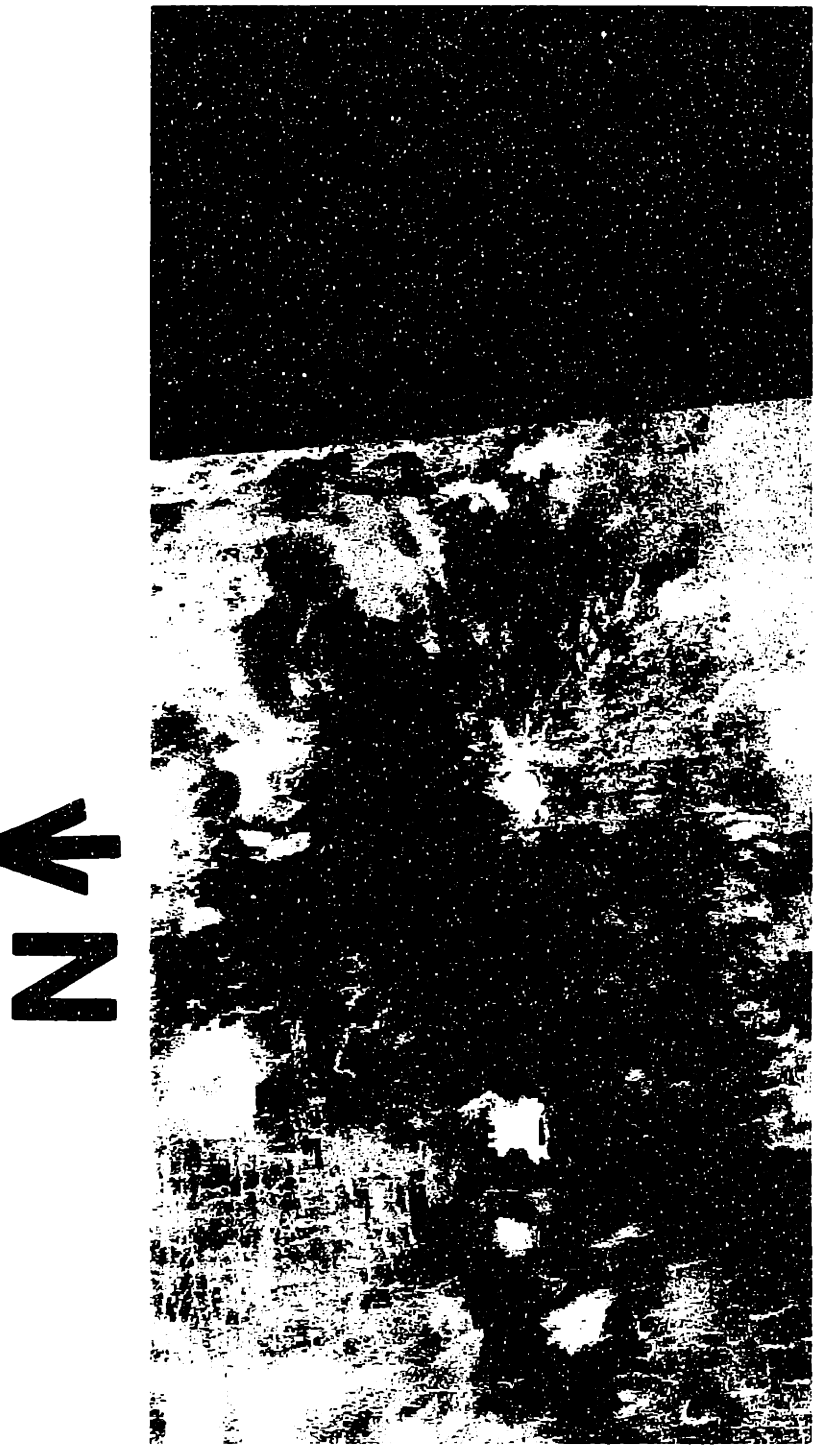

Figure 5b.

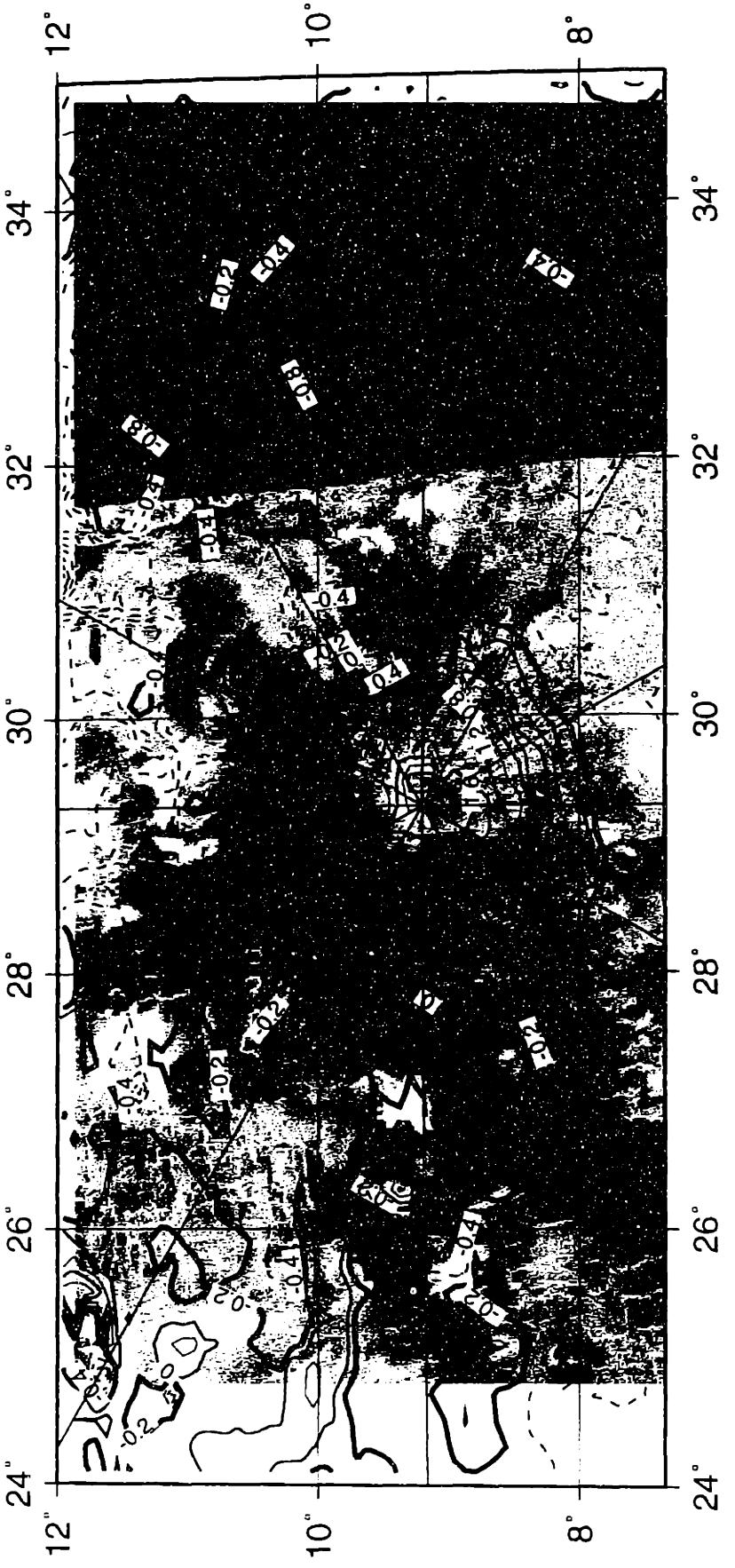

Figure5c.

Figure 5d.

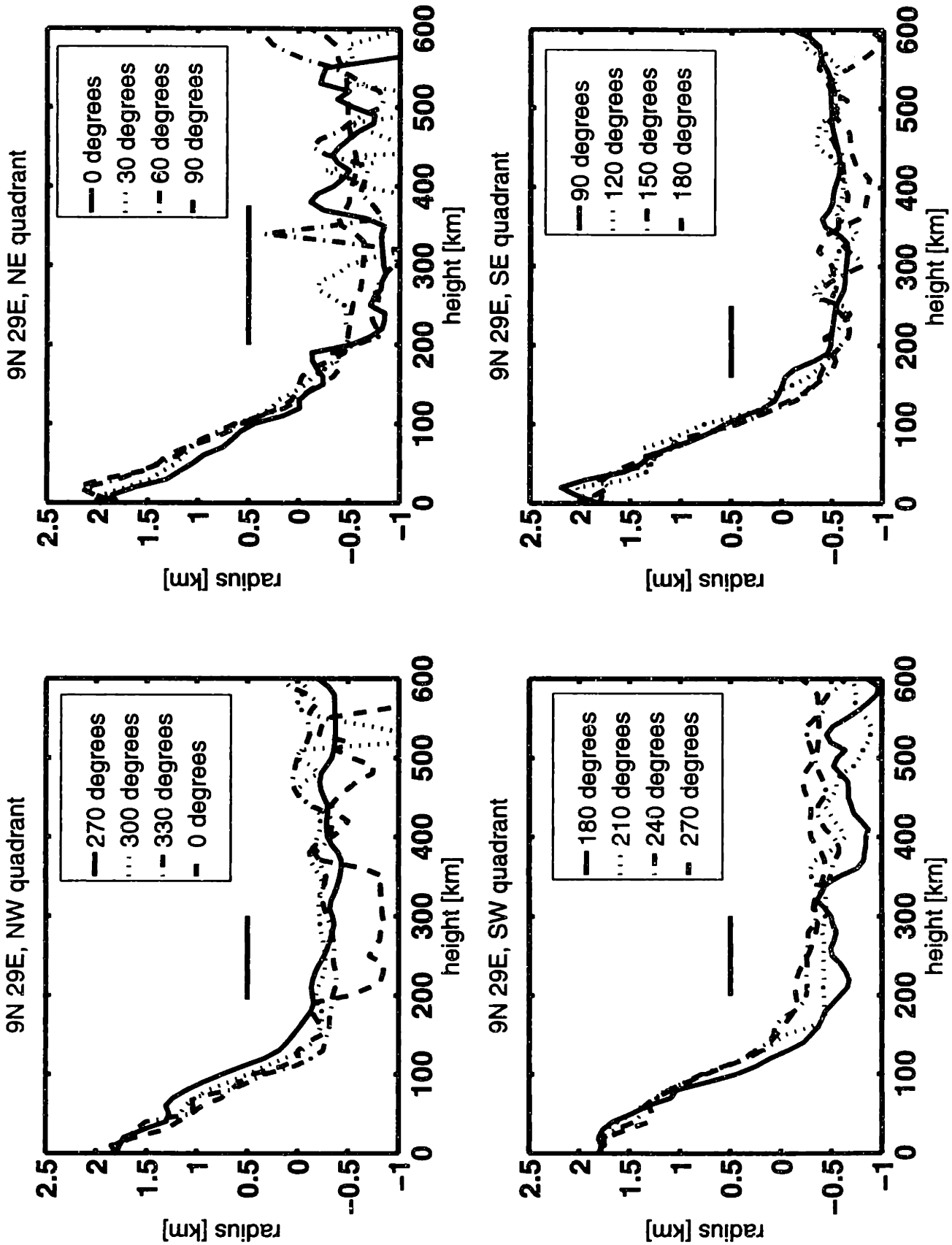
9N 29E, NE quadrant
0 degrees
30 degrees
60 degrees
90 degrees
radius [km]
height [km]
9N 29E, SE quadrant
90 degrees
120 degrees
150 degrees
180 degrees
radius [km]
height [km]
9N 29E, NW quadrant
270 degrees
300 degrees
330 degrees
0 degrees
radius [km]
height [km]
9N 29E, SW quadrant
180 degrees
210 degrees
240 degrees
270 degrees
radius [km]
height [km]

Figure 5e.

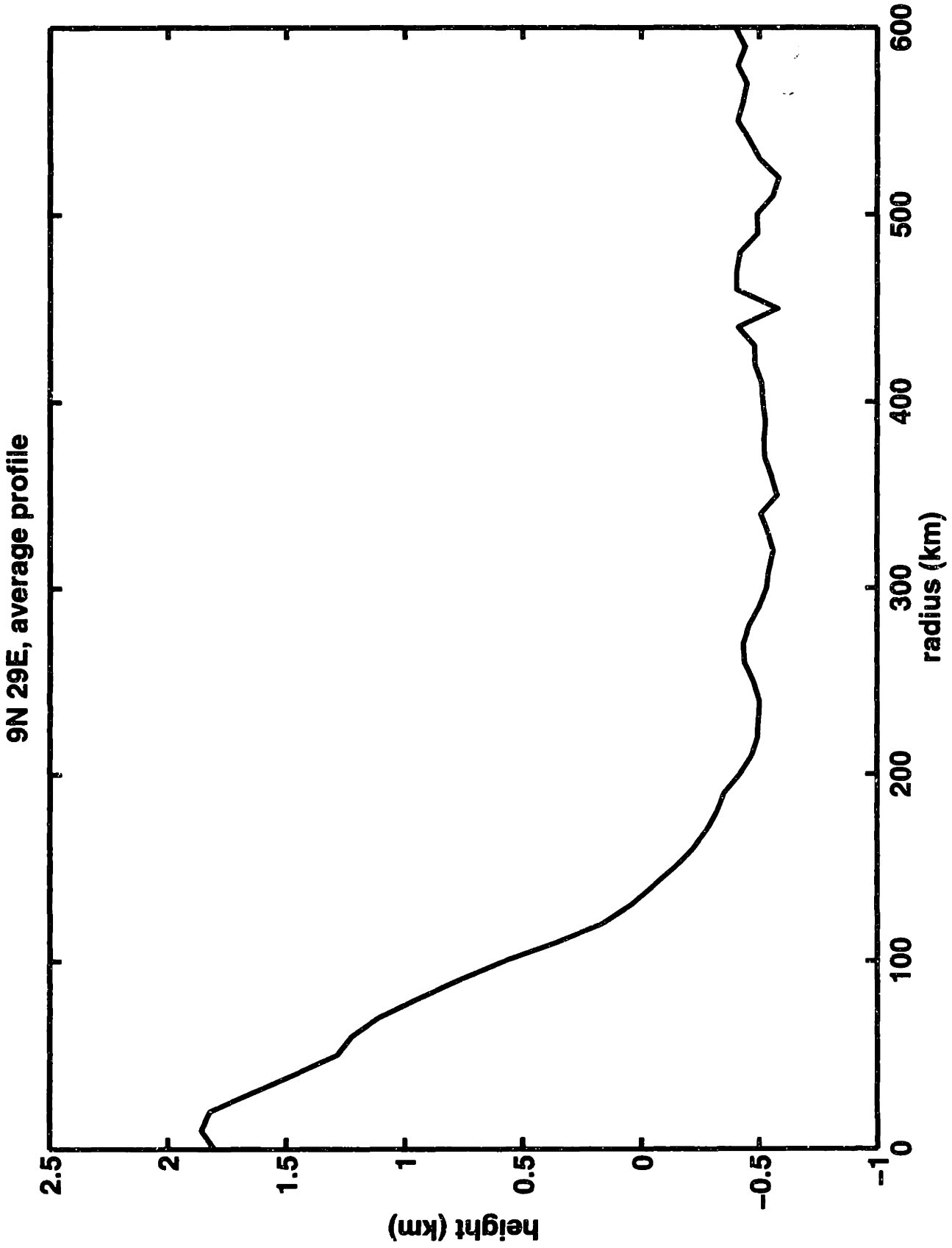
9N 29E, average profile
height (km)
radius (km)
2.5
2
1.5
1
0.5
0
−0.5
−1
0
100
200
300
400
500
600

Figure 5f.

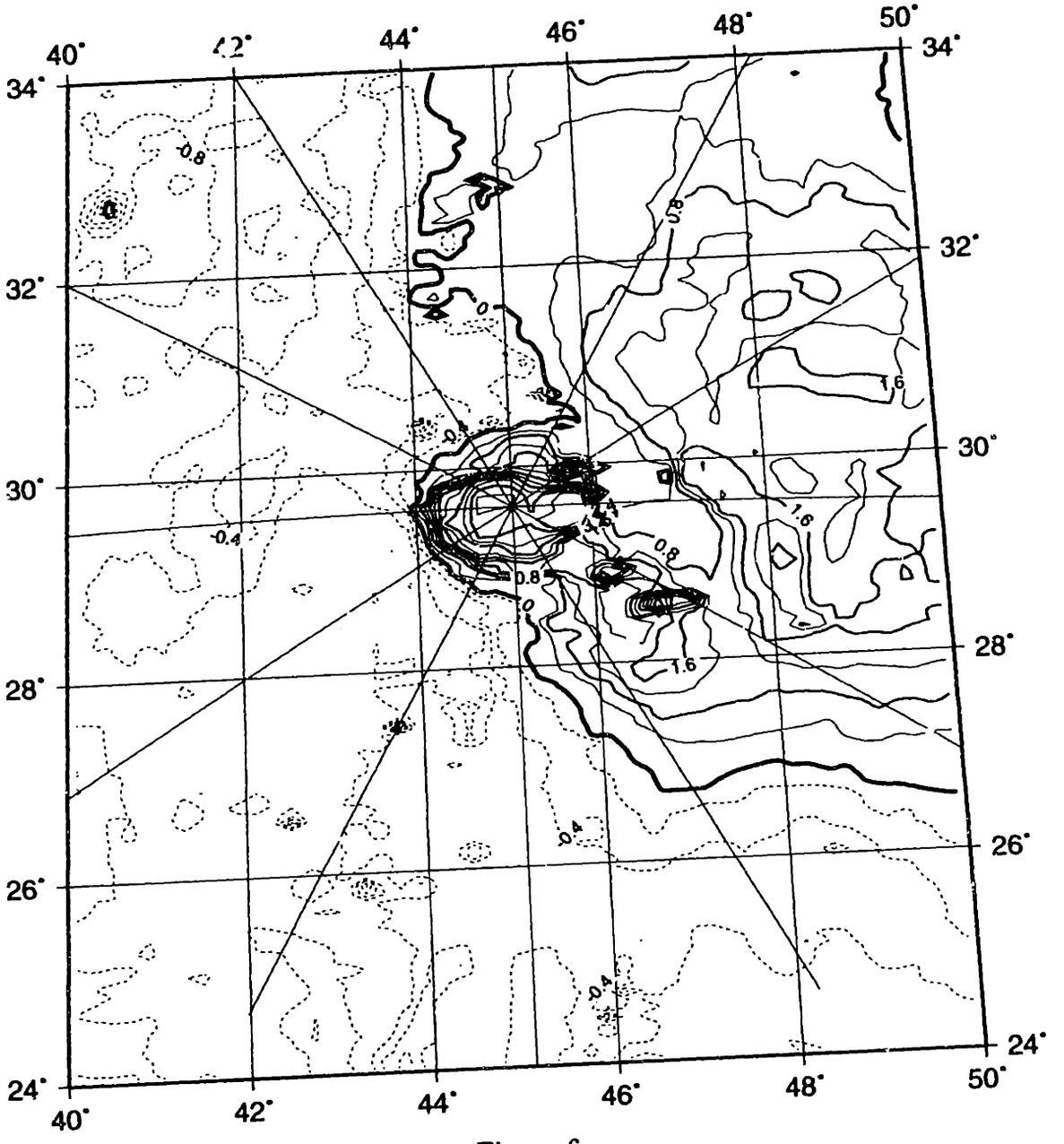

Figure 6a.

Z ←

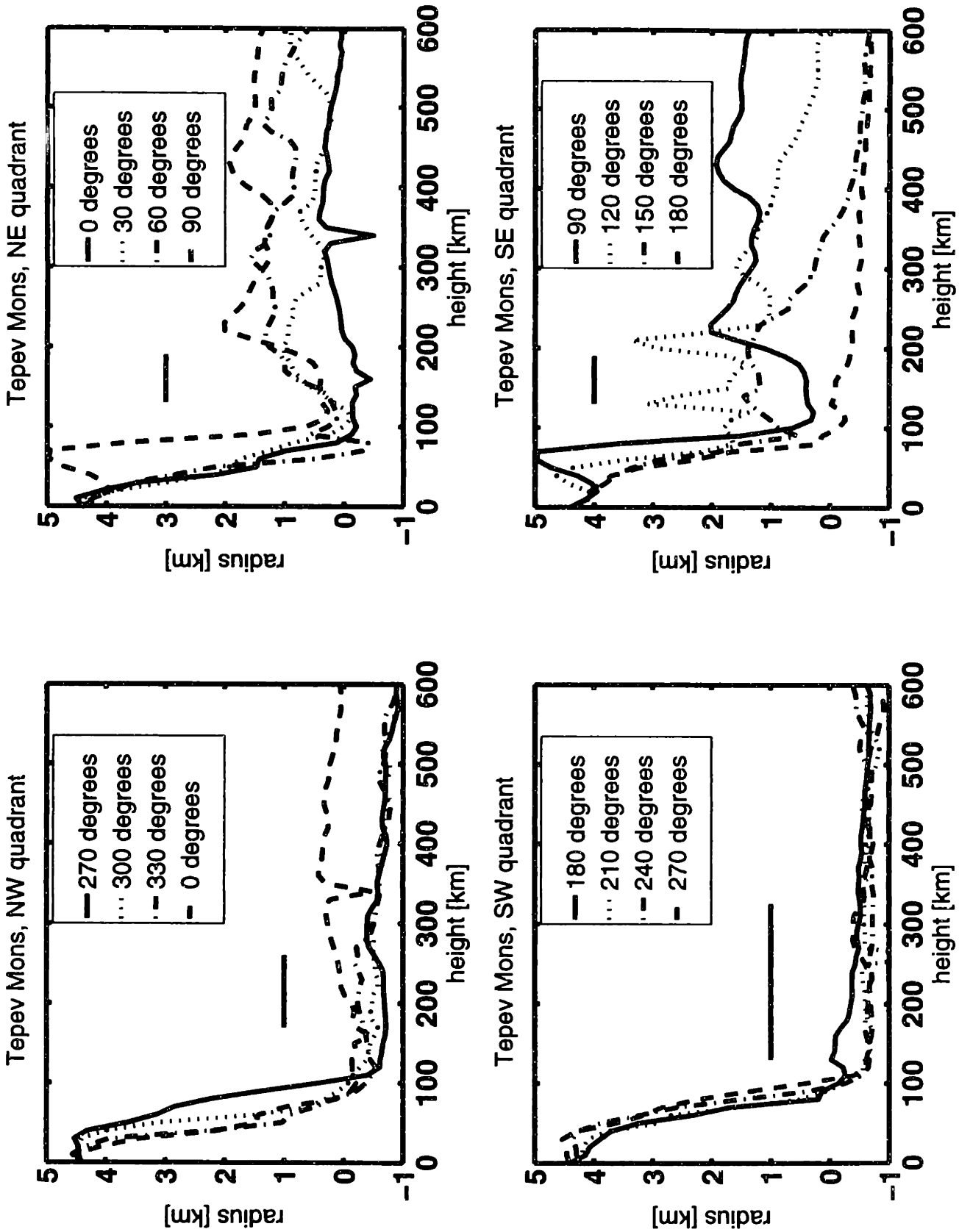
Tepev Mons, NE quadrant
0 degrees
30 degrees
60 degrees
90 degrees
radius [km]
height [km]
Tepev Mons, SE quadrant
90 degrees
120 degrees
150 degrees
180 degrees
radius [km]
height [km]
Tepev Mons, NW quadrant
270 degrees
300 degrees
330 degrees
0 degrees
radius [km]
height [km]
Tepev Mons, SW quadrant
180 degrees
210 degrees
240 degrees
270 degrees
radius [km]
height [km]

Figure 6c.

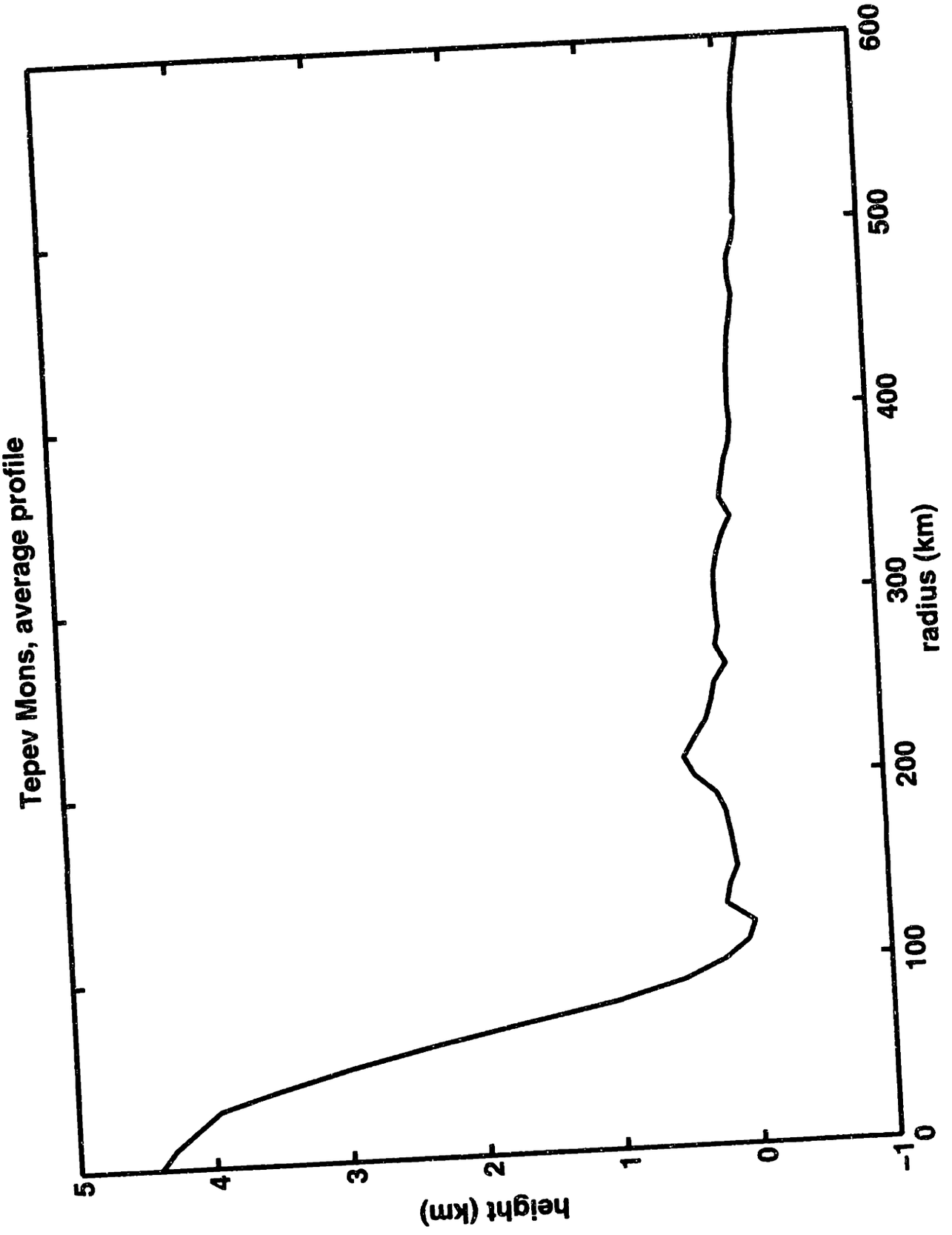
Tepev Mons, average profile
height (km)
radius (km)
5
4
3
2
1
0
-1
0
100
200
300
400
500
600

Figure 6d.

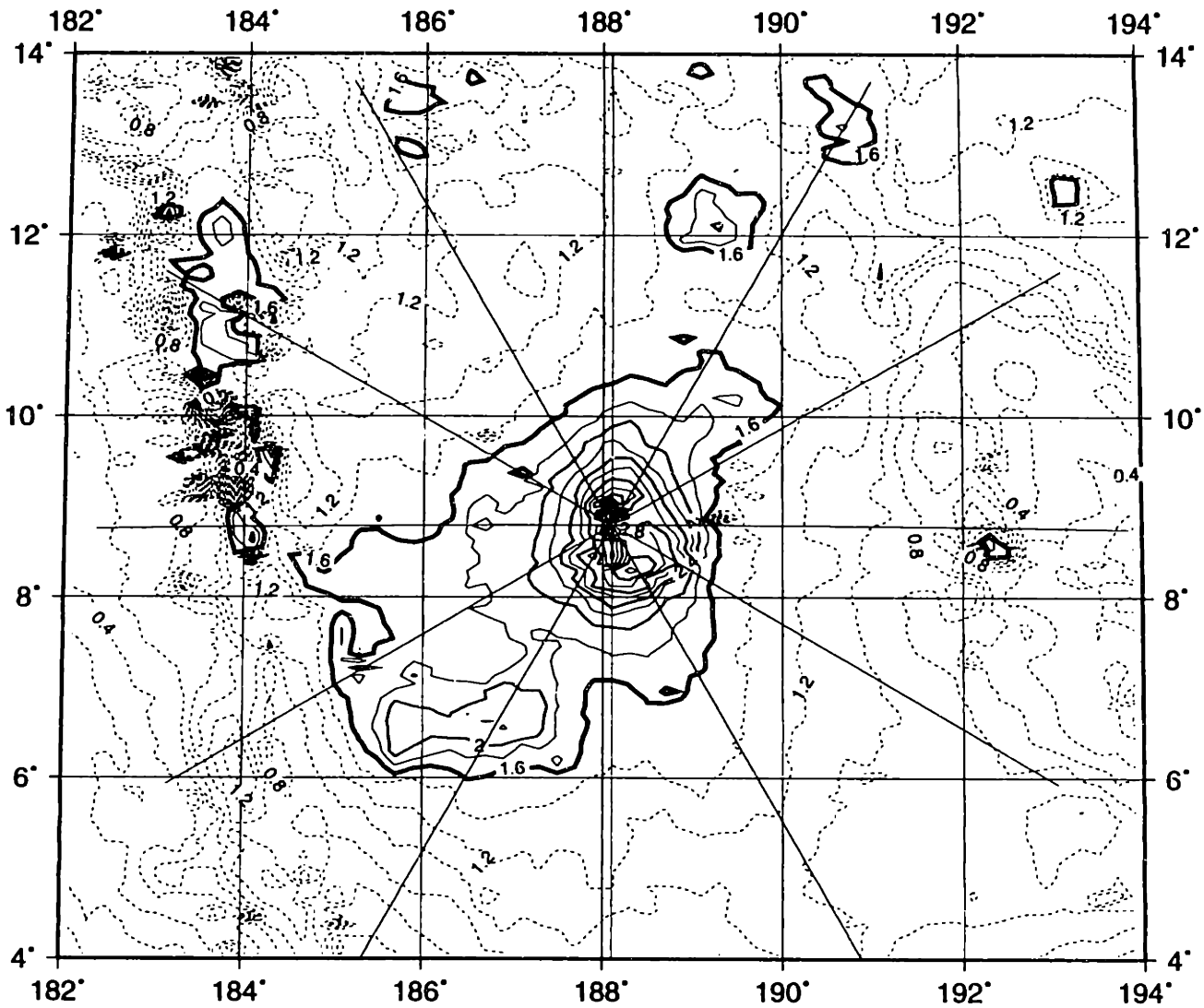

Figure 7a.

Figure 7b.

Figure 7c.

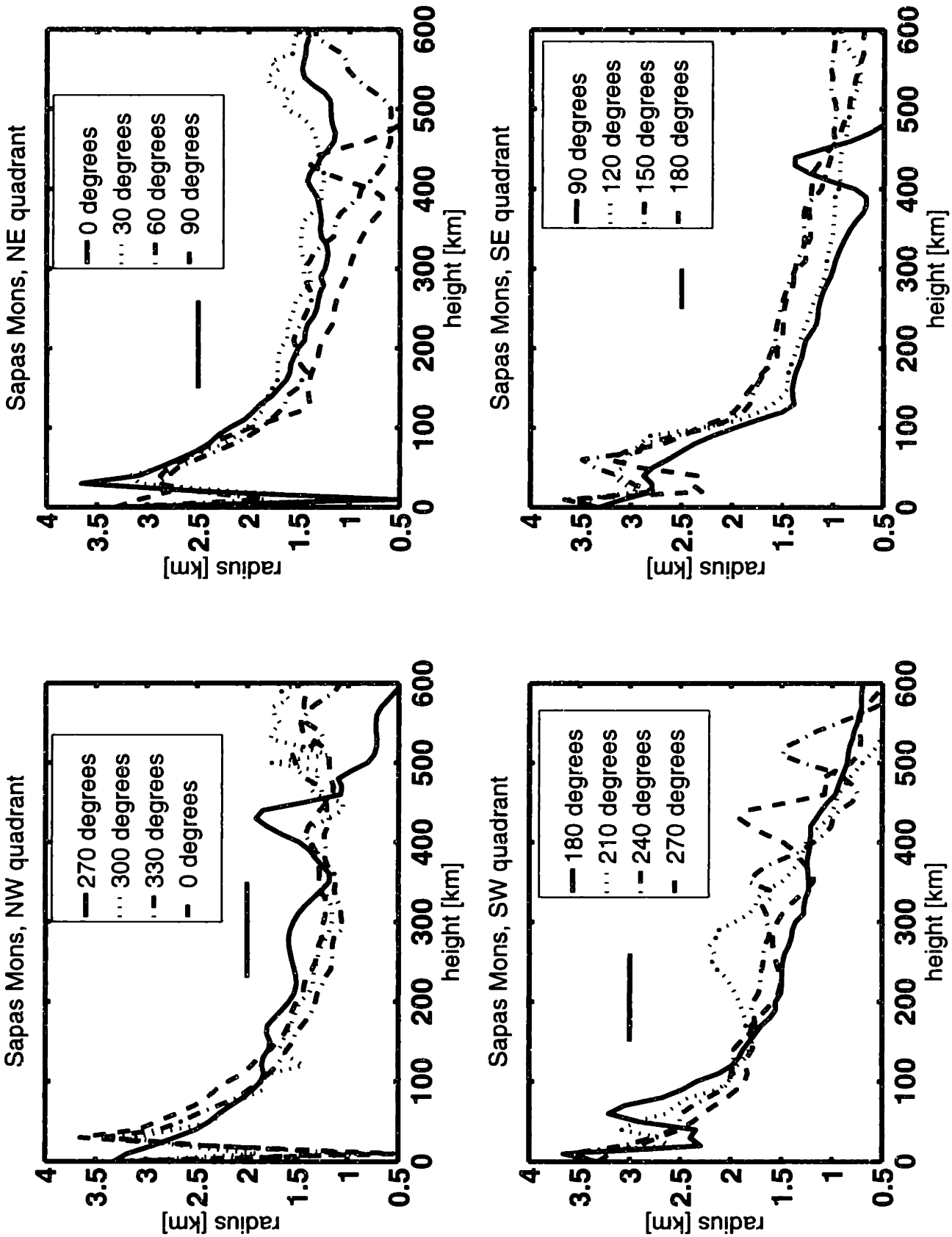
Sapas Mons, NE quadrant
0 degrees
30 degrees
60 degrees
90 degrees
radius [km]
height [km]
Sapas Mons, SE quadrant
90 degrees
120 degrees
150 degrees
180 degrees
radius [km]
height [km]
Sapas Mons, NW quadrant
270 degrees
300 degrees
330 degrees
0 degrees
radius [km]
height [km]
Sapas Mons, SW quadrant
180 degrees
210 degrees
240 degrees
270 degrees
radius [km]
height [km]

Figure 7d.

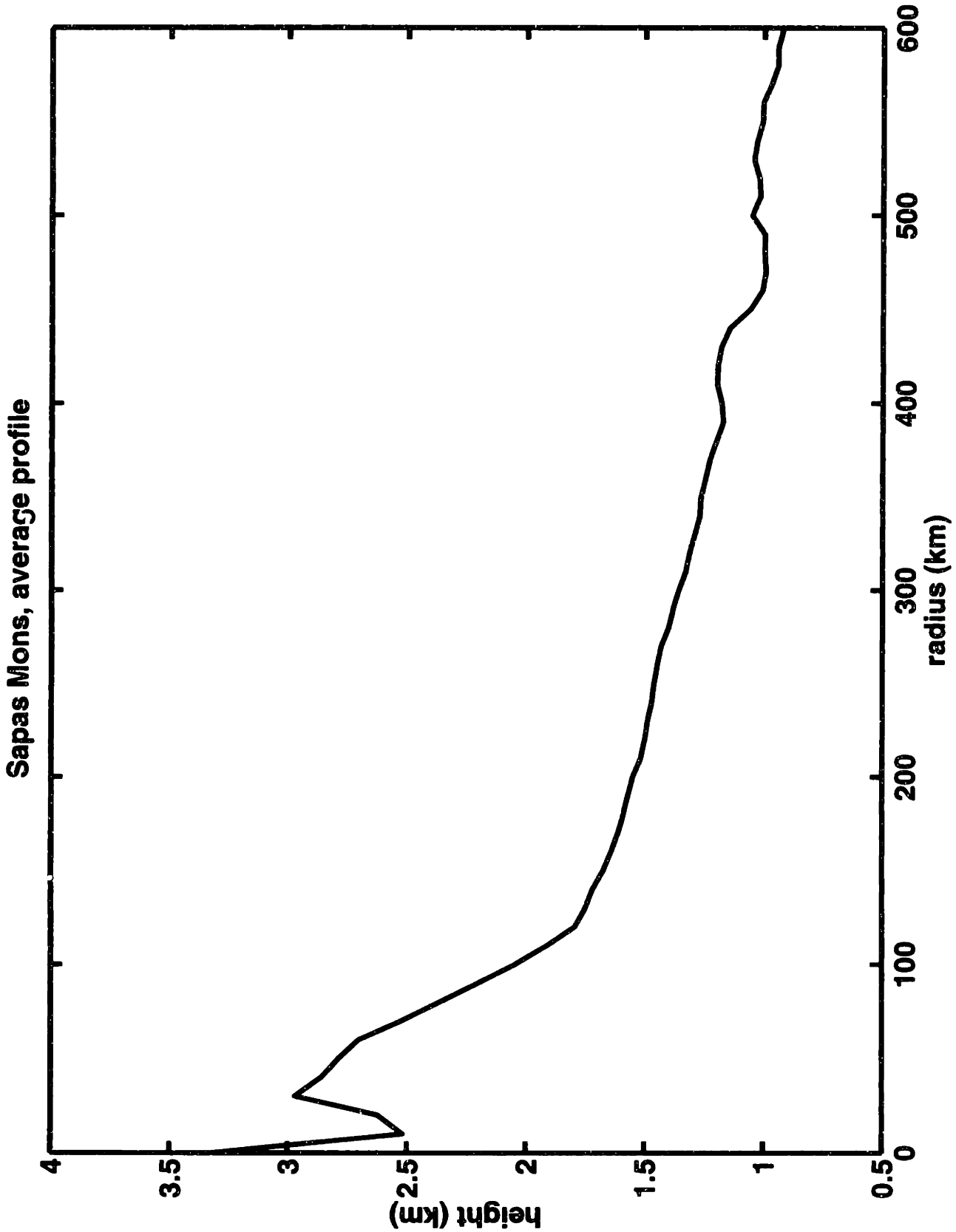
Sapas Mons, average profile
height (km)
radius (km)
4
3.5
3
2.5
2
1.5
1
0.5
0
100
200
300
400
500
600

Figure 7e.

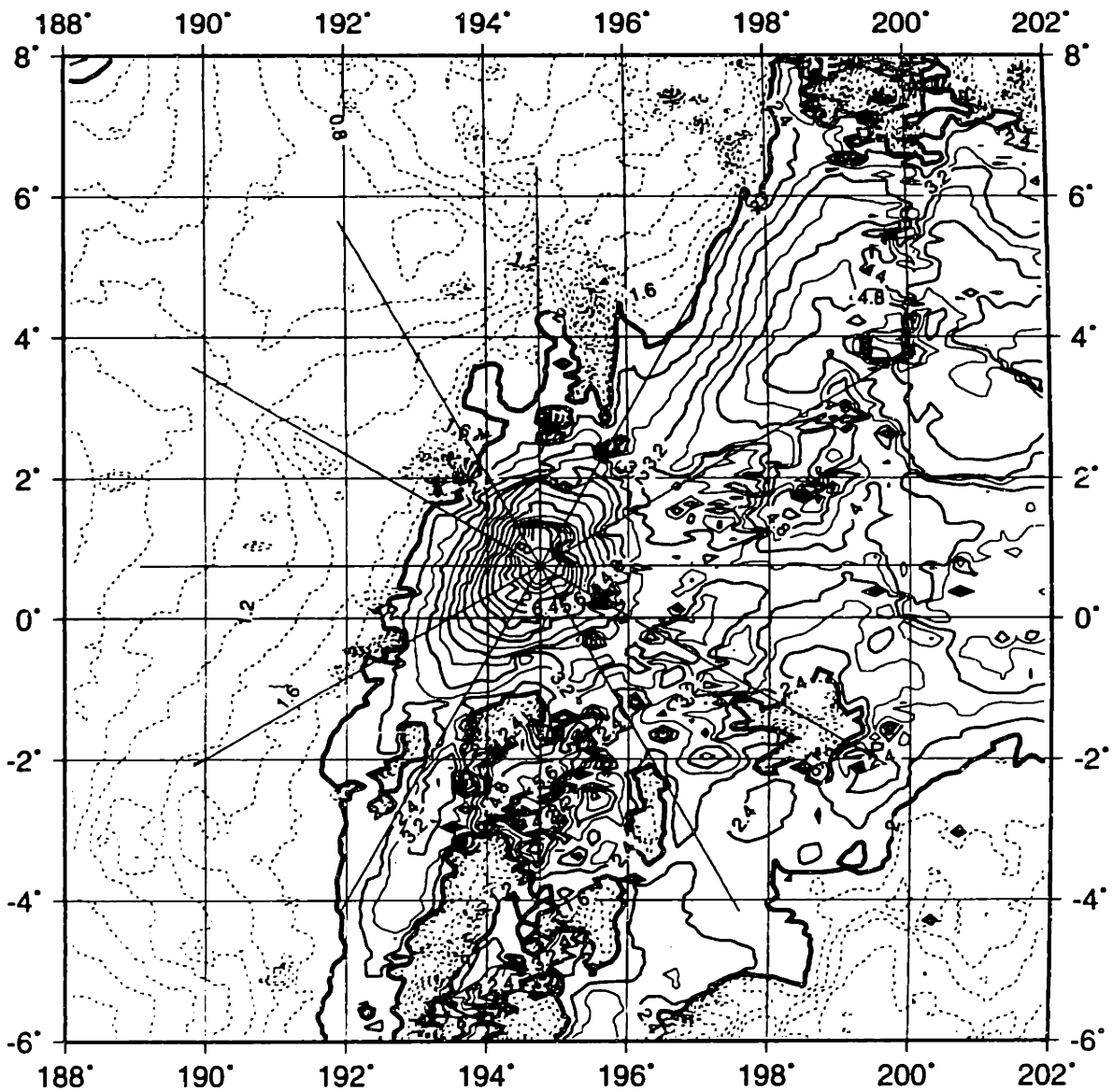

Figure 8a.

Figure 8b.

Figure 8c.

Figure 8d.

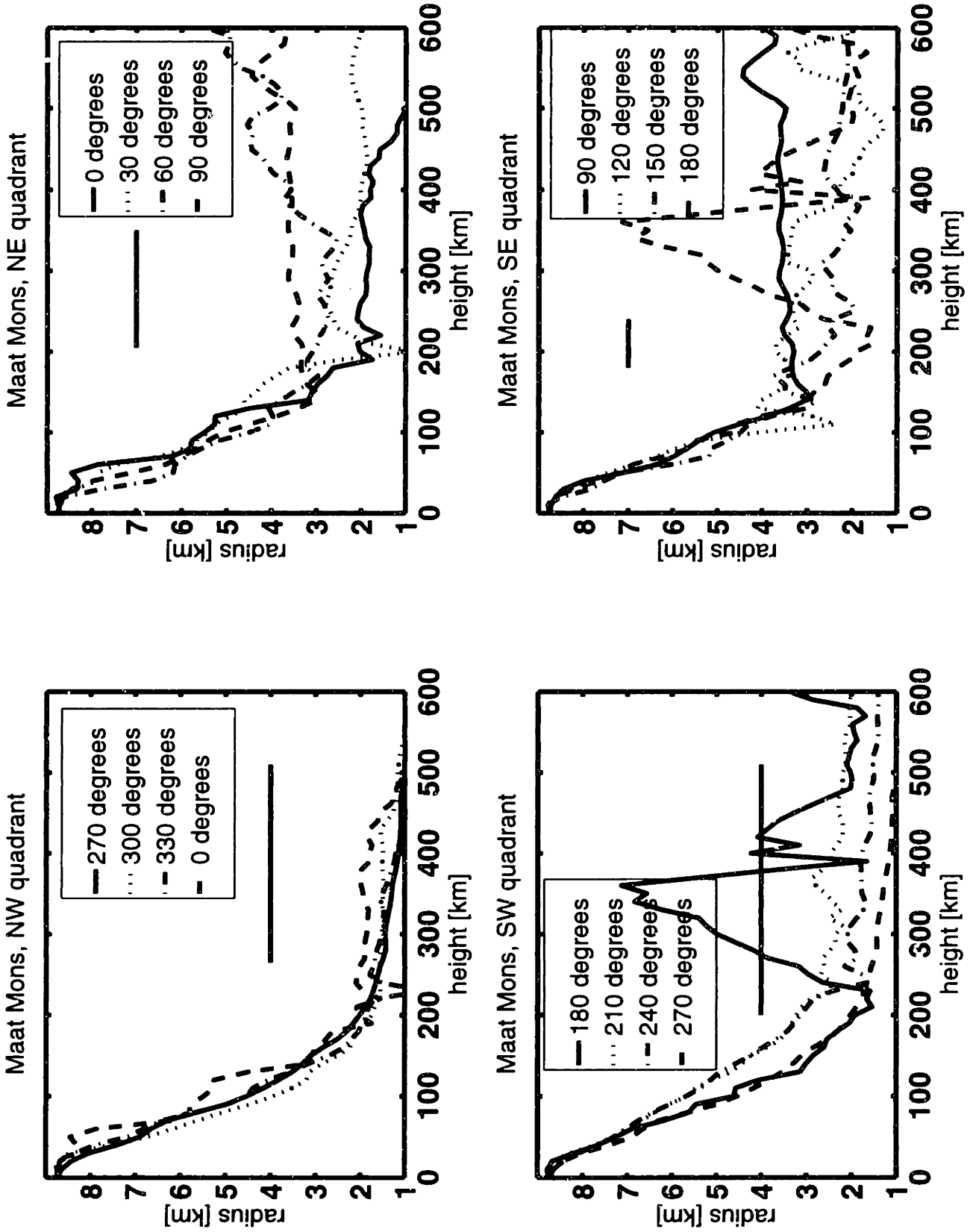
Maat Mons, NE quadrant
0 degrees
30 degrees
60 degrees
90 degrees
radius [km]
height [km]
Maat Mons, SE quadrant
90 degrees
120 degrees
150 degrees
180 degrees
radius [km]
height [km]
Maat Mons, NW quadrant
270 degrees
300 degrees
330 degrees
0 degrees
radius [km]
height [km]
Maat Mons, SW quadrant
180 degrees
210 degrees
240 degrees
270 degrees
radius [km]
height [km]

Figure 8e.

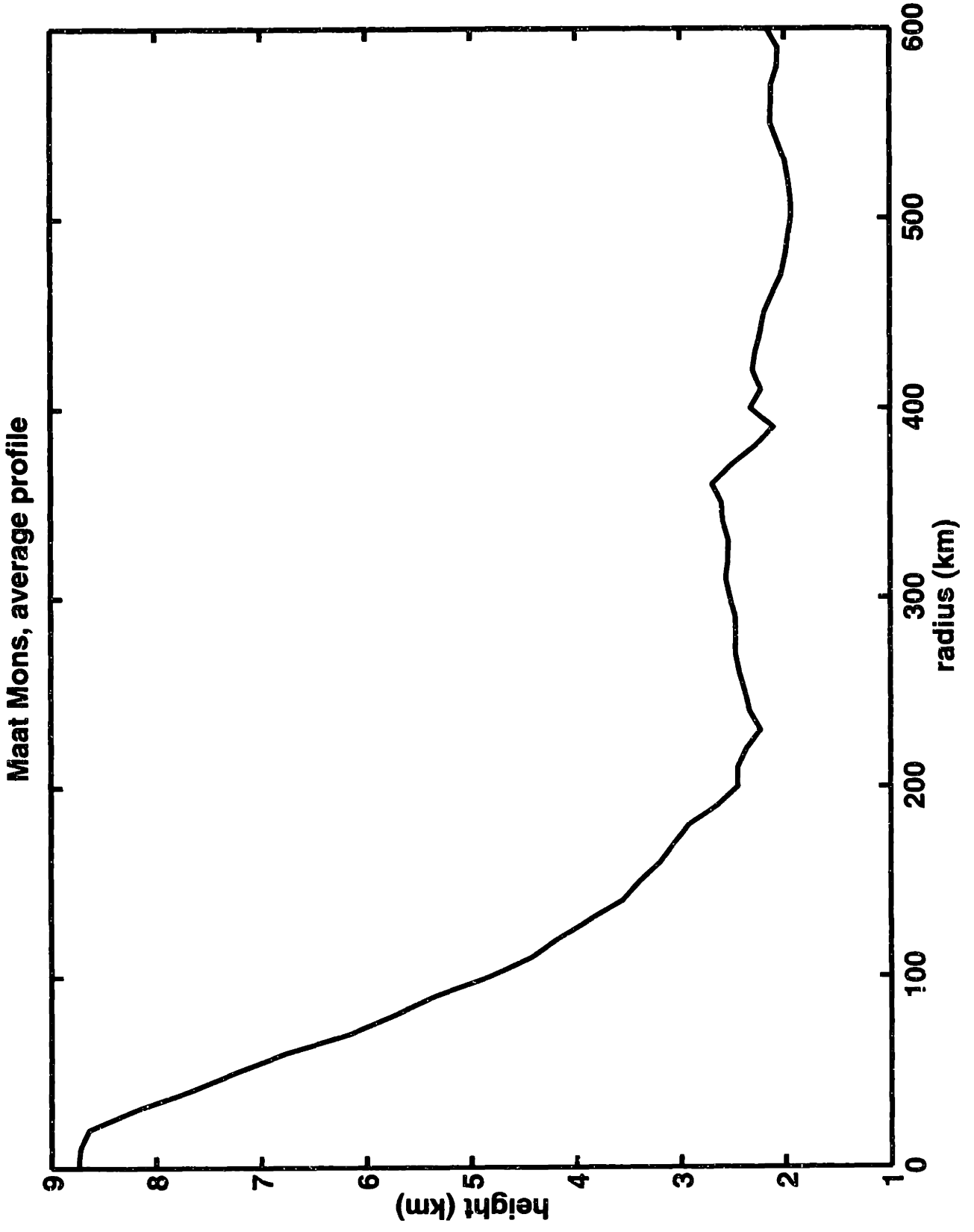
Maat Mons, average profile
height (km)
radius (km)
0
100
200
300
400
500
600
1
2
3
4
5
6
7
8
9

Figure 8f.

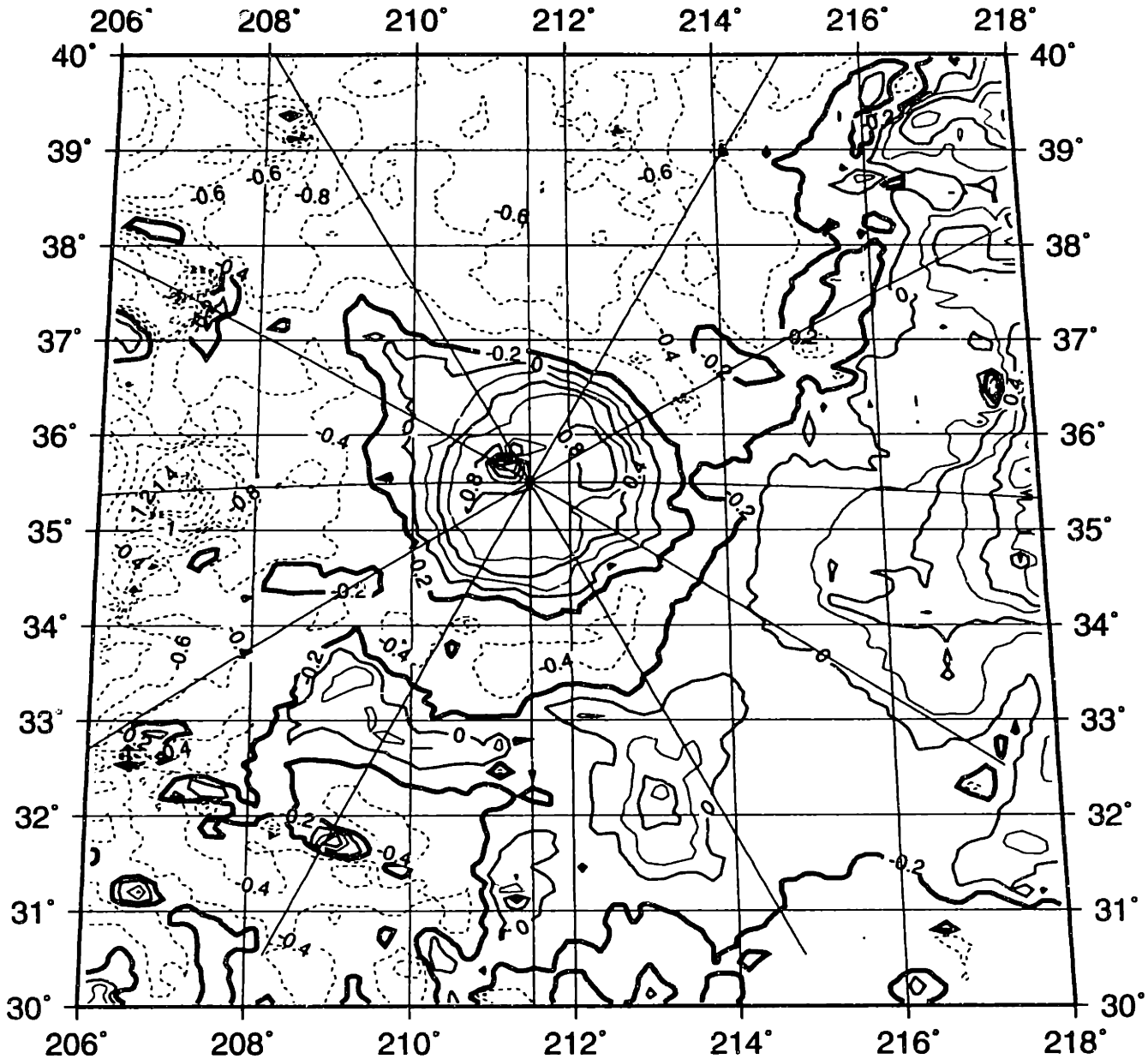

Figure 9a.

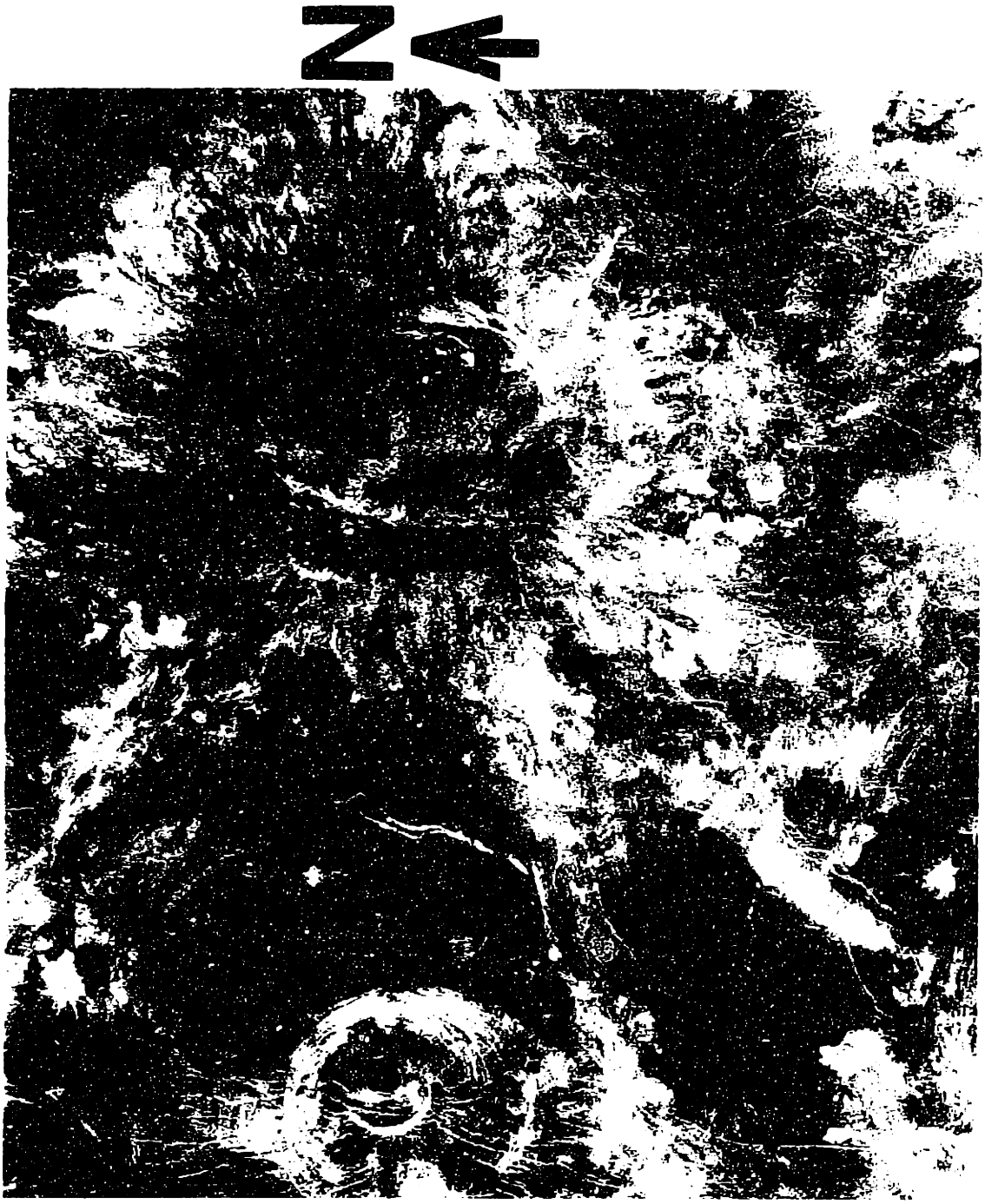

Figure 9b.

Figure 9c.

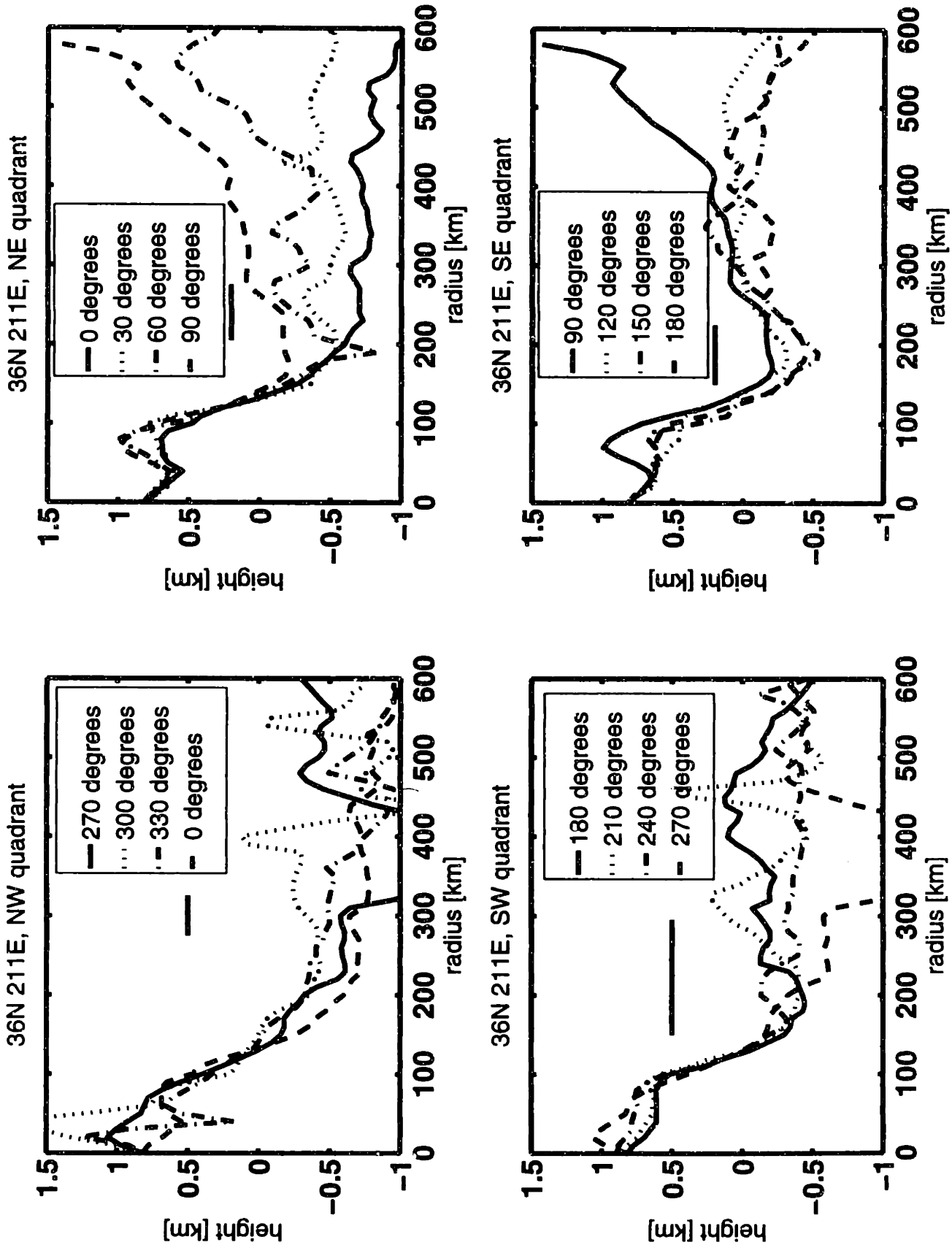
36N 211E, NE quadrant
0 degrees
30 degrees
60 degrees
90 degrees
height [km]
radius [km]
36N 211E, SE quadrant
90 degrees
120 degrees
150 degrees
180 degrees
height [km]
radius [km]
36N 211E, NW quadrant
270 degrees
300 degrees
330 degrees
0 degrees
height [km]
radius [km]
36N 211E, SW quadrant
180 degrees
210 degrees
240 degrees
270 degrees
height [km]
radius [km]

Figure 9d.

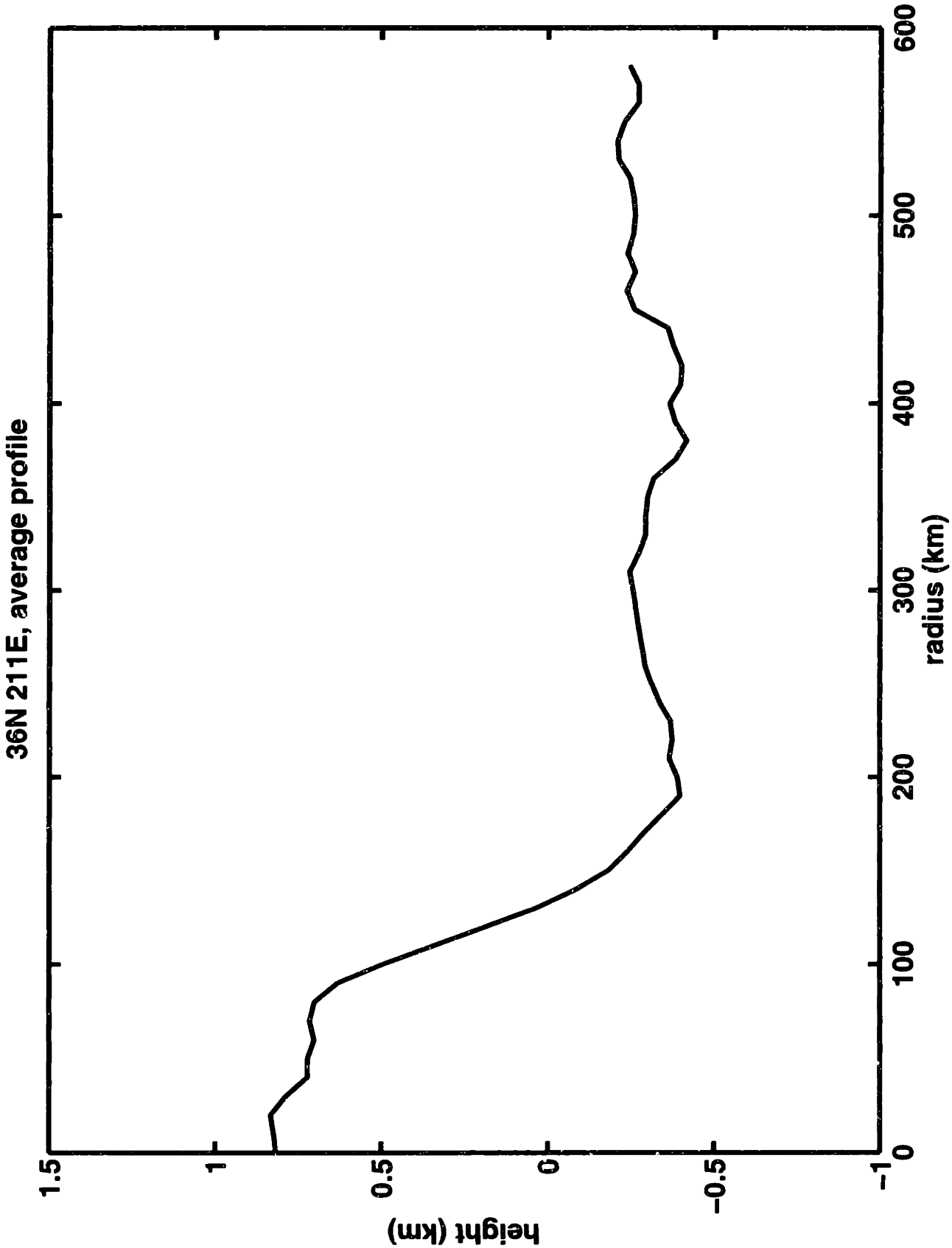
36N 211E, average profile
height (km)
radius (km)
1.5
1
0.5
0
−0.5
−1
0
100
200
300
400
500
600

Figure 9e.

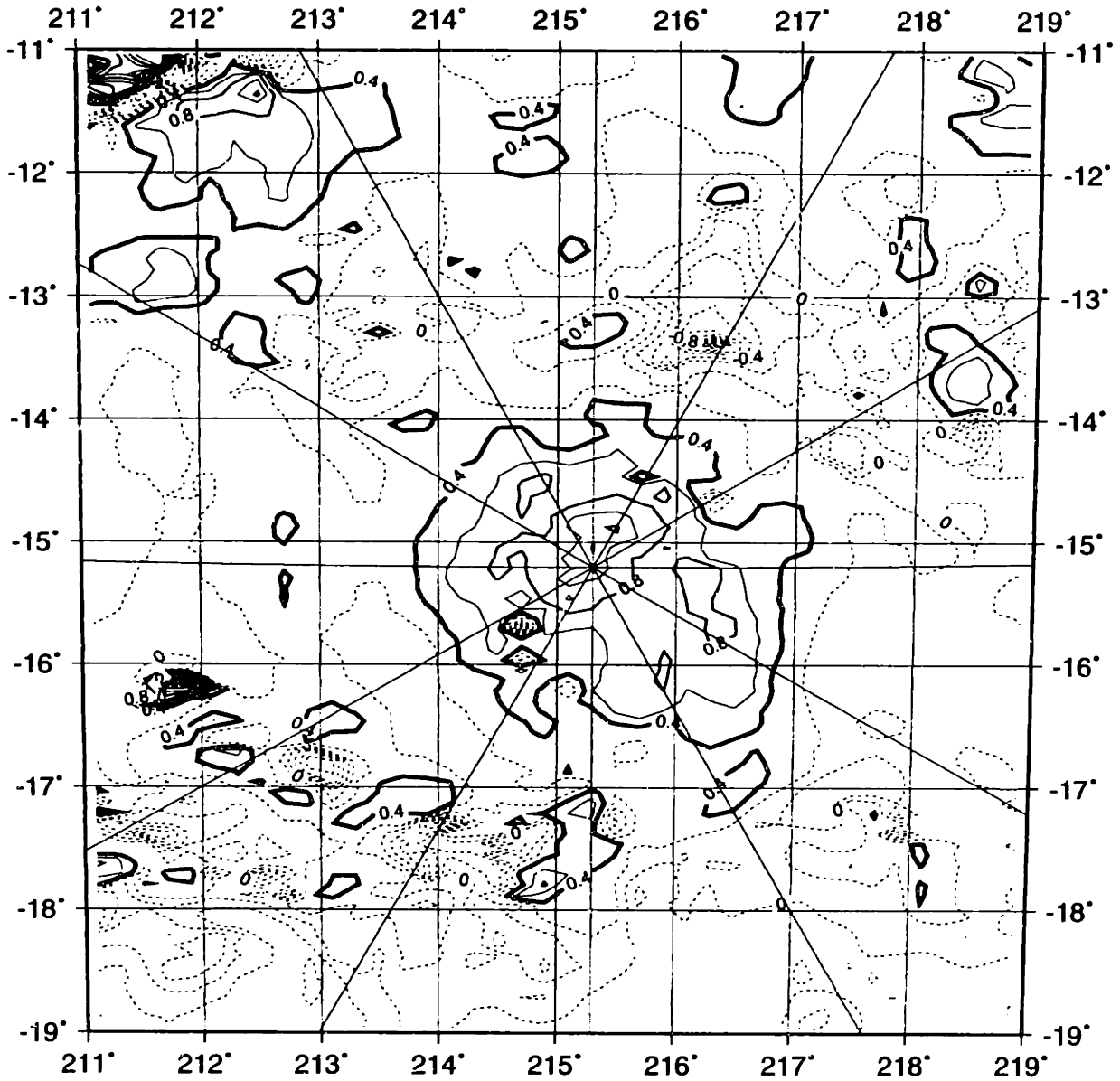

Figure 10a.

Figure 10b.

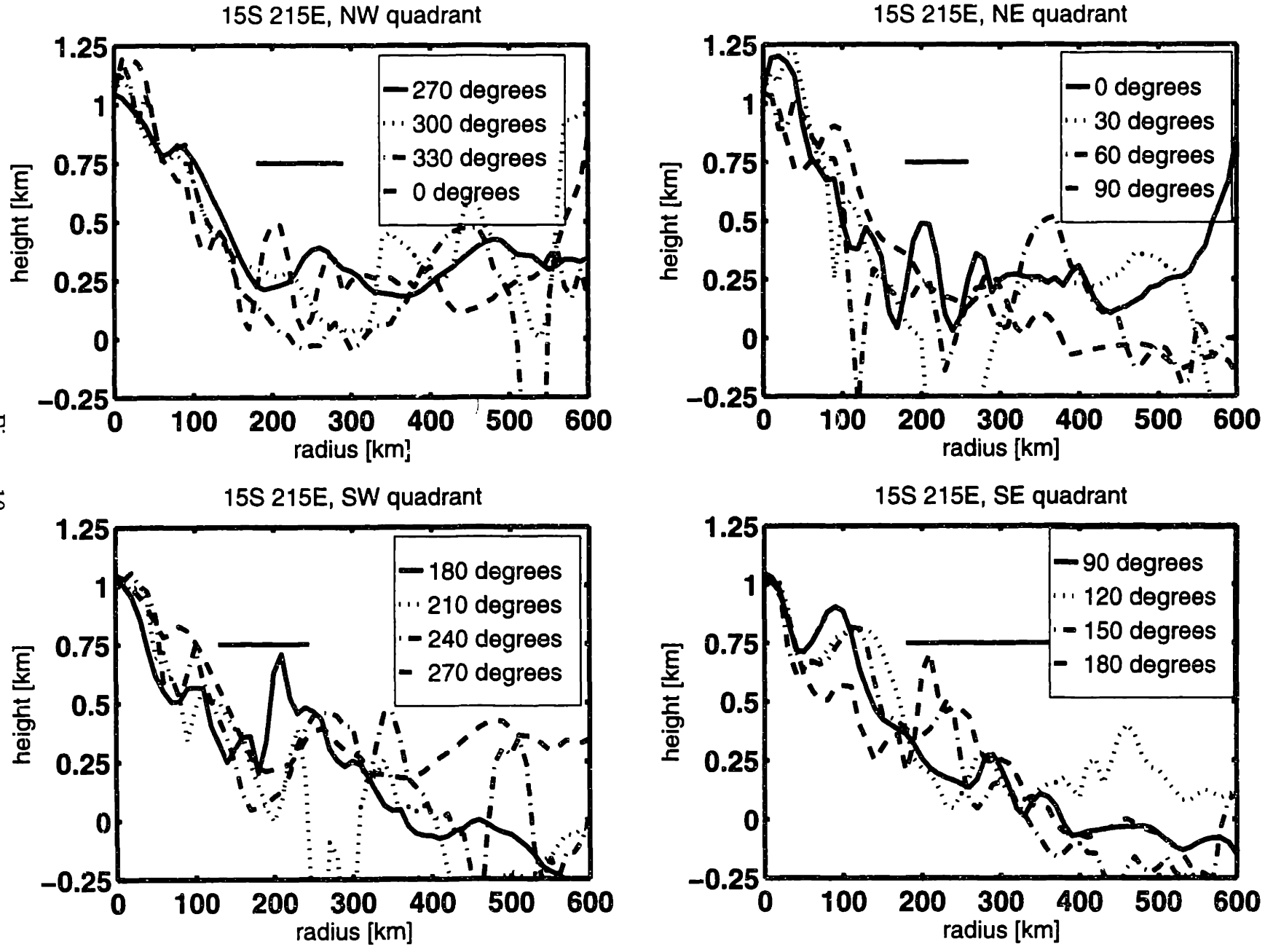
15S 215E, NW quadrant
270 degrees
300 degrees
330 degrees
0 degrees
height [km]
radius [km]
15S 215E, NE quadrant
0 degrees
30 degrees
60 degrees
90 degrees
height [km]
radius [km]
15S 215E, SW quadrant
180 degrees
210 degrees
240 degrees
270 degrees
height [km]
radius [km]
15S 215E, SE quadrant
90 degrees
120 degrees
150 degrees
180 degrees
height [km]
radius [km]

Figure 10c.

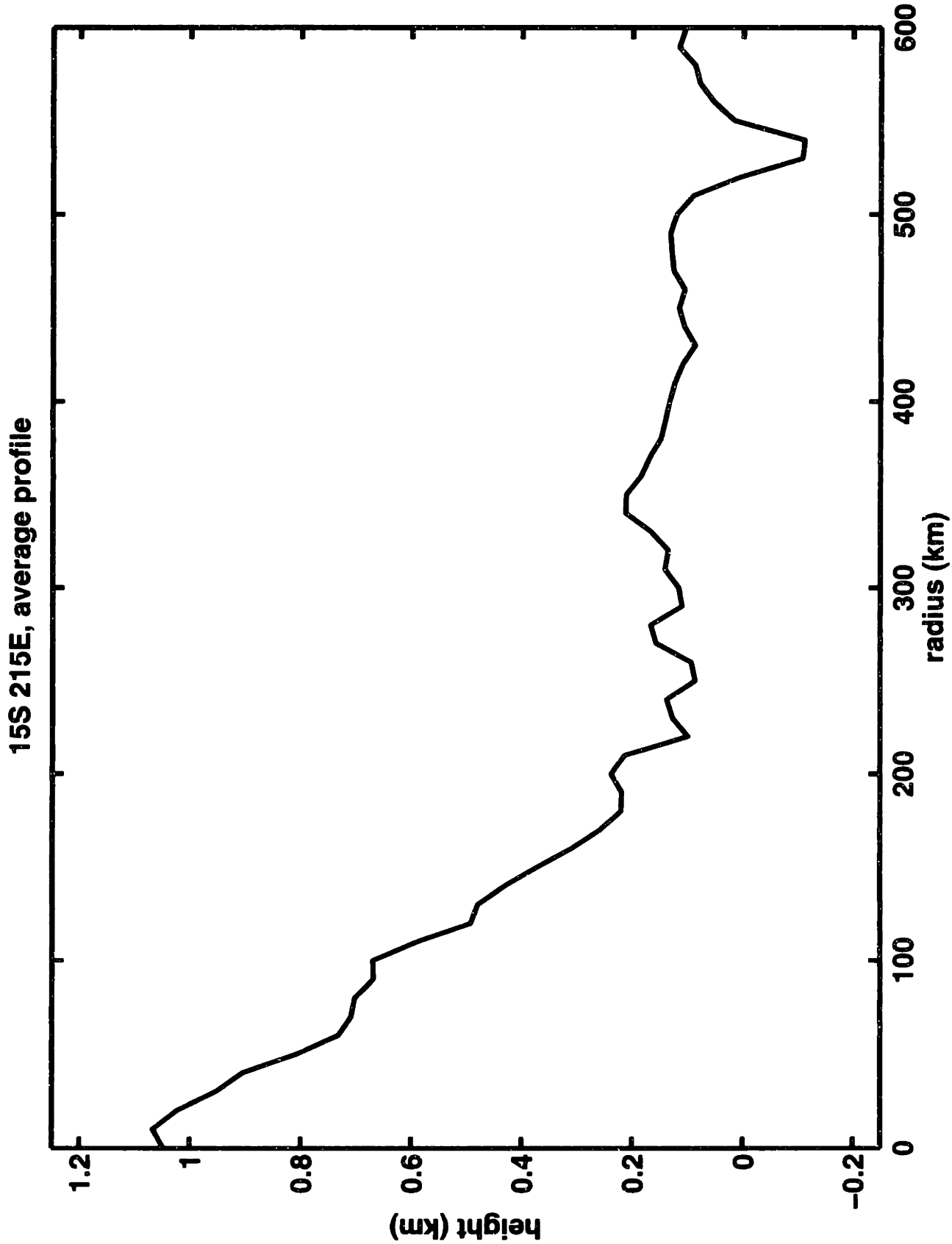
15S 215E, average profile
height (km)
radius (km)
1.2
1
0.8
0.6
0.4
0.2
0
−0.2
0
100
200
300
400
500
600

Figure 10d.

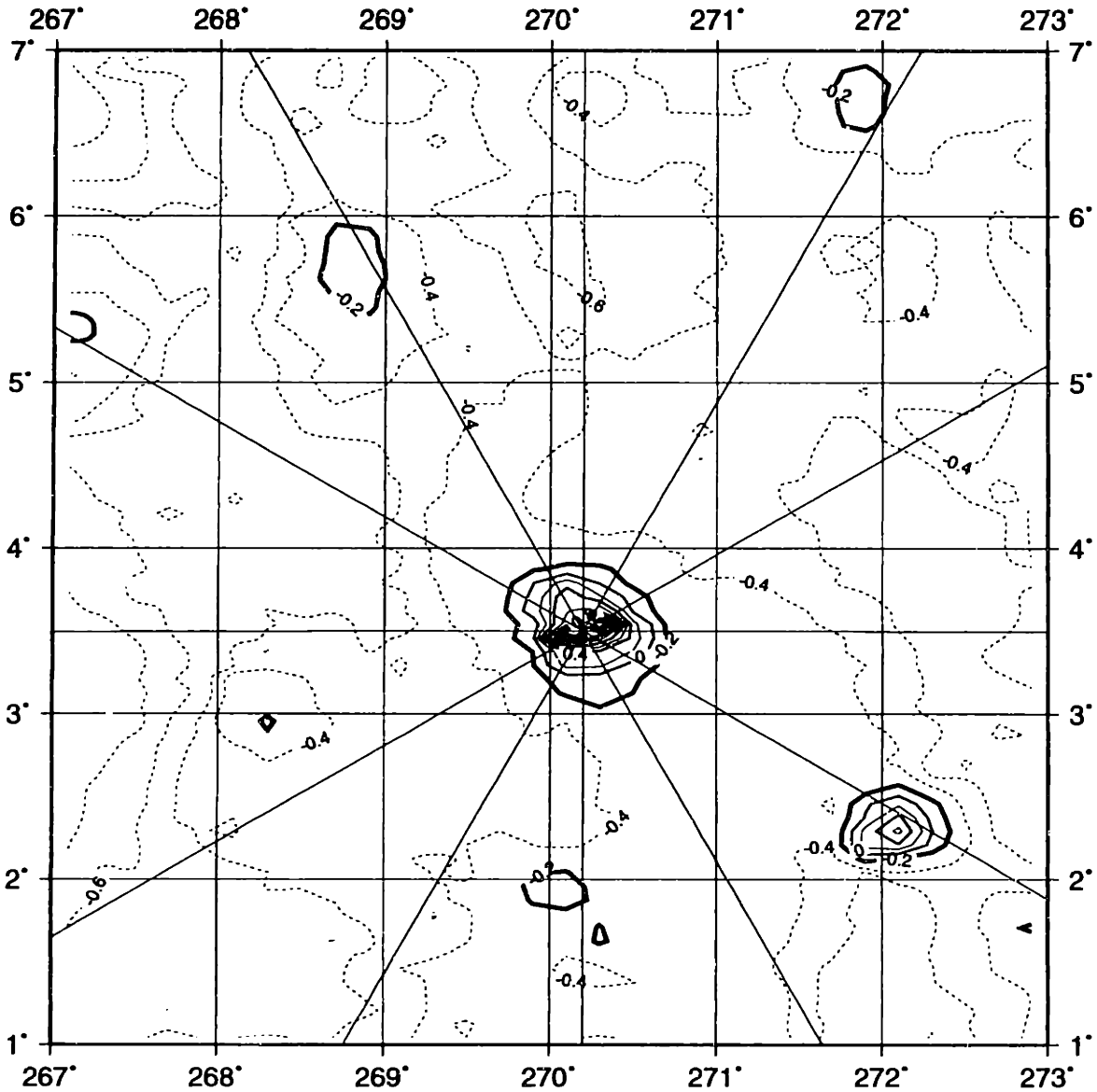

Figure 11a.

Figure 11b.

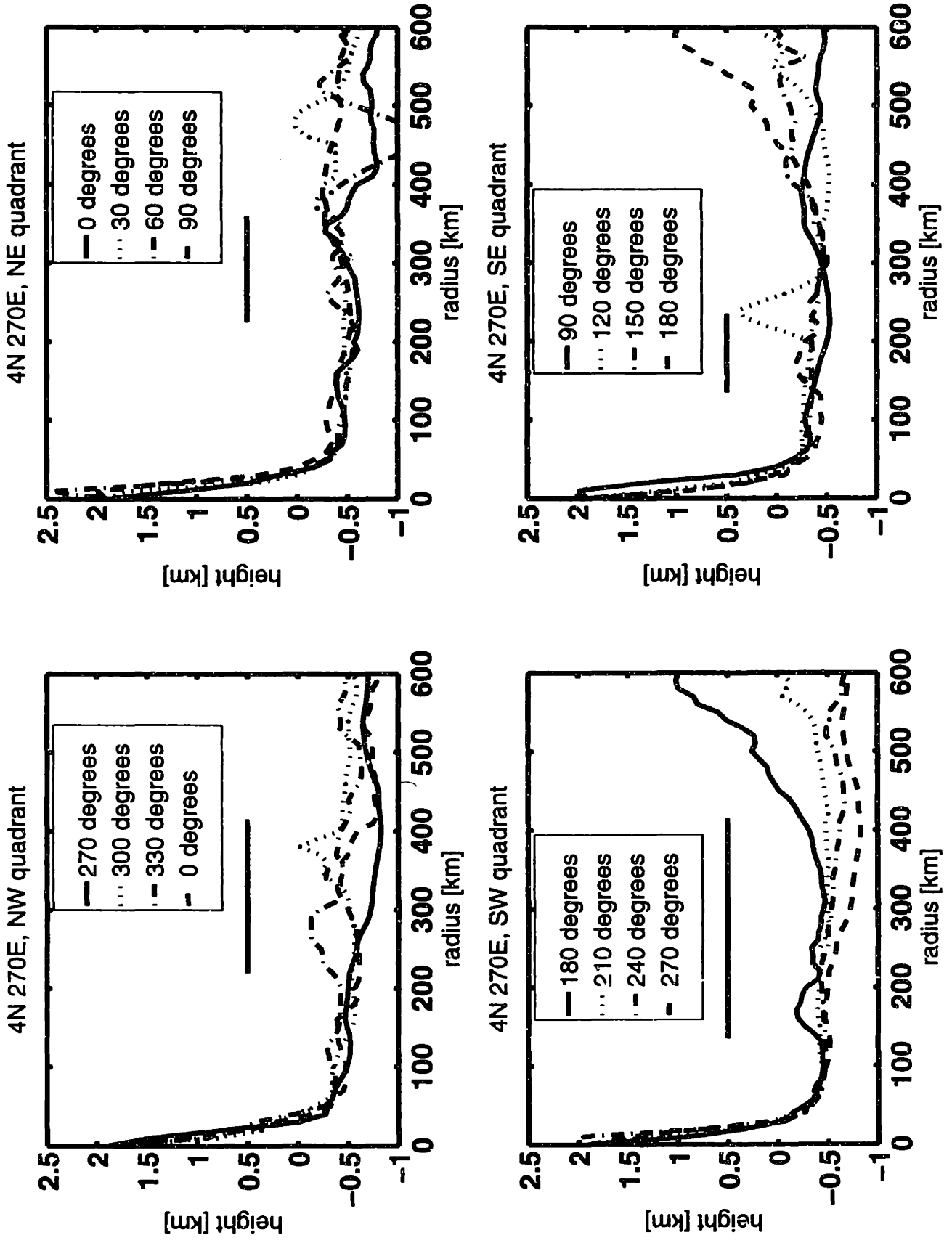
4N 270E, NE quadrant
0 degrees
30 degrees
60 degrees
90 degrees
height [km]
radius [km]
4N 270E, SE quadrant
90 degrees
120 degrees
150 degrees
180 degrees
height [km]
radius [km]
4N 270E, NW quadrant
270 degrees
300 degrees
330 degrees
0 degrees
height [km]
radius [km]
4N 270E, SW quadrant
180 degrees
210 degrees
240 degrees
270 degrees
height [km]
radius [km]

Figure 11c.

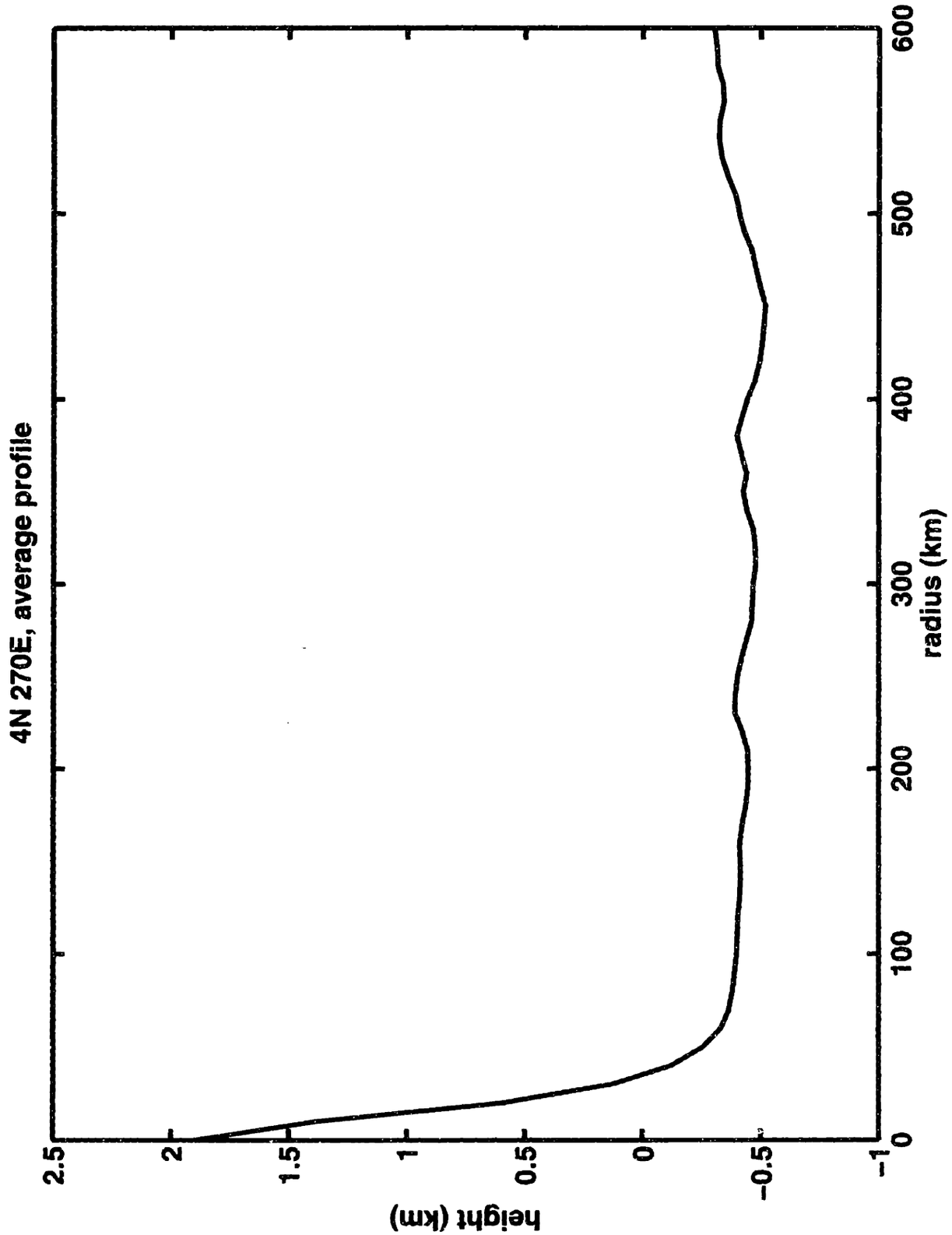
4N 270E, average profile
height (km)
radius (km)
2.5
2
1.5
1
0.5
0
−0.5
−1
0
100
200
300
400
500
600

Figure 11d.

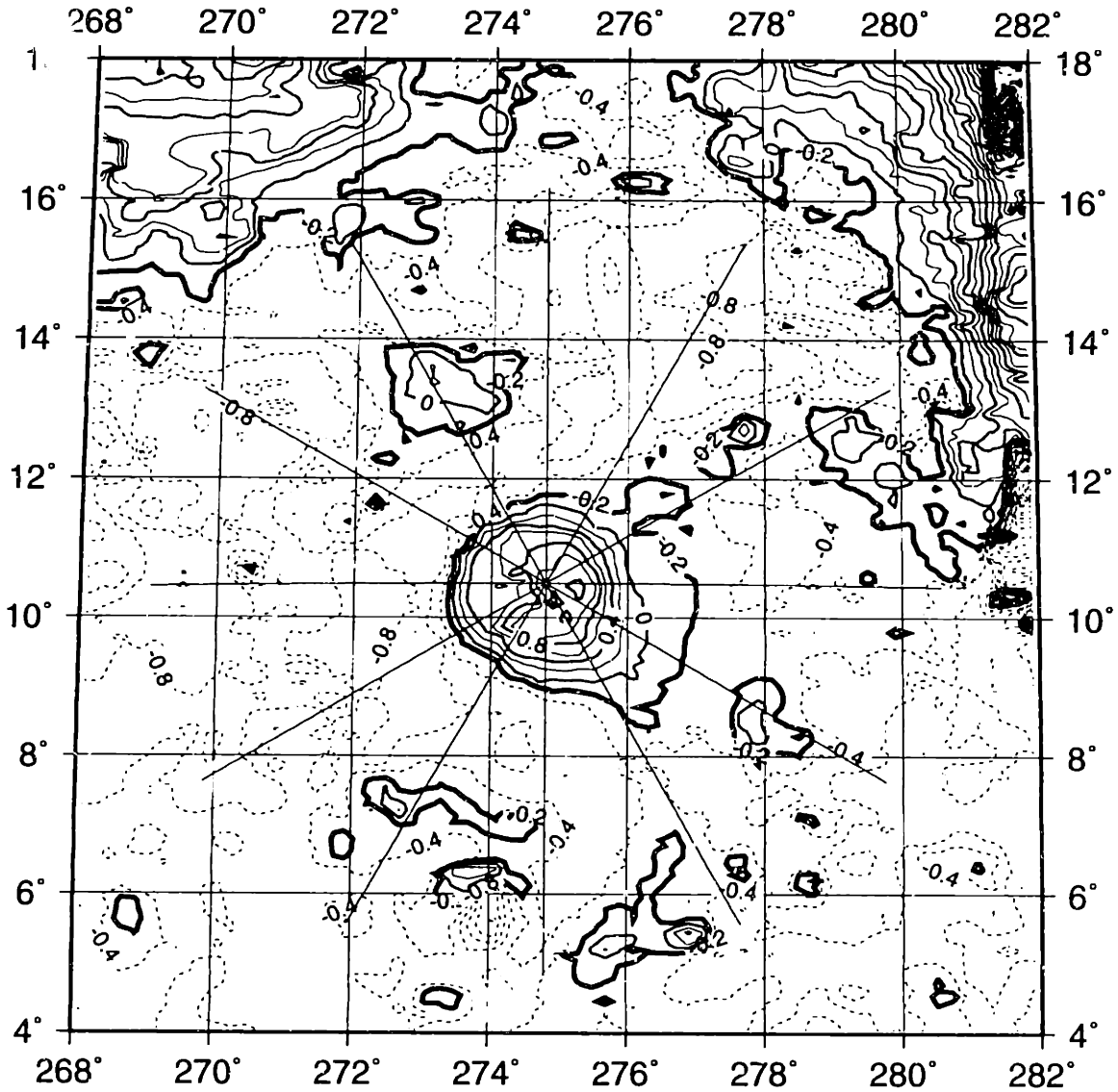

Figure 12a.

Figure 12b.

Figure 12c.

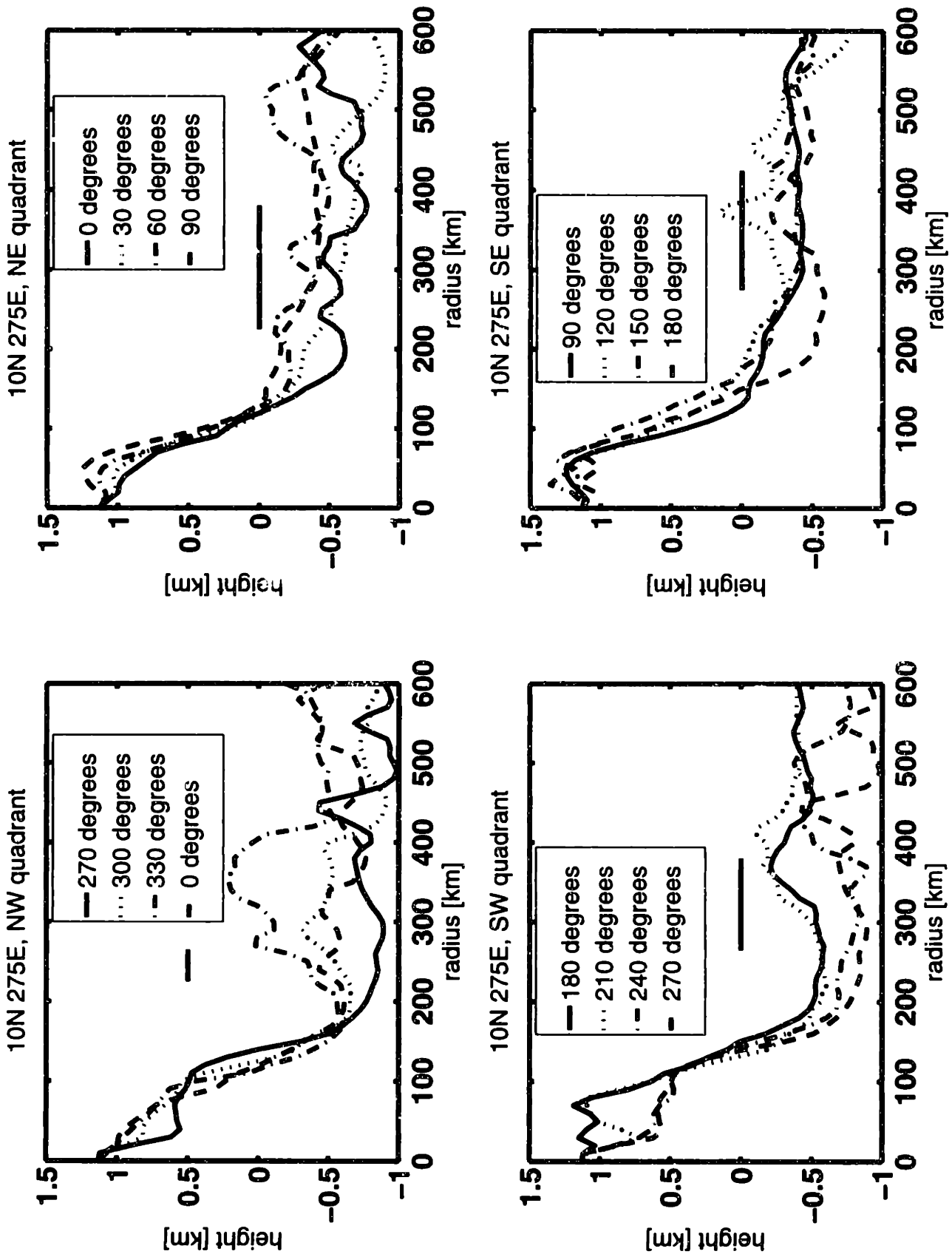
10N 275E, NE quadrant
0 degrees
30 degrees
60 degrees
90 degrees
height [km]
radius [km]
10N 275E, SE quadrant
90 degrees
120 degrees
150 degrees
180 degrees
height [km]
radius [km]
10N 275E, NW quadrant
270 degrees
300 degrees
330 degrees
0 degrees
height [km]
radius [km]
10N 275E, SW quadrant
180 degrees
210 degrees
240 degrees
270 degrees
height [km]
radius [km]

Figure 12d.

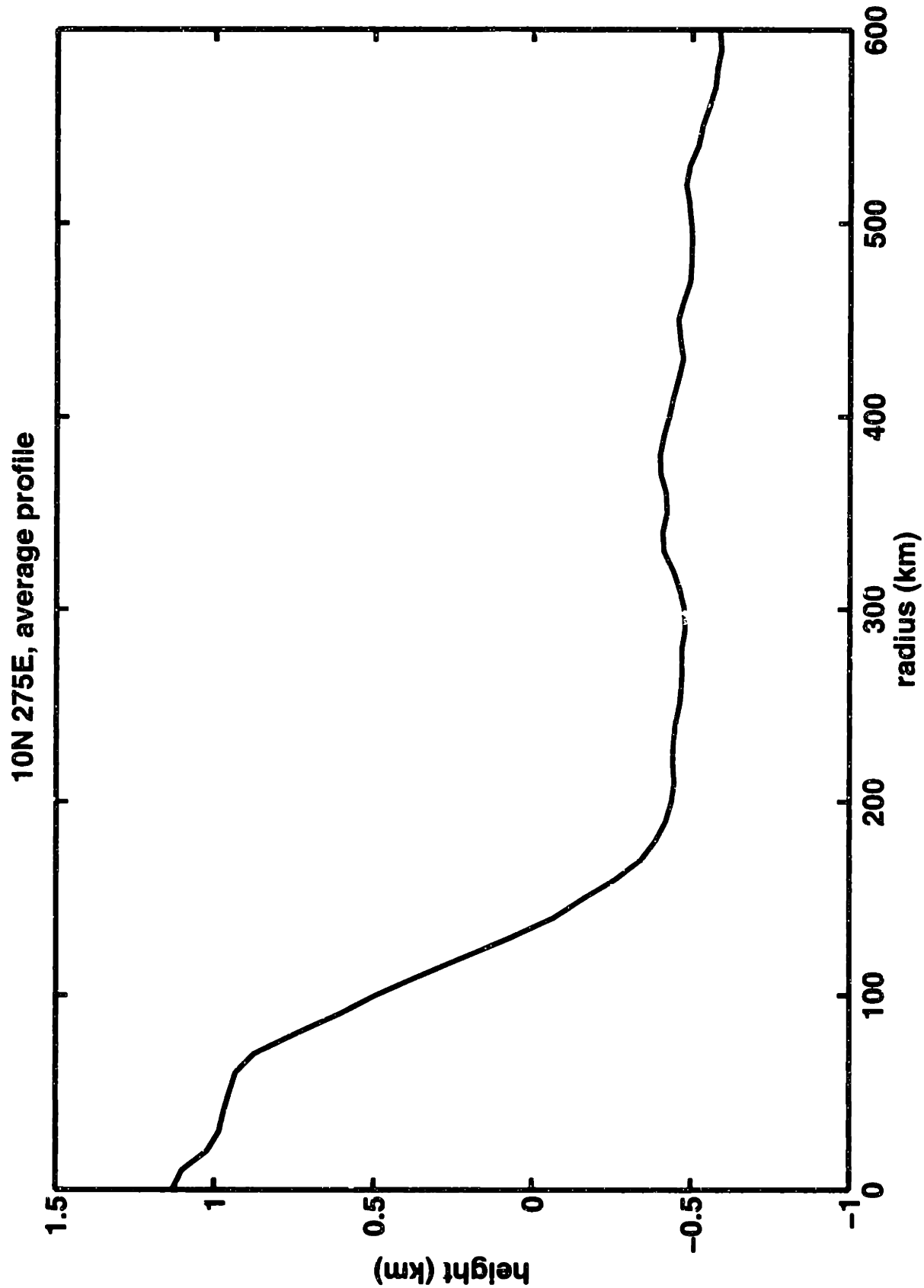
10N 275E, average profile
height (km)
radius (km)
1.5
1
0.5
0
−0.5
−1
0
100
200
300
400
500
600

Figure 12e.

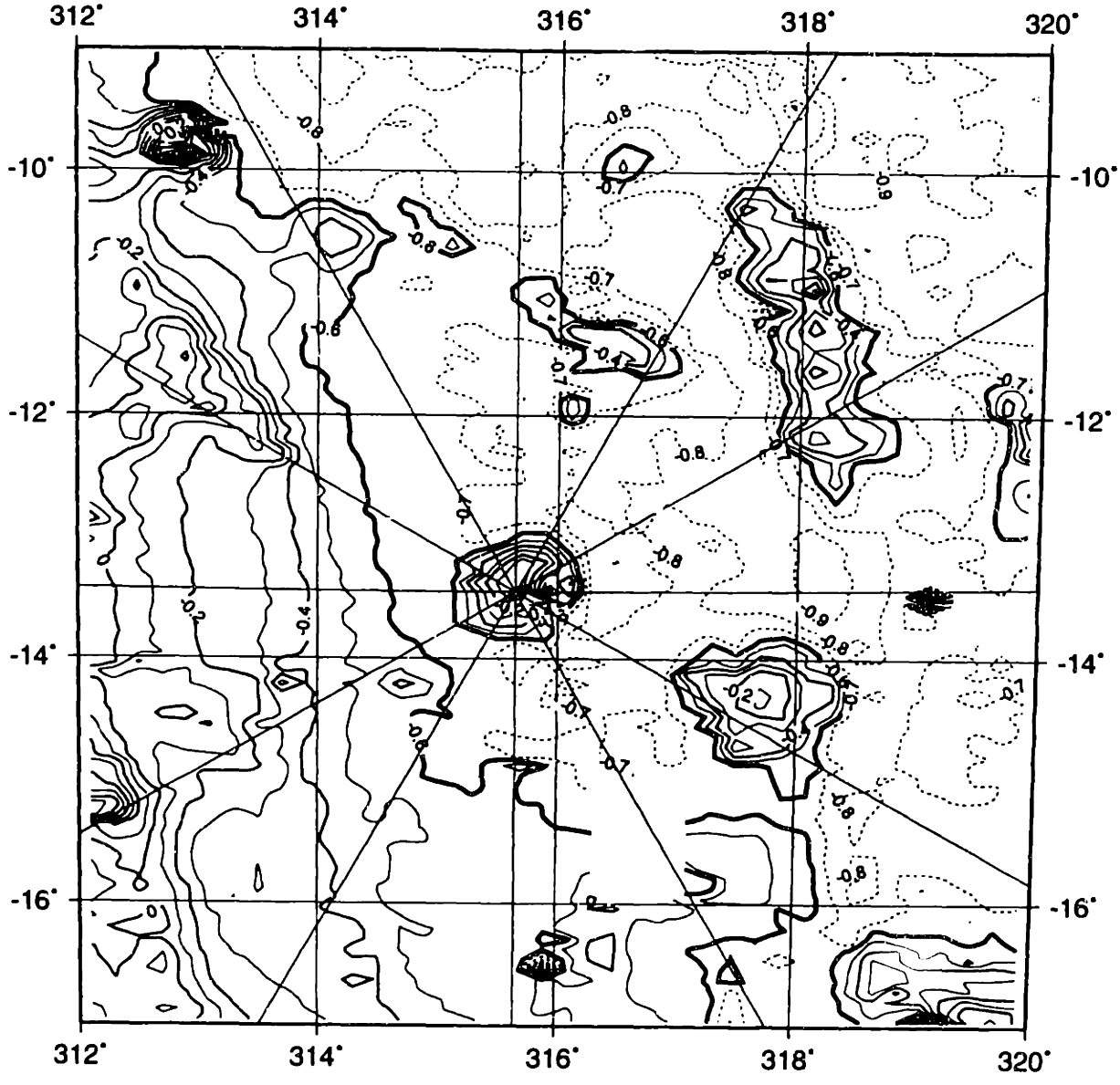

Figure 13a.

Figure 13b.

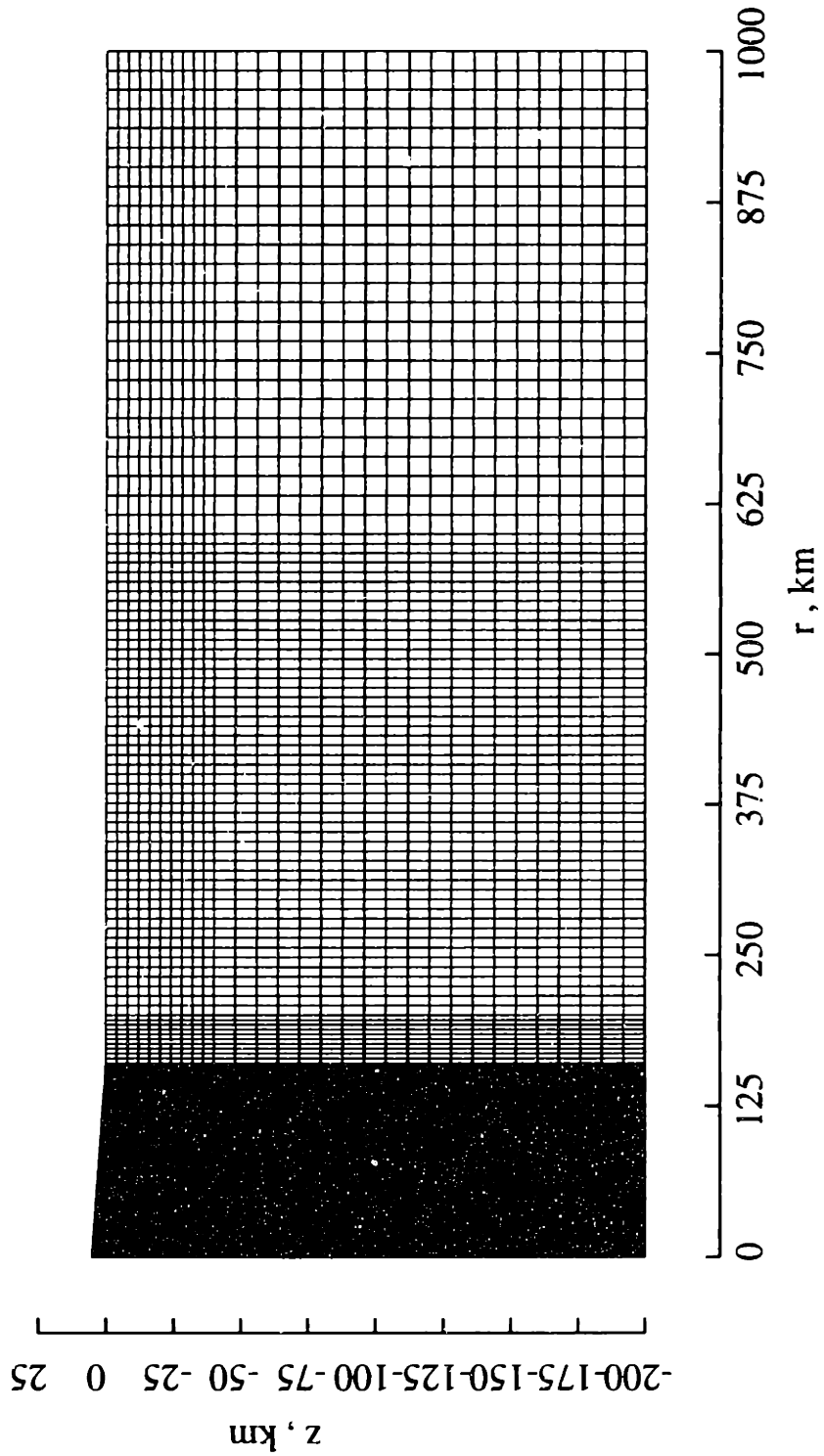
0
125
250
375
500
625
750
875
1000
r , km
-200 -175 -150 -125 -100 -75 -50 -25 0 25
z , km

Figure 14a.

Figure 14b.

Figure 15a.

Figure 15b.

Figure 15c.

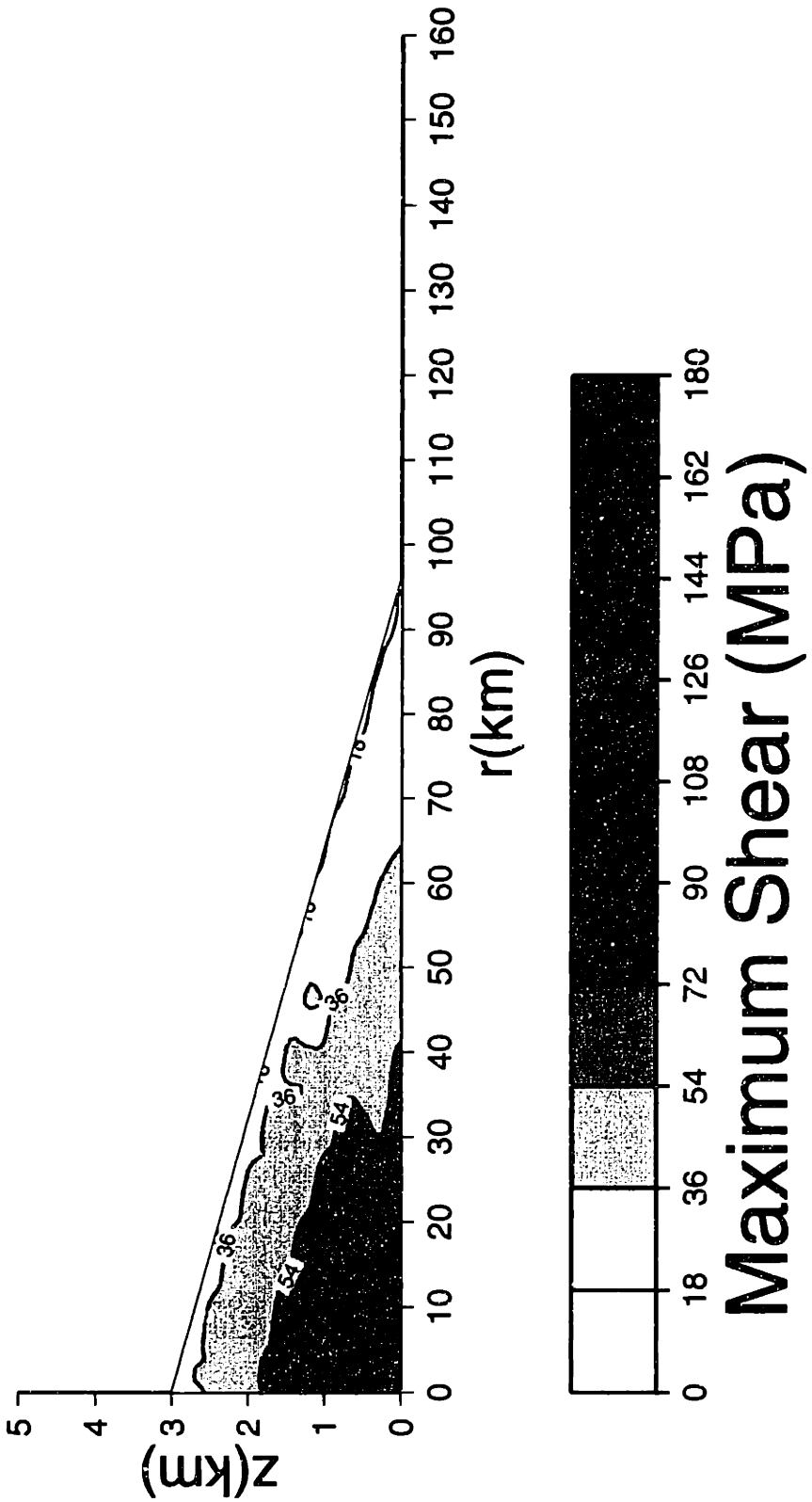
z(km)
0
1
2
3
4
5
r(km)
0 10 20 30 40 50 60 70 80 90 100 110 120 130 140 150 160
18
36
36
54
54
Maximum Shear (MPa)
0 18 36 54 72 90 108 126 144 162 180

Figure 15d.

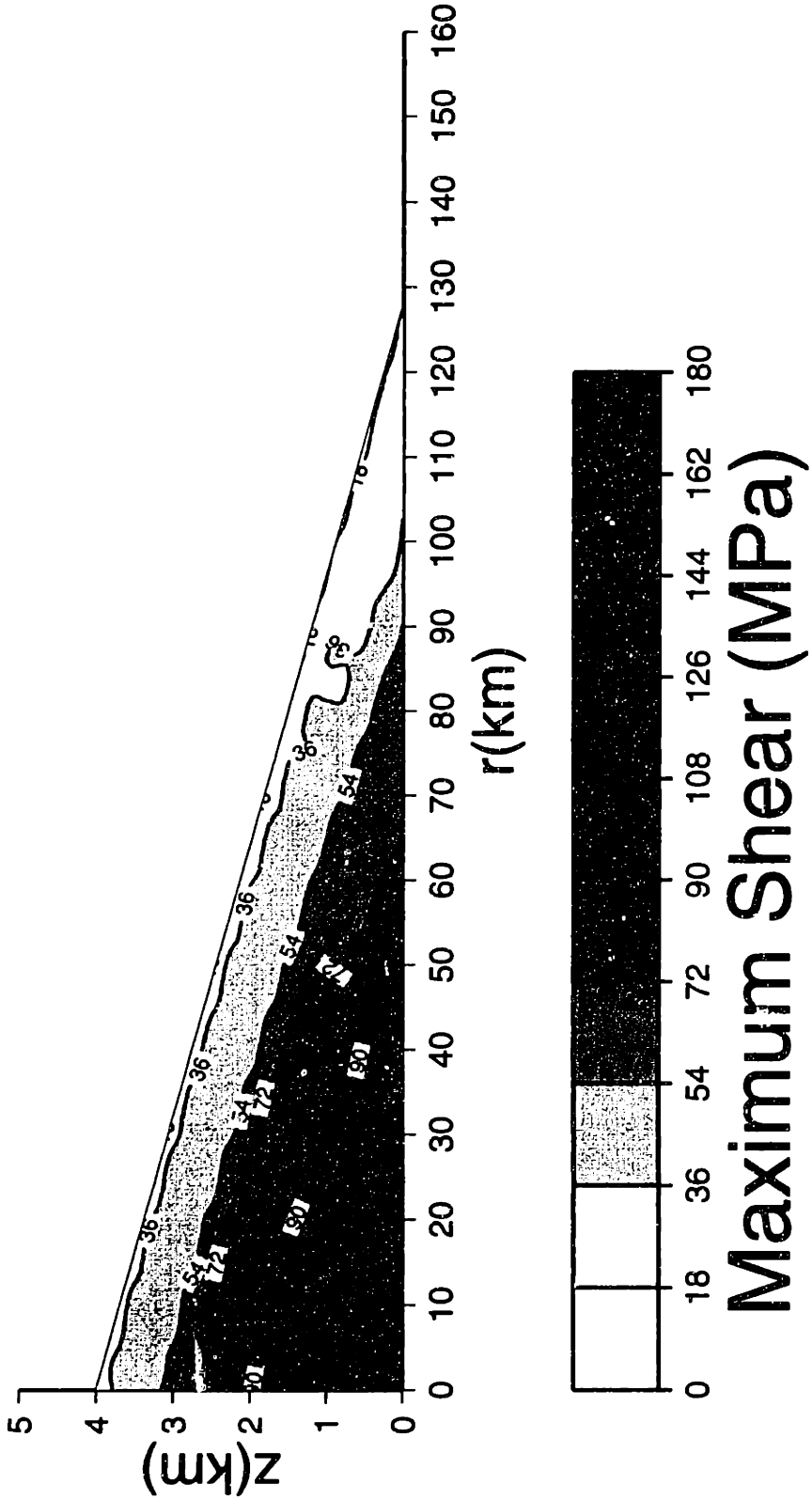
z(km)
r(km)
Maximum Shear (MPa)
0 10 20 30 40 50 60 70 80 90 100 110 120 130 140 150 160
0 1 2 3 4 5
0 18 36 54 72 90 108 126 144 162 180
18
36
54
72
90

Figure 15e.

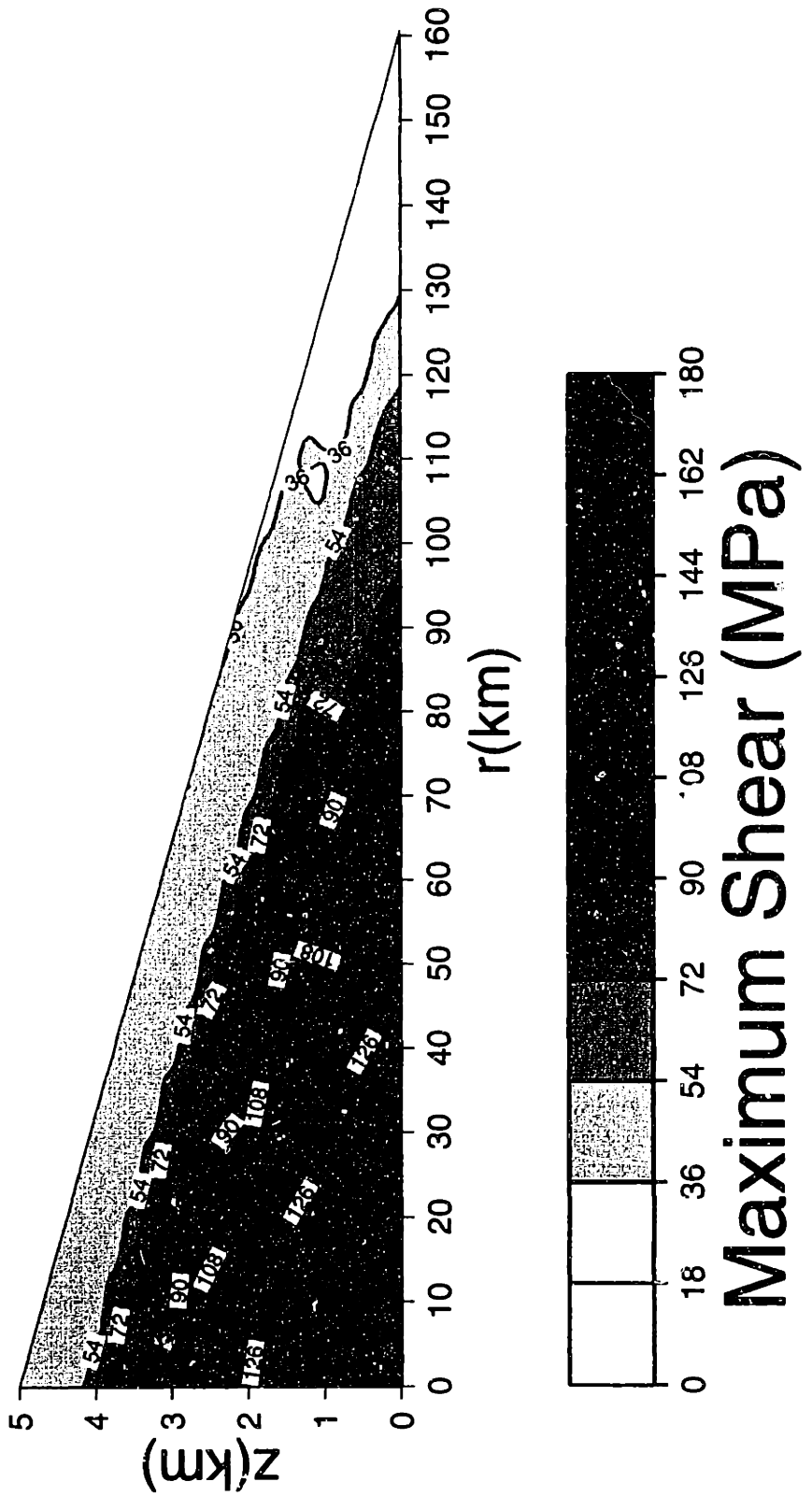

Figure 15f.

Figure 16a.

Figure 16b.

Figure 16c.

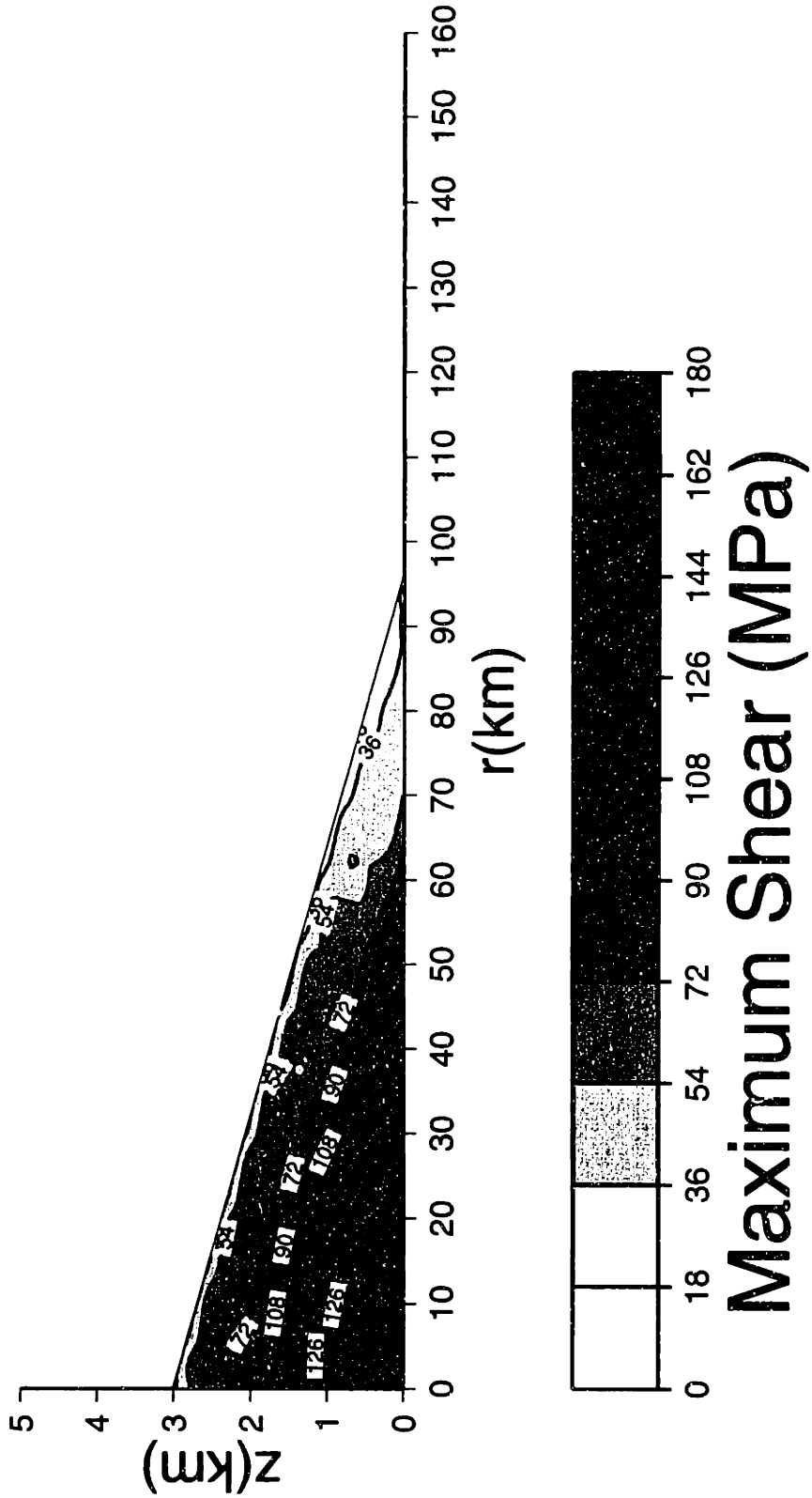
z(km)
r(km)
Maximum Shear (MPa)
0 18 36 54 72 90 108 126 144 162 180
0 10 20 30 40 50 60 70 80 90 100 110 120 130 140 150 160
0 1 2 3 4 5
36
54
72
90
108
126

Figure 16d.

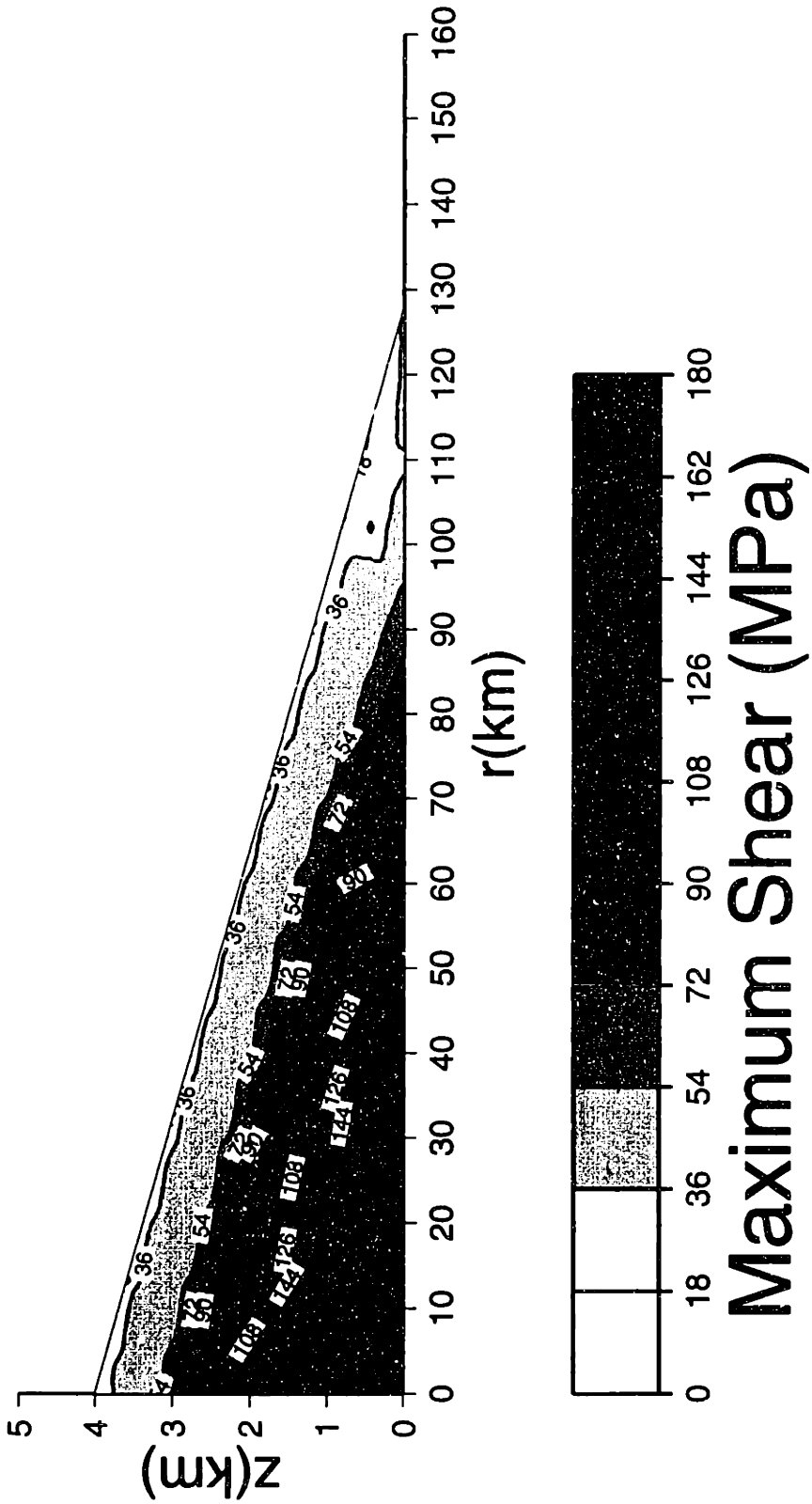

Figure 16e.

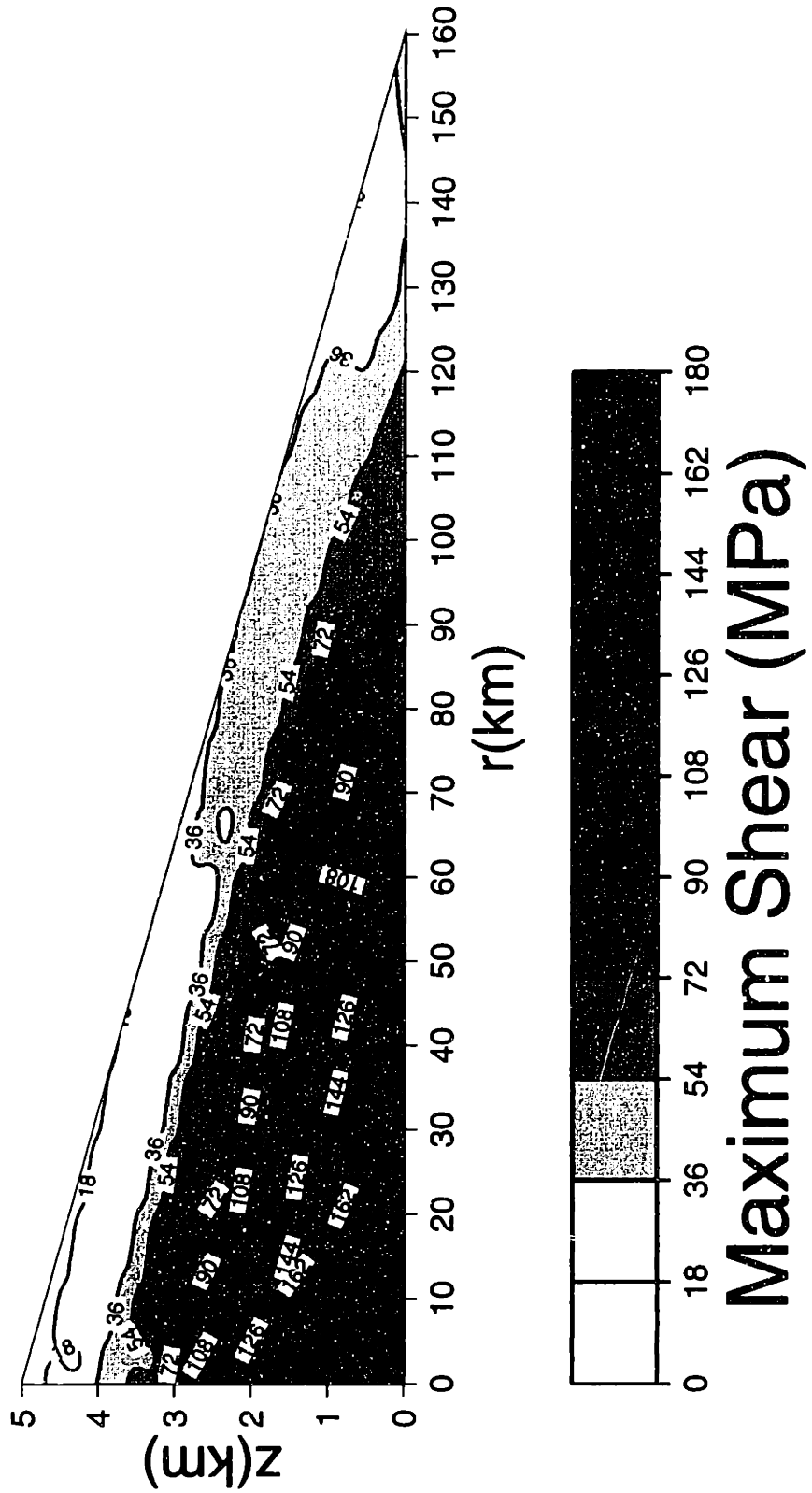
z(km)
r(km)
Maximum Shear (MPa)
0
1
2
3
4
5
0 10 20 30 40 50 60 70 80 90 100 110 120 130 140 150 160
0 18 36 54 72 90 108 126 144 162 180

Figure 16f.

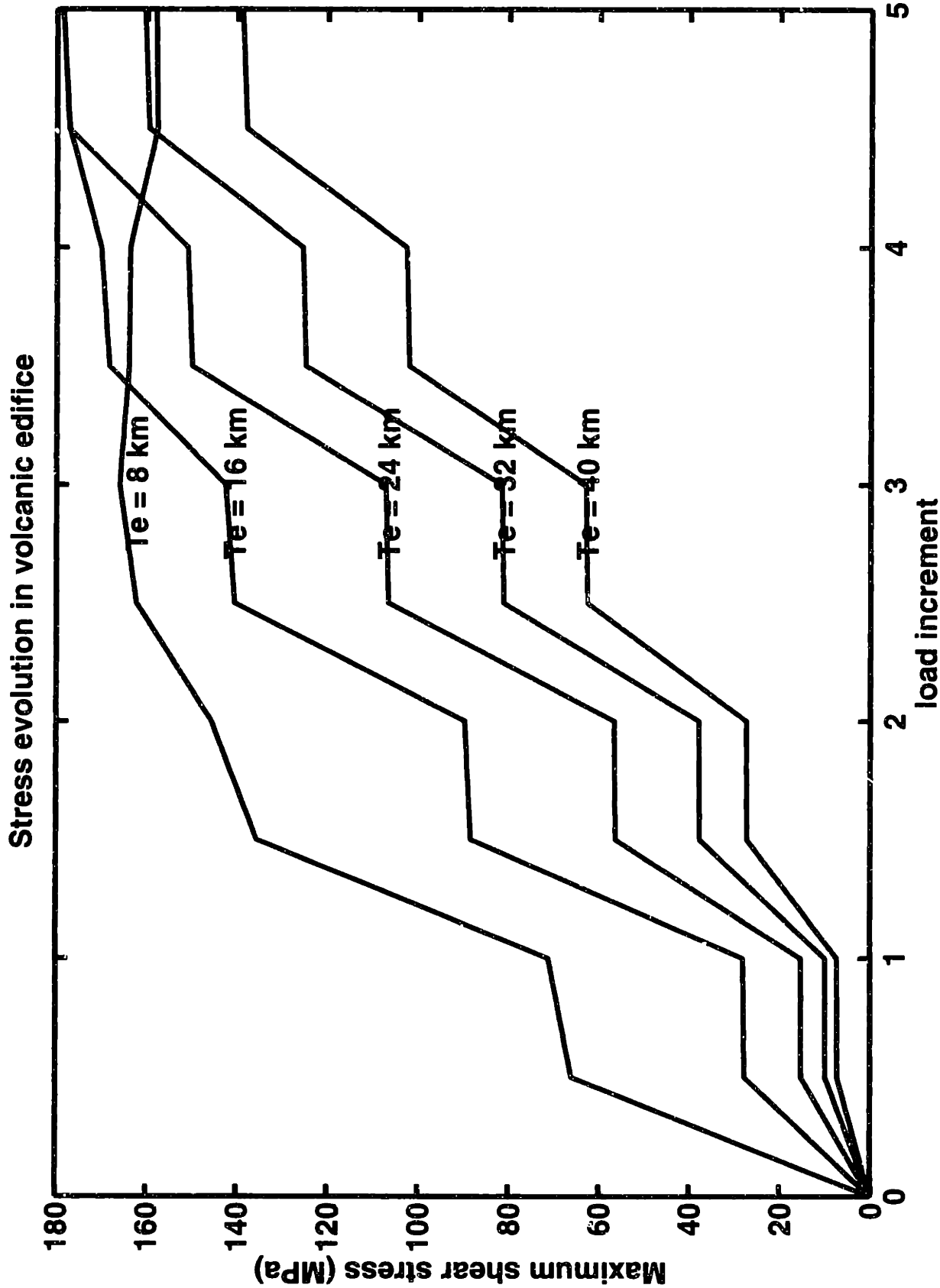
Stress evolution in volcanic edifice
Maximum shear stress (MPa)
load increment
Te = 8 km
Te = 16 km
Te = 24 km
Te = 32 km
Te = 40 km
0
20
40
60
80
100
120
140
160
180
1
2
3
4
5

Figure 17.

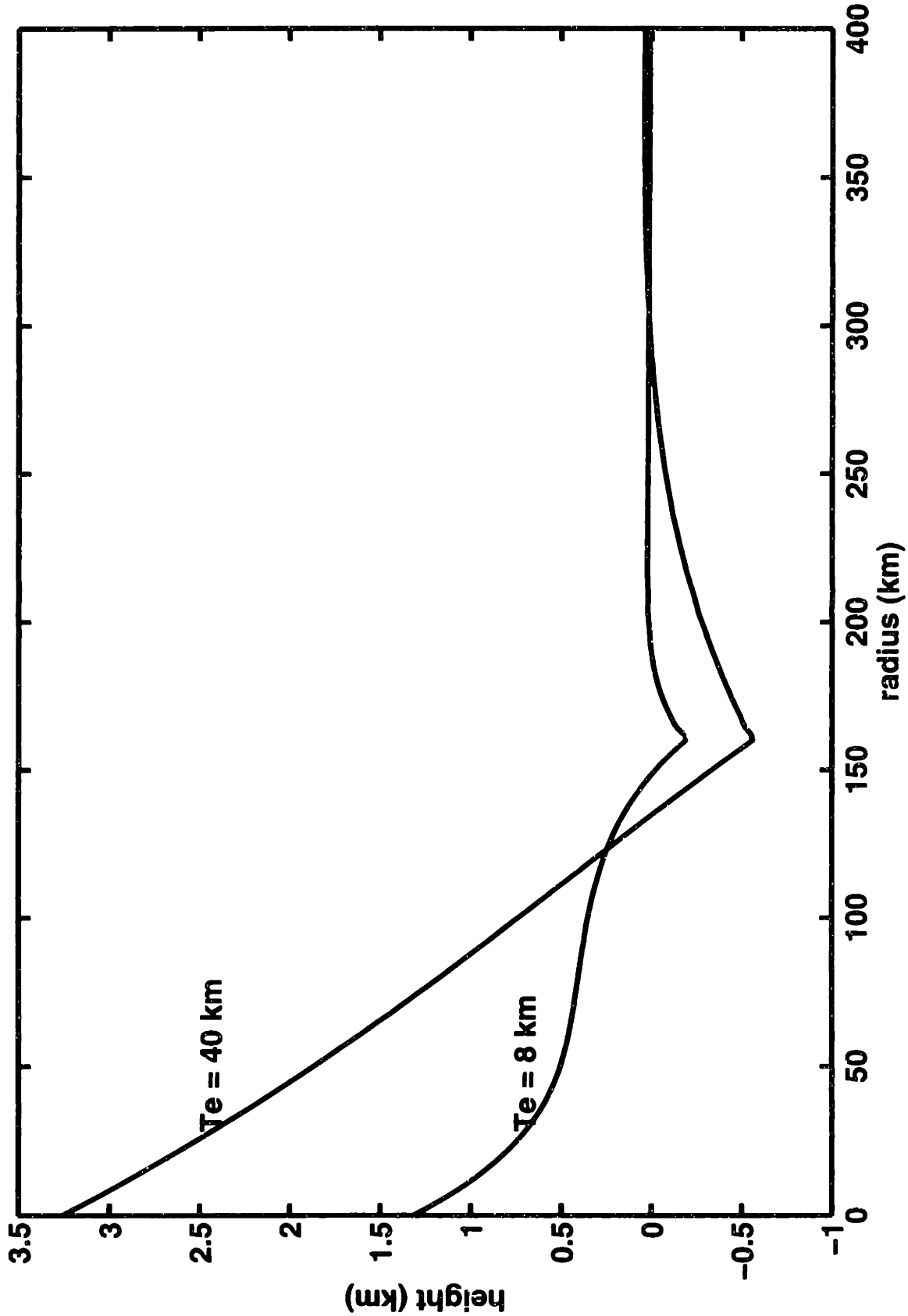
height (km)
radius (km)
Te = 40 km
Te = 8 km
3.5
3
2.5
2
1.5
1
0.5
0
−0.5
−1
0
50
100
150
200
250
300
350
400

Figure 18.

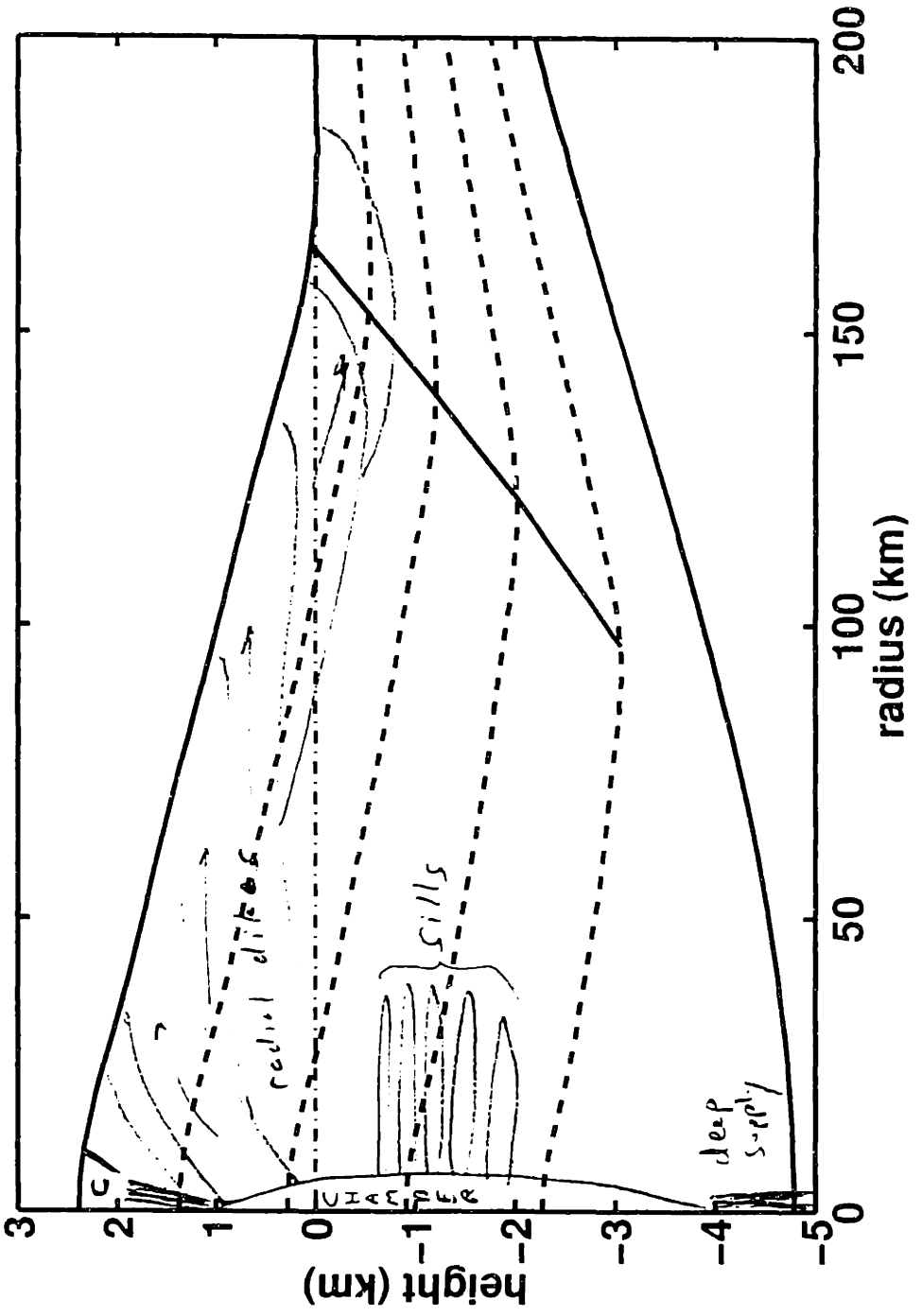

Figure 19.

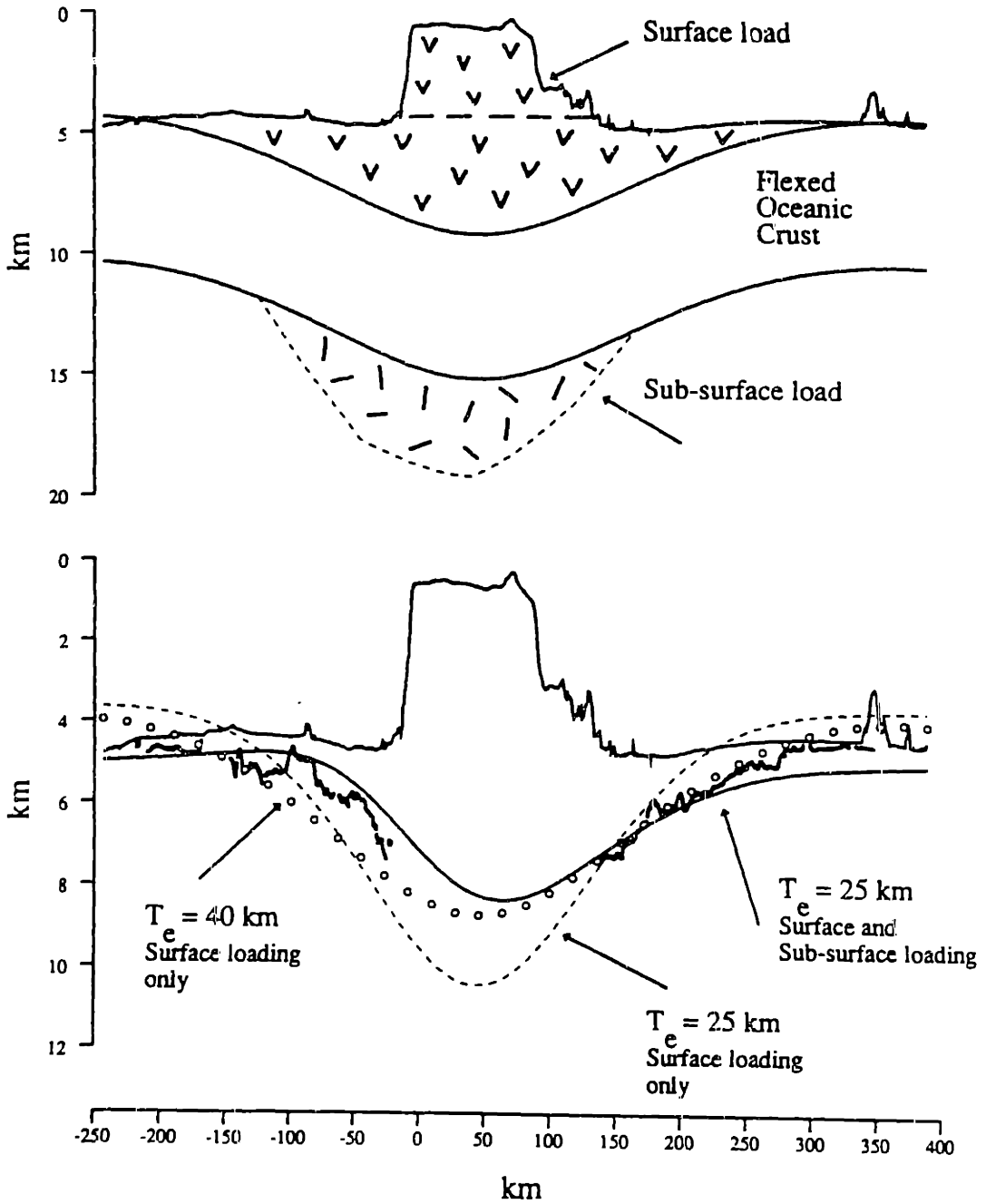
Surface load
Flexed
Oceanic
Crust
Sub-surface load
km
0
5
10
15
20
T_e = 40 km
Surface loading
only
T_e = 25 km
Surface and
Sub-surface loading
T_e = 25 km
Surface loading
only
2
4
6
8
10
12
-250
-200
-150
-100
-50
0
50
100
150
200
250
300
350
400
km

Figure 20a.

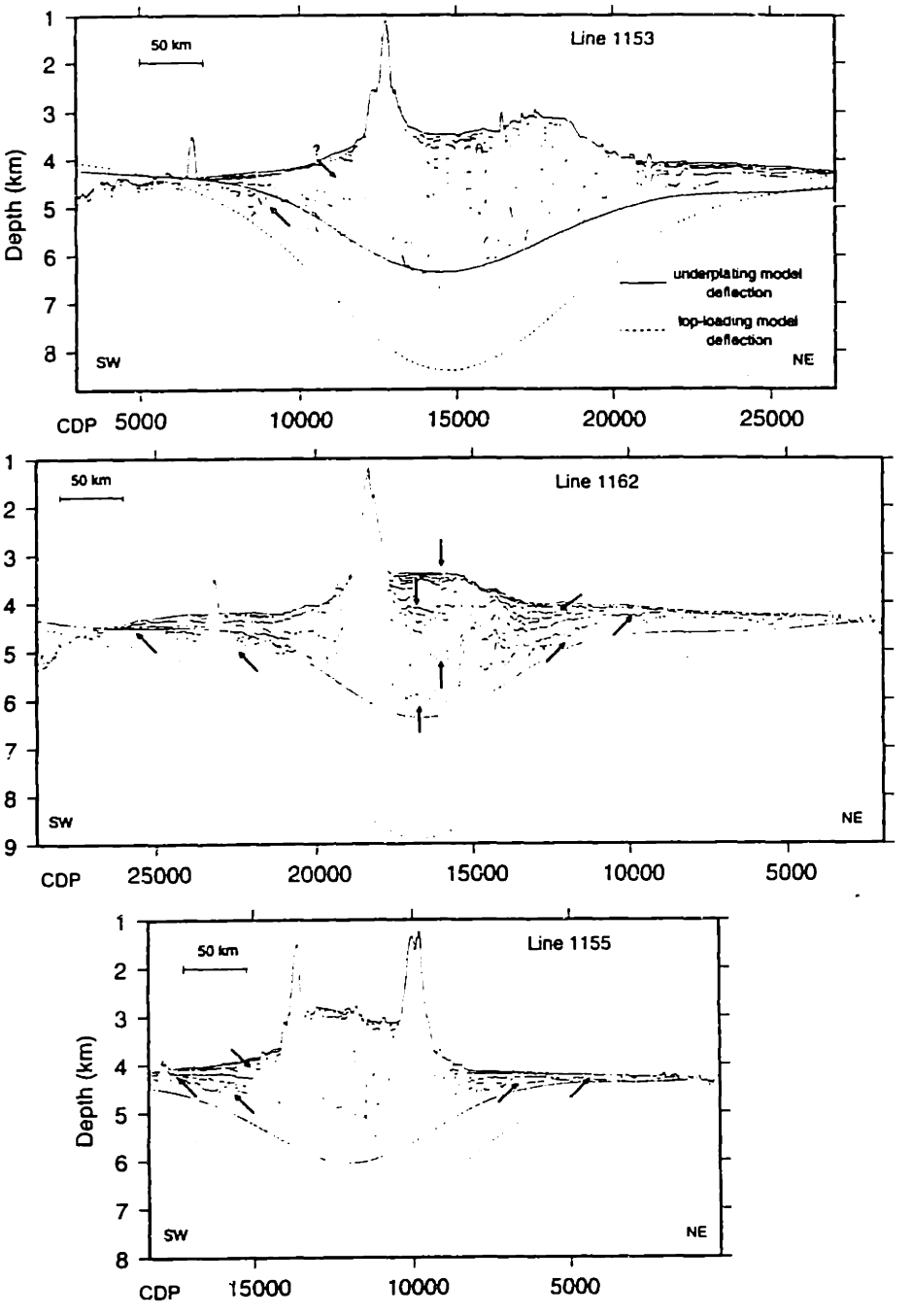
Line 1153
50 km
Depth (km)
SW
NE
underplating model deflection
top-loading model deflection
CDP 5000 10000 15000 20000 25000
Line 1162
50 km
SW
NE
CDP 25000 20000 15000 10000 5000
Line 1155
50 km
Depth (km)
SW
NE
CDP 15000 10000 5000

Figure 20b.

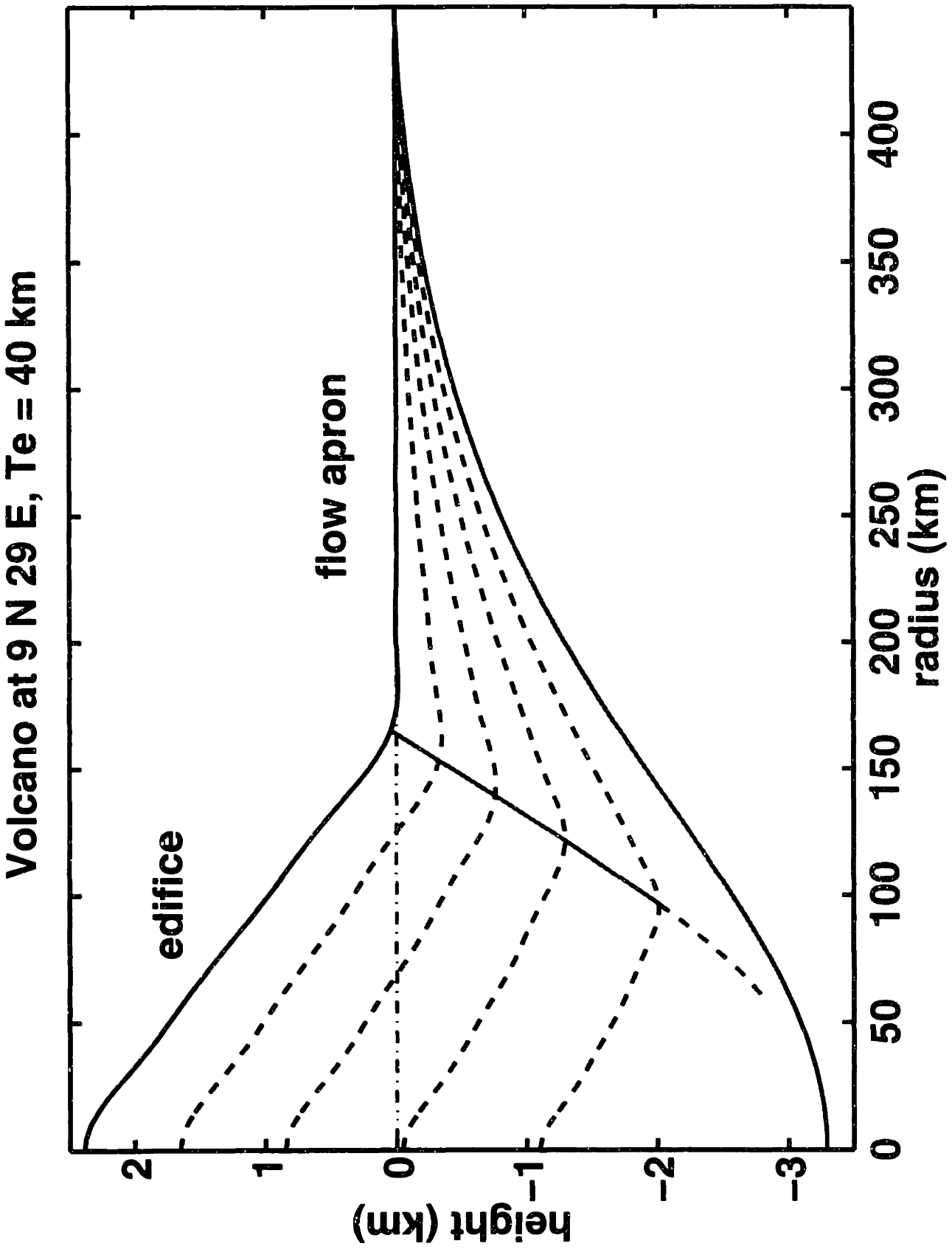
Volcano at 9 N 29 E, Te = 40 km
edifice
flow apron
height (km)
2
1
0
−1
−2
−3
0
50
100
150
200
250
300
350
400
radius (km)

Figure 21a.

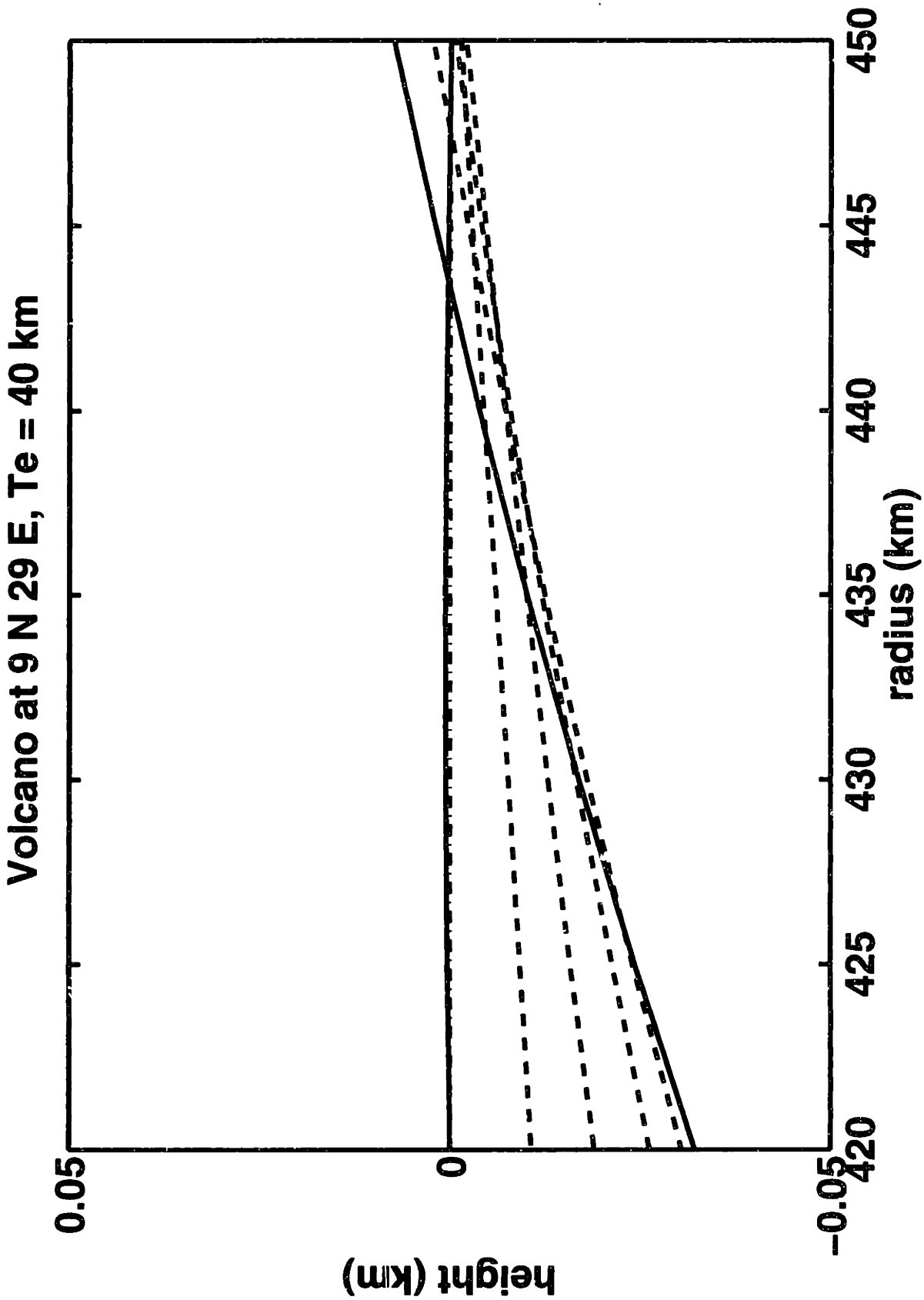
Volcano at 9 N 29 E, Te = 40 km
height (km)
radius (km)
0.05
0
−0.05
420
425
430
435
440
445
450

Figure 21b.

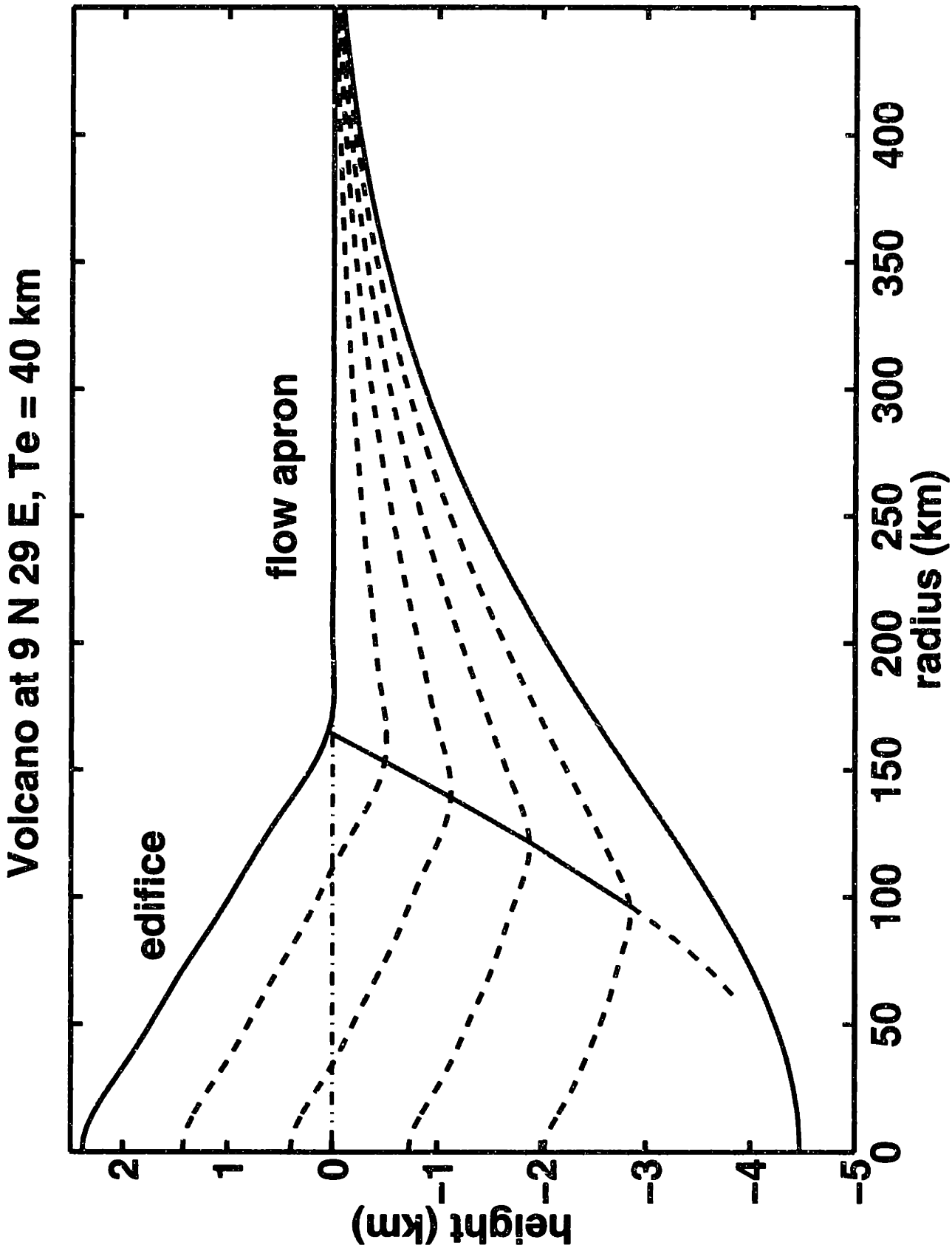
Volcano at 9 N 29 E, Te = 40 km
edifice
flow apron
height (km)
radius (km)
2
1
0
−1
−2
−3
−4
−5
0
50
100
150
200
250
300
350
400

Figure 21c.

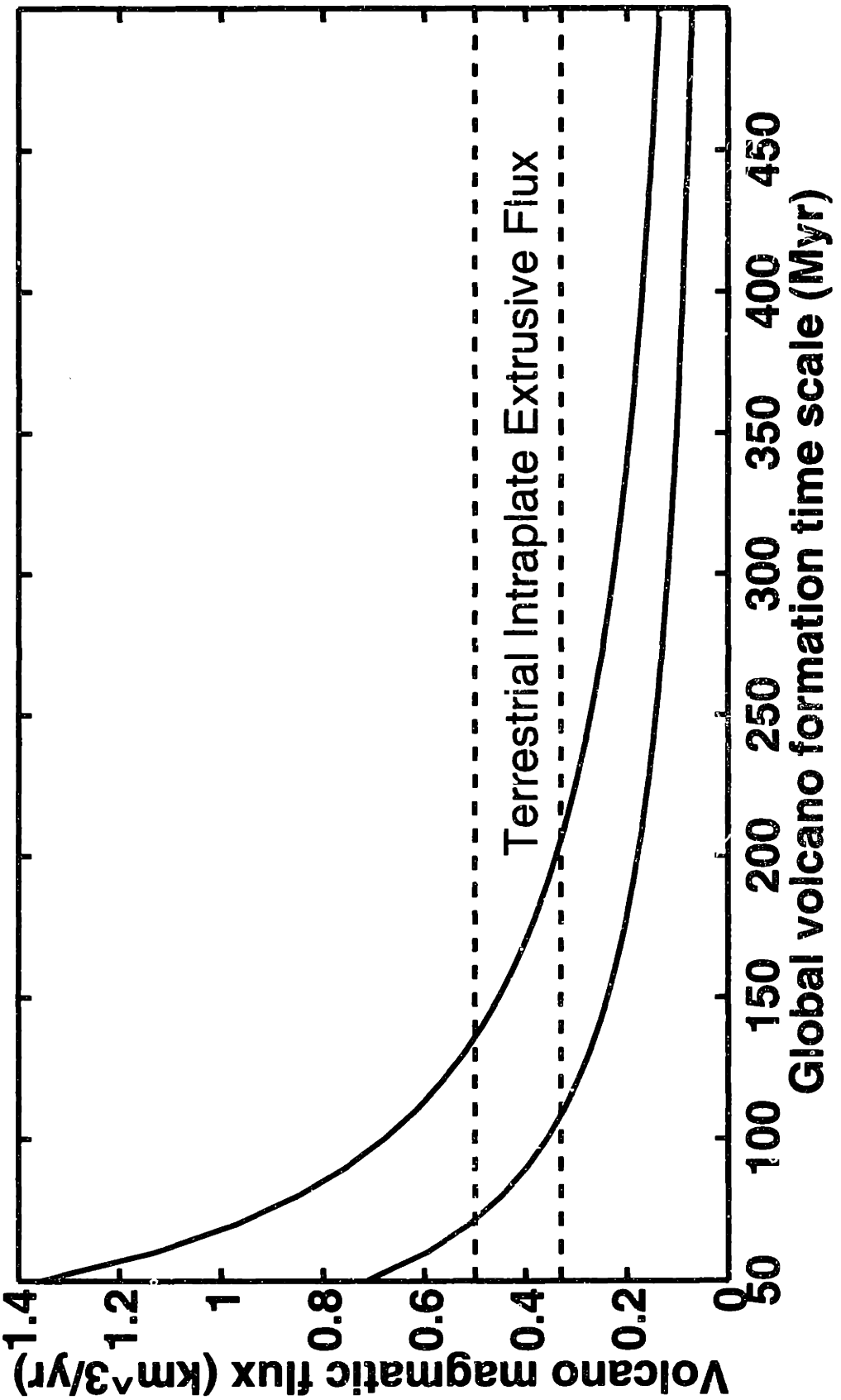
Terrestrial Intraplate Extrusive Flux
Volcano magmatic flux (km^3/yr)
Global volcano formation time scale (Myr)
0
0.2
0.4
0.6
0.8
1
1.2
1.4
50
100
150
200
250
300
350
400
450

Figure 22.

Chapter 5

Comparative Volcanology and Future Directions

After considering a broad survey of large volcanoes on the terrestrial planets, it is helpful to compare and contrast the characteristics of volcanoes of each planet, and to isolate the factors that give each planet a distinctive style of large volcano construction. Whereas Chapters 2, 3 and 4 each focused on the volcanoes on individual planets, with only occasional discussion of volcanoes on other planets, I attempt below to apply the insights gained from each planet to a more general understanding of the evolution of volcanoes on the terrestrial planets. Some of the ideas developed in this process, however, require much more than a simple discussion before they can be confirmed. Therefore, a final section is devoted to detailed suggestions for future studies that build on the methods and conclusions of this thesis.

Comparative Volcanology on the Terrestrial Planets

Venus-Earth contrasts

Several critical factors account for the distinct structural style of volcanoes on Venus, compared with those of Earth (and Mars). The lack of liquid water at the surface of Venus

contributes in several ways. There is no buoyancy from an ocean layer to reduce the effective density of the load, so the magnitude of horizontal compressive stresses in a given size edifice will be about a factor of $(8.87/9.8) \times (2800/1800) \approx 1.4$ greater on Venus than in oceanic settings on Earth. The absence of a hydrated low-permeability sediment layer at a volcano base (see Chapter 3) results in a welded basal boundary condition at all large volcanoes on Venus.

Water also affects the mechanics of faulting by its role as a pore fluid in volcanic rocks. Pore fluid pressure reduces the effective pressure in the rock, bringing it closer to failure. For rocks with high pore pressure, the magnitude of differential stress that can be supported is greatly reduced. This effect is seen in seismic studies of the island of Hawaii [*Wyss et al.*, 1992b], where the maximum shear stress at a depth of 7 km in the edifice was found to be 3 ± 2 MPa. This value is much smaller than the hundreds of MPa maximum shear stresses found in the finite element models. Low differential stress levels, such as those observed at Hawaii, make it possible for small perturbations in stress to reorient the principal stress axes, since stress increments associated with dike intrusion and magma chamber inflation or deflation will be much larger relative to the ambient field, which can lead to rapid changes in the direction of magma propagation. Horizontal compressive stress levels in such volcanoes would be easy to overcome, and principal stress reorientation would be possible in all parts of the edifice that experience high pore pressures. On Venus, there is no surface water, and thus no pore fluid (except for perhaps CO_2; but it is not likely that significant CO_2 pressures could be maintained. Thus, differential stress levels in edifices on Venus will likely approach those in the finite element models, except in areas where the failure criterion was exceeded (faulting would reduce the differential stresses there). Given differential stress magnitudes of hundreds of MPa, it will be much more difficult for small stress perturbations to reorient the principal stresses. Such reorientation requires a strong source (such as a well-supplied, inflating magma chamber), and perhaps assistance from other sources of stress, such as regional stress (transmitted through the welded basal boundary). Even so, the extent of

stress field reorientation would be restricted to the vicinity of the source.

Basal boundary condition

The finite element structural models presented in this thesis indicate that the basal boundary condition plays a critical role in a volcano's structural evolution. Large volcanoes on Earth (Chapter 3) exhibit both welded and detached basal boundary conditions. The largest volcanoes in the Tharsis region of Mars (Chapter 4) exhibit evidence indicating partial to complete detachments at their bases. The existence of welded basal boundary conditons at other volcanoes on Mars, however, cannot be ruled out (a search for such volcanoes would be a worthwhile project). Large volcanoes on Venus were all found to exhibit characteristics consistent with a welded basal boundary condition. This uniformity can be attributed to the lack of water at the surface of Venus. The layer of low-permeability clay sediment required to form a detachment on Earth [*Iverson*, 1995] must be subaqueously deposited. Water is also necessary to act as the pressurized pore fluid in the sediment layer [*Iverson*, 1995]. The existence of large flood features, valley networks and other fluvial terrain on Mars indicates that Mars once had a substantial quantity of water at the surface [e.g., *Carr*, 1987]. A substantial amount of water likely remains frozen beneath the surface of Mars [*Carr*, 1987]. Martian regolith, however, is believed to exhibit very high porosities [*Squyres et al.*, 1992a]. Thus, even assuming the presence of liquid water, it may be difficult to generate high pore pressures in a Martian detachment. *Tanaka* [1985] proposed an alternative mechanism for generating basal spreading at Olympus Mons. Recognizing the difficulty of forming extensive high pore-fluid pressure zones beneath Olympus Mons, he proposed that a material consisting of about 10% interstitial ice would have a very low shear strength and could therefore accommodate slip at the volcano's base. Regardless of which mechanism forms basal detachments on Mars, water likely plays an important role. The presence of water at the surfaces of Earth and Mars allows development of analogous volcano structures, as discussed in Chapter 2. The unique style of volcanoes on Venus arises in part from the

lack of water at the surface: no detachment-forming layers are deposited, and the lack of pore fluid inhibits shallowly-rooted mass wasting of volcano flanks.

A welded basal boundary condition can restrict the size of large volcanoes. Horizontal compressive stresses prevent ascent of magma to the shallow edifice and surface regions, thereby inhibiting volcano growth. This is one factor that accounts for the small size of basally welded volcanoes on Earth (Chapter 3), compared with that of basally detached volcanoes. Stresses associated with formation and expansion of a magma chamber counteract the flexurally-induced horizontal compression, allowing magma ascent. A balance between the flexural and magma-chamber-related stress fields determines the size of welded-base volcanoes (see Chapter 3). The maintenance of a magma chamber requires a steady supply of magma: on Earth, plate motion removes a volcano from the underlying mantle magma source, eventually halting volcano growth. Plate tectonics does not currently operate on Venus [*Solomon et al.*, 1992] and is not likely to have operated during the time of large volcano construction (i.e., since the global resurfacing event). Thus, a volcano on Venus will remain stationary over its mantle magma source. Assuming that Venus plumes are as long-lived as terrestrial plumes, the amount of material that supplies an entire chain of volcanoes on Earth is available to a single volcano on Venus. As discussed above, differential stress magnitudes are likely much greater in Venus volcanoes than in terrestrial volcanoes. This state should act to restrict the growth of Venus volcanoes, tending to make them smaller than welded-base terrestrial volcanoes (such as those in the Galápagos or Marquesas chains). Many Venus volcanoes, however, are much larger than welded-base terrestrial volcanoes (see Chapters 3 and 4). Evidently the lack of plate motion on Venus assures a long-term supply of magma to the magma chamber. Magma chamber expansion will reorient principal stresses in the edifice, allowing sustained growth of the volcano. Thus, welded-base volcanoes on Venus can grow to much larger size than their terrestrial counterparts because of the lack of horizontal motion of the lithosphere.

Mars is considered to have been a "one-plate planet" for most of its history [*Head and*

Solomon, 1981]. As is the case with Venus, the lithosphere will remain stationary over a hotspot. A given hotspot will thus supply a single volcano, allowing sustained edifice growth even for a basally welded volcano. The presence of water at the surface of Mars likely enables the formation of detachments beneath the Tharsis Montes and Olympus Mons (Chapter 2), further facilitating edifice growth. The surface gravitational acceleration on Mars is less than half that of Earth or Venus, thus favoring the construction of tall edifices at relatively low stress levels. Given this combination of favorable circumstances, it is not surprising that the Tharsis volcanoes of Mars are the largest on the terrestrial planets.

Moat filling and trans-edifice tectonics

As noted in Chapter 4, no volcanoes on Venus exhibit circumferential tectonic features surrounding the edifice (although several, such as Sapas Mons and Tepev Mons, exhibit such features on the edifice flanks; these are attributed to magma chamber activity [*Keddie and Head* [1994b] and *Campbell and Rogers* [1994], respectively]). Encircling graben have been observed around the Tharsis Montes and other large volcanoes on Mars [*Comer et al.*, 1985]. These graben are attributed to radial extensional stress from flexure of the lithosphere beneath the load of the volcanoes [*Comer et al.*, 1985]. No such features have been observed at large terrestrial oceanic hotspot volcanoes; such features, if they existed, would probably be buried by volcano-derived sediments, debris, and mass-wasting deposits. A volcanic field discovered at the Hawaiian flexural arch [*Lipman et al.*, 1989], however, suggests that the lithospheric stress state enabled magma ascent. A state of horizontal principal tension is consistent with this observation. Volcanic fields at terrestrial flexural arches may cover tectonic features caused by flexural stresses.

Absence of trans-edifice graben on Venus

There are several possible explanations for the lack of flexurally-related graben around large volcanoes on Venus. The first is that plate flexure stresses are not transmitted to the moat

filling material. This is likely the case for terrestrial moats, which are filled with fragmented material that cannot support appreciable differential stresses. Graben would not be able to form in such material. If, however, the moats around Venus volcanoes are filled with solidified flows welded to the base of the lithosphere, as we propose, we would expect that flexural stresses would be transmitted to the moat fill. A second possibility is that flexural stresses are small enough such that few or no graben form. This scenario is increasingly likely with increasing T_e. Even for a model with $T_e = 40$ km, however, the failure criterion is exceeded at the top of the lithosphere. A third possibility is that the graben do form but are covered by later apron flows. If this were the case, however, we might expect to see a few exposed graben around volcanoes in an early stage of development, or partly-covered graben around more mature volcanoes. Instead, no surrounding graben are observed around any of the 145 large volcanoes in the data base.

The results of the finite element models in Chapters 2–5 suggest partial resolutions of this problem. In an incrementally-grown volcano, a given load increment feels stresses only from its own loading and from subsequent loads. Assuming that the first moat filling units are welded to the lithosphere (as at the base of the edifice), flexural stress will be transmitted from the lithosphere to the moat fill. Flexurally-induced horizontal extensional stress will decrease with increasing height (age) in the apron portion of the moat fill. Faulting will be less likely to occur in the low-stress upper part of the moat. In the model of Figure 21a in Chapter 4, the region of highest extensional stress occurs at a radius of 260 km, beneath about 0.7 km of moat fill. The region of the plate most likely to fail will thus be buried by a signficant thickness of moat filling material exhibiting lower degreees of horizontal extension. For cases with thinner lithosphere than the model of Figure 21a, flexurally-related extensional stresses will be much larger, perhaps great enough to cause graben formation and propagation upwards through the flow apron and the exposed surface beyond the apron. The complete absence of such features is thus another indication that large volcanoes form only on relatively thick lithosphere.

Another interpretation of the finite element predictions may provide a better explanation for the lack of graben around Venus volcanoes. If moat filling material beneath Venus volcanoes is both welded to the top of the lithosphere and structurally connected to the edifice, it is reasonable to assume that the horizontal compressive stresses predicted for all basally-welded model edifices would also be induced in the moat fill. This horizontal compression would counteract extensional stresses transmitted from the top of the lithosphere to the moat fill, thus inhibiting or preventing the formation of circumferential graben. Figures 15 and 16 of Chapter 4 show that the entire surface of the edifice experiences horizontal principal compression ($\sigma_1 \approx \sigma_{rr}$ or $\sigma_1 = \sigma_{\theta\theta}$). Flexural stresses at the surface of the plate achieve horizontal principal tension ($\sigma_1 \approx \sigma_{rr}$) only near the very edge of the edifice load. Transmission of horizontal compressive stress through the edifice-flow-apron structural unit will move the region of flexurally-induced horizontal extension beyond the edge of the apron. This region may be far enough away from the major part of the load (the edifice and moat fill beneath it) such that stresses never exceed the failure criterion (and graben are not observed).

Moat filling on Mars

The above discussion of stress states in the moat filling material has great relevance to the observed circumferential graben around the Tharsis Montes on Mars. In Chapter 2, these graben were interpreted to be indicative of horizontal extension in the lithosphere supporting the load of the volcanoes [*Comer et al.*, 1985]. The results from the study of Venus volcanoes, however, raise several questions. The most basic concerns the setting of the faults: are the Tharsis Montes graben on the lithosphere surrounding the volcanoes, on material that fills a flexural moat, or on the flanks of the edifices? Consider the graben associated with Pavonis Mons (Figure 4 of Chapter 2). The graben in the eastern and southeastern sectors, for example, are clearly on the edifice flanks. These graben may be related to movement of the flanks along a detachment (as proposed in Chapter 2); alternatively, they may be related to

activity in a magma chamber, as proposed for flank graben on Sapas Mons [*Keddie and Head*, 1994b] and Tepev Mons [*Campbell and Rogers*, 1994] on Venus. The very prominent graben to the north-northeast, however, are more equivocal. They may be at the very edge of the edifice, or in a relatively flat region beyond the edifice. The quality of currently available topography is not sufficient to make such a distinction. If the graben are on the edifice, they may be attributable to flank movement or magma chamber activity, as proposed above. For either of these mechanisms, the resulting graben do not reflect the state of stress in the lithosphere, and thus their positions cannot be used to constrain lithospheric properties. If the graben are not on the edifice, their relationship to a moat and moat-filling material must be established. If the graben are located in a topographic depression, they are likely attributable to lithospheric stresses from flexure. If they are not in a depression, then they are likely located on material that fills a moat. Such moat filling material would not be expected to develop graben, because stress would decrease with increasing height in an incrementally filled moat (as described above for Venus volcanoes). Such scenarios would depend greatly on the basal boundary condition during edifice construction and moat filling, for both the edifice and the moat-filling material. For example, if a large portion of a moat were filled in a short time, the incremental load argument would not apply, and the filled moat surface could develop enough stress to support graben.

This thesis and other studies of moat-filling material at large volcanoes also have implications for the interpretation of the absence of graben around Olympus Mons. The massive edifice of Olympus Mons places an unusually large load on the lithosphere. Stresses caused by flexure of the lithosphere beneath such a load would likely be great enough to induce faulting near the surface of the lithosphere, yet no graben indicative of such failure are observed. *Comer and Solomon* [1981] termed this "the Olympus Mons paradox". *Thurber and Toksöz* [1978] and *Comer et al.* [1985] used the absence of graben to constrain the elastic thickness of the lithosphere (T_e) supporting Olympus Mons, yielding a lower bound $T_e > 150$ km. The results of this thesis and other studies of moat filling at volcanoes on the terrestrial planets

suggest a resolution to the "paradox". For example, the lithosphere beneath the Hawaiian Islands is known to be deflected beneath the load (from seismic and gravity data [e.g., *Watts and ten Brink*, 1989; *Wessel*, 1993]), and to be filled with slump and slide material derived from the edifices [*Moore et al.*, 1989]. No circumferential graben surrounding the Hawaiian Islands have been observed in bathymetric data or sonar imaging [e.g., *Moore et al.*, 1989]. This absence of graben might be used to infer a very thick lithosphere supporting the islands, but in fact the elastic plate thickness for Hawaii is constrained by gravity and seismic studies to the range 25-45 km [*Watts and ten Brink*, 1989; *Wessel*, 1993]. It is likely that moat filling deposits at Hawaii obscure flexural deformation of the surface of the lithosphere. If the Olympus Mons aureole is analogous to the large slumps and slides that fill flexural moats around Hawaii and other large volcanoes on Earth, as I have suggested in Chapter 2, then the aureole deposits fill the moat around Olympus Mons, concealing the surface of the lithosphere. Graben that may have formed there will not be able to coherently propagate upwards through the (possibly kilometers-thick) layer of fragmented material which constitutes the moat fill. Graben, therefore, will not be evident around Olympus Mons, except perhaps beyond the edge of the aureole. Thus, the absence of graben does not constrain the value of T_e at Olympus Mons.

Future Directions

Mars

The methods described in Chapter 2 can be applied to other large volcanoes on Mars. In Chapter 2, I concentrated on four of the largest volcanoes in the Tharsis region. This region also includes several shields significantly smaller in radius and height than the Tharsis Montes. Based on ratios of caldera volumes to edifice volumes and caldera floor elevations, *Robinson and Garbeil* [1994] concluded that the flanks of these structures have been buried by up to several kilometers of regional plains lavas. Thus, significant portions of these

edifices are now hidden from view: *Robinson and Garbeil* [1994] calculate that the largest of these buried edifices, Biblis Patera and Uranius Patera, may be comparable in volume to the Tharsis Montes. The Elysium region of Mars contains three large shield volcanoes. The largest of these, Elysium Mons, is comparable in size to the Tharsis Montes. It exhibits circumferential graben at the edge of the edifice, a scarp on the eastern flank, and radial fractures on the flanks [*Hall et al.*, 1986; *Cattermole*, 1992] Other isolated large shields, such as Apollonaris Patera and Tyrrhena Patera, are also candidates for further study. A comprehensive survey of large Martian volcanoes can be undertaken, along the lines of the study of the Tharsis volcanoes described in Chapter 2. First, the primary tectonic and structural features of the volcanoes should be identified. Then the stress state in the edifices should be modeled using the numerical techniques described above. The set of conditions controlling the structural evolution of each volcano (including basal boundary condition, elastic plate thickness, and loading history) most consistent with observations can then be determined. The results can be used to determine if conditions such as the basal boundary condition or lithospheric thickness vary systematically with region or age (as determined by stratigraphy and crater statistics). The results of the global survey can then be compared and contrasted with those for Venus (reported in Chapter 4); it can then be seen whether volcanoes on Mars display a characteristic style, or alternatively are more diverse than their counterparts on Venus.

A series of new missions to Mars will greatly improve the quality of data regarding large volcanoes. The Mars Global Surveyor (MGS) mission, scheduled to start acquiring data in early 1998, will carry an imaging system (the Mars Orbiter Camera or MOC) and a sensitive altimeter (the Mars Orbiter Laser Altimeter, or MOLA). The MOLA observations will be particularly useful, since currently available topographic data for Mars are of low resolution and limited accuracy. Detailed topographic profiles across the Tharsis volcanoes will resolve important details of the topography of the edifice, caldera structure, scarp relief, and structure of aureole and lobate deposits. The observations will determine the degree to

which flexual moats around volcanoes are filled, which can help resolve the questions about trans-edifice graben and aureole deposits raised above. The data may also help to constrain the formation mechanism of the Olympus Mons basal scarp.

As discussed earlier, current constraints on the thickness of the lithosphere supporting large volcanoes on Mars based on the location (or absence) of graben have been called into question. An independent estimate of this quantity can be found by calculating the admittance and coherence of gravity with topography. The new topography data collected by the Mars Global Surveyor mission, in conjunction with currently available solutions for the gravity field of Mars (to spherical harmonic degree and order 50 [*Smith et al.*, 1993; *Konopliv and Sjogren*, 1995]), as well as improved solutions to be expected after MGS, will allow calculation of gravity/topography admittance and coherence. This calculation is best performed in the spectral domain; a powerful new method for localizing global spectral data [*Simons*, 1995] (such as spherical harmonic expansions) provides a means to obtain independent estimates of T_e for each volcano.

Earth

There are a number of experiments that could confirm or refute our conclusions about the behavior of large volcanoes on Earth. We have suggested that a layer of clay sediment is required for the formation of a basal detachment. A direct sample of material from a decollement would be of great help in determining the accuracy of this suggestion. An extension of the Hawaii Scientific Drilling Project [*Hawaii Scientific Drilling Project*, 1995], planned to reach the base of the Mauna Loa/Mauna Kea volcanic pile, may provide such evidence. A similar hole on Reunion [*Rançon et al.*, 1989], if also extended to the base of the volcanic pile, could provide independent information.

The existence of the basal decollement beneath Hawaii is well-established because of data collected by extensive seismic and geodetic networks on the island. The volcano chains I assign to the welded base category (Galápagos, Marquesas, and Canary) are much less

extensively instrumented. Future seismological and geodetic campaigns to these volcanoes are necessary to confirm the conclusions reached in Chapter 3. Determination of the focal mechanisms of edifice earthquakes would be useful in several ways. Such studies could confirm the proposed absence of decollement structures beneath the edifices. They could also be used to constrain the stress state in the edifice (as done by *Wyss et al.* [1992b] and others for Hawaii). Geodetic surveys also could detect the presence or absence of basal detachments. If the conclusions presented in Chapter 3 are correct, such studies would fail to find basal detachments and would find the edifice stress state dominated by horizontal compression, except in the region around the magma chamber.

Venus

At present, direct constraints on the thickness of the elastic lithosphere (T_e) supporting large volcanoes are scarce (see the gravity-topography admittance and coherence modeling at Atla Regio by *Phillips* [1994]). The structural models presented above suggest that large shield volcanoes are difficult to form on thin lithosphere, and perhaps will only form on lithospheres thicker than some threshold value. Estimates of T_e at a variety of volcanoes on Venus would help in assessing the validity of this hypothesis. As discussed above for Mars, analysis of gravity-topography admittance and coherence, using the spatial-spectral localization method of *Simons* [1995], is an effective way of estimating T_e. The most recent available spherical harmonic representation of the gravity field of Venus is to degree and order 90 [*Konopliv*, 1995b] (topography is available to degree and order 360 [*Rappaport and Plaut*, 1994]). The gravity expansion has a maximum resolution of about 420 km (although the true resolution depends on position [*Konopliv*, 1995b]). Such resolution should be sufficient to extract a flexural signal, allowing estimation of T_e, although contributions from dynamic support may be present at wavelengths overlapping those of the flexural signal [*Kiefer*, 1994].

The models of moat filling at large volcanoes on Venus presented in Chapter 4 suggest an independent method for estimating T_e. As discussed in that chapter, the radius of the

edge of a flexural moat depends on two parameters: the flexural wavelength λ_f (in turn dependent on T_e) and the characteristic wavelength of the edifice (for large values of λ_f and T_e the effect of edifice wavelength will be small). If moats are filled with flows up to the original level of the surface, measurements of flow unit radii from radar images can be used to determine the moat edge radii of large volcanoes on Venus. Given the flow unit and edifice radii (as measured in Chapter 4), it is possible to invert for T_e. Errors or asymmetries in the measured radii are potentially large sources of error in T_e, as are preexisting topographic irregularities around and beneath the flow apron. For a relatively symmetric volcano in an area with relatively smooth basement topography, however, this method may yield useful constraints on T_e.

Finite element improvements

Improvements to the finite element models presented in this thesis can help further our understanding of large volcanoes. Increasing the number of elements and load increments in an edifice (refining the mesh) will allow for more realistic loading histories and magma chamber geometries. The current method of incremental loading requires that the edifice be defined *a priori*. Deflections are calculated after the edifice is defined, so the resulting edifice profile may be somewhat unrealistic and moat fill cannot be taken into account. Modifications that allow self-consistent edifice construction and emplacment of solid moat fill would add an important degree of realism (especially for modeling Venus volcanoes).

Ground Truth

I conclude with an observation concerning the future of volcano studies in the Solar system. As for volcanoes on Earth, those most extensively explored become those most thoroughly understood. The greatest advances in understanding will be made when scientists are able to make detailed measurements *in-situ*. I do not expect to see scientists standing on Maat

Mons in my lifetime, but as for Olympus Mons ...

References

Alexandrovich, J. M., Radiolarian biostratigraphy of ODP leg 111, site 677, eastern equatorial Pacific, late Miocene through Pleistocene, in *Proc. ODP, Sci. Results, vol. 111*, edited by K. Becker, H. Sakai, et al., pp. 245–262, Ocean Drilling Program, College Station, Tex., 1989.

Ancochea, E., F. Hernán, A. Cendrero, J. M. Cantagrel, J. M. Fúster, E. Ibarrola, and J. Coello, Constructive and destructive episodes in the building of a young oceanic island, La Palma, Canary Islands, and genesis of the Caldera de Taburiente, *J. Volcanol. Geotherm. Res.*, *60*, 243–262, 1994.

Anderson, E. M., *The Dynamics of Faulting and Dyke Formation with Applications to Britain*, Oliver and Boyd, Edinburgh, 2nd ed., 206 pp., 1951.

Ando, M., The Hawaii earthquake of November 29, 1975: Low dip angle faulting due to forceful injection of magma, *J. Geophys. Res.*, *84*, 7616–7626, 1979.

Arch, J., and A. Maltman, Anisotropic permeability and tortuosity in deformed wet sediments, *J. Geophys. Res.*, *95*, 9035–9045, 1990.

Arkani-Hamed, J., and M. N. Toksoz, Thermal evolution of Venus, *Phys. Earth Planet. Inter.*, *34*, 232–250, 1984.

Arnadottir, T., and P. Segall, A fault model for the 1989 Kilauea south flank earthquake from leveling and seismic data, *Geophys. Res. Lett.*, *18*, 2217–2220, 1991.

Arvidson, R. E., R. Greeley, M. C. Malin, S. R. S., N. Izenberg, J. J. Plaut, E. R. Stofan, and M. K. Shepard, Surface modification of Venus as inferred from Magellan observations of Plains, *J. Geophys. Res.*, *97*, 13,303–13,318, 1992.

Barron, E. J., and J. M. Whitman, Oceanic sediments in space and time, in *The Sea, 7, The Oceanic Lithosphere*, edited by C. Emiliani, pp. 689–731, Wiley, New York, 1981.

Behrmann, J. H., K. Brown, J. C. Moore, A. Mascle, and E. Taylor, Evolution of structures and fabrics in the Barbados Accretionary Prism. Insights from Leg 110 of the Ocean Drilling Program, *J. Struct. Geol.*, *10*, 577–591, 1988.

Beiersdorf, H., and J. H. Natland, Sedimentary and diagenetic processes in the Central Panama Basin since the late Miocene: The lithology and composition of sediments from Deep Sea Driling Project sites 504 and 505, in *Initial Reports of the Deep Sea Drilling*

Project, edited by J. R. Cann, M. G. Langseth, J. Honnorez, R. P. V. Herzen, S. M. White, and et al., vol. 69, pp. 343–383, U.S. Government Printing Office, Washington, D.C., 1983.

Bird, R. T., and R. A. Pockalny, Late Cretaceous and Cenozoic seafloor and oceanic basement roughness: Spreading rate, crustal age and sediment thickness correlations, *Earth Planet. Sci. Lett.*, *123*, 239–254, 1994.

Bonneville, A., J. Barriot, and R. Bayer, Evidence from geoid data of a hotspot origin for the Southern Mascarene Plateau and Mascarene Islands (Indian Ocean), *J. Geophys. Res.*, *93*, 4199–4212, 1988.

Borgia, A., Dynamical basis of volcanic spreading, *J. Geophys. Res.*, *99*, 17791–17804, 1994.

Borgia, A., and B. Treves, Volcanic plates overriding the ocean crust: Structure and dynamics of Hawaiian volcanoes, in *Ophiolites and Their Modern Oceanic Analogues*, edited by L. M. Parson, B. J. Murton, and P. Browning, Geolog. Soc. Lond. Spec. Pub. 60, pp. 277–299, 1992.

Brace, W. F., Permeability of crystaline and argillaceous rocks, in *Int. J. Rock Mech. Min. Sci. Geomech. Abstr.*, 17, pp. 241–251, Pergamon Press, 1980.

Bredehoeft, J. D., and B. B. Hanshaw, On the maintenance of anomalous fluid pressure, *Geol. Soc. Am. Bull.*, *79*, 1097–1106, 1968.

Brousse, R., J.-P. Chevalier, M. Denizot, and B. Salvat, Étude géomorphologie des Isles Marquises, *Cahiers du Pacifique*, *21*, 9–74, 1978.

Bryan, C. J., A possible triggering mechanism for large Hawaiian earthquakes derived from analysis of the 26 June 1989 Kilauea south flank sequence, *Bull. Seismol. Soc. Am.*, *82*, 2368–2390, 1992.

Byerlee, J., Friction of rocks, *Pure Appl. Geophys.*, *116*, 615–626, 1978.

Byrne, T., and D. Fisher, Evidence for a weak and overpressured décollement beneath sediment-dominated accretionary prisms, *J. Geophys. Res.*, *95*, 9081–9097, 1990.

Campbell, B. A., and P. G. Rogers, Bell Regio, Venus: Integration of remote sensing data and terrestrial analogs for geologic analysis, *J. Geophys. Res.*, *99*, 21,153–21,171, 1994.

Campbell, J. F., Bathymetric Atlas of the Southeast Hawaiian Islands, UNIHI-SEAGRANT-MR-87-01, 21 pp., 1987.

Carr, M. H., Water on Mars, *Nature*, *326*, 30–35, 1987.

Carracedo, J. C., The Canary Islands: An example of structural control on the growth of large oceanic-island volcanoes, *J. Volcanol. Geotherm. Res.*, *60*, 225–241, 1994.

Cattermole, P., *Mars: The Story of the Red Planet*, Chapman and Hall, London, 224 pp., 1992.

Chadwick, Jr., W. W., and J. H. Dieterich, Mechanical modeling of circumferential and radial dike intrusion on Galapagos volcanoes, *J. Volcanol. Geotherm. Res.*, *66*, 37–52, 1995.

Chadwick, Jr., W. W., and K. A. Howard, The pattern of circumferential and radial eruptive fissures on the volcanoes of Fernandina and Isabela islands, Galapagos, *Bull. Volcanol.*, *53*, 259–275, 1991.

Chevallier, L., and W. J. Verwoerd, A numerical model for the mechanical behavior of intraplate volcanoes, *J. Geophys. Res.*, *93*, 4182–4198, 1988.

Chevallier, L., and W. J. Verwoerd, Influence of temperature on the distribution of stress and displacement in a volcano: A numerical approach, *Bull. Volcanol.*, *52*, 413–425, 1990.

Christofferson, E., and M. M. Hamill, A radial pattern of sea-floor deformation in the south-western Caribbean Sea, *Geology*, *6*, 341–344, 1978.

Clague, D. A., and G. B. Dalrymple, The Hawaiian-Emperor volcanic chain, part 1, Geologic evolution, in *Volcanism in Hawaii, vol. 1*, edited by R. W. Decker, T. L. Wright, and P. H. Stauffer, U. S. Geol. Surv. Prof. Pap. 1350, pp. 5–54, 1987.

Clague, D. A., and R. P. Denlinger, Role of olivine cumulates in destabilizing the flanks of Hawaiian volcanoes, *Bull. Volcanol.*, *56*, 425–434, 1994.

Clague, D. A., and J. G. Moore, Comment, *Geology*, *19*, 1049–1050, 1991.

Coello, J., et al., Evolution of the eastern volcanic ridge of the Canary Islands based on new K-Ar data, *J. Volcanol. Geotherm. Res.*, *53*, 251–274, 1992.

Collins, J. A., F. Duennebier, and Shipboard Scientific Party, Site survey and underway geophysics, in *Proc. ODP, Init. Repts.*, edited by A. Dziewonski, R. Wilkens, J. Firth, et al., *136*, pp. 27–34, Ocean Drilling Program, College Station, Tex., 1992.

Comer, R. P., Thick plate flexure, *Geophys. J. R. Astron. Soc.*, *72*, 101–113, 1983.

Comer, R. P., and S. C. Solomon, The Olympus Mons paradox: Why hasn't the Martian lithosphere failed under the load (abstract), *Lunar Planet. Sci. 12*, pp. 166–168, 1981.

Comer, R. P., S. C. Solomon, and J. W. Head, Mars: Thickness of the lithosphere from the tectonic response to volcanic loads, *Rev. Geophys.*, *23*, 61–92, 1985.

Crisp, J. A., Rates of magma emplacement and volcanic output, *J. Volcanol. Geotherm. Res.*, *20*, 177–211, 1984.

Crosson, R. S., and E. T. Endo, Focal mechanisms and locations of earthquakes in the vicinity of the 1975 Kalapana earthquake aftershock zone 1970-1979: Implications for the tectonics of the south flank of Kilauea Volcano, island of Hawaii, *Tectonics*, *1*, 495–542, 1982.

Cullen, A. B., A. R. McBirney, and R. D. Rogers, Structural controls on the morphology of Galapagos shields, *J. Volcanol. Geotherm. Res.*, *34*, 143–151, 1987.

Cyr, K. E., and H. J. Melosh, Tectonic patterns and regional stresses near coronae, *Icarus*, *102*, 175–184, 1993.

Dañobeitia, J. J., J. P. Canales, and G. A. Dehghani, An estimation of the elastic thickness of the lithosphere in the Canary Archipelago using admittance function, *Geophys. Res. Lett.*, *21*, 2649–2652, 1994.

Davies, T. A., Mesozoic and Cenozoic sedimentation in the Pacific Ocean basin, in *The Ocean Basins and Margins, vol. 7A*, edited by A. E. M. Nairn, F. G. Stehli, and S. Uyeda, pp. 65–88, Plenum, New York, 1985.

Davis, D., J. Suppe, and F. A. Dahlen, Mechanics of fold-and-thrust belts and accretionary wedges, *J. Geophys. Res.*, *88*, 1153–1172, 1983.

Decker, R. W., Dynamics of Hawaiian volcanoes: An overview, in *Volcanism in Hawaii, vol. 2*, edited by R. W. Decker, T. L. Wright, and P. H. Stauffer, *U.S. Geol. Surv. Prof. Pap.*, 1350, pp. 997–1018, 1987.

Delaney, P. T., R. S. Fiske, A. Miklius, A. T. Okamura, and M. K. Sako, Deep magma body beneath the summit and rift zones of Kilauea volcano, Hawaii, *Science*, *247*, 1311–1316, 1990.

Desonie, D. L., R. A. Duncan, and J. H. Natland, Temporal and geochemical variability of volcanic products of the Marquesas hotspot, *J. Geophys. Res.*, *98*, 17,649–17,665, 1993.

Dieterich, J. H., Growth and persistence of Hawaiian volcanic rift zones, *J. Geophys. Res.*, *93*, 4258–4270, 1988.

Donahue, T. M., and J. B. Pollack, Origin and evolution of the atmosphere of Venus, in *Venus*, edited by D. M. Hunten, L. Colin, T. M. Donahue, and V. I. Moroz, pp. 1003–1036, Univ. Arizona Press, Tucson, 1983.

Duffield, W. A., L. Stieltjes, and J. Varet, Huge landslide blocks in the growth of Piton de la Fournaise, La Réunion, and Kilauea volcano, Hawaii, *J. Volcanol. Geotherm. Res.*, *12*, 147–160, 1982.

Duncan, R. A., and D. A. Clague, Pacific plate motion recorded by linear volcanic chains, in *The Ocean Basins and Margins, vol. 7A*, edited by A. E. M. Nairn, F. G. Stehli, and S. Uyeda, pp. 89–121, Plenum, New York, 1985.

Duncan, R. A., J. Backman, and L. Peterson, Reunion hotspot activity through Tertiary time: Initial results from the Ocean Drilling Program, leg 115, *J. Volcanol. Geotherm. Res.*, *36*, 193–198, 1989.

Dvorak, J., An earthquake cycle along the south flank of Kilauea Volcano, Hawaii, *J. Geophys. Res.*, *99*, 9533–9541, 1994.

Dvorak, J. J., F. W. Klein, and D. A. Swanson, Relaxation of the south flank after the 7.2-magnitude Kalapana earthquake, Kilauea Volcano, Hawaii, *Bull. Seismol. Soc. Am.*, *84*, 133–141, 1994.

Dziewonski, A., R. Wilkens, J. Firth, et al., *Proc. ODP, Init. Repts.*, *136*, College Station, Tex., Ocean Drilling Program, 1992.

Earthwatch Press, *Hiking Map and Guide: Hawaii Volcanoes National Park*, 1992.

Eaton, J. P., and K. J. Murata, How volcanoes grow, *Science*, *132*, 925–938, 1960.

Elsworth, D., and B. Voight, Dike intrusion as a trigger for large earthquakes and the failure of volcano flanks, *J. Geophys. Res.*, *100*, 6005–6024, 1995.

Epp, D., Implications of volcano and swell heights for thinning of the lithosphere by hotspots, *J. Geophys. Res.*, *89*, 9991–9996, 1984.

Ernst, R. E., J. W. Head, E. Parfitt, E. Grosfils, and L. Wilson, Giant radiating dyke swarms on Earth and Venus, *Earth Sci. Rev.*, *39*, 1–58, 1995.

Feighner, M. A., and M. A. Richards, Lithospheric structure and compensation mechanisms of the Galapagos Archipelago, *J. Geophys. Res.*, *99*, 6711–6729, 1994.

Filmer, P., M. K. McNutt, and C. J. Wolfe, Elastic thickness of the lithosphere in the Marquesas and Society Islands, *J. Geophys. Res.*, *98*, 19,565–19,577, 1993.

Filmer, P., M. K. McNutt, H. F. Webb, and D. J. Dixon, Volcanism and archipelagic aprons in the Marquesas and Hawaiian Islands, *Mar. Geophys. Res.*, *16*, 385–406, 1994.

Filmer, P. E., Flexure of the lithosphere in the vicinity of the Marquesas Islands, Ph.D. thesis, Massachusetts Institute of Technology, Cambridge, 234 pp., 1991.

Fischer, K. M., M. K. McNutt, and L. Shure, Thermal and mechanical constraints on the lithosphere beneath the Marquesas swell, *Nature*, *322*, 733–736, 1986.

Fiske, R. S., and E. D. Jackson, Orientation and growth of Hawaiian volcanic rifts: The effect of regional structure and gravtitational stresses, *Proc. Roy. Soc. Lond., Ser. A.*, *329*, 299–326, 1972.

Ford, P. G., and G. H. Pettengill, Venus topography and kilometer-scale slopes, *J. Geophys. Res.*, *97*, 13,103–13,114, 1992.

Fornari, D. J., and J. F. Campbell, Submarine topography around the Hawaiian Islands, in *Volcanism in Hawaii, vol. 1*, edited by R. W. Decker, T. L. Wright, and P. H. Stauffer, U. S. Geol. Surv. Prof. Pap. 1350, pp. 109–124, 1987.

Furumoto, A. S., and R. L. Kovach, The Kalapana earthquake of November 29, 1975: An intra-plate earthquake and its relation to geothermal processes, *Earth Planet. Sci. Lett.*, *18*, 197–208, 1979.

Garcia, M., and M. Kurz, Reply, *Geology*, *19*, 1050–1051, 1991.

Garcia, M. O., M. D. Kurz, and D. W. Muenow, Mahukona: The missing Hawaiian volcano, *Geology*, *18*, 1111–1114, 1990.

Geist, D., K. A. Howard, A. M. Jellinek, and S. Rayder, The volcanic history of Volcán Alcedo, Galápagos Archipelago: A case study of rhyolitic oceanic volcanism, *Bull. Volcanol.*, *56*, 243–260, 1994.

Gillard, D., M. Wyss, and J. S. Nakata, A seismotectonic model for western Hawaii based on stress tensor inversion from fault plane solutions, *J. Geophys. Res.*, *97*, 6629–6641, 1992.

Gillot, P.-Y., and P. Nativel, Eruptive history of the Piton de la Fournaise volcano, Reunion Island, Indian Ocean, *J. Volcanol. Geotherm. Res.*, *36*, 53–65, 1989.

Gillot, P.-Y., J.-C. Lefèvre, and P.-E. Nativel, Model for the structural evolution of the volcanoes of Réunion Island, *Earth Planet. Sci. Lett.*, *122*, 291–302, 1994.

Goff, J. A., A global and regional stochastic analysis of near-ridge abyssal hill morphology, *J. Geophys. Res.*, *96*, 21,713–21,737, 1991.

Got, J.-L., J. Fréchet, and F. W. Klein, Deep fault plane geometry inferred from multiplet relative relocation beneath the south flank of Kilauea, *J. Geophys. Res.*, *99*, 15,375–15,386, 1994.

Grimm, R. E., and R. J. Phillips, Anatomy of a venusian hot spot: Geology, gravity, and mantle dynamics of Eistla Regio, *J. Geophys. Res.*, *97*, 16035–16054, 1992.

Grinspoon, D. H., Was Venus wet? Deuterium reconsidered, *Science*, *238*, 1702–1704, 1987.

Guest, J. E., M. H. Bulmer, J. Aubele, K. Beratan, R. Greeley, J. W. Head, G. Michaels, C. Weitz, and C. Wiles, Small volcanic edifices and volcanism in the plains of Venus, *J. Geophys. Res.*, *97*, 15,949–15,966, 1992.

Hall, J. L., S. C. Solomon, and J. W. Head, Elysium Region, Mars: Tests of lithospheric loading models for the formation of tectonic features, *J. Geophys. Res.*, *91*, 11,377–11,392, 1986.

Handin, J., Strength and ductility, in *Handbook of Physical Constants, Memoir 97*, edited by S. P. Clark, Jr., pp. 223–289, Geol. Soc. Amer., Boulder, Colo., 1966.

Hawaii Scientific Drilling Project, Summary of preliminary results, *GSA Today*, submitted, 1995.

Head, J. W., and S. C. Solomon, Tectonic evolution of the terrestrial planets, *Science*, *213*, 62–76, 1981.

Head, J. W., L. S. Crumpler, J. C. Aubele, J. E. Guest, and R. S. Saunders, Venus volcanism: Classification of volcanic features and structures, associations, and global distribution from Magellan data, *J. Geophys. Res.*, *97*, 13,153–13,197, 1992.

Herrick, R. R., Resurfacing history of Venus, *Geology*, *22*, 703–706, 1994.

Herrick, R. R., and R. J. Phillips, Implications of a global survey of Venusian impact craters, *Icarus*, *111*, 387–416, 1994.

Hey, R., Tectonic evolution of the Cocos-Nazca spreading center, *Geol. Soc. Am. Bull.*, *88*, 1404–1420, 1977.

Hey, R., G. L. Johnson, and A. Lowrie, Recent plate motions in the Galapagos area, *Geol. Soc. Am. Bull.*, *88*, 1385–1403, 1977.

Hoernle, K., and H.-U. Schminke, The role of partial melting in the 15-Ma geochemical evolution of Gran Canaria: A blob model for the Canary hotspot, *J. Petrol.*, *34*, 599–626, 1993.

Hoffert, M., A. Person, C. Courtois, A. M. Karpoff, and D. Trauth, Sedimentology, mineralogy, and geochemistry of hydrothermal deposits from holes 424, 424A, 424B and 424C (Galapagos spreading center), in *Initial Reports of the Deep Sea Drilling Project, vol. 54*, edited by B. R. Rosendahl, R. Hekinian, et al., pp. 339–376, Washington, D. C., U.S. Government Printing Office, 1980.

Holcomb, R. T., and R. C. Searle, Large landslides from oceanic volcanoes, *Mar. Geotechnology*, *10*, 19–32, 1991.

Holik, J. S., and P. D. Rabinowitz, Structural and tectonic evolution of oceanic crust within the Jurassic quiet zone, offshore Morocco, in *Geology and Geophysics of Continental Margins, Memoir 53*, edited by J. S. Watkins, F. Zhiqiang, and K. J. McMillen, pp. 259–282. Amer. Assoc. Petrol. Geol., Tulsa, Okla., 1992.

Hubbert, M. K., and W. W. Rubey, Role of fluid pressure in mechanics of overthrust faulting: I. Mechanics of fluid-filled porous solids and its application to overthrust faulting, *Geol. Soc. Am. Bull.*, *70*, 115–166, 1959.

Iverson, R. M., Can magma-injection and groundwater forces cause massive landslides on Hawaiian volcanoes?, *J. Volcanol. Geotherm. Res.*, *66*, 295–308, 1995.

Jackson, E. D., E. I. Silver, and G. B. Dalrymple, Hawaiian-Emperor chain and its relation to Cenozoic circumpacific tectonics, *Geol. Soc. Am. Bull.*, *83*, 601–618, 1972.

Janes, D. M., S. W. Squyres, D. L. Bindschadler, G. Baer, G. Schubert, V. L. Sharpton, and E. R. Stofan, Geophysical models for the formation and evolution of coronae on Venus, *J. Geophys. Res.*, *97*, 16,055–16,068, 1992.

Johnson, C. L., and D. T. Sandwell, Lithospheric flexure on Venus, *Geophys. J. Int.*, *119*, 627–647, 1994.

Keddie, S. T., and J. W. Head, Height and altitude distribution of large volcanoes on Venus, *Planet. Space Sci.*, *42*, 455–462, 1994a.

Keddie, S. T., and J. W. Head, Sapas Mons, Venus: Evolution of a large shield volcano, *Earth Moon Planets*, *65*, 129–190, 1994b.

Keddie, S. T., and J. W. Head, Formation and evolution of volcanic edifices on the Dione Regio rise, Venus, *J. Geophys. Res.*, *100*, 11,729–22,754, 1995.

Kennett, J. P., *Marine Geology*, Prentice-Hall, Englewood Cliffs, N.J., 813 pp., 1982.

Kiefer, W. S., High Rayleigh number convection and its relationship to gravity and topography on Venus (abstract), *Eos Trans. AGU, 75*, 215, Spring Meeting suppl., 1994.

Koch, D. M., A spreading drop model for plumes on Venus, *J. Geophys. Res., 99*, 2035–2052, 1994.

Kolla, V., and R. B. Kidd, Sedimentation and sedimentary processes in the Indian Ocean, in *The Ocean Basins and Margins, vol. 6*, edited by A. E. M. Nairn, and F. G. Stehli, pp. 1–50, Plenum, New York, 1982.

Konopliv, A. S., Venus spherical harmonic gravity model to degree and order 75, personal communication, 1995a.

Konopliv, A. S., Venus spherical harmonic gravity model to degree and order 90, personal communication, 1995b.

Konopliv, A. S., and W. L. Sjogren, Venus spherical harmonic gravity model to degree and order 60, *Icarus, 112*, 42–54, 1994.

Konopliv, A. S., and W. L. Sjogren, The JPL Mars gravity field, Mars50c, based upon Viking and Mariner 9 doppler tracking data, Tech. Rep. 95-5, JPL, NASA, Pasadena, 1995.

Krumbein, W. C., and L. L. Sloss, *Stratigraphy and Sedimentation*, W. H. Freeman and Co., San Francisco, second ed., 660 pp., 1963.

Kruse, S., Magnetic lineations on the flanks of the Marquesas Swell: Implications for the age of the seafloor, *Geophys. Res. Lett., 15*, 573–576, 1988.

Larson, R. L., and W. C. Pitman, III, World-wide correlation of Mesozoic magnetic anomalies, and its implications, *Geol. Soc. Am. Bull., 83*, 3645–3662, 1972.

Lénat, J.-F., P. Bachèlery, A. Bonneville, and A. Hirn, The beginning of the 1985-1987 eruptive cycle at Piton de la Fournaise (la Reunion); new insights in the magmatic and volcano-tectonic systems, *J. Volcanol. Geotherm. Res., 36*, 209–232, 1989a.

Lénat, J.-F., P. Vincent, and P. Bachèlery, The offshore continuation of an active basaltic volcano: Piton de la Fournaise (Reunion Island, Indian Ocean); structural and geomorphological interpretation from Sea Beam mapping, *J. Volcanol. Geotherm. Res., 36*, 1–36, 1989b.

Li, Y., C. H. Thurber, and C. G. Munson, Profile of discontinuities beneath Hawaii from S to P converted seismic waves, *Geophys. Res. Lett., 19*, 111–114, 1992.

Liang, B., C. Kisslinger, and C. Bryan, Estimate of the stress field in Kilauea's south flank, Hawaii, *Geophys. J. Int., 123*, 213–231, 1995.

Lipman, P. W., Declining growth of Mauna Loa during the last 100,000 years: Rates of lava accumulation vs. gravitational subsidence, in *Mauna Loa Revealed: Structure, Composition, History, and Hazards*, edited by J. M. Rhodes, and J. P. Lockwood, Geophysical Monograph 92. American Geophysical Union, Washington, 348 pp., 1995.

Lipman, P. W., and J. G. Moore, Mauna Loa lava accumulation rates at the Hilo drill site: Formation of lava deltas during a period of declining overall volcanic growth, *J. Geophys. Res.*, *101*, 11,631–11,641, 1996.

Lipman, P. W., J. P. Lockwood, R. T. Okamura, D. A. Swanson, and K. M. Yamashita, Ground deformation associated with the 1975 magnitude-7.2 earthquake and resulting changes in activity of Kilauea Volcano, *U. S. Geol. Surv. Prof. Pap. 1276*, 45 pp., 1985.

Lipman, P. W., D. A. Clague, J. G. Moore, and R. T. Holcomb, South Arch volcanic field–Newly identified young lava flows on the sea floor south of the Hawaiian Ridge, *Geology*, *17*, 611–614, 1989.

Lockwood, J. P., and P. W. Lipman, Holocene eruptive history of Mauna Loa volcano, in *Volcanism in Hawaii, vol. 1*, edited by R. W. Decker, T. L. Wright, and P. H. Stauffer, *U.S. Geol. Surv. Prof. Pap.*, 1350, pp. 509–535, 1987.

Macario, A., W. F. Haxby, J. A. Goff, W. B. F. Ryan, S. C. Cande, and C. A. Raymond, Flow line variations in abyssal hill morphology for the Pacific-Antarctic Ridge at 65° S, *J. Geophys. Res.*, *99*, 17,921–17,934, 1994.

MacFarlane, D. J., and W. I. Ridley, An interpretation of gravity data for Tenerife, Canary Islands, *Earth Planet. Sci. Lett.*, *4*, 481–486, 1968.

Mackwell, S. J., M. E. Zimmerman, D. L. Kohlstedt, and S. S. Scherber, Experimental deformation of dry columbia diabase: Implications for tectonics on Venus, in *Rock Mechanics*, edited by J. J. Deamen, and R. A. Schultz, pp. 207–214, Brookfield, Vt., A. A. Balkema, 1995.

Magee Roberts, K., J. E. Guest, J. W. Head, and M. G. Lancaster, Mylitta Fluctus, Venus: Rift-related, centralized volcanism and the emplacement of large-volume flow units, *J. Geophys. Res.*, *97*, 15,991–16,015, 1992.

Malahoff, A., Geology of the summit of Loihi submarine volcano, in *Volcanism in Hawaii, vol. 1*, edited by R. W. Decker, T. L. Wright, and P. H. Stauffer, U. S. Geol. Surv. Prof. Pap. 1350, pp. 133–144. 1987.

Malinverno, A., Inverse square-root dependence of mid-ocean-ridge flank roughness on spreading rate, *Nature*, *352*, 58–60, 1991.

McBirney, A. R., and H. Williams, *Geology and Petrology of the Galápagos Islands*, mem. 118, Geol. Soc. Amer., Boulder, Colo., 197 pp., 1969.

McCoy, F. W., and C. Sancetta, North Pacific sediments, in *The Ocean Basins and Margins, vol. 7A*, edited by A. E. M. Nairn, F. G. Stehli, and S. Uyeda, pp. 1–64, Plenum, New York, 1985.

McGarr, A., On the state of lithospheric stress in the absence of applied tectonic forces, *J. Geophys. Res.*, *93*, 13,609–13,617, 1988.

McGill, G. E., Hotspot evolution and Venusian tectonic style, *J. Geophys. Res.*, *99*, 23149–23161, 1994.

McGovern, P. J., and S. C. Solomon, Estimates of elastic plate thicknesses beneath large volcanoes on Venus (abstract), in *International Colloquium on Venus*, pp. 68–70, Houston, Tex., Lunar and Planetary Institute, 1992.

McGovern, P. J., and S. C. Solomon, State of stress, faulting, and eruption characteristics of large volcanoes on Mars, *J. Geophys. Res.*, *98*, 23553–23579, 1993.

McGovern, P. J., and S. C. Solomon, Factors affecting the growth, development, and structure of large volcanoes on Venus (abstract), *Lunar Planet. Sci. 26*, pp. 939–940, 1995.

McGovern, P. J., M. Simons, and S. C. Solomon, Estimates of elastic lithosphere thickness and heat flux beneath large volcanoes on Venus (abstract), *Lunar Planet. Sci. 26*, pp. 941–942, 1995.

McNutt, M. K., and L. Shure, Estimating the Compensation Depth of the Hawaiian Swell with Linear Filters, *J. Geophys. Res.*, *91*, 13915–13923, 1986.

McNutt, M. K., K. Fischer, S. Kruse, and J. Natland, The origin of the Marquesas Fracture Zone ridge and its implications for the nature of hot spots, *Earth Planet. Sci. Lett.*, *91*, 381–393, 1989.

Melosh, H. J., and A. Raefsky, The dynamical origin of subduction zone topography, *Geophys. J. Roy. Astron. Soc.*, *60*, 333–354, 1980.

Melosh, H. J., and A. Raefsky, Anelastic response of the Earth to a dip slip earthquake, *J. Geophys. Res.*, *88*, 515–526, 1983.

Melosh, H. J., and C. A. Williams, Jr., Mechanics of graben formation in crustal rocks: A finite element analysis, *J. Geophys. Res.*, *94*, 13,961–13,973, 1989.

Menard, H. W., Archipelagic aprons, *Bull. Amer. Assoc. Petrol. Geol.*, *40*, 2195–2210, 1956.

Monnereau, M., and A. Cazenave, Depth and geoid anomalies over oceanic hotspot swells: A global survey, *J. Geophys. Res.*, *95*, 15429–15438, 1990.

Moore, J. C., S. Roeske, N. Lundberg, J. Schoonmaker, D. S. Cowan, E. Gonzales, and S. E. Lucas, Scaly fabrics from Deep Sea Drilling Project cores from forearcs, in *Structural Fabrics in Deep Sea Drilling Project Cores from Forearcs*, edited by J. C. Moore, Memoir 166, pp. 55–73, Geol. Soc. Amer., Boulder, Colo., 160 pp., 1986.

Moore, J. G., Subsidence of the Hawaiian Ridge, in *Volcanism in Hawaii*, edited by R. W. Decker, T. L. Wright, and P. H. Stauffer, vol. 1, *U.S. Geol. Surv. Prof. Pap., 1350*, pp. 85–100, 1987.

Moore, J. G., and J. F. Campbell, Age of tilted reefs, Hawaii, *J. Geophys. Res.*, *92*, 2641–2646, 1987.

Moore, J. G., D. A. Clague, R. T. Holcomb, P. W. Lipman, W. R. Normark, and M. E. Torresan, Prodigious submarine landslides on the Hawaiian Ridge, *J. Geophys. Res.*, *94*, 17465–17484, 1989.

Morgan, W. J., Deep mantle convection plumes and plate motions, *Bull. Amer. Assoc. Pet. Geol.*, *56*, 203–213, 1972.

Morgan, W. J., Hotspot tracks and the opening of the Atlantic and Indian Oceans, in *The Sea, vol. 7, The Oceanic Lithosphere*, edited by C. Emiliani, pp. 443–487, Wiley, New York, 1981.

Mouginis-Mark, P. J., L. Wilson, and M. T. Zuber, The physical volcanology of Mars, in *Mars*, edited by H. H. Kieffer, B. M. Jakosky, C. W. Snyder, and M. S. Matthews, pp. 424–452, Univ. Arizona Press, Tucson, 1992.

Nakamura, K., Why do long rift zones develop in Hawaiian volcanoes - a possible role of thick oceanic sediments, *Bull. Volcanol. Soc. Japan*, *25*, 255–269, 1980.

Namiki, N., and S. C. Solomon, Impact crater densities on volcanoes and coronae on Venus: Implications for volcanic resurfacing, *Science*, *265*, 929–933, 1994.

Natland, J. H., and M. K. McNutt, Submarine stages of Marquesan volcanism (abstract), *Eos Trans. AGU*, *68*, 1451, Fall meeting suppl., 1987.

Naumann, T., and D. Geist, Morphologic development of Galapagos shield volcanoes: Evidence from Cerro Azul, Isabela Island (abstract), *Eos Trans. AGU*, *74*, 643, 1993.

Nordlie, B. E., Morphology and structure of the western Galapagos volcanoes and a model for their origin, *Geol. Soc. Am. Bull.*, *84*, 2391–2956, 1973.

Owen, S., P. Segall, J. Freymueller, A. Miklius, R. Denlinger, T. Árnadóttir, M. Sako, and R. Bürgmann, Rapid deformation of the south flank of Kilauea volcano, Hawaii, *Science*, *267*, 1328–1332, 1995.

Parfitt, E. A., and J. W. Head, Buffered and unbuffered dike emplacement on Earth and Venus: Implications for magma reservoir size, depth, and rate of magma replenishment, *Earth Moon Planets*, *61*, 249–281, 1993.

Parmentier, E. M., and P. C. Hess, Chemical differentiation of a convecting planetary interior: Consequences for a one-plate planet such as Venus, *Geophys. Res. Lett.*, *19*, 2015–2018, 1992.

Pavri, B., J. W. Head, K. B. Klose, and L. Wilson, Steep-sided domes on Venus: Characteristics, geologic setting, and eruption conditions from Magellan data, *J. Geophys. Res.*, *97*, 13,445–13,478, 1992.

Peterson, D. W., and R. B. Moore, Geologic history and evolution of geologic concepts, island of Hawaii, in *Volcanism in Hawaii, vol. 1*, edited by R. W. Decker, T. L. Wright, and P. H. Stauffer, *U.S. Geol. Surv. Prof. Pap.*, 1350, pp. 149–189, 1987.

Phillips, R. J., Estimating lithospheric properties at Atla Regio, Venus, *Icarus*, *112*, 147–170, 1994.

Phillips, R. J., R. F. Raubertas, R. E. Arvidson, I. C. Sarkar, R. R. Herrick, N. Izenberg, and R. E. Grimm, Impact craters and Venus resurfacing history, *J. Geophys. Res.*, *97*, 15,923–15,948, 1992.

Pollard, D. D., Elementary fracture mechanics applied to the structural interpretation of dykes, in *Mafic Dyke Swarms*, edited by H. C. Halls and W. F. Fahrig, Geol. Assn. of Canada Spec. Paper 34, pp. 5–24, 1987.

Price, M., and J. Suppe, Mean age of rifting and volcanism on Venus deduced from impact crater densities, *Nature*, *372*, 756–757, 1994.

Rançon, J. P., P. Lerebour, and T. Augé, The Grand Brule exploration drilling: New data on the deep framework of the Piton de la Fournaise volcano. Part 1: Lithostratigraphic units and volcanostructural implications, *J. Volcanol. Geotherm. Res.*, *36*, 113–127, 1989.

Rappaport, N. R., and J. J. Plaut, A 360-degree and -order model of Venus topography, *Icarus*, *112*, 27–33, 1994.

Rees, B. A., R. S. Detrick, and B. J. Coakley, Seismic stratigraphy of the Hawaiian flexural moat, *Geol. Soc. Am. Bull.*, *105*, 189–205, 1993.

Robinson, M. S., and H. Garbeil, Volumes and depth of burial of the lesser Tharsis volcanoes (abstract), in *Lunar Plan. Sci. 25*, pp. 1141–1142, Lunar and Planetary Institute, Houston, Tex., 1994.

Rowland, S. K., and D. C. Munro, The caldera of Volcan Fernandina: A remote sensing study of its structure and recent activity, *Bull. Volcanol.*, *55*, 97–109, 1992.

Rowland, S. K., D. C. Munro, and V. Perez-Oviedo, Volcán Ecuador, Galapágos Islands: Erosion as a possible mechanism for the generation of steep-sided basaltic volcanoes, *Bull. Volcanol.*, *56*, 271–283, 1994.

Rubin, A. M., A comparison of rift-zone tectonics in Iceland and Hawaii, *Bull. Volcanol.*, *52*, 302–319, 1990.

Rubin, A. M., and D. D. Pollard, Origin of blade-like dikes in volcanic rift zones, in *Volcanism in Hawaii, vol. 2*, edited by R. W. Decker, T. L. Wright, and P. H. Stauffer, *U.S. Geol. Surv. Prof. Pap.*, 1350, pp. 1449–1470, 1987.

Ryan, M. P., Neutral buoyancy and the mechanical evolution of magmatic systems, in *Magmatic Processes: Physiochemical Principles*, edited by B. O. Mysen, Geochem. Soc. Spec. Pub. 1, pp. 259–287, Univ. Park, Penn., 1987.

Ryan, M. P., The mechanics and three-dimensional internal structure of active magmatic systems: Kilauea volcano, Hawaii, *J. Geophys. Res.*, *93*, 4213–4248, 1988.

Ryan, M. P., Neutral-buoyancy controlled magma transport and storage in mid-ocean ridge magma reservoirs and their sheeted-dike complex: A summary of basic relationships, in *Magmatic Systems*, edited by M. P. Ryan, pp. 97–138, Academic Press, San Diego, 1994.

Ryan, M. P., J. Y. K. Blevins, A. T. Okamura, and R. Y. Koyanagi, Magma reservoir subsidence mechanics: Theoretical summary and application to Kilauea volcano, Hawaii, *J. Geophys. Res.*, *88*, 4147–4181, 1983.

Sakimoto, S. E. H., and M. T. Zuber, The spreading of variable-viscosity axisymmetric radial gravity currents: Applications to the emplacement of Venusian 'pancake' domes, *J. Fluid Mech.*, *301*, 65–77, 1995.

Schaber, G. G., R. G. Strom, H. J. Moore, L. A. Soderblom, R. L. Kirk, D. J. Chadwick, D. D. Dawson, L. R. Gaddis, J. M. Boyce and J. Russell, Geology and distribution of impact craters on Venus: What are they telling us?, *J. Geophys. Res.*, *97*, 13,257–13,302, 1992.

Schlich, R., The Indian Ocean: Aseismic ridges, spreading centers, and oceanic basins, in *The Ocean Basins and Margins, vol. 6*, edited by A. E. M. Nairn and F. G. Stehli, pp. 51–147, Plenum, New York, 1982.

Schubert, G., S. C. Solomon, D. L. Turcotte, M. J. Drake, and N. H. Sleep, Origin and thermal evolution of Mars, in *Mars*, edited by H. H. Kieffer, B. M. Jakosky, C. W. Snyder, and M. S. Matthews, pp. 147–183, Univ. Arizona Press, Tucson, Ariz., 1992.

Schultz, R. A., Brittle strength of basaltic rock masses with applictations to Venus, *J. Geophys. Res.*, *98*, 10,883–10,895, 1993.

Sen, G., and R. E. Jones, Cumulate xenolith in Oahu, Hawaii: Implications for deep magma chambers and Hawaiian volcanism, *Science*, *249*, 1154–1157, 1990.

Senske, D. A., G. G. Schaber, and E. R. Stofan, Regional topographic rises on Venus: Geology of Western Eistla Regio and comparison to Beta Regio and Atla Regio, *J. Geophys. Res.*, *97*, 13,395–13,420, 1992.

Shaw, H. R., The fracture mechanisms of magma transport from the mantle to the surface, in *Physics of Magmatic Processes*, pp. 201–264, Princeton Univ. Press, Princeton, N. J., 1980.

Shipboard Scientific Party, Site 74, in *Initial Reports of the Deep Sea Drilling Project, vol. 8*, edited by J. I. Tracey, Jr., et al., pp. 621–674, U.S. Government Printing Office, Washington, D.C., 1971a.

Shipboard Scientific Party, Site 75, in *Initial Reports of the Deep Sea Drilling Project, vol. 8*, edited by J. I. Tracey, Jr., et al., pp. 675–709, U.S. Government Printing Office, Washington, D.C., 1971b.

Shipboard Scientific Party, Site 239, in *Initial Reports of the Deep Sea Drilling Project*, edited by E. S. W. Simpson, R. Schlich, et al., *vol. 25*, pp. 25–63, U.S. Government Printing Office, Washington, D.C., 1972.

Shipboard Scientific Party, Site 367, in *Initial Reports of the Deep Sea Drilling Project*, edited by Y. Lancelot, E. Seibold, et al., *41*, pp. 163–232, U.S. Government Printing Office, Washington, D.C., 1977a.

Shipboard Scientific Party, Site 368, in *Initial Reports of the Deep Sea Drilling Project*, edited by Y. Lancelot, E. Seibold, et al., *41*, pp. 233–326, U.S. Government Printing Office, Washington, D.C., 1977b.

Shipboard Scientific Party, Site 369, in *Initial Reports of the Deep Sea Drilling Project*, edited by Y. Lancelot, E. Seibold, et al., *41*, pp. 327–421, U.S. Government Printing Office, Washington, D.C., 1977c.

Shipboard Scientific Party, Site 505: Sediments and ocean crust in an area of low heat flow south of the Costa Rica rift, in *Initial Reports of the Deep Sea Drilling Project*, edited by J. R. Cann, M. G. Langseth, J. Honnorez, R. P. V. Herzen, S. M. White, et al., *69*, pp. 175–214, U.S. Government Printing Office, Washington, D.C., 1983.

Shipboard Scientific Party, Sites 677 and 678, in *Proc. ODP, Init. Repts.*, edited by K. Becker, H. Sakai, et al., *111*, pp. 253–346, College Station, Tex., (Ocean Drilling Program), 1988.

Shipboard Scientific Party, Site 842, in *Proc. ODP, Init. Repts.*, edited by A. Dziewonski, R. Wilkens, J. Firth, et al., *136*, pp. 37–63, College Station, Tex., (Ocean Drilling Program), 1992a.

Shipboard Scientific Party, Site 843, in *Proc. ODP, Init. Repts.*, edited by A. Dziewonski, R. Wilkens, J. Firth, et al., *136*, pp. 65–99, College Station, Tex., (Ocean Drilling Program), 1992b.

Simkin, T., Origin of some flat-topped volcanoes and guyots, in *Studies in Earth and Space Sciences: A Memoir in Honor of Harry Hammond Hess*, edited by R. Shagam, R. B. Hargraves, W. J. Morgan, F. B. V. Houten, C. A. Burk, H. D. Holland, and L. C. Hollister, Geol. Soc. of Amer. Mem. 132, pp. 183–193, Boulder, Colo., 1972.

Simkin, T., Geology of Galápagos Islands, in *Galapagos*, edited by R. Perry, Key Environments series, pp. 15–41, Pergamon Press, Oxford, 1984.

Simons, M., Localization of gravity and topography: Constraints on the tectonics and mantle dynamics of Earth and Venus, Ph.D. thesis, Massachusetts Institute of Technology, Cambridge, 209 pp., 1995.

Simons, M., S. C. Solomon, and B. H. Hager, Admittance constraints on the thickness of the Venusian lithosphere? (abstract), *Lunar Planet. Sci. 26*, pp. 1305–1306, 1995.

Smith, D. E., F. J. Lerch, R. S. Nerem, M. T. Zuber, G. B. Patel, S. K. Fricke, and F. G. Lemoine, An improved gravity field for Mars: Goddard Mars Model 1, *J. Geophys. Res.*, *98*, 20,871–20,889, 1993.

Snyder, C. W., and V. I. Moroz, Spacecraft exploration of Mars, in *Mars*, edited by H. H. Kieffer, B. M. Jakosky, C. W. Snyder, and M. S. Matthews, pp. 71–119, Univ. Arizona Press, Tucson, 1992.

Solomon, S. C., et al., Venus tectonics: An overview of Magellan observations, *J. Geophys. Res.*, *97*, 13,199–13,256, 1992.

Squyres, S. W., S. M. Clifford, R. O. Kuzmin, J. R. Zimbelman, and F. M. Costard, Ice in the Martian regolith, in *Mars*, edited by H. H. Kieffer, B. M. Jakosky, C. W. Snyder, and M. S. Matthews, pp. 523–554, Univ. Arizona Press, Tucson, 1992a.

Squyres, S. W., D. M. Janes, G. Baer, D. L. Bindschadler, G. Schubert, E. L. Sharpton, and E. R. Stofan, The morphology and evolution of coronae on Venus, *J. Geophys. Res.*, *97*, 13,611–13,634, 1992b.

Staudigel, H., and H.-U. Schminke, The Pliocene seamount series of La Palma/Canary Islands, *J. Geophys. Res.*, *89*, 11,195–11,215, 1984.

Staudigel, H., G. Feraud, and G. Giannerini, The history of intrusive activity on the island of La Palma (Canary Islands), *J. Volcanol. Geotherm. Res.*, *27*, 299–322, 1986.

Stofan, E. R., V. L. Sharpton, G. Schubert, G. Baer, D. L. Bindschadler, D. M. Janes, and S. W. Squyres, Global distribution and characteristics of coronae and related features on Venus: Implications for origin and relation to mantle processes, *J. Geophys. Res.*, *97*, 13,347–13,378, 1992.

Stofan, E. R., S. E. Smrekar, D. L. Bindschadler, and D. A. Senske, Large topographic rises on Venus: Implications for mantle upwelling, *J. Geophys. Res.*, *100*, 23,317–23,327, 1995.

Strom, R. G., G. G. Schaber, and D. D. Dawson, The global resurfacing of Venus, *J. Geophys. Res.*, *99*, 10899–10926, 1994.

Swanson, D. A., W. A. Duffield, and R. S. Fiske, Displacement of the south flank of Kilauea Volcano: The result of intrusion of magma into the rift zones, *U.S. Geol. Surv. Prof. Pap.*, 963, p. 39, 1976.

Tanaka, K. L., Ice-lubricated gravity spreading of the Olympus Mons aureole deposits, *Icarus*, *62*, 191–206, 1985.

ten Brink, U., Volcano spacing and plate rigidity, *Geology*, *19*, 397–400, 1991.

ten Brink, U. S., and T. M. Brocher, Multichannel seismic evidence for a subcrustal intrusive complex under Oahu and a model for Hawaiian volcanism, *J. Geophys. Res.*, *92*, 13,687–13,707, 1987.

ten Brink, U. S., and A. B. Watts, Seismic stratigraphy of the flexural moat flanking the Hawaiian Islands, *Nature*, *317*, 421–424, 1985.

Thomas, P. J., S. W. Squyres, and M. H. Carr, Flank tectonics of Martian volcanoes, *J. Geophys. Res.*, *95*, 14,345–14,355, 1990.

Thurber, C. H., and A. E. Gripp, Flexure and seismicity beneath the south flank of Kilauea volcano and tectonic implications, *J. Geophys. Res.*, *93*, 4271–4278, 1988.

Thurber, C. H., and M. N. Toksöz, Martian lithospheric thickness from elastic flexure theory, *Geophys. Res. Lett.*, *5*, 977–980, 1978.

Thurber, C. H., Y. Li, and C. Johnson, Seismic detection of a low-velocity layer beneath the southeast flank of Mauna Loa, Hawaii, *Geophys. Res. Lett.*, *16*, 649–652, 1989.

Tilling, R. I., and J. J. Dvorak, Anatomy of a basaltic volcano, *Nature*, *363*, 125–133, 1993.

Turcotte, D. L., How does Venus lose heat?, *J. Geophys. Res.*, *100*, 16,931–16,940, 1995.

Vogt, P. R., Volcano height and plate thickness, *Earth Planet. Sci. Lett.*, *23*, 337–348, 1974a.

Vogt, P. R., Volcano spacing, fractures, and the thickness of the lithosphere, *Earth Planet. Sci. Lett.*, *21*, 235–252, 1974b.

Waggoner, D. G., The age and alteration of central Pacific oceanic crust near Hawaii, site 843, in *Proc. ODP, Sci. Results*, edited by R. H. Wilkens, J. Firth, J. Bender, et al., *136*, pp. 119–132, Ocean Drilling Program, College Station, Tex., 1993.

Walker, G. P. L., "Coherent intrusion complexes" in large basaltic volcanoes- a new structural model, *J. Volcanol. Geotherm. Res.*, *50*, 41–54, 1992.

Walsh, J. B., and W. F. Brace, The effect of pressure on porosity and the transport properties of rock, *J. Geophys. Res.*, *89*, 9425–9431, 1984.

Watters, T. R., and D. M. Janes, Coronae on Venus and Mars: Implications for similar structures on Earth, *Geology*, *23*, 200–204, 1995.

Watts, A. B., Crustal structure, gravity anomalies and flexure of the lithosphere in the vicinity of the Canary Islands, *Geophys. J. Int.*, *119*, 648–666, 1994.

Watts, A. B., and U. S. ten Brink, Crustal structure, flexure, and subsidence history of the Hawaiian Islands, *J. Geophys. Res.*, *94*, 10,473–10,500, 1989.

Wessel, P., Thermal Stresses and the Bimodal Distribution of Elastic Thickness Estimates of Oceanic Lithosphere, *J. Geophys. Res.*, *97*, 14177–14193, 1992.

Wessel, P., A reexamination of the flexural deformation beneath the Hawaiian Islands, *J. Geophys. Res.*, *98*, 1217–12190, 1993.

Wessel, P., and W. H. F. Smith, Free software helps map and display data, *Eos Trans. AGU*, *72*, 441, 1991.

White, R., and D. McKenzie, Magmatism at rift zones: The generation of volcanic continental margins and flood basalts, *J. Geophys. Res.*, *94*, 7685–7729, 1989.

Wilson, J. T., Evidence from ocean islands suggesting movement in the earth, *Royal Soc. London Philos. Trans., ser. A*, *258*, 145–167, 1965.

Wilson, L., J. W. Head, III, and E. A. Parfitt, The relationship between the height of a volcano and the depth to its magma source zone: A critical reexamination, *Geophys. Res. Lett.*, *19*, 1395–1398, 1992.

Wolfe, C. J., M. K. McNutt, and R. S. Detrick, The Marquesas archipelagic apron: Seismic stratigraphy and implications for volcano growth, mass wasting, and crustal underplating, *J. Geophys. Res.*, *99*, 13591–13608, 1994.

Wyllie, P. J., Solidus curves, mantle plumes, and magma generation beneath Hawaii, *J. Geophys. Res.*, *93*, 4171–4181, 1988.

Wyss, M., Hawaiian rifts and recent Icelandic volcanism: Expressions of plume generated radial stress fields, *J. Geophys*, *47*, 19–22, 1980.

Wyss, M., and R. Y. Koyanagi, Seismic gaps in Hawaii, *Bull. Seism. Soc. Am.*, *82*, 1373–1387, 1992.

Wyss, M., B. Liang, W. R. Tanigawa, and X. Wu, Comparison of orientations of stress and strain tensors based on fault plane solutions in Kaoiki, Hawaii, *J. Geophys. Res.*, *97*, 4769–4790, 1992a.

Wyss, M., D. Gillard, and B. Liang, An estimate of the absolute stress tensor in Kaoiki, Hawaii, *J. Geophys. Res.*, *97*, 4763–4768, 1992b.

Zuber, M. T., and P. J. Mouginis-Mark, Caldera subsidence and magma chamber depth on the Olympus Mons volcano, Mars, *J. Geophys. Res.*, *97*, 18,295–18,307, 1992.

Zucca, J. J., and D. P. Hill, Crustal structure of the southeast flank of Kilauea volcano, Hawaii, from seismic refraction measurements, *Bull. Seismol. Soc. Am.*, *70*, 1149–1159, 1980.